Volcanic gases and the reaction of sulfur dioxide with aluminosilicate glasses

Christian Josef Renggli

2018

A thesis submitted for the degree of Doctor of Philosophy of

The Australian National University

Declaration

The work in this thesis is my own except where otherwise acknowledged.

I certify that the presented thesis does not contain research previously submitted for a degree at a university.

Christian Josef Renggli

May 2018

Acknowledgments

I thank my supervisor Penny King for the guidance, trust and inspiration to follow my own ideas. Penny is a role model as a researcher and supervisor, but also as an engaged leader in the university's community, supporting and standing up for others and fighting for equity in science and beyond. I thank Dick Henley for his mentorship and many thought provoking ideas that were critical for the success of this research. Marc Norman was always supportive and I thank him for his contribution to the development of a model for volcanic gas composition on the Moon. My advisors Trevor Ireland, Richard Arculus and Pierre Delmelle contributed thoughts and ideas in seminars, at morning teas and conferences, which helped this project to move forward.

The research presented in this thesis was supported by Australian Research Council funding to Penny King (DP150104604 and FT130101524) and an ANU PhD scholarship to myself.

I thank all the members of the ANU SPEC-E Lab for their help with analysis, feedback on presentations and supportive collegiality. The help from Ulli Troitzsch and Terry Mernagh was invaluable. It has been a real pleasure to work with Andrew Palm on experiments and data analysis and I am looking forward to continue doing so in the future. I appreciated the useful group discussions with Rachel Kirby, Leo Pure, Liane Loiselle and Shannon McConachie.

I am grateful for the support from the RSES administrators on which I could always rely. In particular I thank Maree Coldrick, Robyn Petch and Josephine Magro. Thanks to those who've helped me with analytical work at RSES and elsewhere, including Paul Guagliardo, Linda McMorrow, Michael Turner, Jill Middleton, Antony Burnham and Charles Le Losq.

RSES is a great place to do a PhD, in particular because of the supportive student and ERC cohort, with whom I've been privileged to share many great adventures (thanks to Jennifer Prichard, Jessica Lowczak and Morgan Williams for organizing an unforgettable trip to the red center), parties, many cakes (!) and trips to the coast. I've been lucky to share my office with wonderfully supportive people, Patrick Goodarzi and Shayne Lakey.

I would not have made it through these four years without my friends, mates and housemates, in particular Rose Manceau, Joëlle D'Andrès, Emmanuel and Claire David and Julien Ducommun. Thank you for sharing great evening and your support in more difficult moments!

Playing music has kept me over the water, provided the necessary distraction and allowed me to let off some steam. Thanks to Robert Burne, who's introduced me to the National Capital Orchestra (and the ooids of course) and who has become a friend and mentor. The NCO was like a second family and I am grateful for many musical moments. Thanks to Lenny Weiss for introducing me to new Australian music and allowing me to help out in the Canberra Youth Orchestra, it was a blast. Thanks also to Nesha Aine and Matthew Gambrill for all the musical fun and a great holiday in Sydney. It's great to have you as friends!

I also thank all my friends back home, who've taken it up on themselves to come the long way and visit me in Australia. Thanks Fabian Feissli, May Szedlak and Stefan Naef.

I apologize to my parents, my brother Andreas and my grandmother for having been so far away for such a long time. Thank you for your support that you've always given me!

Abstract

Volcanic gases are an important part of the volatile cycle in active planetary systems and contribute significantly to the mobilization and transport of metals to planetary surfaces. On Earth, Venus, Mars and Io, SO_2 is the most abundant corrosive species in volcanic gases, and basalts are ubiquitous on these planetary bodies. The reaction between SO_2 and silicate rocks forms oxidized sulfate and reduced sulfide. This reaction is a key process in the formation of porphyry deposits. In volcanic eruption plumes SO_2 reacts with volcanic ash and is scavenged onto the surface of the ash particles. Knowledge of the reaction mechanisms between volcanic gas and rocks, minerals and glasses, and processes controlling the metal mobilization and transport in volcanic gas can constrain models of volatile and metal budgets of planetary crusts and surfaces.

Using thermochemical modelling, I present a new model for the composition of volcanic gas on the Moon and compare it to a terrestrial volcanic gas from Erta Ale volcano (Ethiopia). The main species in lunar volcanic gas are H_2, S_2 and CO. This finding is in contrast to previous studies which suggested that CO was the sole driver of explosive volcanic eruptions on the Moon. This lunar volcanic gas has a lower capacity for metal transport compared to the Cl- and H_2O-rich volcanic gas from Erta Ale volcano.

To identify how SO_2-glass reactions occur at high temperature and to investigate what might promote and limit these reactions, I present results from an experimental study. Pure SO_2 was reacted with silicate glasses in the system anorthite-diopside-albite and with Fe-bearing natural basaltic glasses.

The sulfate reaction products are relatively enriched in Ca compared to the silicate glass composition, in particular in experiments with Fe-free anorthite-diopside glasses. On these Fe-free glasses $CaSO_4$ is the sole observed phase in the coatings at 800 °C, whereas at 600 °C minor amounts of $MgSO_4$ were detected. At 800 °C, the flux of Ca from the silicate glass to the surface exceeds that of Mg by a factor of up to 330, whereas at 600 °C this factor is only 3. The rate of reaction is not constant, decreasing by an order of magnitude from 1 h to 24 h at 800 °C.

The reaction of SO_2 with tholeiitic basalt glasses produces coatings of $CaSO_4$, $MgSO_4$, Na_2SO_4 and oxides including Fe_2O_3 and TiO_2. In addition, the reaction modifies the basalt glass because Ca, Mg and Na are lost to the coating. This results in the nucleation of crystalline spherulites and needles including SiO_2, Al_2O_3, as well as Fe-Na-rich and Mg-rich pyroxenes.

The results suggest that the structural properties of the silicate glass substrate control the diffusive transport of Ca, Na, Mg, Fe and Ti to the surface which in turn controls the overall reaction rate and the formation of sulfates, oxides and silicates. These findings can be applied to predicting reactions on planetary surfaces and at shallow levels within their crusts.

Table of Contents

1 Introduction

In this thesis, I first present a comparative study of a new model for the composition, speciation and metal transport in a volcanic gas on the Moon with a terrestrial volcanic gas from Erta Ale volcano (Ethiopia). Second, I present results from experiments investigating the reactive behavior of $SO_{2(g)}$ with basaltic aluminosilicate glasses at high temperature (600 – 800 °C). These investigations are concerned with the composition, properties and reactive behavior of volcanic gas.

1.1 Volcanic gas and sulfur dioxide

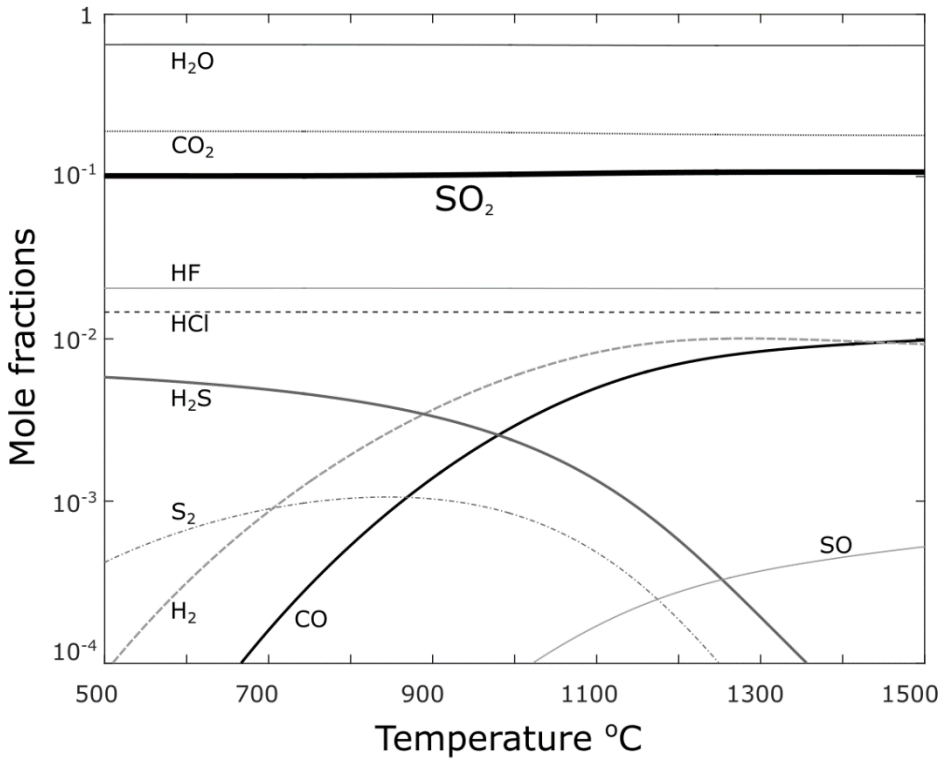

Figure 1-1: Calculated speciation of a terrestrial volcanic gas (Chapter 2) based on an analysis from Erta Ale volcano sampled at 1084 °C (Zelenski et al., 2013). The diagram shows the mole fractions of the major gas species calculated by Gibbs Free Energy minimization. $SO_{2(g)}$ is the third most abundant gas species.

Volcanic gases on Earth primarily consist of $H_2O_{(g)}$, $CO_{2(g)}$ and $SO_{2(g)}$ in addition to minor species including $HF_{(g)}$, $HCl_{(g)}$, $H_2S_{(g)}$, $CO_{(g)}$, $H_{2(g)}$, $S_{2(g)}$ and $SO_{(g)}$ (Figure 1-1). Emitted at high temperatures of up to 1100 °C, volcanic gases are an important component of global volatile and metal cycles (Nriagu, 1989; Hinkley et al., 1999; Halmer et al., 2002; Mather et al., 2012; Allard et al., 2016; Henley and Hughes, 2016).

In addition to these volatile species, volcanic gases transport significant amounts of metals at high temperatures, which are deposited with decreasing temperature and pressure (Symonds et al., 1987; Le Cloarec et al., 1992; Symonds et al., 1992; Africano et al., 2002; Aiuppa et al., 2004; Zelenski et al., 2013). Metals transported in volcanic gases include alkalis, chalcophiles such as Cu, Zn, Ga, Pb, As, Te, Cd and Se, highly siderophile elements including Re, Os, Au, Ir and Pt, and siderophile elements like Ni, Fe, Mo, and Co (Zelenski et al., 2013). In the gas phase, the metals are predominantly transported as chlorides and sulfides, but also as bromides, oxides, fluorides, iodides and elemental gas (Symonds et al., 1987; Wahrenberger et al., 2002). At fumaroles, these metals are deposited as highly diverse mineral assemblages, including oxides, silicates, sulfides, sulfates, halides and native metals (Symonds et al., 1987; Africano et al., 2002; Wahrenberger et al., 2002; Zelenski et al., 2013; Balic-Zunic et al., 2016). Metals are mobilized from silicates by degassing and volatilization or by reactive element mobilization. On the Moon, a volatile-poor planetary body (Heiken et al., 1991), volcanic gas must have had a significantly different composition. How this difference affects metal transport and deposition is discussed in Chapter 2.

Gaseous sulfur dioxide, the third most abundant volcanic gas species (Figure 1-1), is a symmetric molecule with a S^{4+} cation bonding to two O^{2-} anions. The charge distributions over the molecule are such that the S-atom has a partial positive charge, and the O-atoms have partial negative charges (Grabowsky et al., 2012). This uneven charge distribution makes $SO_{2(g)}$ a highly reactive gas species, which readily chemisorbs onto silicate materials (Henley et al., 2015).

Globally, volcanoes emit 15-21x10^{12} g of $SO_{2(g)}$ into the atmosphere every year (Halmer et al., 2002). This is equivalent to approximately 20 km^3 of pure $SO_{2(g)}$ at 1000 °C. Large cataclysmic eruptions may emit the same amount of $SO_{2(g)}$ in a single event, such as the large explosive eruption of Mount Pinatubo in June 1991 emitting ~20x10^{12} g of $SO_{2(g)}$ (Bluth et al., 1992). These large gas fluxes have a significant potential effect on global element cycles in volcanic systems as the gas reacts with silicates in the sub-volcanic environment and in the plumes of explosive eruptions.

1.2 Gas-solid reaction environments in volcanic systems

1.2.1 Terrestrial volcanic systems

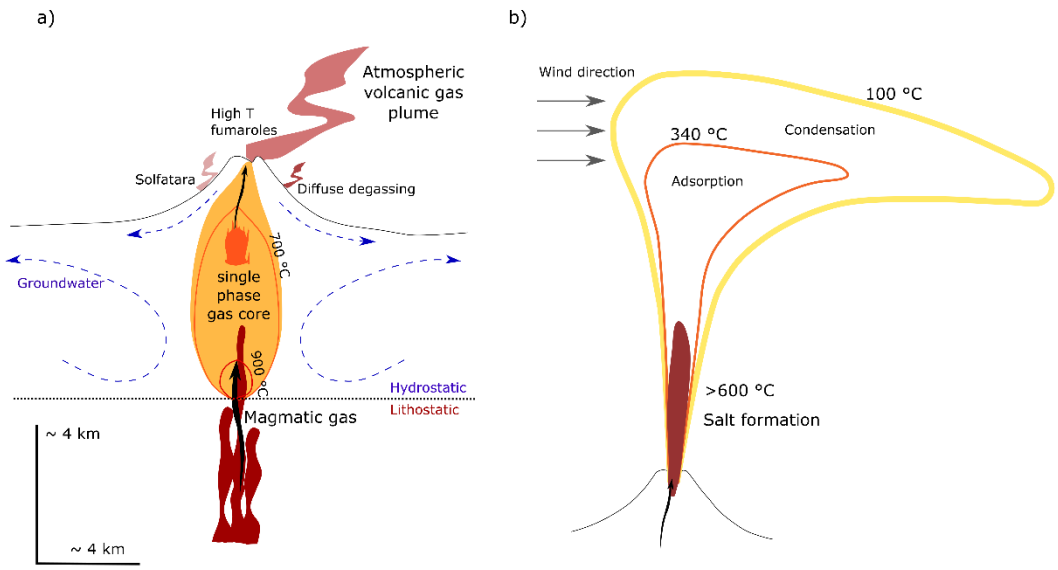

Figure 1-2: Volcanic environments where reactions between $SO_{2(g)}$ and aluminosilicates occur at high temperature. a) The gas expands from its magmatic source to form a high temperature single phase gas core at T > 600 °C (after Henley et al., 2015; Henley and Seward, 2018). b) Explosive volcanic eruption plume with a high temperature core where gas and ash particles react to form salts (after Oskarsson, 1980).

Figure 1-2 shows the two volcanic environments where high temperature reactions between $SO_{2(g)}$ and aluminosilicates occur. First, as the volcanic gas expands from its magmatic source it forms a high temperature gas core in the subvolcanic environment. This single-phase gas core corresponds to a high temperature gas-solid reactor which is continuously replenished by hot reactive gas (Henley and McNabb, 1978; Henley and Berger, 2013; Henley et al., 2015; Henley and Hughes, 2016; Henley et al., 2017; Henley and Seward, 2018). Second, similar gas-solid reactions occur in the core of hot volcanic eruption columns where up to 40% of the $SO_{2(g)}$ may be scavenged from the gas phase (Óskarsson, 1980; Ayris et al., 2013; Delmelle et al., 2018).

In both processes anhydrite ($CaSO_4$) is a primary product of the reaction with $SO_{2(g)}$. In the subvolcanic environment the sulfate is further associated with sulfide ore minerals such as bornite and chalcopyrite forming valuable porphyry and skarn deposits (Henley et al., 2015; Henley et al., 2017). On volcanic ashes, salts further include other sulfates and halides (Rose, 1977; Óskarsson, 1980; Gislason et al., 2011; Barone et al., 2016).

Ayris et al. (2013) investigated the reaction between $SO_{2(g)}$ and glasses (tephrite, phonolite, dacite and rhyolite) at temperatures of up to 800 °C. Anhydrite, the predominant reaction product, was observed after only 30 s of reaction with a gas mixture containing 1 mol% $SO_{2(g)}$. These authors have suggested that the reaction is limited by the diffusion of Ca^{2+} to the glass surface (see also Delmelle et al., 2018). This limitation of the reaction by diffusion in the glass substrate has previously been observed for the formation of Na_2SO_4 on soda-lime-silica glass reacted with $SO_{2(g)}$ (Douglas and Isard, 1949). These early experiments are further discussed in a review in Chapter 5 of this thesis.

1.2.2 Other planetary bodies

Reactions between $SO_{2(g)}$ and silicate materials also occur on other planetary systems in the solar system. $SO_{2(g)}$ was likely a major gas species in past volcanic processes on Mars, contributing to the large amounts of sulfates on the Martian surface (Gaillard and Scaillet, 2009; King and McLennan, 2010; Franz et al., 2018). On Venus, volcanogenic $SO_{2(g)}$ is emitted into a hot (~450 °C) atmosphere (Glaze, 1999; Vandaele et al., 2017) and on Io, $SO_{2(g)}$ is the dominant volcanic gas species (Kumar, 1985; Zolotov and Fegley, 1999; Zolotov and Fegley, 2000; Doute, 2002). On the Moon and Mercury the oxygen fugacities are below the iron-wüstite buffer (IW) (Rutherford and Papale, 2009; Zolotov et al., 2013), preventing abundant $SO_{2(g)}$ in a volcanic gas phase, even though sulfur was likely an important component of volcanic gases on both bodies (Saal et al., 2008; Nittler et al., 2011).

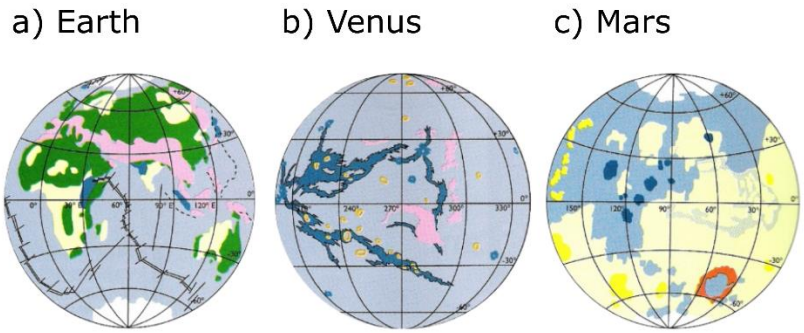

Figure 1-3: Distribution of basalts (blue) on a) Earth, b) Venus and c) Mars. Modified from Beatty et al. (1999).

All terrestrial planets and the Moon have in common that their crustal surfaces to a large part consist of basalts (Figure 1-3; Beatty et al., 1999). For example, the surface of Mars is dominated by tholeiitic basalts, whereas more evolved magmatic rocks are rare, not identified ore missing entirely (McSween et al., 2009). The composition of the surface of Venus is much less well constrained. The early Russian landers of the Venera and Vega missions returned limited data with significant uncertainties, which suggest that large parts

of the planet's surface have a basaltic composition, including tholeiitic basalts (Treiman, 2007). Most basalts on Venus appear to be deposited as lava flows, but calculations have suggested that explosive eruptions, possibly including the formation of basaltic ignimbrites, may have been driven by $SO_{2(g)}$ (Glaze, 1999; Airey et al., 2015). Such eruptions would allow $SO_{2(g)}$ gas-scavenging reactions on Venusian basaltic volcanic ash, similar to those occurring on Earth (Figure 1-2b). On Io $SO_{2(g)}$-rich eruptions are accompanied by hot basalts (Carr, 1986). Volcanic processes on Io include large gas rich plumes, basalt lava flows and pyroclastic deposits (Lopes and Spencer, 2007; Davies et al., 2010; Williams et al., 2011). All of these processes allow extensive reactions between the basalts and $SO_{2(g)}$ at moderate to high temperatures.

The importance of reactions between $SO_{2(g)}$ and rocks on Venus has been noted before, suggesting that this gas species may be removed from the planet's atmosphere via gas-solid reactions. Fegley and Prinn (1989) investigated the reaction between $SO_{2(g)}$ and calcite ($CaCO_3$) to form anhydrite ($CaSO_4$) at 600 – 850 °C. The results suggested that the entire $SO_{2(g)}$ observed in the atmosphere of Venus would be removed by such a reaction in ~1.9×10^6 years (Fegley and Prinn, 1989). Because $SO_{2(g)}$ is also removed by the interaction with ultraviolet sunlight, converting the gas to H_2SO_4 aerosols, the observation of $SO_{2(g)}$ in the planet's atmosphere requires ongoing volcanogenic input of $SO_{2(g)}$ (Fegley and Prinn, 1989). Further, Fegley and Prinn (1989) also described the formation of $CaSO_4$ as a coating on diopside crystals reacted with $SO_{2(g)}$ at 833 °C.

On Io, the S- and Na-rich surface has been suggested to be the product of extensive reaction of silicates with $SO_{2(g)}$ (Johnson and Burnett, 1993; Burnett et al., 1997). These authors conducted reaction experiments between $SO_{2(g)}$ and Na-rich glasses and rocks. The Ca/Na ratio in the silicate controls the formation of the sulfates, with mixtures of $CaSO_4$ and Na-sulfate forming where Ca/Na is high. Where Ca/Na is low only alkali-rich sulfates (Na_2SO_4, K_2SO_4) are observed in the coatings (Johnson and Burnett, 1993; Burnett et al., 1997). The reaction of a Kilauea basalt with a gas mixture of $SO_{2(g)}$ and $O_{2(g)}$ at 850 °C produced $CaSO_4$ and Na-Ca-Mg-sulfate with traces of K and Fe (Johnson and Burnett, 1993), whereas the reaction of the same basalt with pure $SO_{2(g)}$ at 850 °C did not form any sulfate product (Burnett et al., 1997).

Finally, the reaction between $SO_{2(g)}$ and silicates with basaltic compositions may occur when large impacts mobilize both components at high temperatures, allowing their reaction in impact plumes. For example, the Chicxulub impact on the Yucatan Peninsula (Mexico) is estimated to have mobilized two orders of magnitude more $SO_{2(g)}$ compared to annual anthropogenic emissions (Sigurdsson et al., 1992; Pierazzo et al., 2003).

1.3 Objectives and structure of the thesis

This PhD research aims to broaden the understanding of the reactive behavior of volcanic gas. For this purpose, I used a combination of approaches including Gibbs Free Energy minimization calculations and high temperature experiments at atmospheric pressure followed by a diverse range of state-of-the-art analytical methods.

The objective of the first part of this thesis, Chapter 2, is to develop a model for the composition and speciation of a lunar volcanic gas. I use data on volatile concentrations in picritic glass beads from pyroclastic deposits sampled by the Apollo missions, termed orange and green glasses (Saal et al., 2008; Wetzel et al., 2015). I compare this model composition with a terrestrial volcanic gas from Erta Ale volcano (Zelenski et al., 2013). The aim is to investigate the metal transport behavior of these gases by means of thermochemical calculations. The calculations allow an estimation of the pressure and temperature conditions at which metals are transported and deposited from lunar and terrestrial volcanic gases. This chapter is published in *Geochimica et Cosmochimica Act* (Renggli et al., 2017)

As outlined above, $SO_{2(g)}$ is a major reactive species in terrestrial volcanic gases. The objective of the second part of this thesis is to investigate the reactive behavior of $SO_{2(g)}$ with aluminosilicate glasses at high temperatures (600 – 800 °C). The introduction above has highlighted the ubiquity of basalt in planetary crusts and the likelihood of reactions between $SO_{2(g)}$ and basalts on Earth, Venus, Mars and Io. Yet, we know very little about reaction products, mechanisms and rates in this system. For this reason I chose the Anorhtite-Diopside-Albite system for experiments with simple glasses, as an Fe-free analogue for basalts (Morse, 1980). In addition, I have present experiments with Fe-bearing tholeiitic basalt glasses.

The following questions are of importance:

- What are the products in reactions between $SO_{2(g)}$ and basaltic aluminosilicate glasses?
- How does the glass composition affect the gas-solid reaction?
- How do the product coatings evolve with time?
- What is the effect of temperature relative to the glass transition temperature?
- What is the reaction rate controlling mechanism?
- What is the effect of multivalent cations (e.g. $Fe^{2+/3+}$) on the reaction behavior?

In Chapter 3 I present experimental results from reactions between $SO_{2(g)}$ and glasses in the ternary system anorthite-diopside-albite (An-Di-Ab). This system is a simple analogue for basalt glasses (Morse, 1980).

In Chapter 4 I discuss the reaction of $SO_{2(g)}$ with tholeiitic basalt glasses and an Fe-free basalt glass at 700 °C based on experimental work.

Chapter 5 is a review of experimental work on the reaction between $SO_{2(g)}$ and glasses. This chapter provides an overview of experimental work by others and puts my experimental observations presented in Chapters 3 and 4 into their context. This chapter is accepted for publication in *Reviews in Mineralogy & Geochemistry* (Renggli & King, 2018).

Chapter 6 provides a brief summary of the main results of this thesis and discusses avenues for future work.

2 Volcanic gas composition, metal dispersion and deposition during explosive volcanic eruptions on the Moon

This chapter was published in *Geochimica et Cosmochimica Acta*:

Renggli C.J., King P.L., Henley R.W., Norman R.W. (2017) Volcanic gas composition, metal dispersion and deposition during explosive volcanic eruptions on the Moon. Geochimica et Cosmochimica Act, 206, 296-311.

I developed the model for a lunar volcanic gas composition, executed the Gibbs Free Energy minimization calculations, assembled the figures and interpretation and wrote the manuscript. King, Henley and Norman contributed to the design of the model, revised and edited the manuscript.

2.1 Abstract

Transport of metals in volcanic gases on the Moon differs greatly from their transport on the Earth because metal speciation depends largely on gas composition, temperature, pressure and oxidation state. We present a new thermochemical model for the major and trace element composition of lunar volcanic gas during pyroclastic eruptions of picritic magmas calculated at 200-1500 °C and over 10^{-9}-10^{3} bar. Using published volatile component concentrations in picritic lunar glasses, we have calculated the speciation of major elements (H, O, C, Cl, S and F) in the coexisting volcanic gas as the eruption proceeds. The most abundant gases are CO, H_2, H_2S, COS and S_2, with a transition from predominantly triatomic gases to diatomic gases with increasing temperatures and decreasing pressures. Hydrogen occurs as H_2, H_2S, H_2S_2, HCl, and HF, with H_2 making up 0.5 to 0.8 mole fractions of the total H. Water (H_2O) concentrations are at trace levels, which implies that H-species other than H_2O need to be considered in lunar melts and estimates of the bulk lunar composition. The Cl and S contents of the gas control metal chloride gas species, and sulfide gas and precipitated solid species. We calculate the speciation of trace metals (Zn, Ga, Cu, Pb, Ni, Fe) in the gas phase, and also the pressure and temperature conditions at which solids form from the gas. During initial stages of the eruption, elemental gases are the dominant metal species. As the gas loses heat, chloride and sulfide species become more abundant. Our chemical speciation model is applied to a lunar pyroclastic eruption model with isentropic gas decompression. The relative abundances of the deposited metal-bearing solids with distance from the vent are predicted

for slow cooling rates (< 5 °C/s). Close to a volcanic vent we predict native metals are deposited, whereas metal sulfides dominate with increasing distance from the vent. Finally, the lunar gas speciation model is compared with the speciation of a H_2O-, CO_2- and Cl-rich volcanic gas from Erta Ale volcano (Ethiopia) as an analogy for more oxidized planetary eruptions. In the terrestrial Cl-rich gas the metals are predominantly transported as chlorides, as opposed to metallic vapors and sulfides in the lunar gas. Due to the presence of Cl-species, metal transport is more efficient in the volcanic gas from Erta Ale compared to the Moon.

2.2 Introduction

Volcanic gases are an important medium for transporting metallic elements on planetary bodies. Volcanic and magmatic processes, together with impact events, mobilize metals and potentially concentrate them for resource utilization (Colson, 1992). On the Moon, S, F, Cl and a range of metals (e.g. Zn, Ga, Cu, Pb, Ni, Fe) are found coating picritic glass beads in pyroclastic deposits at the Apollo 17 (orange glass) and Apollo 15 (green glass) landing sites (Chou et al., 1975; Meyer et al., 1975; Butler and Meyer, 1976; Wasson et al., 1976; Clanton et al., 1978; McKay and Wentworth, 1992; Hauri et al., 2015). These coatings were deposited from a volcanic gas during decompression and cooling of an eruptive plume (Meyer et al., 1975; Wasson et al., 1976). Lunar volcanic gas is likely to have been dominated by CO (Fegley, 1991; Fogel and Rutherford, 1995; Sutton et al., 2005; Rutherford and Papale, 2009; Nicholis and Rutherford, 2009; Elkins-Tanton and Grove, 2011). The gases are expected to have been very reduced, with an oxygen fugacity ranging from 0.2 log units above the iron-wüstite buffer (IW) to IW -2.5 (Fogel and Rutherford, 1995; Nicholis and Rutherford, 2009).

Deposition of reduced sulfide minerals from volcanic gas is likely to have occurred on other terrestrial planets and differentiated asteroids; for example, Mercury has a high S abundance on the surface that may be related to sulfide mineral deposits (Blewett et al., 2013; Nittler et al., 2014). Similarly, S-driven eruptions are ongoing on Io (Kerber et al., 2009). The reduced lunar volcanic gas model may also be applicable to other reduced planetary bodies such as Vesta and other asteroids. The oxygen fugacity of Vesta is very similar to that of the Moon at IW-2 (Righter and Drake, 1996), suggesting that volcanic gases released in Vestas' early history may have been dominated by similar gas species as on the Moon. Pyroclastic volcanism driven by reduced gases has been suggested for a range of asteroids, resulting in the loss of volatiles as well as basaltic melts on smaller bodies, where eruption velocities exceeded the bodies escape velocities (Wilson and Keil, 1991; Warren and Kallemeyn, 1992; Muenow et al., 1992; Taylor et al., 1993; Wilson and Keil,

1997; Goodrich et al., 2004). It is necessary to understand the composition of the volcanic gas because it affects trace metal transport and speciation (Symonds et al., 1987; Symonds et al., 1990; Symonds et al., 1992; Symonds and Reed, 1993; Wahrenberger et al., 2002). Therefore, gas speciation is critical for estimates of degassing and removal of trace metals from asteroids. Furthermore, the speciation of volatiles may affect the degree to which molecules such as H_2 were lost from early planetary bodies such as Earth, the Moon or Vesta (Sharp et al., 2013).

Major elements in the volcanic gas phase have received significant attention, but gaps remain in our understanding of how metals are transported in the vapor on planetary surfaces. Several studies have addressed volatility and speciation of metals in highly reduced volcanic gases with high C and S and low H concentrations, relevant to the Moon, Mercury and Vesta (Colson, 1992; Fegley and Swindle, 1993; Haskin et al., 1993; Casanova and Aulesa, 2000; Taylor and Martel, 2003; Shearer et al., 2012; Crawford, 2015; Bell et al., 2015). Also, transport of alkali metals and lithophile elements and their species (e.g, SiF_4) have been examined using theoretical models for S-rich, H-poor volcanic gases on Io (Fegley and Zolotov, 2000; Schaefer and Fegley, 2004; Schaefer and Fegley, 2005a; Schaefer and Fegley, 2005b). Furthermore, observations from terrestrial volcanic gases indicate that they effectively redistribute and concentrate metals in the crust and on the surface (Symonds et al., 1990; Henley and Berger, 2013; Zelenski et al., 2013; Henley et al., 2015). None of these studies specifically address the transport of transition metals in reduced volcanic gases relevant to the Moon, nor oxidized H-rich gases relevant to Earth; we address both below.

We model the speciation of metals (Zn, Ni, Pb, Ga, Cu, and Fe) within an expanding volcanic gas during lunar pyroclastic eruptions and gas plume formation, linking it to the formation of pyroclastic deposits. First, we consider the spatial scale of pyroclastic ejecta blankets on the Moon's surface – also known as "dark mantle deposits" when observed remotely − in terms of gas expansion and particulate transport. Second, we determine the concentrations of major components in lunar volcanic gas based on the analysis of volatile elements in Apollo 17 orange glass beads (Saal et al., 2008; Wetzel et al., 2015). Our study differs from previous models of lunar volcanic gas which assumed a close similarity with terrestrial volcanic gas, but lower water concentrations (Fegley, 1991; Fegley, 1992). Third, in context of appropriate physical and chemical variables we estimate trace metal speciation and metal deposition from an explosive eruption on the Moon and compare predictions of the model with the observed metal coatings on lunar glass beads.

On Earth and probably on Mars (King and McLennan, 2010), volcanic gases are more oxidized and dominated by H_2O, SO_2, CO_2 and HCl (Symonds et al., 1990; Oppenheimer et al., 2011; Henley and Berger, 2013). Volcanic gases sampled at the surface can be highly enriched in some trace elements relative to their parent magma, in particular in volatile chalcophile and siderophile elements (Symonds et al., 1990; Africano et al., 2002; Yudovskaya et al., 2008; Henley and Berger, 2013; Zelenski et al., 2013). The ability of volcanic gases to transport metals at high temperatures is recorded at active volcanoes in fumaroles and ash plumes, as well as economically significant occurrences, such as porphyry copper deposits (Henley et al., 2015). Thermochemical modeling of the metal speciation in volcanic gases from Merapi volcano (andesite; Indonesia), St. Augustine volcano (basaltic andesite; USA) and Mount St. Helens (andesite; USA) has shown, that on Earth, many metals, including Zn, Cu, Pb, Ni and Fe, are transported predominantly as chloride species at temperatures from 100 to 1000 °C, with lesser transport as elemental and sulfide species in evolved, water-rich and oxidized subduction-related systems (Symonds et al., 1987; Symonds et al., 1992; Symonds and Reed, 1993). Similar calculations for trace element transport are limited for more reduced, dry and less evolved systems such as might occur in extensional and intraplate tectonic settings.

Hence, in addition to providing a model for lunar volcanic gas speciation and metal transport, we provide a thermodynamic model for major element and trace metal speciation of the volcanic gas from Erta Ale volcano, Ethiopia. This allows us to evaluate the thermochemical model by comparing its results with observations from gas emission at Erta Ale volcano (Zelenski et al., 2013; de Moor et al., 2013). Erta Ale is a basaltic shield volcano emitting high temperature gases (> 1000 °C) with compositions indicating little interaction with the overlying crust or meteoric water, making them an example of a primitive terrestrial basaltic gas (Hammond et al., 2011; Zelenski et al., 2013; de Moor et al., 2013). In comparison to subduction-related systems such as Merapi, St. Augustine and Mount St. Helens, Erta Ale is drier and more reduced. Relative to the lunar gas (Table 2-1), the Erta Ale gas has much more H_2O and Cl and a much higher oxygen fugacity (fO_2) at the fayalite-magnetite-quartz (FMQ) redox buffer (de Moor et al., 2013) which is equivalent to IW+3.6 at 1084 °C (Table 2-1). The terrestrial example may be applicable to more oxidized planets such as Mars, whereas the lunar model is applicable to more reduced compositions such as those inferred for the asteroid Vesta and other small solar system bodies (Wilson and Keil, 1991; Wilson and Keil, 1997).

Table 2-1: Compositions in mole% of the lunar volcanic gas model and composition of a volcanic gas from Erta Ale volcano in Ethiopia (Zelenski et al., 2013; de Moor et al., 2013). The gases are compared using ratios of molar abundances. The oxygen fugacity (fO_2) is given relative to the iron-wüstite buffer (IW). The composition of the lunar volcanic gas at IW is given in the Appendix to Chapter 2.

	Lunar gas	Erta Ale 1084 °C
H	31.83	46.30
O	15.45	42.29
C	15.92	6.52
Cl	0.17	0.50
S	34.65	3.69
F	1.98	0.70
N	0.001	0.001
H/C	2.00	7.11
H/O	2.06	1.09
H/S	0.9	12.6
H/Cl	184.4	92.8
O/C	0.97	6.49
S/C	2.18	0.57
Cl/C	0.01	0.08
F/C	0.12	0.11
H/(F+Cl)	14.8	38.6
fO_2	IW-2	IW+3.6

2.3 A lunar pyroclastic eruption model

2.3.1 Adiabatic expansion of volcanic gas

Explosive volcanism on the Moon is recorded in the form of pyroclastic deposits sampled by all Apollo missions but in particular by Apollo 15 and Apollo 17 (Heiken et al., 1974; Arndt et al., 1984; Arndt and von Engelhardt, 1987; Elkins-Tanton et al., 2003) and dark mantle deposits (inferred to be pyroclastic) observed by remote sensing (McGetchin and Head, 1973; Head, 1976; Gaddis et al., 1985; Head and Wilson, 1992; Weitz et al., 1998; Head et al., 2002; Gaddis et al., 2003). Many of these deposits formed in pyroclastic eruptions when very low viscosity picritic melts were propelled by the expansion of volcanic gas (Heiken et al., 1974; Wilson and Head, 1981; Weitz et al., 1999; Nicholis and Rutherford, 2009). In some cases they can extend up to hundreds of kilometers in diameter, such as the Orientale ring dark mantle deposit (Weitz et al., 1998; Weitz et al., 1999).

The decompression of volcanic gases during explosive eruptions is generally modeled adiabatically (Kieffer, 1982; Kieffer and Sturtevant, 1984; Mastin and Ghiorso, 2001), with constant entropy (isentropic) and constant enthalpy (isenthalpic) expansion as the endmember processes. During lunar volcanic activity we can assume that the atmospheric pressure on the Moon was at the order of 10^{-9} bar (Strobel and Wolven, 2001).

In the lunar environment, the gas expanded into low pressure conditions and it did not require any work against a pressure because the gas expanded freely. Free isenthalpic expansion, also known as the Joule-Thomson process or throttling process, is described by Joule's second law which states that the internal energy of a constant mass of an ideal gas expanding freely is only a function of temperature (Figure 2-1) (Wylen and Sonntag, 1986; Fegley, 2006).

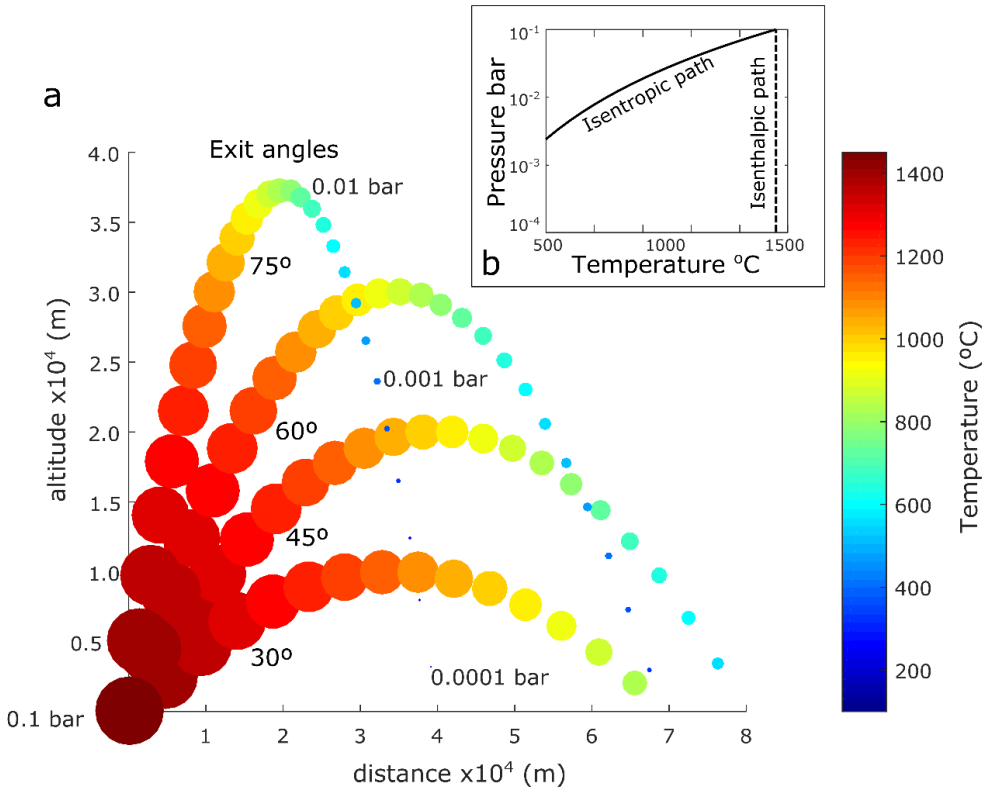

Figure 2-1: (a) Lunar ballistic eruption model. The individual steps along the trajectories are 15 seconds apart. The cooling rate is 3 °C/s with T_1 = 1450 °C and P_1 = 0.1 bar. The pressures along the paths are calculated assuming isentropic decompression according to Equation 2-1 and are labelled along the trajectory with an exit angle of 75°. The exit velocity at the vent is 360 m/s and the maximum distance reached with an exit angle of 45° is 80 km. (b) Isenthalpic decompression is independent of temperature, whereas the isentropic decompression path shows a strong temperature gradient according to Equation 2-1.

In the other endmember decompression path, isentropic expansion, the temperature decreases during decompression because temperature and entropy are conjugate variables (Fegley, 2006). Isentropic expansion is a reversible process, which can be described by:

$$P_2 = \left(\frac{T_2}{T_1}\right)^{\frac{\gamma}{\gamma-1}} P_1 \qquad \textit{Equation 2-1}$$

where P_1 and P_2 are the initial and final pressures, T_1 and T_2 are the initial and final temperatures and γ is the ratio of the heat capacities at constant pressure to constant volume of the gas. The heat capacity ratio of ideal gases can be simplified and described as a function of the number of degrees of freedom (f) of the gas ($\gamma = 1 + \frac{2}{f}$) (Wylen and Sonntag, 1986). The main species of the lunar volcanic gas models, in particular at high temperatures and low pressures, is $CO_{(g)}$ as shown below and suggested previously (Fegley, 1991; Fogel and Rutherford, 1995; Rutherford and Papale, 2009; Nicholis and Rutherford,

2009). $CO_{(g)}$ is a diatomic gas with a linear geometry, two rotational and three translational degrees of freedom ($f = 5$), and a heat capacity ratio of $\gamma = 1.4$.

Here, we first assume that the eruption plume cools and decompresses isentropically (Figure 2-1), following the thermodynamic description of similar sized eruption plumes on Io (Kieffer, 1982). To determine the decompression path, we need a reasonable estimate of temperature and pressure of the gas at the volcanic vent (T_1 and P_1). The Apollo 17 orange and Apollo 15 green volcanic glasses have liquidus temperatures ranging from 1298 to 1448 °C (Delano, 1990). Many glass beads have quenched without nucleating olivine or spinel, therefore the eruption temperature must have been at least the liquidus temperature (Delano, 1990; Saal et al., 2008). Thus, T_1 is assumed to be 1450 °C. The pressure of eruption P_1 is set to 0.1 bar (Figure 2-1). We chose this pressure based on observations and modeling of volcanic eruptions on Jupiter's moon Io where vent pressures lie in the range of 0.01 to 2 bar and transient atmospheric pressures reach 10^{-9} bar (Kieffer, 1982; Zolotov and Fegley, 2001; Strobel and Wolven, 2001; Zhang et al., 2003; Zhang et al., 2004). The Earth's Moon and Io are similar in several physical properties such as average radius, mass, volume, density, surface gravity and escape velocity. On Io, the deposits from volcanic plumes have diameters of up to several hundred kilometers which are similar to the dark ring deposits on the Moon (Weitz et al., 1998; Weitz et al., 1999; Lopes-Gautier et al., 2000; Head et al., 2002; Zhang et al., 2003). The similarity of some plume deposit diameters on the two bodies also suggests similar eruption energies. Different conditions at the vent would result in decompression and cooling paths that are parallel to the one shown in the P-T space (Figure 2-1).

In reality, an isentropic decompression and cooling path is an idealized endmember process (Figure 2-1). In the early stages of decompression at higher temperatures and pressures the eruption plume density could still be high enough so that melt drops or glass beads would interact physically with each other, resulting in non-isentropic friction and other dissipative effects. Such physical interactions of glass beads in the early stages of the eruption have been inferred before (Heiken et al., 1974; Elkins-Tanton et al., 2003). Above the glass transition temperature (e.g., T_g~720 °C for a melt with dry orange glass composition; calculated using (Giordano et al., 2008) the volatiles may have degassed and olivine and ilmenite crystallized in some of the melt droplets. These processes would also have caused a change of the entropy and a deviation from the isentropic decompression path towards a more pressure-dependent path. Nevertheless, for simplicity we consider the isentropic case with T_1=1450 °C and P_1=0.1 bar. Applying these conditions to Equation 2-1 and a diatomic gas with γ=1.4, the gas pressure at T_g is approximately 0.01 bar.

2.3.2 Calculation of a lunar ballistic eruption model

Dark mantle deposits such as the Orientale Ring deposit with a radius of 80 km (Head et al., 2002) demonstrate the extensive size of some explosive volcanic eruption deposits on the Moon. The Orientale deposit belongs to the largest pyroclastic deposits on the Moon which range up to 50,000 km^2 (Wilson and Head, 1981; Head et al., 2002; Gaddis et al., 2003). Some of these very large deposits may have formed in single eruptions. We calculate a simple ballistic eruption model for these lunar pyroclastic eruptions, describing the flight paths of glass beads and the pressure and temperature evolution of the associated gas along the ballistic trajectories (Figure 2-1). The gravity on the Moon is a fraction of that on Earth with g=1.62 m/s^2 resulting in much wider dispersion of pyroclastic eruption products. Consequently, lunar pyroclastic eruptions may have reached altitudes of tens of kilometers. Friction can be neglected due to the absence of an atmosphere and ballistic trajectories can be described as ideal parabola. In order to achieve a radius (r) of 80 km an eruption at an exit angle (α) of 45° requires an exit velocity (v) of ~ 360 m/s calculated from $r = [v^2 \sin(2 * \alpha)]/g$. The calculated velocity is similar to velocities estimated for pyroclastic eruptions on other airless planetary bodies such as Mercury (Kerber et al., 2009). The individual steps along the trajectories shown in Figure 2-1 are 15 s apart with a cooling rate of 3 °C/s. This is the lowest cooling rate within a range of up to 100 °C/s that can be expected (Arndt and von Engelhardt, 1987; Saal et al., 2008). We chose this slow cooling rate because it resulted in the best fit for the concentration profiles of H, S, Cl and F in orange glass beads (Saal et al., 2008). The change in pressure along the trajectories was calculated from the temperature at the individual steps, assuming isentropic decompression of a diatomic gas from P_1=0.1 bar and T_1=1450 °C (Equation 2-1). Here we assume that each glass bead is surrounded by a parcel of gas with which it is in equilibrium and from which the metals are deposited onto the bead. Owing to the different lengths of ballistic trajectories as a function of the exit angles, the pressure and temperature conditions at which the trajectories end vary from ~200 °C and 10^{-5} bar at an exit angle of 75°, to 820 °C and 10^{-2} bar at an exit angle of 30° (Figure 2-1). Higher exit angles result in longer flight paths that terminate at lower temperatures and pressures.

2.4 Calculation of lunar volcanic gas composition

2.4.1 Major components

Concentration profiles of volatiles in lunar volcanic glass beads provide constraints on their concentrations before diffusive degassing and volatile loss (Saal et al., 2008; Wetzel et al., 2015; Chen et al., 2015). Here we use H_2O, S, F, Cl (Saal et al., 2008) and C (Wetzel et al.,

2015) in Apollo 17 orange glass beads to calculate a model for the major element composition of a lunar volcanic gas in pyroclastic eruptions using the maximum loss from diffusive degassing as the bulk composition.

Saal et al. (2008) modeled hydrogen loss from lunar glass beads assuming diffusion as H_2O resulting in H_2O-rich calculated gas compositions (92.99 wt.%), followed by F (6.36 wt.%), S (0.61 wt.%) and Cl (0.03 wt.%) (Table 2-1). The measured H/C ratios in orange glasses are between 2 and 3 (Wetzel et al., 2015). The estimated carbon content of undegassed lunar melt is in the same range as that of terrestrial primitive mid-ocean ridge basalts (Saal et al., 2002; Wetzel et al., 2015). Both C and H_2O are degassed by more than 95% by the end of the volatile-loss in the conduit and at early stages of the eruption (Saal et al., 2008; Wetzel et al., 2015). Therefore, the resulting gas phase, by the end of degassing, has a ratio of H/C near that of the undegassed melt near H/C = 2. For simplification we assume that all volatiles were exsolved from the magma prior to the exit from the vent (Figure 2-1), and this establishes the initial bulk composition of the lunar volcanic gas. Here, we do not consider processes that occurred in the vent. These processes may have included non-simultaneous degassing of different volatiles (Wetzel et al., 2015; McCanta et al., 2017) or separation of gas and melt (Wilson, 2003; Wilson and Head, 2017). We then adjust the oxygen content of the model lunar volcanic gas to match an fO_2 to IW-2 at 1450 °C and 1 bar (Fogel and Rutherford, 1995; Nicholis and Rutherford, 2009). This oxygen fugacity value falls within the suggested range of IW-2.5 to IW+0.2 (Fogel and Rutherford, 1995; Nicholis and Rutherford, 2009). For comparison, and to model the possible effects of oxidation (e.g., Wetzel et al., 2015), we have also calculated the volcanic gas and metal speciation at the IW buffer at 1 bar and 10^{-6} bar and 500 – 1500 °C (Appendix).

The obtained concentrations were normalized to 100 mole%. The resulting composition (Table 2-1) was used as input in a Gibbs Free Energy minimization calculation using the software HSC8 (Roine, 2015) with 49 gas species (Appendix to Chapter 2) to calculate gas speciation. The C-O-H-F-Cl-S species were chosen based on preliminary calculations excluding other species, which had concentrations far below 10^{-30} mole fractions. All thermochemical calculations were made using the Kelvin temperature scale. The complete results of the thermochemical calculations are reported in the Appendix to Chapter 2.

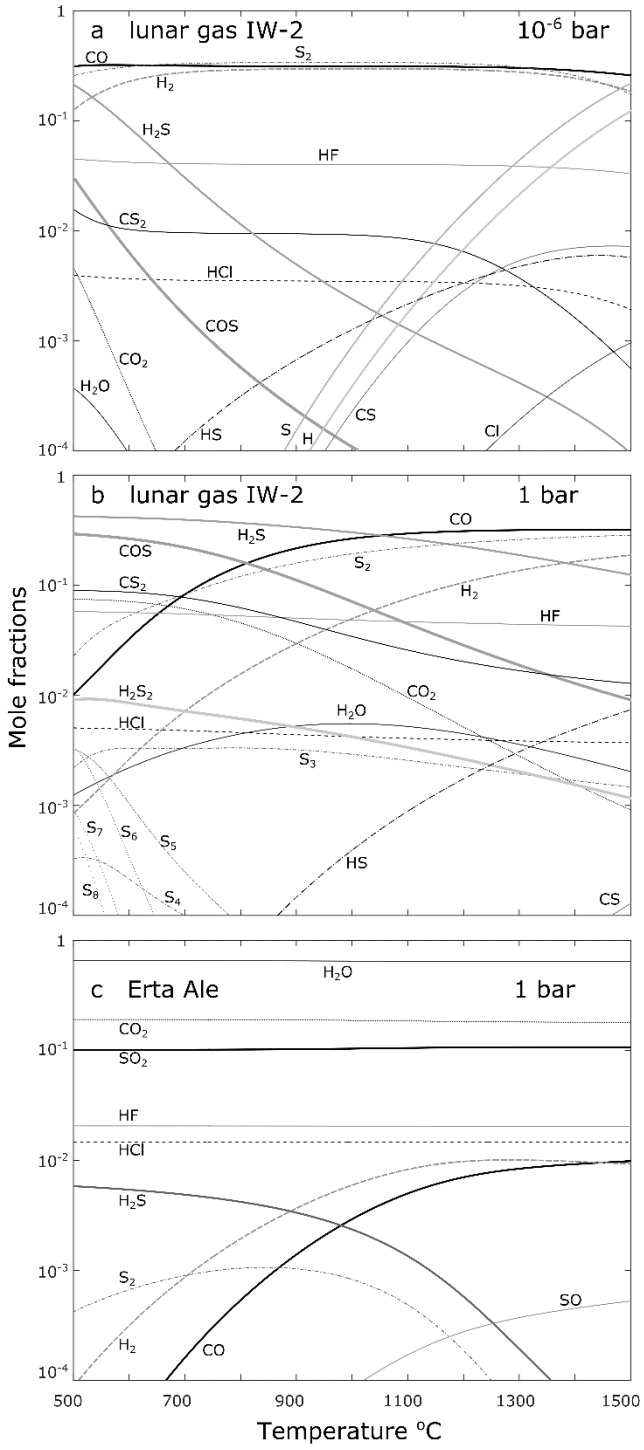

Figure 2-2: Gas speciation of major elements of the lunar volcanic gas at (a) 10^{-6} bar, (b) 1 bar and (c) the Erta Ale gas at 1 bar at temperatures from 500 to 1500 °C. The lunar volcanic gas is dominated by CO, S_2, H_2, H_2S, CS_2 and COS, where triatomic molecules are replaced by diatomic molecules at high temperatures and low pressures. The Erta Ale gas shown was sampled at 1084 °C (Zelenski et al., 2013).

At 1 bar the dominant gas species are CO, S_2 and H_2, followed by H_2S and COS below 800 °C. At 10^{-6} bar CO, S_2 and H_2 are the dominant gas species from 500 to 1500 °C (Figure 2-2). The most abundant S species at both pressure conditions is S_2 followed by H_2S and CS_2 at 10^{-6} bar and COS and H_2S at 1 bar (Figure 2-2). Hydrogen occurs primarily as H_2, H_2S and most Cl and F are bound to HCl and HF. Generally, triatomic gas species are replaced by diatomic and monoatomic species as either pressure decreases or temperature decreases. For example, H_2S, COS and CO_2 are replaced by S_2, CO and H_2 following:

$$2H_2S + 2COS + CO_2 \xrightarrow{\substack{higher\ T\ or \\ lower\ P}} 2S_2 + 3CO + 2H_2 \qquad \textit{Equation 2-2}$$

At IW, the same major gas species dominate (i.e., H_2, CO and S_2) as indicated in the Appendix. As expected, the relative proportions of some of the oxidized species (CO_2, H_2O, SO_2 and SO) are higher at IW relative to IW-2. This effect is most pronounced at low pressure and depends on temperature.

2.4.2 Metal speciation

To calculate the speciation, transport and deposition conditions of the metals found in coatings on lunar glass beads, we added 0.001 mole% of Zn, Ni, Pb, Ga, Cu and Fe to the initial bulk gas composition (Table 2-1). This low concentration of metals is insufficient to deplete Cl, F and S contents which are orders of magnitude more abundant. The metals are included as elemental metallic gases, as well as gas and solid compounds with S, Cl, O and F (Appendix to Chapter 2). Carbon-bearing metal species were omitted since they were below 10^{-30} moles. All solids are modeled as pure endmember phases. The main property controlling metal transport in the gas phase is the vapor pressure of the individual species, which correlates positively with temperature (Thomson, 1946), resulting in the greatest pure metal gas species concentrations at the highest temperatures. The speciation of all metals at 10^{-6} bar in the lunar volcanic gas and at 1 bar in the Erta Ale gas are shown in Figure 2-3 and Figure 2-4 respectively, to show the pressure dependence of the speciation and put it into context with more familiar terrestrial conditions. Metal speciation in the lunar volcanic gas at 1 bar and in the Erta Ale gas at 10^{-6} bar are shown in the Appendix to Chapter 2 for comparison. At 10^{-6} bar in the lunar system Ni, Cu and Fe form predominantly solid species, whereas Zn, Ga and Pb are primarily in the gas phase above 750, 900 and 600 °C respectively (Figure 2-3).

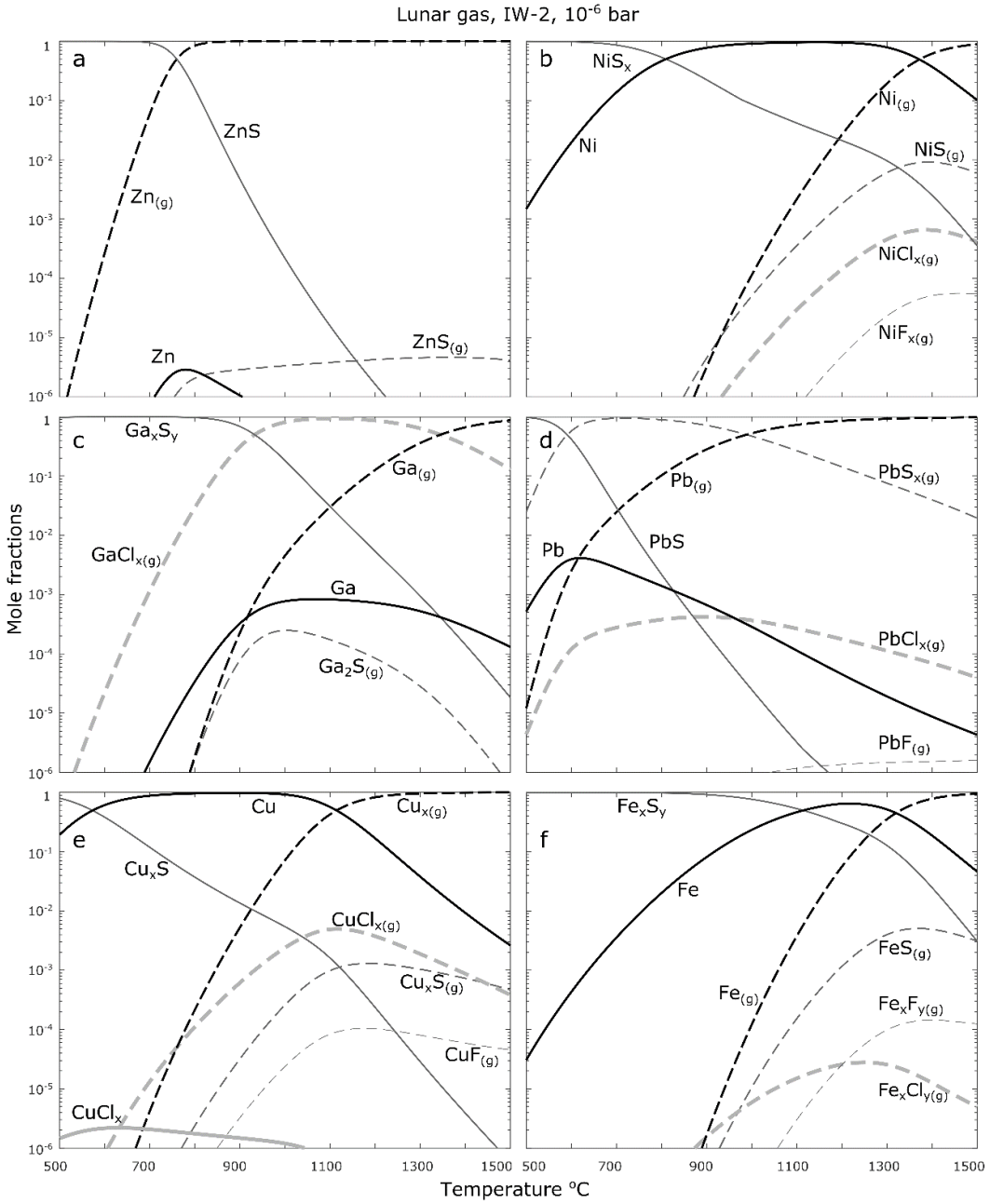

Figure 2-3: Metal speciation of (a) Zn, (b) Ni, (c) Ga, (d) Pb, (e) Cu and (f) Fe in the gas (stippled lines) and solid phase (solid lines) in the lunar volcanic gas at 10^{-6} bar and from 500 to 1500 °C.

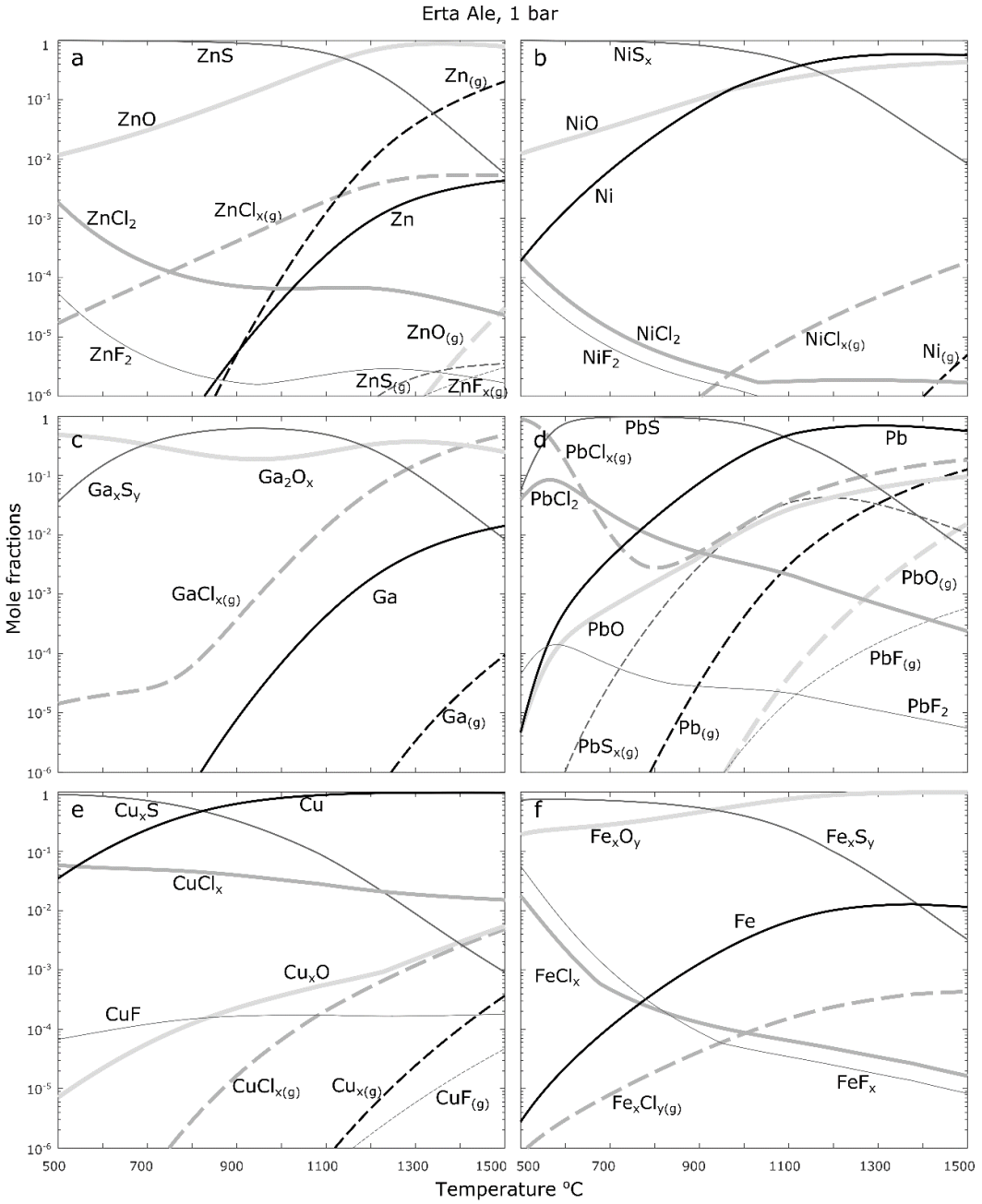

Figure 2-4: Metal speciation of (a) Zn, (b) Ni, (c) Ga, (d) Pb, (e) Cu and (f) Fe in the Erta Ale gas at 1 bar and from 500 to 1500 °C. Stippled lines show species in the gas phase and solid lines show species in the solid phase.

In the S-rich lunar gas, the metal-sulfide solids are the most abundant phases of all metal-bearing solids except at higher temperatures where the elemental metals become more abundant (Cu > 600 °C, Ni and Pb > 800 °C and Fe > 1100 °C) (Figure 2-3). At 1 bar, sulfides are the predominant solid metal phases over the entire temperature range modeled, except for Cu which occurs as an elemental metal above 1300 °C. In contrast, the other metal-bearing solids (elemental metals and metal halides) have much lower concentrations ($X_m < 10^{-6}$) at 10^{-6} bar and below 10^{-3} mole fractions at 1 bar. The temperature at which

elemental metals replace metal sulfides depends on pressure as well as the gas composition. For example, Cu changes its speciation in the lunar gas from sulfide to elemental Cu at 10^{-6} bar at 580 °C and at 1 bar at 1220 °C. In the Erta Ale gas this transition occurs below 500 °C at 10^{-6} bar and at 820 °C at 1 bar because of the lower S content of the Erta Ale gas.

The speciation of metals in the lunar gas phase varies considerably. In particular, chloride gas species are important for the transport of Ga, Cu, Fe and Pb. Gallium is transported mainly as $GaCl_{(g)}$, $GaCl_{2(g)}$ and $GaCl_{3(g)}$ except at high temperatures (> 1300 °C) at very low pressures (e.g. 10^{-6} bar) where elemental $Ga_{(g)}$ dominates. At such high temperatures and low pressures, the metal gas speciation follows a trend similar to the non-metal gas from multiatomic molecules to monoatomic elemental metal gas (i.e. $Ga_{(g)}$). In the case of Fe and Cu, the metal chloride species are important only at lower temperature and pressure conditions. For example, Fe chlorides ($FeCl_{(g)}$, $FeCl_{2(g)}$, $FeCl_{3(g)}$, $Fe_2Cl_{4(g)}$ and $Fe_2Cl_{6(g)}$) are the dominant gas phase at 10^{-6} bar below 900 °C, whereas they are the dominant species at 1 bar from 700 to 1500 °C, and replaced by fluoride species below 700 °C. Fe seems to be more dependent on the differences in the gas compositions with the Fe content in the gas phase strongly controlled by the abundance of Cl in the bulk gas composition.

These calculations also imply that in a lunar volcanic gas the sum of Pb species is more volatile than Zn, despite the lower vapor pressure (P_{vap}) of Pb metal (Lide, 2010). At 1 bar, Pb gas species decrease in concentration from sulfide to metal, oxide, chloride and fluoride. In the lunar gas at 1 bar and temperatures above 1400 °C, Pb is mostly in the gas phase and the gas fraction remains > 0.1 down to 1100 °C. In the Erta Ale gas, Pb is less volatile above 1200 °C with a lower abundance of sulfide gas species but a higher abundance of chloride gas species. Lead changes its speciation from $PbCl_{(g)}$ and $PbCl_{2(g)}$ to $PbCl_{4(g)}$ at 1 bar below 800 °C (Figure 2-4), resulting in the increasing volatility shown in Figure 2-5. Similarly, Ga occurs as $GaCl_{(g)}$ at 10^{-6} bar with decreasing concentrations below 800 °C and above 1300 °C and at 1 bar above 1000 °C. At 1 bar below 1000 °C $GaCl_{3(g)}$ surpasses $GaCl_{(g)}$. More generally for all metallic elements, the sulfide and chloride species in the solid as well as the gas phase become less stable towards higher temperatures and lower pressures in favour of elemental metal species.

Calculations undertaken at both IW and IW-2 (at 10^{-6} and 1 bar), indicate that the same metal species dominate. A few differences exist as documented in the Appendix. At IW, the calculated concentrations of ZnO, NiO, $NiO_{(g)}$, $PbO_{(g)}$, FeO and $FeO_{(g)}$ exceed 10^{-6} mole fractions, compared to IW-2 where they are always below 10^{-6} mole fractions. Iron shows the greatest response to oxidation with FeO reaching ~10^{-1} mole fractions at 1200 °C and 10^{-6} bar.

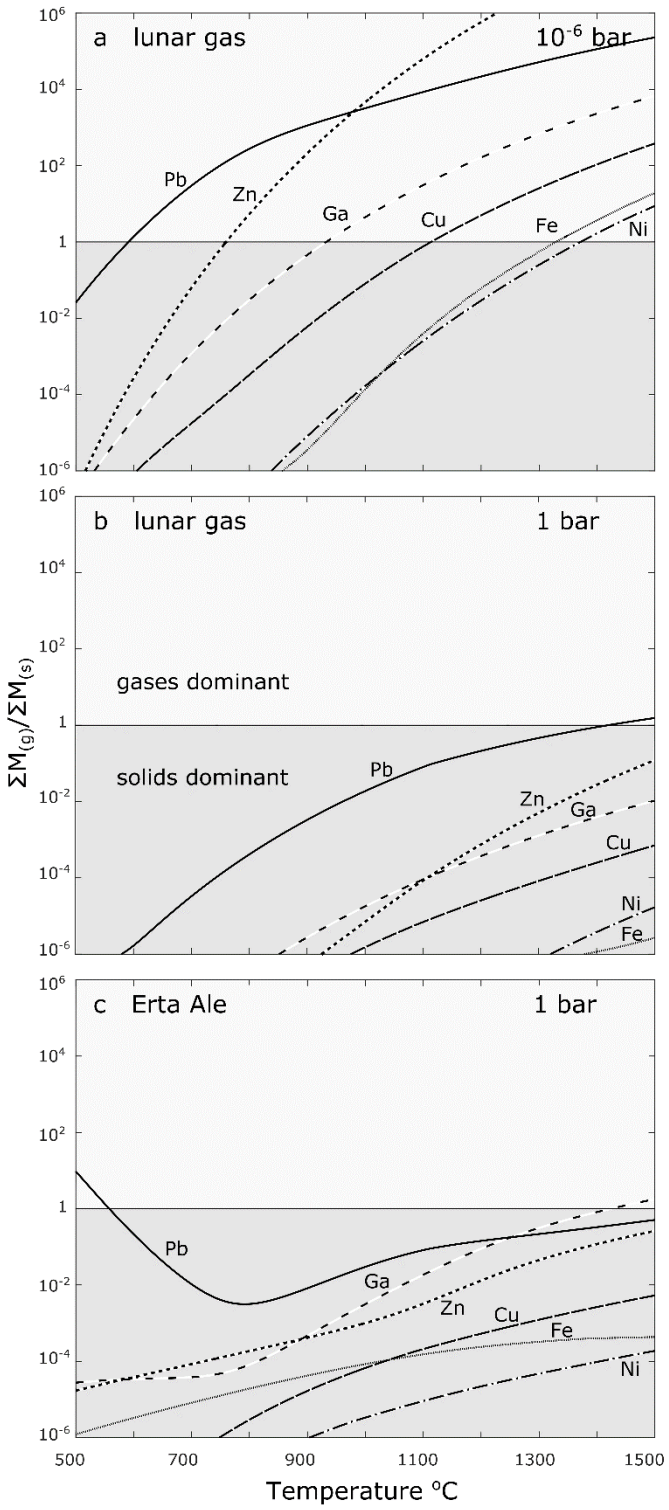

Figure 2-5: Temperature conditions at which metal species are predominantly in the gas phase ($\sum M_{(g)} / \sum M_{(s)} > 1$) and in the solid phase ($\sum M_{(g)} / \sum M_{(s)} < 1$). The ratio is an expression of the relative volatilities of the metals in the volcanic gases. Lunar volcanic gas at (a) 10^{-6} bar and (b) 1 bar, (c) Erta Ale volcanic gas at 1 bar.

2.4.3 Metal distribution between the gas and solid phase

In order to allow a better comparison of the distribution of the metals between the deposited solid phase and the gas phase we summarize all species of a particular metal into one property, which is the molar ratio between the sums of all gas species of the metals to the sums of all metal-bearing solids:

$$\sum M_{(g)} / \sum M_{(s)} \qquad \textit{Equation 2-3}$$

This distribution is shown for all metals in the modeled lunar gas at 10^{-6} and 1 bar in Figure 2-5. When $\sum M_{(g)} / \sum M_{(s)} > 1$, more than half of the metal (on a mole fraction basis) is in the gas phase, and when $\sum M_{(g)} / \sum M_{(s)} < 1$, the metal is predominantly deposited. As indicated above, the main factor influencing metal speciation in the gas phase is the vapor pressure of the individual metals, which depends both on pressure and temperature. The temperatures at which the metals have a vapor pressure of 1 bar are 917 °C (Zn), 1754 °C (Pb), 2245 °C (Ga), 2563 °C (Cu), 2859 °C (Fe) and 2911 °C (Ni) (Lide, 2010). This sequence of metals is only observed in the lunar gas system at 10^{-6} bar at temperatures above 1000 °C. Below this temperature and at higher pressures the sequence differs with Pb being more abundant in the gas phase than Zn due to the stability of Pb-Cl species (see 3.2. for details on Pb speciation).

The pressure and temperature conditions at which equal amounts of metals are in the gas phase and in the solid phase $\left(\sum \mathrm{M_{(g)}} / \sum \mathrm{M_{(s)}} = 1\right)$ are shown in Figure 2-6. For the more refractory metals such as Cu, Fe and Ni, this condition requires much higher temperatures (> 900 °C) at 10^{-6} bar. Lead, Zn and Ga can exist in the vapor phase at very low pressures (< 10^{-6}) even at temperatures below 700 °C. Despite its lower vapor pressure (P_{vap}), Pb is more prevalent at higher pressures and lower temperatures than Zn because Pb has abundant sulfide and chloride species in the gas phase over most of the pressure and temperature range. The isentropic and isenthalpic gas expansion paths (introduced in section 2.1) are also shown in Figure 2-6 and show an envelope of potential pressure and temperature paths. Along a potential decompression and cooling path close to the ideal isentropic path only Zn and Pb would be mostly in the gas phase and all other metals would predominantly remain in the condensed phase.

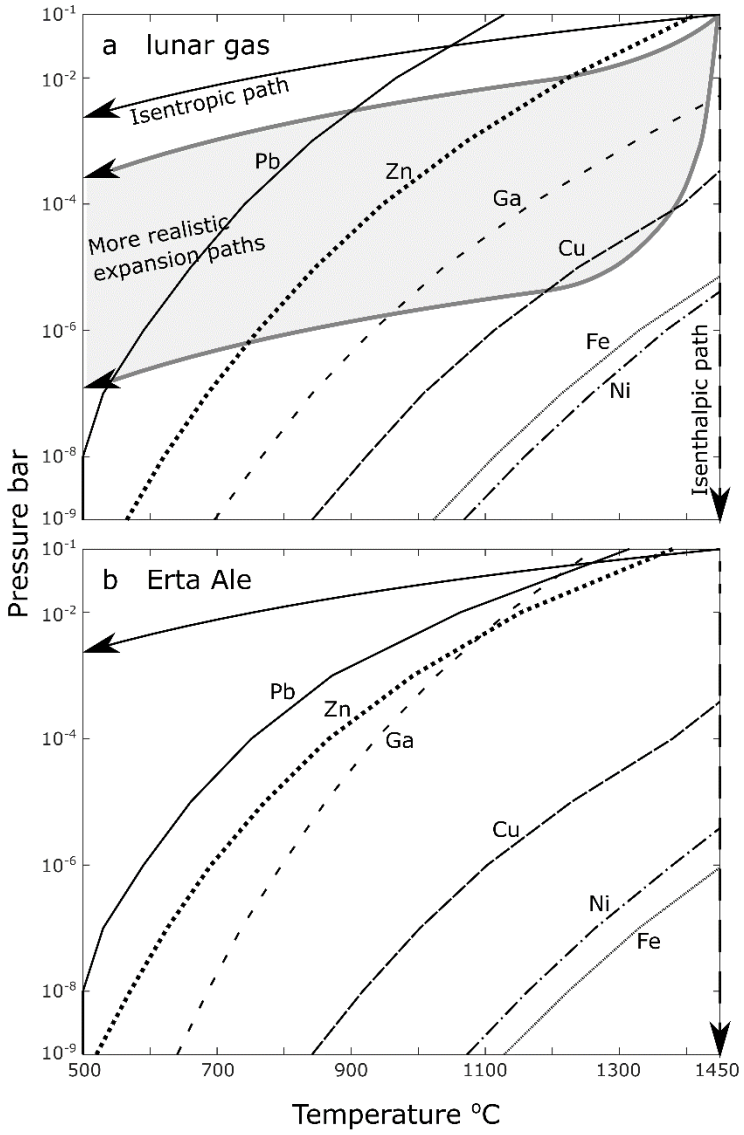

Figure 2-6: Pressure and temperature conditions at which equal amounts of metals are in the gas phase and in the solid phase ($\sum M_{(g)} / \sum M_{(s)} = 1$). (a) Lunar volcanic gas. A real lunar decompression path is expected to be in between the isentropic and isenthalpic paths with initial fast expansion followed by isentropic decompression and cooling as the gas expands to lower pressures and temperatures, as indicated by the shaded area. (b) Erta Ale volcanic gas. The isentropic and isenthalpic adiabatic decompression and cooling paths are shown for an ideal diatomic gas according to Equation 2-1.

2.5 Discussion

2.5.1 Bulk volcanic gas composition

We have shown that the speciation of a lunar volcanic gas is strongly dependent on temperature and pressure. By comparison with previous lunar volcanic gas models (Fegley, 1991; Fegley, 1992), the absence of chlorofluorocarbon species, such as CCl_4, CF_4, $CClF_3$ or CCl_2F_2, as well as more complex S species (SCl_2, S_2Cl or S_2Cl_2) is striking. All these

species are included in our model (Appendix to Chapter 2) but their calculated concentrations are well below 10^{-7} mole fractions. These differences arise because first, the Cl and F concentrations measured in the orange glass beads (Saal et al., 2008) are very low resulting in H/(Cl+F) > 1 compared to 0.001 in the model by Fegley (1992). Second, the thermochemical model predicts that large molecules with more than three atoms are unstable at very low pressures (< 10^{-3} bar). The difference in the bulk gas composition is important, as the availability of halogens affects the degree at which metals are transported in the gas phase, and the formation of chlorofluorocarbon species.

Both our model and those by Fegley (1992) necessarily made assumptions to define a bulk composition for the gas phase. We determined the H, S, F and Cl contents based on calculated loss of volatiles from lunar orange glass beads (Saal et al., 2008), C was based on H/C = 2 (Wetzel et al., 2015) and O was fixed assuming an fO_2 of IW-2 (or IW in the Appendix to Chapter 2). We do not account for the relative solubilities of the different gas species in the melt at different pressures and temperatures; in other words we model a time-integrated bulk composition. We recognize that the gas is likely to change in composition during ascent in the conduit. Nonetheless, we consider that the assumptions are valid because the lunar magma ascended rapidly (Wilson and Head, 2017) allowing vigorous mixing of gas, melt and crystals, and the low H content would have enhanced partitioning of C-O species into the gas phase (e.g.(King and Holloway, 2002).

2.5.2 Metal transport and deposition from lunar volcanic gas

Trace metals transported and deposited from lunar volcanic gas change their speciation considerably over the temperature and pressure range expected in pyroclastic eruption plumes on the Moon. Thermochemical modeling of metal speciation predicts that, when the volcanic gas cools and expands into the near vacuum on the Moon, metals deposit from the gas and coat pyroclastic glass beads at different pressures and temperatures depending on the metal (Figure 2-3). For example, more than 50 % of Ni is deposited at 10^{-6} bar and 1380 °C. Zn is more volatile and at 10^{-6} bar more than 50 % is still in the gas phase below 800 °C.

The speciation in the gas phase varies among the different metals including elemental metal vapors (Zn, Fe, Ni), sulfides (Pb, Ni) and chlorides (Ga, Pb, Cu) (Figure 2-3). This requires a change of speciation during the deposition process, because the speciation is different in the solid phase. For example, $Zn_{(g)}$ has to react with a S gas species in order to form the deposited ZnS. At 10^{-6} bar Ga is in the gas phase as chloride species between 900 and 1350 °C and the deposited species below 900 °C are sulfides requiring reactions during the transition from gas phase Ga chlorides to solid phase Ga sulfides.

In section 2.2, we introduced a ballistic eruption model for lunar pyroclastic eruptions (Figure 2-1). We assumed a cooling rate of 3 °C/s and isentropic decompression according to Equation 3-1. The pressure and temperature conditions at which the ballistic trajectories terminate were shown to be strongly dependent on the flight path lengths as functions of the exit angles (Figure 2-1 and Figure 2-7). The strong pressure and temperature dependence of the metal speciation in the gas and solid phase, as well as the conditions of deposition of the metals onto glass beads, as demonstrated above, suggest that the distribution of metals and their species may vary across deposits formed by such pyroclastic eruptions. As the trajectories terminate at different pressure and temperature conditions, when they are removed from the gas plume, the speciation of deposited metal-bearing solids varies accordingly. Long pathways with high exit angles that terminate at low temperatures and pressures (Figure 2-1) produce considerably higher ratios of sulfides to other solid species (Figure 2-7). For example, for exit angles > 60° the ratio of NiS to other Ni solids is > 10^9. Coatings formed at termination of short trajectories with low exit angles have a much lower ratio of sulfides to other solid species (<10^2). The model predicts that glass bead coatings formed at higher temperatures and pressures will be richer in elemental metals compared to coatings deposited at lower temperatures.

The dependence of metal coating speciation on the exit angles and flight paths predict heterogeneous speciations of glass beads sampled from deposits of a single pyroclastic eruption. For example, the trajectories in Figure 2-2 with 30° and 60° exit angle both terminate at a distance of close to 70 km, but the temperature and pressure conditions at which the two paths terminate are 820 °C (above Tg) and 10^{-2} bar after 220 s for the 30° exit angle and 300 °C and 10^{-4} bar after 390 s for the 60° exit angle. Initially deposited glass beads (30° exit angle) will have coatings with few mole % of elemental metals. These deposits are subsequently covered by glass beads with longer flightpaths (60° exit angle) coated almost entirely by sulfides (ratio of sulfides to other metal-bearing solids larger than 10^6). The resulting deposits with glass beads coated with varying amounts of elemental metals could alternatively have been interpreted to originate from different pyroclastic eruptions propelled by volcanic gases with different compositions.

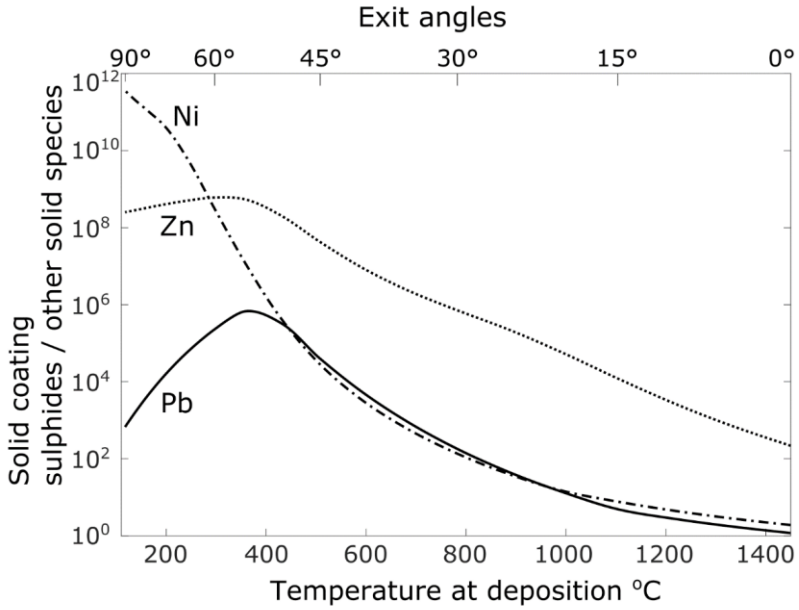

Figure 2-7: The temperatures and associated metal speciation at the terminations of the ballistic eruption trajectories (Figure 2-1) vary according to the exit angles of the trajectories. The ratios of sulfides to other metal species in the deposited metals are shown for Zn, Pb and Ni, indicating a strong dominance of sulfides towards lower temperatures.

In the case of higher cooling rates, the temperature drops quickly along trajectories irrespective of exit angle. For example, if the cooling rate is 100 °C/s the temperatures at the terminations of all trajectories are far below 0 °C resulting in no variation in the speciation of metal-bearing glass bead coatings. Consequently, we predict that the cooling rate of the gas and the transported glass beads in a lunar pyroclastic eruption has a major impact on the speciation of metals in lunar volcanic gases and their distribution in deposits across pyroclastic dark mantle deposits on the Moon.

Here, we compare our model of the metal species in the gas phase with previous work on lunar gas speciation. Also, we compare our predicted metal-bearing solids with published observations of coatings on lunar pyroclastic glass beads. At eruption temperatures of more than 1400 °C and low pressures (10^{-6} bar) all metals are in the gas phase as metallic species. $Zn_{(g)}$ is the dominant Zn-gas species at all conditions for which we have calculated the speciation. This is contrary to previous assumptions that Zn is predominantly transported as $ZnCl_{2(g)}$, due to its lower vapor pressure (Chou et al., 1975; Meyer et al., 1975; Wasson et al., 1976; Paniello et al., 2012). That assumption was made without performing Gibbs Free Energy minimization calculations at lunar conditions, as we present them here. Chloride species are important for the transport of metals (e.g. $GaCl_x$, $CuCl_x$ and Fe_xCl_y) at higher pressures (> 10^{-3} bar) over the entire temperature range, and at lower pressures (10^{-6} bar) limited to lower temperatures (< 1000 °C) (Figure 2-3). Importantly, Zn and Cu are not always transported as similar species. Cu also occurs as $Cu_{2(g)}$ and $CuCl_{x(g)}$, as assumed

previously (Moynier et al., 2006), but Zn predominantly occurs as $Zn_{(g)}$ (Figure 2-3). This affects relative volatilities of these two metals, and as they travel as molecules with different masses the speciation results in different isotopic fractionation (Moynier et al., 2006; Paniello et al., 2012).

Our calculations for the deposited metal-bearing solids are in good agreement with observations. For example, Zn occurs predominantly as ZnS in coatings on lunar glass beads (Butler and Meyer, 1976; Wasson et al., 1976; Butler, 1978; Cirlin and Housley, 1979; Wentworth et al., 2008). Sulfides of Ni and Cu are suggested to occur on the glass beads (Butler and Meyer, 1976). This is in accordance with our predictions, but only if the sulfides are deposited at pressures > 10^{-3} bar, because pure metals dominate at lower pressures. For example, at 10^{-6} bar, metallic Cu is the most abundant solid species above 600 °C, and metallic Ni is the main solid species above 800 °C (Figure 2-3). Depending on the cooling and decompression path of the gas, sulfides will be more or less abundant. If the system cools and decompresses isentropically, we expect that sulfides are the dominant species of Ni, Zn, Pb and Cu (Figure 2-3). Iron has been observed as a sulfide (Butler and Meyer, 1976; Wasson et al., 1976) and has also been observed as metallic Fe (Clanton et al., 1978; Wentworth et al., 2008; McKay et al., 2010; Thomas-Keprta et al., 2014). Both of these solid Fe species form according to our model, but we would expect a higher abundance of sulfides if the decompression occurs isentropically. The deposition of metallic Fe requires a higher pressure dependence of the decompression path and a relatively lower cooling rate, closer to an isenthalpic path. We expect that most lunar volcanic gas cooling and decompression paths are in between the purely isentropic and isenthalpic paths, allowing the deposition of Fe sulfides as well as metallic Fe. For example, a more realistic path may begin with isenthalpic decompression, followed by purely isentropic cooling and decompression (Figure 2-6). In this scenario, metallic Fe would be deposited at low pressures and high temperatures during the early stages of isenthalpic cooling (e.g. 10^{-6} bar and > 1000 °C) and close to the vent, followed by the deposition of Fe sulfides along the isentropic cooling path towards lower temperatures (< 1000 °C) (Figure 2-3).

In summary, metals deposited near the eruption temperature (1450 °C) occur as metallic species, whereas further along the cooling and decompression path (Figure 2-3 and Figure 2-7) sulfides become dominant. We expect glass beads dropped from the pyroclastic cloud after short flight trajectories (Figure 2-1) to be mainly coated with metallic species, whereas beads with longer trajectories are more likely to be coated with sulfides. Sulfur in the form of sulfides from lunar pyroclastic deposits as a resource for construction materials (Casanova and Aulesa, 2000) might be expected far away from a volcanic vent on the

surface of the moon. On the other hand, native metals, of interest as potential resources (Haskin et al., 1993; Taylor and Martel, 2003), are concentrated near the volcanic vents. It is tempting to use our model to predict the distribution of deposited metals around volcanic vents on the Moon because this would inform in situ resource utilization (ISRU). However, we would need better constraints on the distance from the vent, the cooling path, the eruption energy and geometry (Figure 2-1), as well as the total abundance of metals transported and deposited.

2.5.3 Comparison with terrestrial volcanic gas

The Erta Ale volcanic gas represents a modern terrestrial basaltic volcanic gas. The composition of the Erta Ale gas is shown in Table 2-1, as sampled at 1084 °C (Zelenski et al., 2013; de Moor et al., 2013). The H/C ratio for Erta Ale gas is 7.11, reflecting its higher water content, compared to 2 for the lunar gas. Erta Ale also has a much higher oxygen fugacity estimate and Cl content compared to the lunar gas. The calculated speciation of the Erta Ale and lunar volcanic gases at 1 bar and 10^{-6} bar over temperatures from 500 to 1500 °C is shown in Figure 2-2. The Erta Ale gas has the species distribution of H_2O (0.653), CO_2 (0.187), SO_2 (0.106), HF (0.021), HCl (0.015), H_2 (0.008), CO (0.005) and H_2S (0.0015) at 1084 °C and 1 bar in mole fractions.

Nickel and Cu in the gas are the metals that are least affected by the bulk gas composition and fO_2 when comparing the lunar and Erta Ale gases (Figure 2-3, Figure 2-4 and Appendix). At 10^{-6} bar, the metals behave in both gases in a similar manner. The higher Cl content of the Erta Ale gas stabilizes volatile metal chloride gases such as Pb, Zn and Fe. The Pb-Cl concentrations in the gas phase increase towards lower temperatures below 800 °C in the Erta Ale system, apparently because $PbCl_{4(g)}$ is stable at lower temperatures and 1 bar pressure (Figure 2-4). Over the entire temperature range, from 500 to 1500 °C, Ni, Fe, Cu, Zn and Ga are more enriched in the gas phase at 1 bar in the Erta Ale system compared to the lunar volcanic gas (Figure 2-5 and Figure 2-6). The high Cl concentration in the Erta Ale system increases the metal volatilities relative to the lunar volcanic gas. In the Erta Ale system, the iron fluoride concentrations are nearly independent of temperature. Copper chlorides are the dominant Cu gas species at 1 bar below 1450 °C, but only below 750 °C at 10^{-6} bar in the lunar gas. At the sampling conditions of the gas (1084 °C, 1 bar), Pb is the most volatile of the metals studied here. The equilibrium mole fractions of the total of each metal in the gas phase (X_{metal}^{g}) at these conditions are $X_{Pb}^{g} = 6.6*10^{-2}$, $X_{Ga}^{g} = 10^{-2}$, $X_{Zn}^{g} = 2.6*10^{-3}$, $X_{Fe}^{g} = 1.4*10^{-4}$, $X_{Cu}^{g} = 1.8*10^{-4}$ and $X_{Ni}^{g} = 7.7*10^{-6}$. The dominant solid species in equilibrium with this gas are sulfides for Zn, Ni, Ga and Pb. Copper occurs as an elemental metal above 820 °C and Fe as oxides above 920 °C. Below these

temperatures the sulfides are the dominant species of Cu and Fe as well (Appendix to Chapter 2). In comparison, all deposited metal-bearing solids occur as sulfides in the lunar gas at these conditions and the concentrations of the other species are several orders of magnitudes lower.

Our thermochemical modeling extends to much higher temperatures and a larger pressure range than previous speciation calculations of metals in terrestrial volcanic gases from dominantly intermediate composition volcanoes (Symonds et al., 1987; Symonds et al., 1992). Volcanic gases modeled previously, from St. Augustine volcano (Symonds et al., 1992) and Merapi volcano (Symonds et al., 1987), have much higher water concentrations (0.9 mole fractions) compared to Erta Ale volcano (0.65 mole fractions). Within the overlapping temperature range (500 – 1060 °C) we observe similar metal speciation, but the temperatures at which the dominant species change depend on the composition of the volcanic gas. For example, in the Erta Ale gas, we predict that the dominant Zn gas species are chlorides ($ZnCl_{2(g)}$ in particular) below 1100 °C and $Zn_{(g)}$ above. In the Merapi volcanic gas, this transition is predicted to occur at ~1000 °C (Symonds et al., 1987) and in St. Augustine volcanic gases at T >> 1060 °C (Symonds et al., 1992). Our observation of increasing Pb transport below 700 °C, due to the stability of $PbCl_{4(g)}$, is also in agreement with previous modeling (Symonds et al., 1987).

Trace elements in Erta Ale volcanic gas have high concentrations and have been sampled with different methods (Zelenski et al., 2013). Metals deposited at temperatures >1000 °C include oxides and silicates, followed by sulfides, sulfates and halides towards lower temperatures (Zelenski et al., 2013). This trend agrees well with our speciation calculations of the deposited metals in the Erta Ale volcanic gas. The dominant metal-bearing solids of Fe, Zn and Ga above 1000 °C are oxides, followed by sulfides. Chloride and fluoride species increase in abundance below 800 °C, but they only become the dominant species below 500 °C, outside our modeled temperature range. We predict Pb, Ni and Cu to be deposited as elemental metals above 1000 °C, but these phases were not observed by Zelenski et al. (2013), perhaps due to very low abundances in the bulk gas composition. Our calculations do not consider mixing between the volcanic gas and the ambient atmosphere. An adaptation of our model to include mixing with the atmosphere, a wider range of metals, and the use of metal concentrations reported for Erta Ale (Zelenski et al., 2013) may address these differences in the future.

2.5.4 Hydrogen speciation and implications for water on the Moon

Our models show that the most abundant hydrogen species in the lunar volcanic gas is H_2. Abundances of other H-bearing species (HF, HCl and H_2S) (Figure 2-2) are much higher

in the lunar volcanic gas than those of H_2O. Likewise, H-species other than H_2O are also important in the associated lunar melt and as diffusing species during degassing (Hirschmann et al., 2012; Armstrong et al., 2015; Newcombe et al., 2017). Given that the degassing profiles observed in lunar glass beads were modeled as H_2O (Saal et al., 2008), these models may require a re-evaluation. Specifically, H_2 in silicate melts and glasses diffuses much faster than H_2O, OH, HF, HCl and H_2S (Alletti et al., 2007; Zhang, 2011; Hirschmann et al., 2012; Saal et al., 2013; Sharp et al., 2013; Armstrong et al., 2015; Newcombe et al., 2017). Therefore, if some of the hydrogen was lost as fast diffusing H_2, the estimated initial H-abundance in the orange glass beads, and lunar bulk H-contents, may have been underestimated (Saal et al., 2008; Elkins-Tanton and Grove, 2011). In the C-O-H system H_2 become the dominant species (Newcombe et al., 2017), but in the presence of S, F and Cl a large proportion of the hydrogen forms H_2S, HF and HCl (Figure 2-2), resulting in similar abundances of CO and H_2. A better understanding of H-speciation, including an extended range of species such as those abundant in our volcanic gas model, is necessary to constrain the rate of degassing and the resulting composition of the bulk lunar volcanic gas. The high abundance of H_2, HF, HCl and H_2S suggests that the terms "wet", "damp" or "dry" may be misleading, given the inferred relative H_2O abundance. We therefore believe that it may be more appropriate to refer to hydrogen abundance rather than H_2O or water, as previously suggested by Zhang (2011).

If, as we suggest, H_2 is the dominant H species in both volcanic gas and melt this has significant implications for the Moon's bulk composition and how the interior varies in volatile concentrations. Explanations of volatile retention through the proposed giant impact process may need revision, and both the speciation and concentration of volatiles need to be incorporated into petrologic and geophysical models. For example, on Earth, volatiles affect properties of the mantle; separation of the core; the geochemistry and melting zones for basalts; fractional crystallization trends for mantle-derived magmas; and degassing on a planet's surface.

The importance of H_2 degassing resulting in high δD values has been stated before (Demény et al., 2006; Greenwood et al., 2011; Barnes et al., 2013; Saal et al., 2013; Sharp et al., 2013). In contrast, the presence of heavier hydrogen molecules such as HF, HCl and H_2S may reduce the rate of hydrogen loss from planetary bodies to space. This would reduce the degree to which H_2 loss can increase the oxygen fugacity and δD values (Sharp et al., 2013).

2.6 Conclusions

The composition and speciation of a lunar volcanic gas was calculated by applying volatile element concentrations in lunar pyroclastic glass beads (Saal et al., 2008; Wetzel et al., 2015). The gas composition was further used to model the speciation of trace elements abundant in coatings of lunar pyroclastic glass beads (Zn, Ni, Ga, Pb, Cu, Fe). The speciation varies with temperature and more extensively with pressure. The main gas species predicted by our models are CO, CO_2, CS_2, H_2, HF, HCl, COS, CS, S_2, H_2S, H_2S_2 and HS.

The total amount of hydrogen occurring as H_2 in the lunar gas ranges from 0.5 mole fractions to 0.85 mole fractions along the decompression and cooling path. The concentration of H_2O is more than five orders of magnitude lower than that of H_2. The significant concentrations of H_2, HF, HCl, H_2S and H_2S_2 indicate that when modeling H-degassing from lunar glass beads they need to be included. Omission of these species in previous models means that the bulk H-concentration on the Moon may be underestimated. Furthermore, it may be more appropriate to discuss H-species rather than specifically water as H_2O.

Trace metals are transported from the vent in the gas as elemental species, sulfides and chlorides. Most metals are largely deposited as sulfides, as observed in coatings of lunar pyroclastic glass beads (McKay and Wentworth, 1992). We predict variations of the speciation of metal-bearing solids deposited on these glass beads as a function of the temperature and pressure of deposition and therefore expect variations as a function of the distance from volcanic vents on the lunar surface. We expect native metals to be deposited close to the volcanic vents and with increasing distance from the vent sulfide abundances increase.

The lunar volcanic gas model was compared to a volcanic gas from the terrestrial Erta Ale volcanic. The models predict a higher abundance of metal gas species in the Erta Ale system than in the lunar gas. The metals are less volatile in the lunar gas, depositing at much higher temperatures than in the terrestrial system.

Sampling of dark mantle deposits on the Moon in relation to the source vents of the deposits would allow a better estimation of metal and volatile abundances in the lunar mantle sources of these magmas, and the temperature and pressure evolution of ancient lunar pyroclastic eruptions. Furthermore, additional work is required on detailed quantitative investigations of the mineralogy of the phases present in coatings of lunar glass beads from Apollo 15 and Apollo 17 in order to reliably ground truth the thermochemical model.

3 An experimental study of SO_2 reactions with silicate glasses and supercooled melts in the system anorthite-diopside-albite at high temperature

This chapter is in preparation for publication in *Contributions to Mineralogy and Geochemistry*.

Renggli C.J., King P.L., Henley R.W., Guagliardo P., McMorrow L., Turner M., Middleton J.

I conceptualized, prepared and conducted the experiments, performed the data analysis and wrote the manuscript. King and Henley contributed to the experimental objectives and design, edited and corrected the manuscript. Guagliardo assisted in the recording of nanoSIMS maps, NcMorrow helped with the solution ICP-MS analysis, Turner recorded X-ray tomography images, and Middleton helped with the evaluation of the tomography data.

3.1 Abstract

Sulfur dioxide ($SO_{2(g)}$) is the most abundant sulfur-bearing volcanic gas species on Earth. From its magmatic origin at depth to expulsion at the surface via either persistent degassing or large explosive volcanic eruptions, $SO_{2(g)}$ interacts with silicate materials at elevated temperatures. Similar high temperature reactions also occur in the volcanic systems and the atmospheres of Venus, the Galilean moon Io, and in Mars' past, as well in industrial flue-gas processing. We present an experimental investigation of the reaction between $SO_{2(g)}$, glasses and supercooled melts in the system anorthite-diopside-albite ($CaAl_2Si_2O_8$-$CaMgSi_2O_6$-$NaAlSi_3O_8$). The samples were exposed to $SO_{2(g)}$ at 600 – 800 °C for experimental durations of 10 minutes to 24 h. The reactions resulted in the formation of sulfate coatings and modified the near-surface composition of the silicate samples. The predominant sulfate reaction product is $CaSO_4$, with hydrated $MgSO_4$ or Na_2SO_4 also observed in some experiments. In the anorthite-diopside system the reaction extent strongly depends on the temperature relative to the glass transition temperature (T_g). Above T_g, in reactions with supercooled melts, the sulfate-forming reaction is up to 20 times more effective. The overall rate of sulfate formation is controlled by the diffusive flux of Ca, Mg and Na from the increasingly depleted silicate to the surface where the reaction with $SO_{2(g)}$ occurs. The sulfate-forming reaction results in a volume increase relative to the unreacted

silicate. Where this reaction occurs in the subvolcanic environment it may result in the closure of veins, a reduction of the permeability and consequently a decrease in the $SO_{2(g)}$ flux at the surface. An increase in the $SO_{2(g)}$ flux then requires the opening of new veins, which may be accompanied by seismic activity. The strong preferential uptake of Ca into the sulfate reaction product results in a Si- and Al-enriched silicate. In the sulfate the Ca component may be mobilized more easily by secondary processes such as through the interaction with meteoric fluids. We recommend that the products of such gas-solid reactions should be the object of remote and robotic investigations of planetary environments with volcanic histories such as on Mars, Io, Venus and Mercury.

3.2 Introduction

To constrain geochemical cycling and mineral evolution over time it is essential to understand how sulfur dioxide ($SO_{2(g)}$) reacts with silicates. Sulfur dioxide is a major volcanic gas species in terrestrial and planetary environments, including the atmosphere of present-day Venus and Jupiter's moon Io, plus it is likely to have played an important role in volcanic processes on early Mars (Pearl et al., 1979; Zolotov and Fegley, 1998; Glaze, 1999; Franz et al., 2018). In eruption plumes, $SO_{2(g)}$ plays an important role in the alteration of ash particle surfaces and consequently impacts the geochemical pathways of elements from volcanoes into the atmosphere, ocean and soil (Delmelle and Stix 2000; Delmelle et al., 2007; Ayris and Delmelle 2012; Ayris et al., 2013, 2015, Maters et al., 2016, 2017; Pardini et al., 2017; Mueller et al., 2017). In sub-volcanic environments $SO_{2(g)}$ reacts extensively with silicates to form sulfates and sulfide deposits (Henley et al., 2015, 2017). During quiescent periods (Vita et al., 2012; Mori et al., 2013; Henley and Hughes, 2016) volcanic gases filter through the subvolcanic environment with the potential to significantly alter the chemistry and mineralogy of the rocks they pass through (Henley et al., 2015, 2017). This is most significant to a depth of 3-6 km below the surface where the bulk of the $SO_{2(g)}$ has degassed from the magmatic source (Moretti et al., 2003; Aiuppa et al., 2009).

Sulfur dioxide is a highly reactive gas species which readily reacts with metals, basic oxides such as CaO and MgO, and carbonates (e.g. $CaCO_3$) to form sulfates (Gilewicz-Wolter, 1988; Waqif et al., 1992; Allen and Hayhurst, 1996; Gilewicz-Wolter et al., 2004; Hu et al., 2006; Gao and Chen, 2006; Baltrusaitis et al., 2007). The reactions are particularly efficient at high temperatures of up to 900 °C and used to remove the corrosive $SO_{2(g)}$ from flue gases produced during the burning of coal. For example, $SO_{2(g)}$ reacts with CaO to form anhydrite and CaS (Allen and Hayhurst, 1996):

$$2CaO + 2SO_{2(g)} \rightarrow CaSO_4 + CaS \qquad \textit{Equation 3-1}$$

Similarly, $SO_{2(g)}$ may react with multicomponent aluminosilicate glasses to form sulfates (Douglas and Isard, 1949). However, we currently cannot predict how $SO_{2(g)}$ + silicate reactions proceed, despite efforts using both experimental and theoretical approaches (Fegley and Prinn, 1989; Johnson and Burnett, 1993; Burnett et al., 1997; Ayris et al., 2013, 2015; Henley et al., 2015; Maters et al., 2016). Volcanic ash particles, which consist of aluminosilicate glass and crystalline minerals (Delmelle et al., 2018), show evidence of significant surface oxidation and acidification due to the reaction with volcanic gases (Delmelle et al., 2018). It has been proposed that alkali and alkaline earth oxides act as basic surface sites, onto which $SO_{2(g)}$ chemisorbs as a Lewis acid (Waqif et al., 1992; Maters et al., 2016; Delmelle et al., 2018). The primary sulfate observed on volcanic ash particles is anhydrite ($CaSO_4$) (Ayris et al., 2013, 2015; Barone et al., 2016; Delmelle et al., 2018), but $MgSO_4$, Na_2SO_4, $FeSO_4$ and K_2SO_4 have also been observed in coatings on volcanic ash particles from the Eyjafjallajökull eruption in April 2010 (Gislason et al., 2011).

The reaction between $SO_{2(g)}$ and volcanic ash was investigated experimentally by Ayris et al. (2013). These authors studied the reaction of tephrite, phonolite, dacite and rhyolite glasses, at temperatures up to 800 °C and for up to 1 hour reaction time, with a gas mixture containing 1 mol% $SO_{2(g)}$. Anhydrite was observed on all glasses reacted above 600 °C, and above 300 °C for all glasses except for rhyolite, and for durations from as short as 30 seconds. The efficiency of the $SO_{2(g)}$ scavenging was inferred to by controlled by the Ca^{2+} content of the glass and the diffusion of Ca^{2+} to the reaction interface (Ayris et al., 2013). Based on these experiments, volcanic ash may scavenge up to 73% of $SO_{2(g)}$ from a large explosive volcanic eruption plume (Ayris et al., 2013; Delmelle et al., 2018).

The reaction of $SO_{2(g)}$ with a Ca^{2+}-rich aluminosilicate such as anorthite results in the formation of the sulfate anhydrite, Ca-depleted aluminosilicate and reduced sulfur. The balance of charges is ensured by the disproportionation of sulfur (S^{4+}) in the $SO_{2(g)}$ reactant to form products containing oxidized S^{6+} and reduced S^{2-} (or another reduced S-species such as a S radical). The reaction has the following form, as first proposed by (Burnham, 1979):

$$2CaAl_2Si_2O_8 + 3SO_{2(g)} \rightarrow 2CaSO_4 + 2Al_2SiO_5 + 2SiO_2 + 0.5S_{2(g)} \quad \textit{Equation 3-2}$$

Quartz (SiO_2) and Al_2SiO_5 represent the Si- and Al-rich products, which depend on the temperature conditions of the reactions. At higher temperatures andalusite may be replaced by sillimanite, and in more aluminous systems mullite or corundum may become stable. In hydrous systems, these components may form clay minerals.

The reaction is initiated by chemisorption of polar $SO_{2(g)}$ molecules onto partially positively charged surface sites on the silicate (Henley et al., 2015). Once all surface sites have been occupied by $SO_{2(g)}$ the reaction proceeds via Ca^{2+} diffusion from the silicate substrate to the surface (Ayris et al., 2013; Henley et al., 2015; Maters et al., 2016; Delmelle et al., 2018; Renggli and King, 2018).

In the system anorthite-diopside-albite (An-Di-Ab) additional sulfate-forming reactions may occur. These reactions require the mobilization of Mg^{2+} and Na^{+} cations from the reactant silicate to form $MgSO_4$ and Na_2SO_4. The reactions of diopside and albite with $SO_{2(g)}$ can be written as:

$$CaMgSi_2O_6 + 3SO_{2(g)} \rightarrow CaSO_4 + MgSO_4 + 2SiO_2 + 0.5S_{2(g)} \quad \textit{Equation 3-3}$$

$$4NaAlSi_3O_8 + 3SO_{2(g)} \rightarrow 2Na_2SO_4 + 2Al_2SiO_5 + 10SiO_2 + 0.5S_{2(g)} \quad \textit{Equation 3-4}$$

At high temperatures these reactions have upper limits given by the thermal stabilities of the sulfates. $MgSO_4$ and $CaSO_4$ decompose above 900 °C and 1200 °C respectively (Rowe et al., 1967; Du, 2000), whereas Na_2SO_4 has a liquidus temperature (T_l) of 884 °C and may vaporize ($Na_2SO_{4(s)} = Na_2SO_{4(g)}$) (Stern and Weise, 1966; Freyer et al., 1998). In addition, Na_2SO_4 passes through two or three phase transitions below 240 °C, depending on the cooling or heating path (Freyer et al., 1998). Processes affecting the chemical and mineralogical evolution of anhydrous mafic and intermediate magmas can be fruitfully explored using the An-Di-Ab system (Morse, 1980). This system provides a convenient way to evaluate a range of compositions relevant to nature because it includes Na, Ca and Mg – that vary substantially in natural melts – and that react readily with $SO_{2(g)}$. Whilst we ultimately wish to understand reactions of $SO_{2(g)}$ with natural materials, this study allows us to investigate the behavior of Na, Ca and Mg while avoiding complications that arise from adding multivalent elements such as Fe.

Here, we present results from reaction experiments between $SO_{2(g)}$ and aluminosilicate glasses and supercooled melts in the An-Di-Ab system with the aim to improve the understanding of the reaction mechanisms. The investigated silicate compositions have glass transition temperatures (T_g) ranging from 722 °C (diopside) to 863 °C (anorthite) (Russell & Giordano, 2005). Above T_g the materials behave as supercooled melts and below T_g as solid glasses. Experiments were performed at 600 to 800 °C for 10 minutes to 24 hours and analyzed using a range of methods including Raman spectroscopy, inductively coupled plasma mass spectrometry (ICP-MS), scanning electron microscopy with energy-dispersive X-ray spectroscopy (SEM/EDS) and nanoscale secondary ion mass spectrometry (nanoSIMS). We observed complete coverage of all silicate glasses with sulfates within few minutes of exposure to $SO_{2(g)}$ at 600 and 800 °C.

Table 3-1: Starting anorthite-diopside-albite glass reactants and sulfate products. The ratio of non-bridging oxygens over the number of tetrahedrally coordinated network-forming cations in the glass structure (NBO/T; calculated assuming all Al_2O_3 is tetrahedrally coordinated), the liquidus temperature (T_l) and the glass transition temperature (T_g) (Russell & Giordano 2005) are calculated for the glasses.

			Diopside	$An_{15}Di_{85}$	$An_{36}Di_{64}$	$An_{48}Di_{52}$	Anorthite	$An_{65}Di_{25}Ab_{10}$	Albite	An_5Ab_{95}	$An_{27}Ab_{73}$
	Glass composition in wt.%	SiO_2	57.1	54.4	51.2	49.6	43.2	48.3	68.7	67.4	61.8
		Al_2O_3	0.0	7.0	15.8	20.2	36.7	27.3	19.4	20.4	24.1
		CaO	25.5	24.6	23.2	22.1	19.8	19.3	0	1.1	5.5
		MgO	17.5	13.9	9.9	7.8	0.0	3.9	0	0	0
		Na_2O	0.0	0.0	0.0	0.0	0.0	1.2	11.8	11.2	8.6
		Total	100.1	99.9	100.1	99.7	99.7	100.0	99.9	100.1	100.0
	NBO/T		2.00	1.48	0.94	0.70	0.00	0.29	0.00	0.00	0.00
	T_l (°C)		1391.5	1350	1274	1350	1553	~1440	1118	~1200	~1370
	T_g (°C) (Russell & Giordano 2005)		722	729	746	760	863	~790	797	799	812
Experimental conditions and reaction products	600 °C	10 min									
		1 h	$CaSO_4$	$CaSO_4$, $MgSO_4$			$CaSO_4$	$CaSO_4$, $MgSO_4$	Na_2SO_4	$CaSO_4$	
		24 h									
	700 °C	1 h							Na_2SO_4	$CaSO_4$	
		24 h									
		72 h									$CaSO_4$
	800 °C	1 h	$CaSO_4$ + di		$CaSO_4$	$CaSO_4$ + di	$CaSO_4$		Na_2SO_4	$CaSO_4$	
		24 h									

di: indicates the occurrence of diopside crystllization in the glass substrate near the reaction interface (see Figure 3-5)

3.3 Methods

3.3.1 Choice of starting materials

Experiments were performed with glasses and supercooled melts in the system An-Di-Ab (Figure 3-1). The compositions include the endmembers anorthite, diopside and albite, the eutectic $An_{36}Di_{64}$ glass, two additional compositions in the An-Di binary system ($An_{15}Di_{85}$ and $An_{48}Di_{52}$) both with liquidus temperatures of 1350 °C, $An_{27}Ab_{73}$ (Lee et al., 2010), and a ternary $An_{65}Di_{25}Ab_{10}$. The compositions, liquidus temperatures, glass transition temperatures (Morse, 1980; Russell and Giordano, 2005) and degrees of polymerization, as the number of non-bridging oxygen atoms per aluminosilicate tetrahedron (NBO/T), are given in Table 3-1. The An-Ab glasses are fully polymerized with NBO/T = 0. The An-Di glasses show a range of NBO/T values (Table 3-1), where the most depolymerized glasses have the highest Mg contents. The samples diopside, $An_{15}Di_{85}$, $An_{36}Di_{64}$ and $An_{48}Di_{52}$ behave as supercooled melts in experiments at 800 °C.

3.3.2 Experimental set-up

The albite silicate glass was synthesized from chemical grade oxide (SiO_2, Al_2O_3) and carbonate (Na_2CO_3) powders. The powders were mixed and ground before melting at 1500 °C for 10 minutes. The melt was quenched, reground and homogenized prior to re-melting at 1500 °C. This process was repeated to obtain a homogeneous glass. The diopside and anorthite endmember glasses were provided by B. Fegley. Intermediate (An-Di) glasses were synthesized by mixing the powdered endmembers glasses and melted at 1500 °C. The synthesized glasses were homogeneous and free of crystallites. They were broken into chips and polished on the top surface to ¼ μm. The polished glass chips were washed with methanol to remove any organic materials.

High temperature experiments were run in a vertical tube furnace. The glass chips, with the polished surface facing upwards, were placed on a Pt tray suspended from an alumina rod. The use of Pt has the additional benefit of catalyzing the equilibrium dissociation of $SO_{2(g)}$ (Luthra and Worrell, 1978; Zolotov and Fegley, 1999). Before the exposure to $SO_{2(g)}$, the samples were flushed under $Ar_{(g)}$ for 2 minutes to allow for thermal equilibration. The $SO_{2(g)}$ flow rate during the experiment was set to 50 sccm. At the end of the experiment the furnace was purged with $Ar_{(g)}$ for 2 minutes before lifting the Pt tray with the samples out of the furnace. The samples were immediately placed in a desiccator to avoid hydration of the surface materials. For each experimental run four glass aliquots of the same composition were reacted to be used for different analytical investigation (Dalby et al., 2018; Palm et al., 2018).

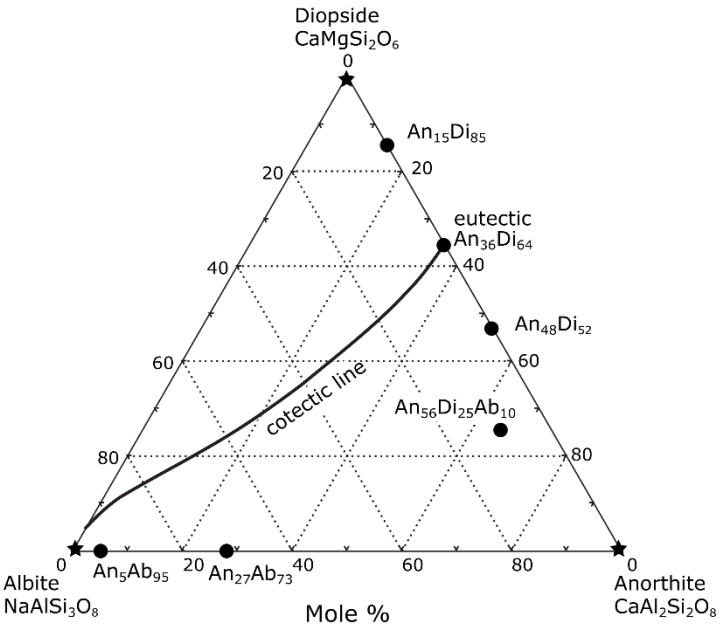

Figure 3-1: Ternary diagram of the Anorthite-Diopside-Albite system in mol% shows the compositions used in this study.

3.3.3 Analytical methods

Micro-Raman spectroscopy was used to characterize the phases formed as reaction products in the coatings. The technique was chosen because it can determine mineral structure and also identify any secondary processes such hydration (Mernagh et al., 2018). Raman measurements were made with a Renishaw 2000 Raman Microscope using a wavelength of 532 nm with a spot size of ~1 µm. The resulting power on the sample through a 100x objective lens was approximately 3 mW. At these conditions the Raman sampling volume extends up to 3 µm into the sample.

Field emission scanning electron microscopy (FE-SEM) was used as the principal method to document the sulfate reaction products formed on the glass surfaces. The samples were carbon coated and imaged using a Hitachi S-4300 SE/N FE-SEM. High-magnification secondary electron images were taken at a short working distance of ~3 mm and low voltages of 3 to 5 kV using an in-lens detector and 0.6 nA beam current. Additional images and energy-dispersive X-ray spectra (EDS) were recorded at 15 kV and a working distance of 25 mm using a 80 mm^2 silicon drift detector.

The bulk compositions of the sulfate reaction products formed in experiments with anorthite-diopside glasses and supercooled melts were determined by dissolving the sulfates and measuring the Ca and Mg concentrations in the obtained solutions with a Varian 820 inductively coupled plasma mass spectrometer (ICP-MS). The sulfate-coated samples were placed in plastic containers which had been cleaned overnight in 10% nitric

acid solutions. The sulfates were then dissolved ultrapure water and placed in an ultrasonic bath to destabilize the coating mechanically. After 30 hours, nitric acid was added increasing the solubility of sulfate and stabilizing the solutions. The samples were checked under a polarizing light microscope to ensure that no sulfates were left on the surfaces. Additionally, three blank solutions were prepared. The solutions were diluted by an order of magnitude and analyzed for the isotopes ^{24}Mg, ^{25}Mg, ^{26}Mg, ^{43}Ca and ^{44}Ca. Multi-element AccuTrace standards (AccuStandard Inc.) with cation concentrations of 10 ppm, 50 ppm, 100 ppm and 1000 ppm, and blank solutions were measured prior to sample analysis and again after each 14 sample analysis. Samples with high concentrations were diluted by an additional factor of ten.

After dissolving the sulfate coatings from the glass chips for ICP-MS analysis, the surface areas of the chips were measured using X-ray micro-CT imaging (XCT). The micro-CT measurements allow us to normalize solution ICP-MS data to the specific surface area of each chip and to calculate the absolute amounts of reaction products and rates. We recorded the XCT images at the CTLab at the ANU, using a laboratory-based machine that was built in-house (Wildenschild and Sheppard, 2013; Dalby et al., 2018). The obtained images had a voxel size (i.e. 3D pixel) of 1.7 μm. The grayscale tomogram was processed using the image processing software Mango, developed by the Department of Applied Mathematics at the ANU. The surface area was determined by laying a continuous mesh over the glass chips, defined by a steep gradient in the grayscales from the glass to the surrounding air. The obtained surface area measurements have estimated uncertainties of 10%.

Crystalline silicates formed in some of the reacted supercooled melts and were documented with high-resolution elemental maps with the CAMECA NanoSIMS 50L at the Centre for Microscopy, Characterisation and Analysis, at the University of Western Australia. The samples were mounted in resin, cross-sectioned, polished and gold coated. The ion source was a Hyperion (H200) oxygen ion source, with a spot size of approximately 100 nm, at an impact energy of 16 keV and a beam current of 12.5 pA. The elemental maps were recorded in multicollection mode, allowing the simultaneous measurement of seven ion species. The field of view was 50 μm^2 at a resolution of 512 x 512 pixels.

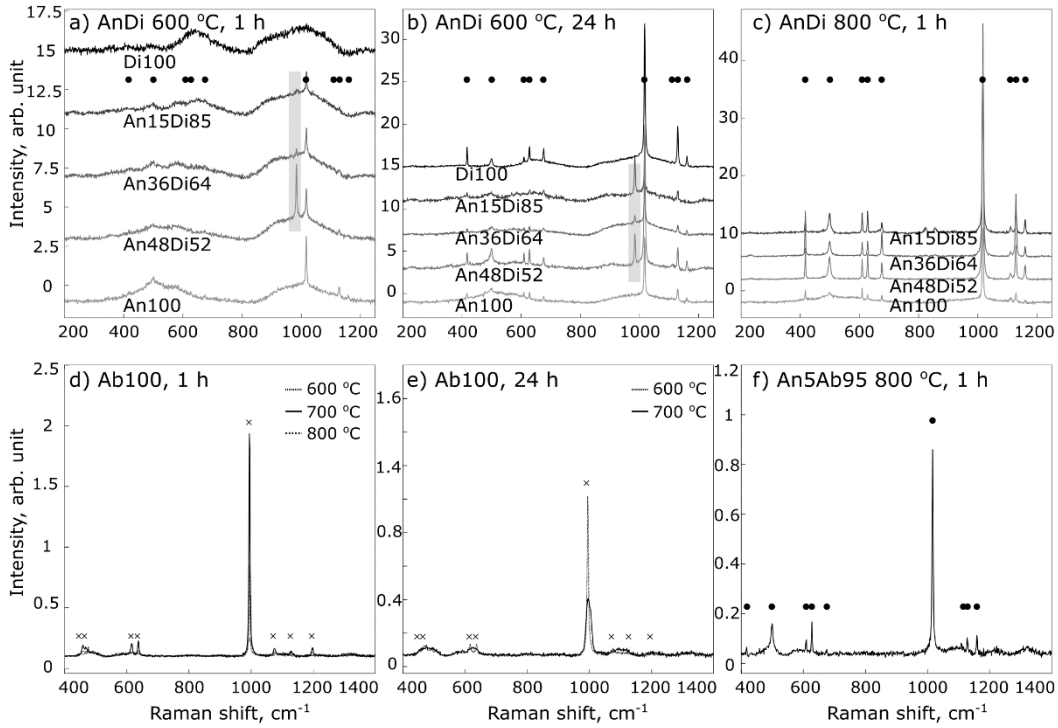

Figure 3-2: Raman spectra of the surface coatings on reacted An-Di, Ab and An-Ab samples. Black dots indicate the main anhydrite peaks (Liu et al., 2009), x indicate the Na_2SO_4 (phase III) peaks (Hapanowicz and Condrate, 1996), and grey boxes show the main peaks of $MgSO_4 \cdot 7H_2O$ (epsomite; (Wang et al., 2006). a) An-Di, 600 °C, 1 h, the spectra show the sulfate coating (sharp peaks), including anhydrite and epsomite, and broad bands from the underlying glasses. b) An-Di, 600 °C, 24 h. Anorthite and diopside endmember glasses form $CaSO_4$ and the intermediate glasses contain epsomite in addition. c) An-Di, 800 °C, 1 h. $CaSO_4$ is the only phase detected in the coatings of all An-Di glasses and supercooled melts. d) Ab, 600, 700 & 800 °C, 1 h. Na_2SO_4 (phase III) is the only sulfate in the coating. e) Ab, 600 & 700 °C, 24 h. Only Na_2SO_4 (phase III) is observed in the coating. f) An_5Ab_{95}, 800 °C, 1h. Only $CaSO_4$ is detected in the coating.

3.4 Results

3.4.1 Raman spectroscopy of reaction products

Raman spectra indicate that sulfate mineral phases formed as coatings on the reacted glass and supercooled melt chips (Figure 3-2 and Table 3-1). We identify different combinations of three phases: 1) $CaSO_4$ (anhydrite), with a main band at 1017 cm^{-1} (Liu et al., 2009); 2) $MgSO_4 \cdot 7H_2O$ with a strong band at 984 cm^{-1} (Wang et al., 2006) and; 3) Na_2SO_4 with the strongest band at 992 cm^{-1} (phase III; Hapanowicz and Condrate, 1996; Choi and Lockwood, 2005). The Raman spectra have different relative band intensities due to varying phase abundances and crystallinities of the sulfate grains (Figure 3-2). Furthermore, where the coatings have thicknesses ≤ 1 µm, the Raman laser also probes the glass substrates, observed as broad Raman bands (Figure 3-2).

The spectra of the coatings on the An-Di glasses reacted at 600 °C for 1h show the broad bands of the silicate glass substrates with sharp bands related to anhydrite (1017 cm^{-1}), except for the diopside glass which had a very thin coating not detected by Raman. The coatings on the $An_{48}Di_{52}$, $An_{15}Di_{85}$ and $An_{36}Di_{64}$ glasses also contain $MgSO_4 \cdot 7H_2O$. After 24 h Raman records the same mineralogy in the coatings, but with much higher band intensities. Surprisingly, the Mg-rich diopside glass is coated only by anhydrite with no evidence of any dry or hydrated Mg-sulfate. At 800 °C, where diopside, $An_{15}Di_{85}$, $An_{36}Di_{64}$ and $An_{48}Di_{52}$ are above T_g and behave as supercooled melts, after 1 h of reaction, only the coatings (>2 µm thick) are detected and, unlike the reactions at 600 °C, Mg-sulfates are absent in the reaction products.

The albite glass reacted with $SO_{2(g)}$ to form Na_2SO_4 (phase III) at all experimental conditions, at 600, 700 and 800 °C for 1 h and 24 h, and also within 10 minutes at 600 °C (Appendix). Previously, it has been suggested that Na_2SO_4 should not form as a reaction product between albite and $SO_{2(g)}$ (Burnett et al., 1997). At 600 - 800 °C the stable phase is the hexagonal Na_2SO_4 I which transforms to Na_2SO_4 III at 240 °C, which should subsequently transform to thenardite (Na_2SO_4 V) at 180 °C (Freyer et al., 1998). This final transformation to thenardite was not observed in any experiment and was likely kinetically inhibited. Textural features of the Na_2SO_4 coating on the albite glass are likely affected by the transformation from the high temperature phase, upon cooling. Surprisingly, no Na_2SO_4 was observed on the $Ab_{95}An_5$ glass, despite its high Na-content: only anhydrite was observed (Figure 3-2). Mixed Na-Ca-sulfates such as glauberite were not observed in any experiment (cf. Palm et al., 2018).

3.4.2 Surface textures

The investigation of the surface coating textures provides insights into the sulfate growth mechanisms. Similar textures of coatings – or "scales" as they are termed in corrosion literature (Birks et al., 2006) – are known from the oxidation and corrosion of metals and metal oxides (Bastow et al., 1981; Evans et al., 1983; Suo, 1995; Tolpygo and Clarke, 1998a, b; Chason et al., 2013). The sulfate reaction products were imaged by field emission scanning electron microscopy (FE-SEM), providing high-resolution images of the sulfate coating textures (Figures 3-3 and 3-4).

The sulfate coatings can be classified into two groups, continuous and discontinuous coatings (Figures 3-3 and 3-4). The continuous coatings can further be distinguished into three groups, as a) equigranular and undeformed coatings; b) deformed coatings, and; c) coatings with different grain-size populations (Figure 3-3). Their textures vary strongly with composition, experimental duration and temperature. Sulfate grain-sizes range from

50 nm in diameter on the diopside glass reacted at 600 °C for 1 hour, to tens of microns thick crusts on some supercooled melts reacted at 800 °C for 24 hours.

On the anorthite endmember glasses, the anhydrite coatings form equigranular textures with grain diameters of up to 2.5 µm, with no significant deformation features (Figure 3-3a to d), except for small hillocks and protrusions on glasses reacted for 24 h (Figure 3-3b and d). On the diopside endmember glasses, the anhydrite grains are generally smaller with less pronounced crystal faces (Figure 3-3i to l). Anhydrite grains are up to 100 times larger in coatings of diopside supercooled melts reacted at 800 °C compared to 600 °C.

The textures of the three intermediate anorthite-diopside glasses and supercooled melts ($An_{15}Di_{85}$, eutectic $An_{36}Di_{64}$, $An_{48}Di_{52}$) behave similarly across temperature and experimental duration. SEM images of the coating textures on the eutectic $An_{36}Di_{64}$ sample are shown in Figure 3-3, representative for all intermediate anorthite-diopside samples, and the other images are compiled in the Appendix Figure 9-1. The sulfates formed on the intermediate samples always form continuous coatings.

Magnesium sulfate ($MgSO_4 \cdot 7H_2O$) is only observed microscopically on the intermediate glasses reacted for 24 h, at 600 °C (Figure 3-3f). The grains are semi-euhedral with slightly rounded facets. This is due to later hydration to the more stable $MgSO_4 \cdot nH_2O$ polymorph from $MgSO_4$ grains formed at experimental conditions.

At 800 °C no $MgSO_4$ is observed in the coatings, which is in agreement with the Raman measurements. The coatings are thick, wrinkled and buckled at the grain size of 2.5 µm and at the overall coating thickness of hundreds of microns. After 24 hours the small-scale texture is similar on $An_{15}Di_{85}$ and $An_{36}Di_{64}$, with long whiskers and protrusions extending from the sulfate coating (Appendix Figure 9-1). Over longer length scales the coatings on all intermediate An-Di supercooled melts, formed at 800 °C, are wrinkled and buckled extensively (Figure 3-3g and h). These textural features are self-similar over two orders of magnitude. Small wrinkles extend over 5 to 10 µm, superimposing large buckles in the coating over 100-200 µm. The buckles are hollow within and not infilled by additional sulfate, as observed where the buckles were cracked after the experiment (Figure 3-3h).

The albite glass is discontinuously coated by Na_2SO_4 (Figure 3-4). At 600 °C sulfate grains have well developed crystal facets and form isolated groups of up to six individual crystals (Figure 3-4a), whereas the grain morphologies are less well developed and become polycrystalline at higher temperatures (800 °C, Figure 3-4b). After 1 h at 800 °C Na_2SO_4 forms rounded features with leaf shaped crystals and twinned grains, some of which appear to extend from the surface outward. These textures are lost after 24 hours where the sulfates form piles of needle shaped crystals with diameters of only 100 nm (Appendix Figure 9-2).

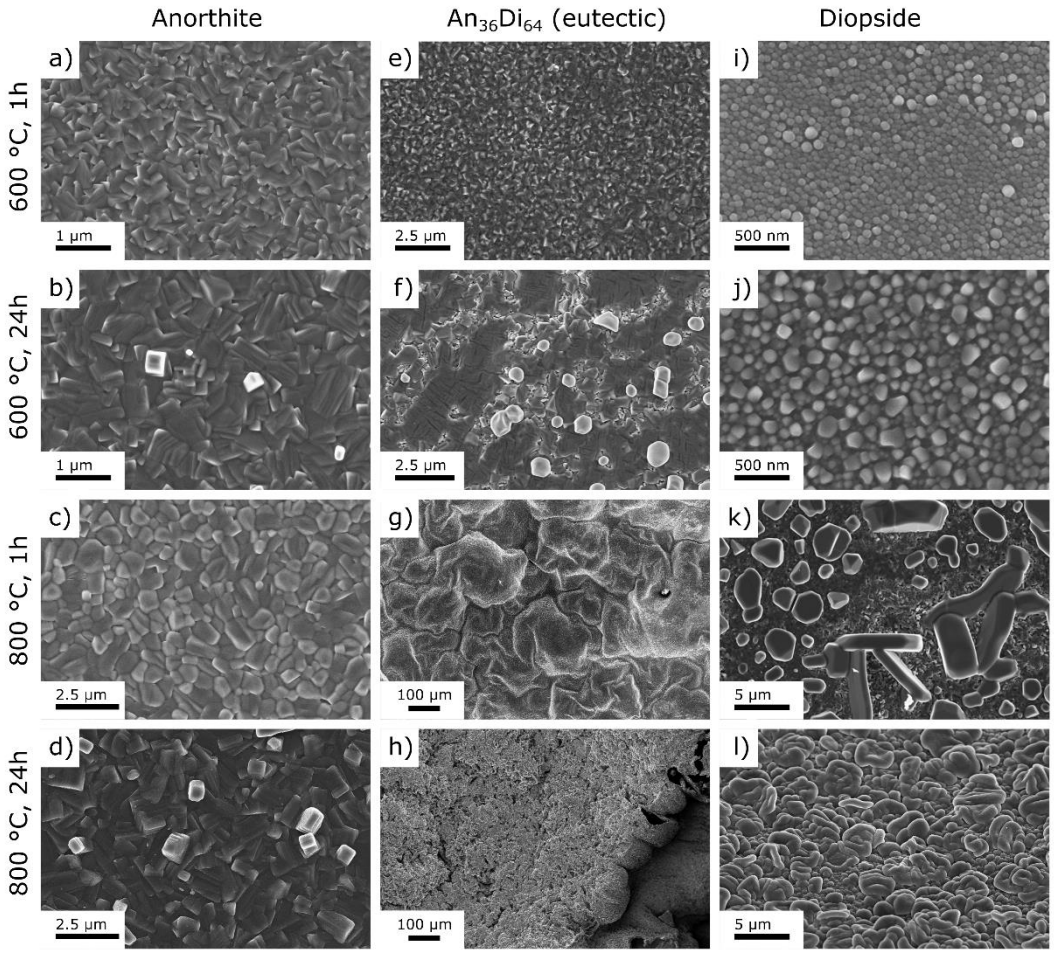

Figure 3-3: Secondary electron SEM images of the sulfate textures observed on reacted glasses. Left: anorthite; Middle: eutectic $An_{36}Di_{64}$; Right: diopside. The images show the textures at 600 °C (top row: 1 hour, second row: 24 hours) and 800 °C (third row: 1 hour, forth row: 24 hours). a) Continuous coating of $CaSO_4$ grains with sizes of 200 nm. b) Larger grain sizes ($CaSO_4$) of 360 nm with some grains extending outwards from the coating surface. c) Grain sizes of up to 1 µm in diameter. d) Multiple $CaSO_4$ grains extend as hillocks from the sulfate coating. Grain sizes are comparable to those after 1h reaction at 800 °C, but the texture is less uniform. e) Continuous coating of $CaSO_4$ and epsomite on the eutectic $An_{36}Di_{64}$ with very small grain sizes. Epsomite has been detected in this coating, but the grains are not apparent. f) Coating consisting of large $CaSO_4$ grains and epsomite grains with rounded morphologies sitting on top of the $CaSO_4$. g) Thick coating of $CaSO_4$ is wrinkled and buckled forming a very rough surface. h) With increasing experimental duration wrinkling and buckling of the thick $CaSO_4$ coating increases significantly. i) Poorly crystallized nano-sized (70 nm) grains of $CaSO_4$. j) Increasing reaction time results in slightly larger grain sizes (100 nm) and the development of some crystal faces on the grains. k) At 800 °C the $CaSO_4$ texture on the diopside supercooled melt changes dramatically, forming larger well-developed crystals with diameters of more than 5 µm. l) Continuous coating of $CaSO_4$ on diopside supercooled melt formed at 800 °C over 24 hours.

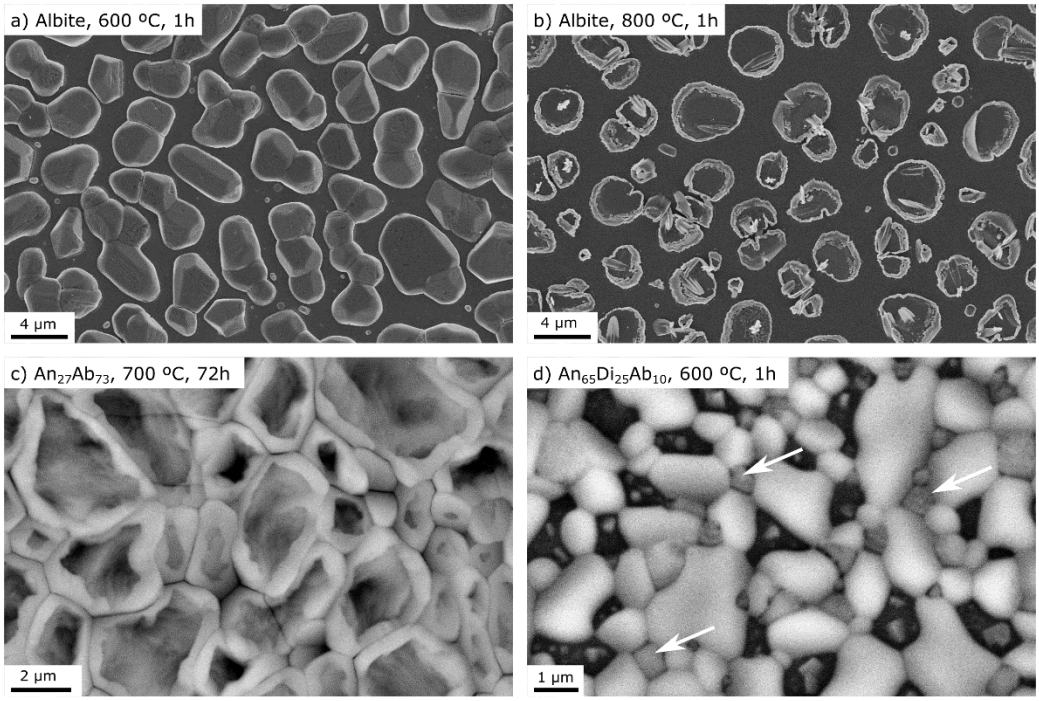

Figure 3-4: SEM images of the surfaces of reacted albite-bearing glasses. a) albite glass reacted at 600 °C for 1 hour with well crystallized grains of Na_2SO_4. b) albite glass reacted at 800 °C for 1 hour. The Na_2SO_4 grains are have poor crystal habit likely because the temperature is close to the liquidus temperature of Na_2SO_4 (884 °C). c) $An_{27}Di_{73}$ glass reacted at 700 °C for 72 hours. The glass is continuously coated with $CaSO_4$, forming a chicken wire texture as individual grains appear bent upwards at grain boundaries. d) $An_{65}Di_{25}Ab_{10}$ glass reacted at 600 °C for 1 hour. Backscattered electron image shows large $CaSO_4$ grains and smaller epsomite grains indicated by arrows. The substrate glass appears in darker gray shades.

3.4.3 Composition of the surface material, solution ICP-MS, EDS

We examined the bulk compositions of the sulfate reaction products from the $SO_{2(g)}$ reaction experiments with the An-Di compositions by dissolving the sulfates in water and analyzing them with solution ICP-MS. Measuring the Ca- and Mg-concentrations in the sulfate coatings provides the relative molar abundances of $CaSO_4$ and $MgSO_4$ formed during the reaction. The data is presented as molar fraction of Ca/(Ca+Mg) in sulfate ($X_{Ca}^{sulfate}$) which we compared with X_{Ca}^{glass} in the unreacted silicates (Table 3-2). We measured several isotopes of Ca (^{43}Ca and ^{44}Ca) and Mg (^{24}Mg, ^{25}Mg, ^{26}Mg) to check for the reliability of the analysis. The analysis of the different isotopes provided the same element concentrations. Calcium and Mg isotopes did not show any fraction due to the gas-solid reaction at the experimental temperatures of 600 and 800 °C. The molar concentrations of Ca and Mg are equivalent to those of the sulfates $CaSO_4$ and $MgSO_4$.

Table 3-2: Relative molar concentrations of Ca and Mg in the unreacted An-Di glasses and in sulfate reaction products, determined from solution ICP-MS. The total amounts of sulfate reaction products are given in µmol/m². The rates of reaction are given as the parabolic reaction constant (µmol/m²/(min$^{1/2}$)).

	Temperature (°C)	Time (min)	$X_{Ca}^{silicate}$	$X_{Ca}^{sulfate}$	Surface area determined by XCT (m²)	Sulfate amount (µmol/m²)	Uncertainty (µmol/m²)	Parabolic reaction constant (µmol/m²/(min$^{1/2}$))	Flux (J) of cations from glass to sulfate (mol/m²/s)		Relative fluxes
									JCa	JMg	JCa/JMg
An_0Di_{100}	600	60	0.500	0.674	2.88E-05	3.7E+02	4.0E+01	5.E+01	6.9E-08	3.3E-08	2.1
$An_{15}Di_{85}$			0.541	0.742	2.77E-05	7.1E+02	7.3E+01	9.E+01	1.5E-07	5.1E-08	2.9
$An_{36}Di_{64}$			0.610	0.759	2.42E-05	2.9E+03	3.0E+02	4.E+02	6.0E-07	1.9E-07	3.2
$An_{48}Di_{52}$			0.658	0.774	1.63E-05	3.7E+03	3.8E+02	5.E+02	8.0E-07	2.3E-07	3.4
$An_{100}Di_0$			1.000	1.000	1.71E-05	4.9E+03	5.0E+02	6.E+02	1.3E-06		
An_0Di_{100}	600	1440	0.500	0.739							
$An_{15}Di_{85}$			0.541	0.617							
$An_{36}Di_{64}$			0.610	0.641							
$An_{48}Di_{52}$			0.658	0.853							
$An_{100}Di_0$			1.000	1.000							
An_0Di_{100}	800	60	0.500	0.975	2.40E-05	5.4E+03	5.4E+02	7.E+02	1.5E-06	3.7E-08	39.1
$An_{15}Di_{85}$			0.541	0.993	1.31E-05	1.0E+04	1.0E+03	1.E+03	2.9E-06	2.0E-08	140.7
$An_{36}Di_{64}$			0.610	0.849	4.80E-05	1.7E+04	1.8E+03	2.E+03	4.0E-06	7.1E-07	5.6
$An_{48}Di_{52}$			0.658	0.977	1.73E-05	1.1E+04	1.1E+03	1.E+03	3.0E-06	6.9E-08	42.6
$An_{100}Di_0$			1.000	1.000	2.24E-05	7.2E+03	7.3E+02	9.E+02	2.0E-06		
An_0Di_{100}	800	1440	0.500	0.953	2.70E-05	7.0E+03	7.1E+02	5.E+01	7.7E-08	3.8E-09	20.3
$An_{15}Di_{85}$			0.541	0.997	3.15E-05	1.5E+04	1.5E+03	1.E+02	1.7E-07	5.1E-10	334.5
$An_{36}Di_{64}$			0.610	0.991	6.98E-05	2.8E+04	2.8E+03	4.E+02	3.2E-07	3.0E-09	106.2
$An_{48}Di_{52}$			0.658	0.995	3.45E-05	1.6E+04	1.6E+03	2.E+02	1.8E-07	9.0E-10	202.3
$An_{100}Di_0$			1.000	1.000	2.81E-05	7.8E+03	7.9E+02	2.E+01	9.1E-08		

3.4.4 Surface areas of the An-Di chips measured by X-ray computed tomography

Gas-solid reactions are critically dependent on the surface areas of the reacted solids (Szekely et al., 1976). In order to obtain absolute amounts of formed sulfates we measured the surface areas of the An-Di chips, after dissolving the sulfate coatings for solution analysis, using XCT. We could not measure the surface areas with the more conventional BET (Brunauer-Emmett-Teller) method (Brunauer et al., 1938), because the surface areas of the glass chips are too small for an accurate or precise result. Instead, XCT provided surface area data for the An-Di glasses and supercooled melts reacted at 600 °C for 1 h, and at 800 °C for 1 and 12 h (Table 3-2). The glass chips have surface areas ranging from $1.3x10^{-5}$ to $4.8x10^{-5}$ m^2. The estimated uncertainties of the surface area measurements are 10%.

Dividing the molar amounts of sulfates ($CaSO_4$ + $MgSO_4$), obtained from the solution ICP-MS analysis, with the surface areas gives the molar amounts for each glass chips as μmol/m^2 (Table 3-2). The values range from $4x10^2$ μmol/m^2 of sulfates on the diopside glass reacted for at 600 °C for 1 h, to $2.8x10^4$ μmol/m^2 of sulfates on the eutectic $An_{36}Di_{64}$ supercooled melt reacted at 800 °C for 24 h. For a single composition, the amounts of sulfate formed at 800 °C may be up to 15x greater than coatings formed at 600 °C (Table 3-2).

3.4.5 Crystallization of the substrate glass observed by nanoSIMS

As a consequence of forming Ca-, Mg- and Na-sulfate reactants and the loss of Ca^{2+}, Mg^{2+} and Na^+ from the aluminosilicate glass, the reacted substrates are chemically altered. Crystallization of silicates in the reacted silicate substrates near the surface was observed in the diopside, $An_{15}Di_{85}$ and $An_{48}Di_{52}$, reacted at 800 °C for one hour and 24 hours (Table 3-1). These samples have T_g < 800 °C (Table 3-1) and are supercooled melts at these experimental conditions and hence more allow crystallization. In all three cases the silicate crystallized was diopside, identified by Raman spectroscopy. The most extensive crystallization was observed in the diopside sample reacted at 800 °C for 24 hours (Figure 3-5). The crystallization rim extended approximately 10 μm from the surface into the interior of the substrate. The silicate below the crystallization rim is depleted in Mg and enriched in Ca, as revealed by nanoSIMS. Surprisingly, no crystallization was observed in the eutectic sample even though it was above the glass transition temperature. Also, no crystallization was observed in the An endmember glass and the Ab-bearing glasses.

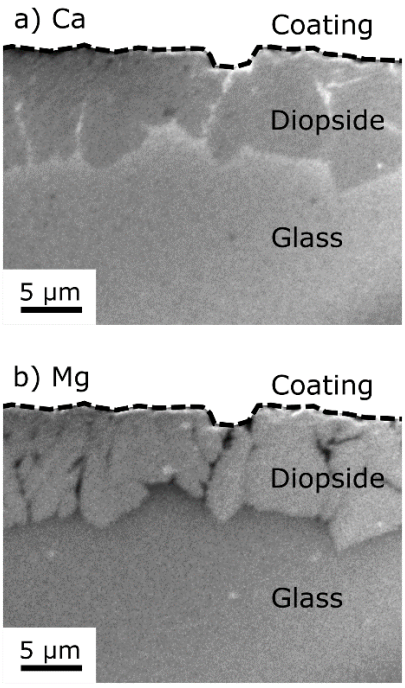

Figure 3-5: nanoSIMS count maps of a cross-section into a diopside sample reacted at 800 °C for 24 hours. Lighter gray-scale values indicate higher count rates. The stippled black line indicates the interface between the reacted glass below and the sulfate coating above after the reaction. During sample preparation the sulfate coating was lost from the surface. The maps show the crystallization of diopside at the reaction interface. a) Ca-map; Ca is slightly enriched around diopside crystals. b) Mg-map; Mg is depleted around and between diopside crystals.

3.5 Discussion

3.5.1 Textural evolution of sulfates

Textural features observed in the sulfate coatings may be primary, due to processes operating during the gas-solid reaction at high temperature, or secondary, during storage of the samples at room temperature in a desiccator or during analysis in air (e.g., via hydration of the sulfates during Raman analysis). In our experiments $MgSO_4$ is observed in its hydrated form $MgSO_4 \cdot 7H_2O$ (Figure 3-2). Sulfate hydration could only be observed in the coatings on the An-Di glasses containing $MgSO_4$ formed at 600 °C, whereas no sulfate hydration was observed in the coatings formed at 800 °C, which only contain dry $CaSO_4$ (Table 3-1). For this reason, we only consider textural features of coatings which consist of $CaSO_4$.

Following the initial chemisorption reaction, which uses up all available surface reaction sites (Delmelle et al., 2018), the $SO_{2(g)}$ can no longer directly bond to the glass surface. From this monolayer of chemisorbed $SO_{2(g)}$ on the glass or supercooled melt, sulfate grains nucleate.

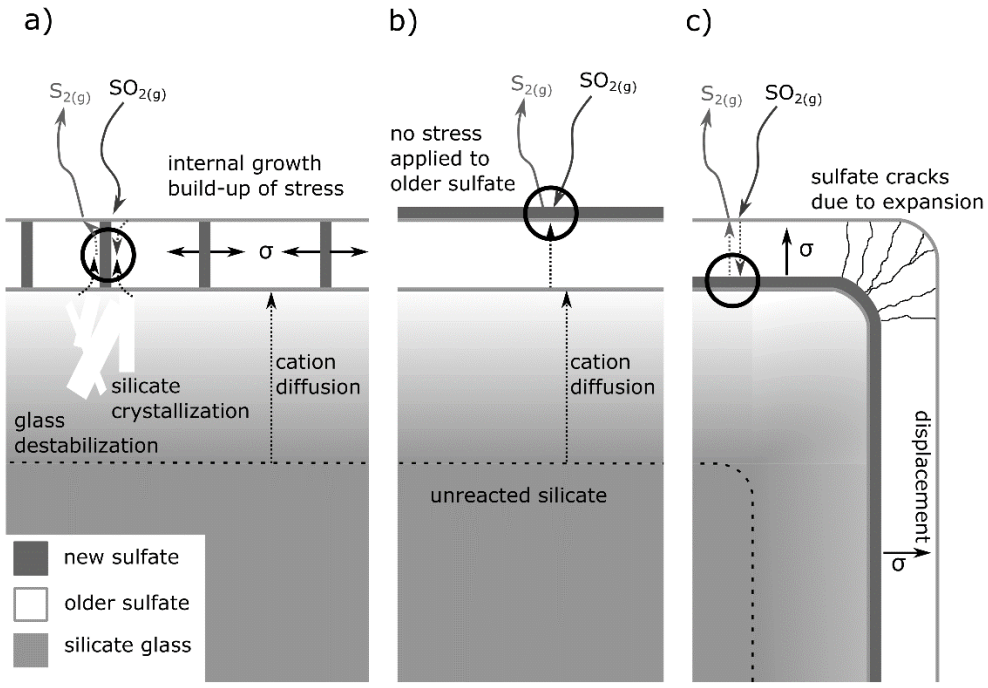

Figure 3-6: Schematic drawings of three possible sulfate growth mechanisms of continuously coated glasses. Depending on relative rates of gas and cation migration through the older sulfate coating, new sulfate (dark gray) may form in different ways. a) Gas molecules and cations migrate through the sulfate coating, preferentially along grain boundaries. New sulfate growth occurs at and along grain boundaries. This results in a lateral expansion of the coating and accumulates stresses within the coating. These stresses are dissipated through deformation of the coating (see Figure 3-7). b) The sulfate-forming cations migrate fast through the old sulfate coating, new sulfate forms at the surface of the coating. c) The gas migrates fast through the sulfate coating, new sulfate forms at the interface between the glass substrate and the older sulfate coating. The old sulfate is pushed outward, resulting in expansive cracks where the glass isn't flat. This was not observed in any experiment.

The different types of initial textures are most apparent at conditions where the reaction has not yet proceeded far, such as on the endmember glasses (An, Di and Ab) reacted at 600 °C for 1 hour (Figure 3-3a and i, Figure 3-4a) or 10 minutes (Appendix). The initial sulfate grains have rounded morphologies at 600 °C. With time, and amount of reaction, the grains develop crystal facets and grain sizes increase. At higher temperatures (800 °C) the grains sizes are significantly larger and crystal facets develop earlier (Figure 3-3, Appendix). For the reaction to continue, mass transport mechanisms are required to bring the gas and the alkaline earth or alkali metals into contact. For the sulfate coating to be bridged by the reactants three mechanisms are possible. They depend on the relative rates at which the gas and cation components can migrate through the sulfate. These mechanisms are illustrated in Figure 3-6.

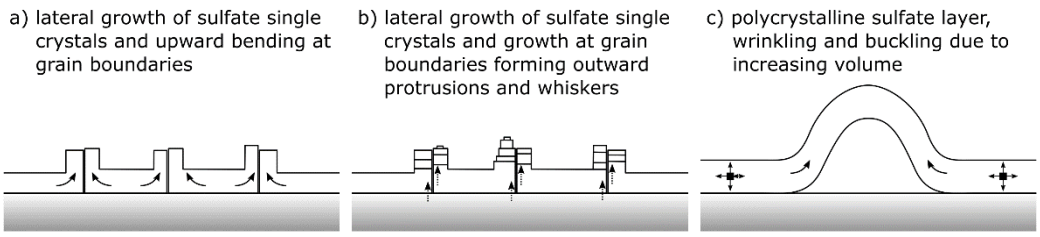

Figure 3-7: Modes of stress dissipation in growing sulfate coatings. a) Lateral expansion of sulfate single crystals causes upward bending at grain-boundaries. This results in chicken-wire textures (Figure 3-4c). b) Sulfate formation at grain boundaries and triple junctions allows preferential accumulation and creates hillocks and protrusions (Figure 3-3d). c) Lateral expansion and increasing volume requires bending and buckling of the sulfate coating (Figure 3-3g and h) (Renggli & King, 2018).

First, the diffusive transport of the reactant $SO_{2(g)}$ and product $S_{2(g)}$ species through the continuous sulfate coating is very fast. In this case new sulfate forms at the silicate surface, below sulfate that formed before. The result is, that the older sulfate coating is displaced away from the glass surface. At corners of the reacted glass chips this growth of the coating would result in extensional cracks (Figure 3-6c). Such cracks were not observed in any experiment.

Second, the outward diffusion of the alkaline earth ions through the sulfate coating exceeds that of the inward diffusion of $SO_{2(g)}$. In this case new sulfate is formed on the outer surface of the sulfate coating (Figure 3-6b). In this case no stresses would be generated in the sulfate coating and it would grow evenly across the surface.

Third, the gas species and the cations migrate at comparable rates through the sulfate coating. We argue that the supply of cations from the substrate to the reaction within the coating is rate-limiting. This occurs most efficiently along grain boundaries and in the pore space of the coating (Figure 3-6a). Consequently, the coating grows internally and expands, causing the build-up of stresses, which can be dissipated by the deformation of the coating. A high reaction rate would therefore result in a high degree of deformation in the coating, as observed in the experiments (Figures 3-3 and 3-4).

The stress in the sulfate coating can be dissipated in different ways, as drawn in Figure 3-7. In the case of a thin coating consisting of a monolayer of flat grains, with a small grain size distribution, two modes of stress dissipation textures have been observed. Lateral growth of the grains parallel to the glass surface focusses the strain at the grain boundaries such that the grains bend upwards (Figure 3-7a). We observed the resulting texture on a $An_{27}Ab_{73}$ glass, reacted with $SO_{2(g)}$ at 700 °C for 72 hours (Figure 3-4c). The same type of texture was also observed on a plagioclase-rich anorthosite rock reacted at 600 °C for 96 hours (Henley et al., 2015) and can be described as a chicken-wire texture. Growth of

sulfate is focused preferentially in areas of the coating where the migration rate of $SO_{2(g)}$ and cations through the coating is fast, such as at grain boundaries. In this case new sulfate accumulates and may pile up to form hillocks and protrusions (Figure 3-7b), which are observed on anorthite glasses reacted at 600 and 800 °C for 24 hours (Figure 3-3b and d). Finally, large sulfate coatings with thicknesses of several microns deform at a larger coating (Figure 3-7c). The increase in volume of the coating results in buckling and bending at distances of few microns to more than 100 microns, as observed on the $An_{15}Di_{85}$, $An_{36}Di_{64}$ (Figure 3-3g and h) and $An_{48}Di_{52}$ reacted with $SO_{2(g)}$ at 800 °C.

Discontinuous coatings, as observed on albite glasses (Figure 3-4), develop less complex textures as the glass surface remains exposed to the gas, crystals likely nucleate preferentially on rough surfaces and discontinuities, and complex deformation textures do not occur. In this case, diffusion is only necessary in the glass substrate; for example, to bring Na to the surface to continue the formation of Na_2SO_4. This diffusion of cations in the glass has been suggested to be the rate-limiting factor in the case of the reaction between volcanic ash and $SO_{2(g)}$ bearing gas (Ayris et al., 2013). Details in the texture of the Na_2SO_4 coatings produced as part of this work are difficult to interpret because, as documented by Raman spectroscopy, the Na_2SO_4 coatings have experienced a phase transition from the hexagonal high temperature phase Na_2SO_4 I to the Na_2SO_4 III phase below 240 °C.

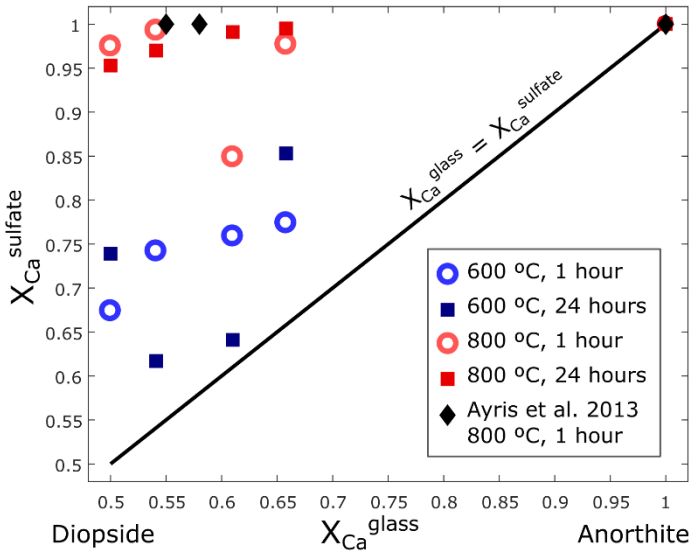

Figure 3-8: Relative molar concentrations of Ca and Mg in the unreacted anorthite-diopside glasses and supercooled melts, and the respective sulfate coatings given as X_{Ca} = Ca/(Ca+Mg). In all experiments the sulfates are relatively enriched in Ca. At 600 °C the enrichment is moderate, whereas at 800 °C the sulfates almost exclusively consist of $CaSO_4$. We include data from Ayris et al., (2013), who observed pure $CaSO_4$ at 800 °C on reacted volcanic ashes ($X_{Ca}^{tephrite}$ = 0.55, X_{Ca}^{dacite} = 0.58, $X_{Ca}^{phonolite}$ = 1, $X_{Ca}^{rhyolite}$ = 1).

3.5.2 Mineralogic consequences of the $SO_{2(g)}$-glass reactions

3.5.2.1 Relative enrichment of Ca in the sulfate

The analysis of the sulfate reaction products with solution ICP-MS provides information on the composition of the coatings formed on different An-Di glasses and supercooled melts (Table 3-2). Here, we consider the $X_{Ca}^{sulfate}$ and X_{Ca}^{glass} to describe the relative abundances of the alkaline earths in the reactants and reaction products. The unreacted anorthite-diopside glasses range from 0.5 for the diopside endmember to 1 for the Mg-free anorthite endmember (Table 3-2 and Figure 3-8). If both Ca and Mg equally partition into the sulfate then $X_{Ca}^{sulfate} = X_{Ca}^{glass}$. Instead, $X_{Ca}^{sulfate} > X_{Ca}^{glass}$, indicating that Ca is preferentially incorporated in the sulfate, consistent with the near-ubiquity of anhydrite. The degree to which Mg is mobilized and incorporated in the sulfate strongly depends on the experimental temperature. At 600 °C, a significant amount of Mg is incorporated in the sulfates formed on the diopside endmember glass and the intermediate An-Di glasses. In these experiments the glasses are below their glass transition temperatures (T_g, 722 to 760 °C; Table 3-1). The second set of experiments at 800 °C, above T_g where the samples are supercooled melts, reveals only very minor Mg in the sulfate, instead it is almost entirely $CaSO_4$ with $X_{Ca}^{sulfate} \sim 1$. This observation is in agreement with Ayris et al. (2013) who measured $X_{Ca}^{sulfate} \sim 1$ on tephrite, dacite, phonolite and rhyolite glasses reacted at 800 °C for 1 h.

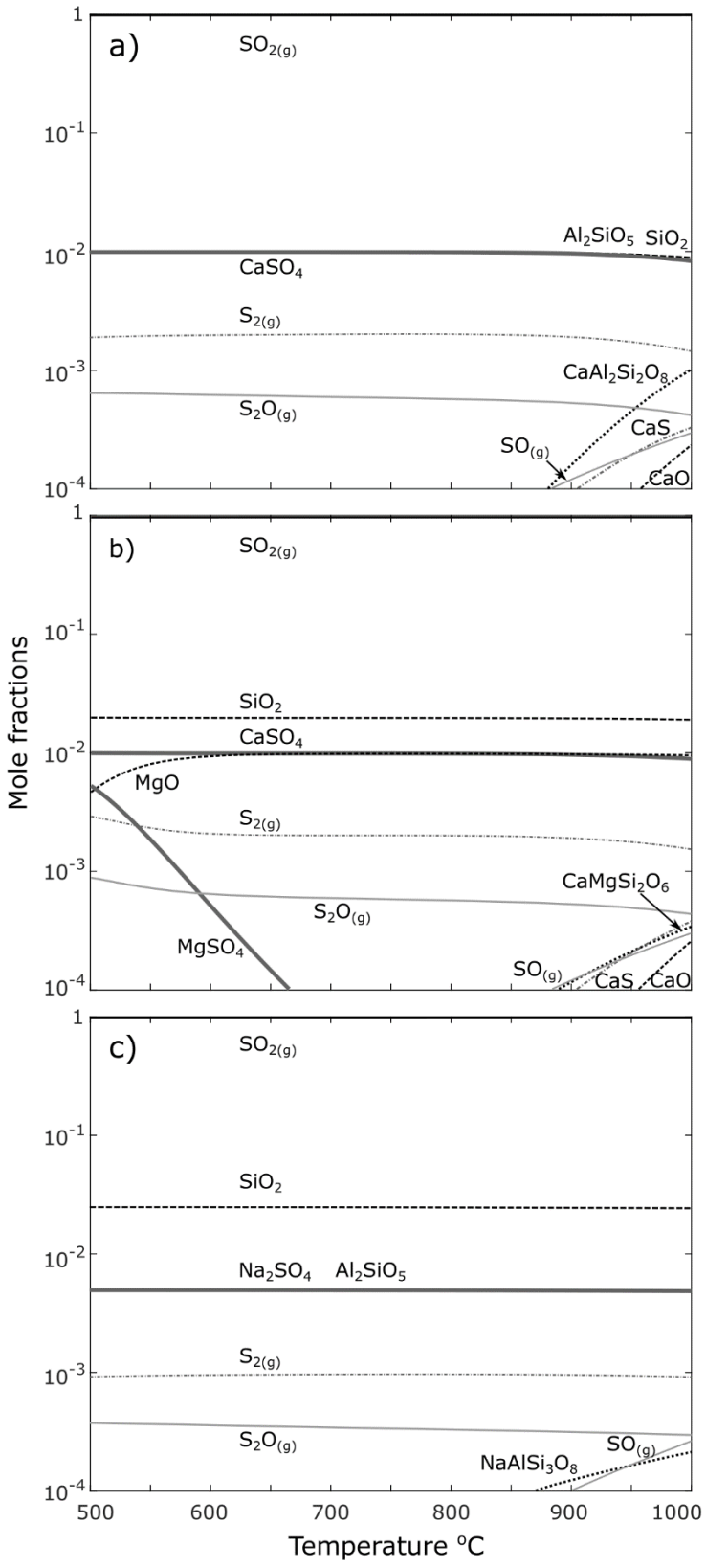

Figure 3-9: Gas and solid speciation calculated using a Gibbs Free energy minimization approach and the software HSC8 by Outotec. As an input we chose a molar $SO_{2(g)}$/silicate molar ratio of 100/1 to ensure that the gas is in excess as in the experiments. a) Reaction between $SO_{2(g)}$ and anorthite. b) Reaction between $SO_{2(g)}$ and diopside. c) Reaction between $SO_{2(g)}$ and albite.

3.5.2.2 Thermodynamic considerations

The experiments have shown the preferential formation of $CaSO_4$ over $MgSO_4$ in experiments with glasses containing CaO and MgO components. At 600 °C $MgSO_4$, hydrated to $MgSO_4 \cdot 7H_2O$, has been observed by Raman spectroscopy, but at 800 °C it is absent (Figure 3-2). Furthermore, the chemical analysis of the sulfate coatings has shown that $X_{Ca}^{sulfate} \sim 1$ at 800 °C (Figure 3-8). Here, we consider if this absence of Mg in the sulfate coating at 800 °C may be controlled by the thermochemical stability of $MgSO_4$.

We conducted Gibbs Free Energy minimization calculations of the speciation of gases and solids in $SO_{2(g)}$ reactions in the system An-Di-Ab, shown in Figure 3-9. The calculations were performed using the software package HSC8 (Roine, 2015), which is based on the JANAF database (Chase, 1998). We calculated equilibrium models using the crystalline endmember phases instead of glasses, for which thermodynamic data is sparse. This allows a further examination of the An-Di-Ab system in reactions with $SO_{2(g)}$. We chose a molar $SO_{2(g)}$/mineral ration of 100/1 to reflect the high gas flux in the experiments.

The gas phase includes the species $SO_{2(g)}$, $SO_{3(g)}$, $SO_{(g)}$, $S_2O_{(g)}$, $O_{2(g)}$, $O_{3(g)}$, $S_{2(g)}$, $S_{3(g)}$, $S_{4(g)}$, $S_{5(g)}$, $S_{6(g)}$, $S_{7(g)}$ and $S_{8(g)}$. In the anorthite system the calculation includes the solids $CaAl_2Si_2O_8$, $CaSO_4$, CaS, Al_2SiO_5 and SiO_2, in the diopside system the solids $CaMgSi_2O_6$, $CaSO_4$, CaS, $MgSO_4$, MgO, MgS and SiO_2 and in the albite system the solids $NaAlSi_3O_8$, Na_2SiO_4, Na_2O, Na_2S, Al_2SiO_5 and SiO_2. The calculations reveal a rapidly decreasing stability of $MgSO_4$ at temperatures above 500 °C in the diopside system. At 600 °C $MgSO_4$ is still a minor phase in the system, but at 800 °C its calculated abundance has dropped two orders of magnitude compared to 600 °C. At the higher temperatures magnesium remains as MgO in the reacted aluminosilicate. The formation of $CaSO_4$ only becomes limited at T > 900 °C (Figure 3-9a & b). These thermodynamic calculations can explain the observed relative enrichment of Ca in the sulfates relative to the unreacted glasses and supercooled melts in the system An-Di at 800 °C (Figure 3-8).

The calculations of the reaction between $SO_{2(g)}$ and albite glass shows that the formation of Na_2SO_4 is thermochemically favored (Figure 3-9c). In this calculation we did not discriminate between $Na_2SO_{4(s)}$ and $Na_2SO_{4(l)}$, but the formation of Na_2SO_4 does not seem to be affected by the change of the phases state. These results are in contrast to Burnett et al. (1997) who suggested that albite should not react with $SO_{2(g)}$ to form Na_2SO_4 based on thermochemical calculations. These authors also conducted experiments reacting albite with SO_2, which did not result in the formation of sulfates.

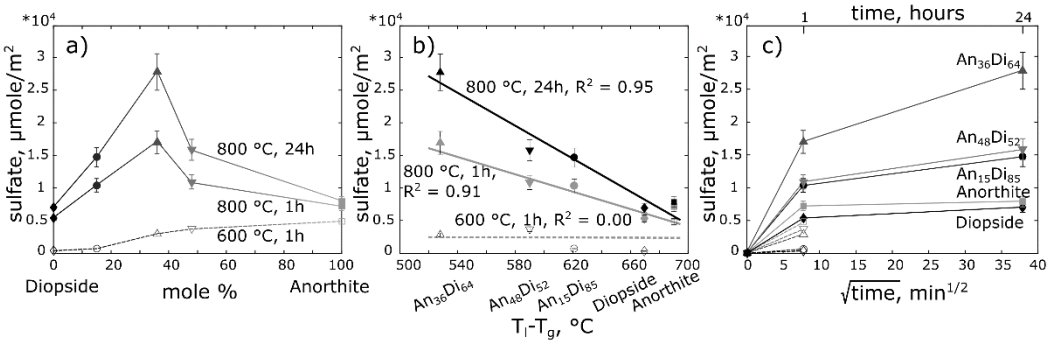

Figure 3-10: a) Total sulfate coating the reacted glasses (µmole/m^2) versus the glass composition in the system anorthite-diopside. At 600 °C the amount of sulfate increases with increasing anorthite component. At 800 °C the amount of sulfate reaction product reaches a maximum at the eutectic An-Di composition. The degree of sulfate formation inversely correlates with the liquidus temperatures, except for anorthite, which is the only sample in this system remaining below T_g at 800 °C (Table 3-1). b) Amount of reaction product as a function of the difference between the liquidus temperature (T_l) and the glass transition temperature (T_g). At 800 °C these properties are inversely correlated, whereas at 600 °C there is no correlation. The R^2 values of the trendlines are given in the figure. c) Amount of reaction as a function of the square-root of time. Within the first hour the rate of reaction is approximately an order of magnitude higher than the rate in the following 24 hours, at 800 °C. At 600 °C the rates of reaction are an order of magnitude lower than at 800 °C.

3.5.2.3 Amount of sulfate formed

We consider the amount of sulfate formed on the An-Di glasses in µmol/m^2 as a function of three different variables. First, as a function of the anorthite content, which represents the relative abundance of Ca; second, as a function of the difference between the liquidus temperature (T_l) and glass transition temperature (T_g) – that is, the anorthite content is a function of T_l-T_g; and third, as a function of time providing estimates of the reaction rate (Figure 3-10).

First, at 600 °C and over one hour, the anorthite glass forms >10x more sulfate than the diopside glass. For this experimental series there is a gradual increase in sulfate content with An-content of the glass and also X_{Ca}^{glass} (Figure 3-10a). At 800 °C, sulfate formation has a clear maximum at the eutectic An-Di composition and the endmembers produce the least sulfate (Figure 3-10a). The $SO_{2(g)}$ reaction with $An_{15}Di_{85}$ and $An_{48}Di_{52}$ supercooled melts , both of which have the same liquidus temperature of 1350 °C, produces the same quantity of reaction products per unit area within 10% analytical uncertainty.

Second, considering the amount of sulfate formation as a function of the temperature difference T_l-T_g, we observe negative correlations at 800 °C but no trend at 600 °C (Figure 3-10b). For experiments at temperatures below T_g (i.e. 600 °C) the liquidus temperature does not affect the amount of sulfate formation. The anorthite glass is the only sample which is below its glass transition (863 °C, Table 3-1) in all experiment presented

here. Consequently, we do not observe a large increase in the amount of sulfate formed from 600 to 800 °C (Table 3-2, Figure 3-10).

Third, we consider the amount of reaction as a function of time (Figure 3-10c). At 600 °C we only have data for 1 h experiments. At 800 °C we have data on the amount of sulfate formed after 1 h and after 24 h. We observe rapid sulfate formation within the first hour, whereas the rate is significantly lower up to 24 h (Figure 3-10c).

3.5.2.4 Crystallization in the substrate

Crystallization and strong depletion of sulfate-forming cations in the near-surface silicates may affect the rates of sulfate formation. As the glass and supercooled melt compositions change and crystallization occurs, the rates of diffusion likely change because they are a function of the composition and differ between crystalline and amorphous materials. If cation diffusion in the substrate is the rate-limiting step these reactions, the overall rate of sulfate formation would evolve with time accordingly.

The reaction of Fe-free silicate glasses and supercooled melts with $SO_{2(g)}$ involves multiple interrelated processes, not all of which are observed in every experiment. They include a heterogeneous reaction at the interface, diffusion of gas through a growing and texturally evolving sulfate layer, diffusive mass transport in the substrate, and changes in the substrate structure as a consequence of the changing composition which can result in crystallization. The overall reaction rate is controlled by the rate of the slowest step in the process and with time the rate-limiting step may change.

3.5.3 Effect of time

3.5.3.1 Rate-limiting steps

The overall rate of the reaction may be controlled by a number of steps. These include the chemical reaction itself, and mass transport processes in the gas phase and in the solid reactant (Szekely et al., 1976). At the high temperatures of 600-800 °C activation energies of chemical reactions are easily overcome and the reactions are not rate-limiting steps (Szekely et al., 1976). Due to the high reaction rate, the consumption of reaction educts ($SO_{2(g)}$ and alkaline earths or alkali metals) occurs almost instantaneously and their supply to the reaction interface becomes rate-limiting (Kubicki & Watts, 2018).

The discussion of the sulfate textures suggested that $SO_{2(g)}$ needs to migrate through the sulfate coating at least partially. In a porous medium, such as the sulfate coating, diffusion of a gas such as $SO_{2(g)}$ strongly depends on the pore size (King et al., 2018). Electron microscopy images of the sulfate coatings (Figure 3-3) show that the sulfate grains form a dense material. The pores have dimensions smaller than the mean free path of the gas at

less than 10 nm. Hence, simple molecular diffusion does not apply and Knudsen diffusion operates (Szekely et al., 1976):

$$D_{K\,SO_{2(g)}} = \frac{d_{pore}}{3}\sqrt{\frac{(8R)T}{\pi M_{SO_{2(g)}}}} \qquad \textit{Equation 3-5}$$

where $D_{K\,SO_{2(g)}}$ is the Knudsen diffusion of $SO_{2(g)}$ in m^2/s, d_{pore} is the pore diameter (< 10 nm), R is the gas constant, T is temperature in K, and $M_{SO_{2(g)}}$ is the molecular mass of $SO_{2(g)}$ in kg/mol (0.064 kg/mol). At 800 °C and a pore diameter of 1nm the Knudsen diffusion of $SO_{2(g)}$ is $logD_{K\,SO_{2(g)}} = -6.7\ m^2/s$, which provides a minimum estimate for the diffusion rate of $SO_{2(g)}$ through the sulfate coating.

On the other hand, the reaction may be limited by diffusive transport of cations in the silicate substrate. Diffusivities of Na, Ca and Mg in albite-anorthite-diopside glasses are not available in the literature. Nevertheless, some crude comparisons with similar compositions are possible. In an $An_{60}Ab_{40}$ plagioclase glass at 800 °C the tracer diffusivities of Na and Ca are $\log D_{Na}^{plag.\ gl.} = -11.8\ m^2/s$ and $\log D_{Ca}^{plag.\ gl.} = -14.7\ m^2/s$ (Behrens, 1992). In albite and jadeite glasses at 800 °C Mg and Ca tracer diffusivities have the following magnitudes; $\log D_{Mg}^{albite\ gl.} = -15.9\ m^2/s$, $\log D_{Mg}^{jadeite\ gl.} = -15\ m^2/s$, $\log D_{Ca}^{albite\ gl.} = -13.2\ m^2/s$ and $\log D_{Ca}^{jadeite\ gl.} = -12.9\ m^2/s$ (Roselieb and Jambon, 2002). Broadly, the diffusivities of these cations follow the order of $D_{Na} > D_{Ca} > D_{Mg}$, but they are all five to eight orders of magnitudes slower than the Knudsen diffusivity of $SO_{2(g)}$ in the sulfate coating. Assuming that the diffusivities of Na, Ca and Mg in albite-anorthite-diopside glasses are of similar relative magnitudes, these very slow rates suggest that the cation diffusivities are the rate controlling steps in $SO_{2(g)}$ reactions with glasses and supercooled melts. Finally, the outward diffusion of the cations needs to be accompanied by outward co-diffusion of oxygen anions in order to maintain charge balance (Sucov and Gorman, 1965).

Sulfidation and oxidation reactions of metals and alloys often pass through multiple stages with different reaction rates. In these gas-metal systems the entire solid educt (i.e. the reduced metal) is consumed and its volume diminishes or "shrinks" (Luthra and Worrell, 1978; Gesmundo et al., 1983; Andersen and Kofstad, 1984). This is commonly described as a shrinking core mechanism (Szekely et al., 1976). Such a mechanism also operates in the reaction between $SO_{2(g)}$ and calcite, where carbonate ions are replaced by sulfate ions (Fegley and Prinn, 1989). The transformation progresses from the surface inwards and the unreacted core shrinks in volume and mass. The mechanism operating in the reaction of

$SO_{2(g)}$ with silicate glasses and supercooled melts is different, because not the entire educt is consumed, the aluminosilicate framework remains intact.

3.5.3.2 Calculation of rate-limiting cation fluxes

The $SO_{2(g)}$ imposes a chemical potential gradient on the glass or supercooled melt, which drives a flux of Na, Ca and Mg cations to the surface to form sulfates. As we do not have reliable data on concentration gradients of the cations in the reacted glasses, their diffusivities cannot be calculated. Instead, we can calculate their fluxes in experiments where the surface areas and the amounts of reaction are determined (Table 3-2). The diffusive flux J_i^{gl} for element i in the reactant glass, gl (mol/m^2/s) is the amount per area per time and defined as:

$$J_i^{gl} = -D\nabla C \qquad \textit{Equation 3-6}$$

Where D is the diffusion coefficient (m^2/s) and ∇C is the concentration gradient of the diffusing element, i. As we have determined the surface areas of the An-Di glasses reacted at 600 °C for 1 h, and the supercooled melts at 800 °C for 1 h and 24 h, as well as the amounts of Ca and Mg in the sulfate coatings, we can calculate the fluxes for these elements in the three experiments (Table 3-2). The fluxes are time-averaged values for the experimental durations of 1 h and 24 h respectively.

The calculated fluxes are proportional to the total amounts of sulfates formed on the glasses as presented above (Figure 3-9, Table 3-2). The calculated fluxes also highlight the differences between Ca and Mg. Furthermore, Table 3-2 gives the relative fluxes of Ca and Mg $\left(J_{Ca}^{gl}/J_{Mg}^{gl}\right)$ allowing the comparison of the two alkaline earth metals. For example, for diopside glass at 600 °C and 1 h $J_{Ca}^{Di\ gl.}$ (6.9 x 10^{-8} mol/m^2/s) is 2.1 times higher than $J_{Mg}^{Di\ gl.}$ (3.3 x 10^{-8} mol/m^2/s), and in the $An_{48}Di_{52}$ experiment the $J_{Ca}^{An_{48}Di_{52}\ gl.}$ (8.0 x 10^{-7} mol/m^2/s) is up to 3.4 times higher than $J_{Mg}^{An_{48}Di_{52}\ gl.}$ (2.3 x 10^{-7} mol/m^2/s). At 800 °C after 24 h, where the relative abundance of Mg in the sulfates is very low, $\left(J_{Ca}^{An_{15}Di_{85}\ gl}/J_{Mg}^{An_{15}Di_{85}\ gl}\right)$ can reach values of up to 334 (Table 3-2).

At 800 °C fluxes could be determined for experiments with 1 h and 24 h durations. Notably, the fluxes are significantly lower when time-averaged 24 h compared to 1 h. The fluxes of Ca are up to 22 times lower over 24 h and the fluxes of Mg are up to 240 times lower over 24 h compared to 1 h at 800 °C.

With increasing duration, the near-surface substrate becomes depleted in Ca and Mg and the composition becomes relatively richer in SiO_2 and Al_2O_3, which may decrease its

surface reactivity (Maters et al., 2016, King et al., 2018, Renggli and King, 2018). The compositional change results in a decreasing diffusion rate and element flux to the surface. The cation depleted glass acts as an insulating layer and the diffusive flux, becomes self-inhibiting (Schaeffer et al., 1986; Cailleteau et al., 2008).

The reaction occurs at a rate which is dependent on the overall amount of reaction, as the rate decreases with the decreasing flux of cations from the glass (Crank, 1975):

$$\frac{dX}{dt} = \frac{k_p}{X} \qquad \textit{Equation 3-7}$$

where t is time, X is the amount of reaction and k_p is the parabolic reaction rate. Integrating this equation and solving it for the amount of reaction gives:

$$X = \sqrt{2k_p t} \qquad \textit{Equation 3-8}$$

This is the form of a second-order reaction where the amount of sulfate formed is a function of the square-root of time (Figure 3-10c). In our experiments the parabolic reaction rate k_p is not constant with time. In order to determine the kinetics of these reactions with decreasing parabolic reaction rates, further experiments (preferably in situ) are necessary to provide a higher time-resolution.

3.5.4 Consequences of Ca-sulfate formation in natural systems

Our experimental results are in agreement with those from Ayris et al. (2013), who also observed that $CaSO_4$ is the major sulfate produced at high temperatures (T > 600 °C) in volcanic plumes. In addition, we observe a strong dependence of the reaction efficiency on the temperature relative to T_g (Figure 3-10), with reaction amount that are up to 15x higher at 800 °C (above T_g) relative to 600 °C (below T_g). For this reason, we suggest that the bulk of the $CaSO_4$ observed on glassy ash particles (Rose, 1977; Delmelle et al., 2007; Barone et al., 2016) is formed at temperatures above T_g of the respective composition (> 650 °C). Fluorine salts have been suggested to form at intermediate temperatures in the eruption plume at 300 – 700 °C (Óskarsson, 1980). Similarly, chlorides have been shown to form most efficiently at 400 – 600 °C on glassy volcanic ash (Ayris et al., 2014). Therefore, sulfates form prior to the halides on volcanic ash particles and only in the high temperature core of the eruption plume.

In the subvolcanic environment where rocks can be exposed to high temperature $SO_{2(g)}$ for much longer periods of time the Ca-sulfate forming reaction may have a more significant impact (Henley et al., 2015, 2017, Henley and Seward, 2018). The experimental results show that in these simple Fe-free systems Ca is much more easily mobilized via the reaction with $SO_{2(g)}$ compared to Mg, Si and Al. The reaction results in a relative enrichment of Mg,

Si and Al in the reacted silicate. As the sulfate reaction product is more easily mobilized by secondary fluids than the silicate, Ca may also be preferentially mobilized and transported by such secondary hydrothermal fluids. Overall, this may positively impact the Ca-flux from volcanic systems to the hydrosphere.

The formation of sulfates via gas-solid reactions reduces the amount of $SO_{2(g)}$ in the volcanic gas phase. At degassing volcanoes the measured $SO_{2(g)}$ flux (de Moor et al., 2013; Zelenski et al., 2013) may be lower than the amount of $SO_{2(g)}$ degassed from the magmatic source (Henley and Hughes, 2016). Future work will require an assessment of how much $SO_{2(g)}$ is removed by gas-solid reactions in the subvolcanic environment, in order to constrain the degassing rates of magmatic gas sources over time.

The sulfate reaction products form on the surface of the glasses. Consequently, the volume of the solid increases during the experiment. Where similar sulfate-forming reactions occur in the subvolcanic environment, such a volume change may have significant implications for the gas and fluid permeability, when the growing sulfates may affect the permeability of the rocks and the flow pathways of the gases (Henley et al., 2017). The positive change in volume may cause the opening of new pore space and counterbalance the loss in permeability caused by the sulfate in the first place. We postulate that the increased volume as gas reacts with rocks may drive seismic events in subvolcanic environments.

As the gas-solid reaction fills and seals veins with sulfates and the permeability decreases new crack-openings and veins are necessary to allow high gas flux. For example, at Galeras volcano (Colombia) long-period seismicity has been attributed to the unsteady flux of magmatic gases recorded at the surface (Fischer et al., 1994). Periods preceding long-period seismic events are accompanied by low $SO_{2(g)}$ emissions at the surface. We suggest that this may be due to the reactive scavenging of the $SO_{2(g)}$ fracture network.

High temperature conditions (> 700 °C) favorable for the formation of $CaSO_4$ in $SO_{2(g)}$-glass reaction also occur on Io and Venus. On Io, eruption plumes reach temperatures of 1200 °C (Zolotov and Fegley, 2000) and magmatic temperatures are as high as 1700 °C (McEwen et al., 1998), in the presence of abundant $SO_{2(g)}$ (Pearl et al., 1979; Kumar, 1985; Doute, 2002). On Venus, the surface temperature is ~ 470 °C and magmatic temperatures of up to 1500 °C may occur (Nimmo and McKenzie, 1998; Glaze, 1999). The search for traces of this gas-solid reaction mechanisms in the rock record, both on Earth and by remote sensing and robotic investigation on other planetary bodies, should therefore focus on the detection of $CaSO_4$ and the diffusive depletion of Ca in altered silicates.

3.6 Summary and conclusions

$SO_{2(g)}$ preferentially extracts Ca from simple Fe-free glasses and supercooled melts, compared to Mg and Na. In the system An-Ab Na_2SO_4 only forms on the endmember albite glass. In the presence of a Ca-component $CaSO_4$ is the only sulfate reaction product in the system An-Ab. In the system An-Di $CaSO_4$ is also the sole sulfate reaction product in reactions with supercooled melts at 800 °C. $MgSO_4$ was only observed in experiments at 600 °C. The sulfates are always relatively enriched in Ca compared to the silicate glass composition ($X_{Ca}^{sulfate} > X_{Ca}^{glass}$). As a consequence, the reacted glasses become Ca depleted, and relatively enriched in Mg and Na, with increasing experimental duration.

Thermochemical calculations (Figure 3-9) are in agreement with the experimental observations, allowing reliable modelling of $SO_{2(g)}$ reaction with Fe-free glasses and supercooled melts. The absence of $MgSO_4$ in the reaction products at 800 °C is predicted by Gibbs Free Energy minimization calculation, which show that Mg preferentially remains as MgO in the aluminosilicate at temperatures above 600 °C. The formation of Na_2SO_4 on albite glasses is thermodynamically favored at our experimental conditions.

The rate of the reaction is limited by the flux of the sulfate-forming cations from the substrate to the surface. Therefore, the rate depends on the diffusivity of these cations. Due to the loss of Ca to the surface, the composition near the surface becomes increasingly depleted and the diffusion coefficients are changing, they are time-dependent. Additionally, crystallization in the subsurface may affect the diffusivities of the cations.

Our experiments have demonstrated, that the physical properties of the solids, in particular the diffusivities, control the rates of reaction between $SO_{2(g)}$ and silicate glasses or supercooled melts. This is likely also the case in the reaction between $SO_{2(g)}$ and crystalline solids. Even though $CaSO_4$ is not the only sulfate that can form in these reactions, it is by far the dominant sulfate phase. The search for traces of this gas-solid reaction mechanisms in the rock record, both on Earth and by remote sensing and robotic investigation on other planetary bodies, should therefore focus on the detection of $CaSO_4$ and the diffusive depletion of Ca in altered silicates.

4 Major element mobilization and mineral formation in reactions between SO_2 and basaltic glasses

This chapter is in preparation for publication in *Journal of Petrology*.

Renggli C.J., King P.L., Palm A.B., Guagliardo P.

I designed, prepared and conducted the experiments, performed the data analysis and written the manuscript. King contributed to the design and conceptualization of the experiments and the interpretation of the data, edited and corrected the manuscript. Palm helped with the interpretation of the experimental data. The collection of nanoSIMS data was conducted in collaboration with P. Guagliardo.

4.1 Abstract

Basalts are ubiquitous in volcanic systems on several planetary bodies, including the Earth, Mars, Venus and the Galilean moon Io, and are commonly associated with sulfur dioxide ($SO_{2(g)}$) degassing. We present the results of an experimental study investigating these reactions between $SO_{2(g)}$ and basaltic glasses. Because the Fe-oxidation state is known to influence cation diffusion in glasses, we examined an Fe-free basalt, and three tholeiitic basalts with a range of Fe^{3+}/Fe_{total} (0.22, 0.33 and 0.79) set by pre-equilibrating the glasses under different oxygen fugacities ($\log fO_2$ values relative to the Ni-NiO buffer of -1.5, 0 and +1 respectively). The basalt glasses were exposed the $SO_{2(g)}$ at 700 °C for 1 h and 24 h. We present observations from the surface coatings formed on the reacted basalt glasses, and from cross-sections through the modified glasses. The coatings are chemically and texturally heterogeneous and include $CaSO_4$, $MgSO_4$ or Na_2SO_4, Fe_2O_3 and TiO_2. The $SO_{2(g)}$-glass reaction results in considerable modification of the basalt glasses causing the oxidation of Fe in the glass and the nucleation of crystal phases including pyroxenes and SiO_2. The mobility and diffusion of Ca, Mg or Na in the basalt glass substrates is the rate-limiting step in the sulfate and oxide forming $SO_{2(g)}$-glass reaction.

4.2 Introduction

Basalts and gaseous sulfur dioxide ($SO_{2(g)}$) are ubiquitous and commonly associated with volcanic processes on terrestrial planets (Basaltic Volcanism Study Project, 1981; Taylor and McLennan, 2009). On Earth, $SO_{2(g)}$ is the most abundant S-bearing volcanic gas species and the third most abundant volcanic gas species overall, after $H_2O_{(g)}$ and $CO_{2(g)}$ (Oppenheimer et al., 2014). On Venus and Io, $SO_{2(g)}$ has been directly measured in the atmosphere and eruptive plumes (Pearl et al., 1979; Kumar, 1985; Glaze, 1999; Doute, 2002; Vandaele et al., 2017), and basalts are the predominant volcanic rock types on Venus (Nimmo and McKenzie, 1998; McSween et al., 2006) and Io (Carr, 1986; Blaney et al., 1995). Finally, on Mars, where $SO_{2(g)}$ has not been measured directly, it has been inferred as a significant volcanic gas species in past eruptions associated with basaltic volcanism (McSween et al., 2006; Gaillard and Scaillet, 2009; King and McLennan, 2010; Franz et al., 2018).

Previous workers have shown that $SO_{2(g)}$ rapidly reacts with geologic materials via chemisorption reactions where the $SO_{2(g)}$ disproportionates to form sulfates and reduced sulfur (gas or sulfides) (Burnham, 1979; Ayris et al., 2013; Henley et al., 2015; Renggli and King, 2018):

$$2SO_{2(g)} + MO_{silicate} \rightarrow MSO_4 + S_{reduced} + silicate(+oxide) \qquad \textit{Equation 4-1}$$

In the subvolcanic environment the chemisorption of $SO_{2(g)}$ on Ca-rich rocks results in the rapid disproportionation of $SO_{2(g)}$ to form sulfate and reduced S, which allows the concurrent deposition of sulfates and sulfides, to produce economically important porphyry and skarn deposits (Henley et al., 2015; Henley et al., 2017), and the silicates become depleted in the sulfate-forming cation (e.g. Ca, Henley et al., 2017). In explosive volcanic eruptions, $SO_{2(g)}$ chemisorption occurs onto ash particles, scavenging the molecule from the gas plume as $CaSO_4$ (Rose, 1977; Ayris et al., 2013; Barone et al., 2016).

Gas-solid reactions such as $SO_{2(g)}$-glass reactions can be rate limited by different steps in the reaction mechanism. These include the transport of the reacting gas to the solid surface, adsorption onto the surface, diffusive transport of ion and electrons in the solid substrate, surface reaction and transport of gaseous reaction products away from the surface (Kreider and Lipiński, 2018). In the case of $SO_{2(g)}$-glass reactions, the sulfate products may form continuous coatings which may act as barriers for the reaction, in which case diffusive transport mechanisms are required in the glass substrate and through the sulfate coating to allow an ongoing reaction (Renggli et al., in prep.; Renggli and King, 2018).

Ayris et al. (2013) have investigated the reaction between $SO_{2(g)}$ and tephrite, phonolite, dacite and rhyolite glasses at temperatures up to 800 °C. They observed the rapid formation of $CaSO_4$ coatings on the ash particles within minutes and at temperatures of 300 °C and above and suggested that the Ca-availability in the glass is the driving force of the reaction. To investigate this further, Renggli et al. (in prep.) studied $SO_{2(g)}$ reactions with anorthite-diopside (AnDi) glasses. They found a temperature dependence in their reaction products, where at 600 °C (below the glass transition temperature T_g) the coatings formed on the $An_{15}Di_{85}$, $An_{36}Di_{64}$ (eutectic glass), and $An_{48}Di_{52}$ glasses contain $CaSO_4$ as well as $MgSO_4$. At 800 °C, the coatings only consist of $CaSO_4$, and $MgSO_4$ is not observed (Renggli et al., in prep.). In the presence of Ca in the glass, even if it is as low as a 5 mole%, $CaSO_4$ is the dominant reaction product on glasses in the anorthite-diopside-albite system (Renggli et al., in prep.). Ayris et al. (2013) and Renggli et al. (in prep.) have shown that the mobility the sulfate-forming cation Ca^{2+} in the glass and its diffusion to the glass surface is the reaction rate-limiting mechanism in $SO_{2(g)}$-glass reactions.

Natural basalt glasses contain Fe and the $SO_{2(g)}$-glass reaction can affect the Fe^{3+}/Fe_{tot} ratio. The most efficient oxidation mechanism in a H-free system is the inward diffusion of electron holes, which are charge compensated by the outward diffusion of divalent cations such as Ca^{2+} and Mg^{2+}, where diffusivities of these cations are the rate-limiting factors (Cooper et al., 1996; Cook and Cooper, 2000; Cooper, 2018). The oxidation mechanism results in the precipitation of CaO and MgO at the glass surface and the nucleation of $(MgFe)_3O_4$ in the oxidized glass (Cooper et al., 1996; Cook and Cooper, 2000). Similarly, the reaction between $SO_{2(g)}$ and Fe-bearing basalt glasses may also affect the valence state of multivalent elements such as $Fe^{2+/3+}$ as the gas has an effective oxygen fugacity of $\log fO_2$ = -12.1 at 700 °C (Renggli and King., 2018), which is 4.2 $\log fO_2$ units above the Ni-NiO buffer.

Here we present experimental results of reactions between $SO_{2(g)}$ and basalt glasses at 700 °C. The glasses were exposed to $SO_{2(g)}$ at atmospheric pressure for 1 and 24 hours. Apart from an Fe-free basaltic glass, the experiments were run with tholeiitic basalt glasses, which were pre-equilibrated at three different oxygen fugacities with Fe^{3+}/Fe_{tot} ratios of 0.22, 0.33 and 0.79, which corresponds to 1.5 $\log fO_2$ units below the Ni-NiO buffer (NNO-1.5), at the Ni-NiO buffer (NNO) and one $\log fO_2$ unit above the buffer (NNO+1) (Table 4-1, Dufresne et al., 2015). Experiments with basalt glasses which exhibit different Fe^{3+}/Fe_{tot} ratios allow us to examine the effect of different degrees of oxidation of the glass on the reaction mechanism. The tholeiitic basalts have glass transition temperatures just above the experimental temperature (700 °C) at 715-745 °C (Ryan and Sammis, 1981).

Table 4-1: Compositions of the basalt glasses reacted with $SO_{2(g)}$ and calculated normative mineralogy of the basalts.

	Fe-free basalt	Tholeiite, NNO-1.5	Tholeiite, NNO	Tholeiite, NNO+1
[wt.%]		Dufresne et al., 2015		
SiO_2	59.2	51.4	51.6	50.9
TiO_2	1.3	2.7	2.1	2.7
Al_2O_3	18.3	12.1	11.6	11.9
Fe_2O_3	0.0	1.6	2.6	5.3
FeO	0.0	8.8	8.8	4.4
MnO	0.0	0.2	0.2	0.2
MgO	11.1	9.9	10.5	9.9
CaO	7.6	10.7	10.3	10.6
Na_2O	1.7	1.5	2.0	1.8
K_2O	0.0	0.4	0.4	0.5
P_2O_5	0.0	0.2	0.3	0.2
Totals	99.2	99.4	100.3	98.3
Fe^{3+}/Fe_{tot}		0.22	0.33	0.79
Fe^{3+}/Na^{+}		0.41	0.50	1.14
NBO/T	0.38	0.80	0.83	0.65
Normative mineralogy (CIPW norm)				
Quartz	16.5	5.1	2.4	7.8
Plagioclase	52.1	37.5	38.5	38.1
Orthoclase	0.0	2.5	2.4	2.8
Corundum	1.7	0.0	0.0	0.0
Diopside	0.0	21.5	22.8	22.1
Hypersthene	27.7	24.9	25.9	14.4
Rutile	1.3	0.0	0.0	0.0
Ilmenite	0.0	5.2	4.0	5.2
Magnetite	0.0	2.3	3.8	6.9
Hematite	0.0	0.0	0.0	0.5
Apatite	0.0	0.5	0.6	0.5

The experimental run products were investigated using scanning electron microscopy, Raman spectroscopy and nanoSIMS element mapping. These analytical methods reveal the chemistry and mineralogy of the different phases in the coatings on the reacted basalt glasses and the chemical modification in the reacted substrates. The $SO_{2(g)}$-glass reaction produced coatings which consist of sulfates ($CaSO_4$, $MgSO_4$ or Na_2SO_4), hematite and Fe-Ti-oxides. We also present observations on the modification features in the glass substrates and discuss the effect of this $SO_{2(g)}$-glass reaction on the normative mineral composition of the basalts.

4.3 Methods

4.3.1 Experimental setup

The experiments were conducted with Fe-bearing tholeiitic basalt glasses from the 1921 Pu'u O'o eruption at Kilauea, Hawai'i (Holloway and Burnham, 1972). The basalts were melted at 1400 °C under controlled fO_2 conditions relative to the Ni-NiO (NNO) buffer. Their compositions were determined with the electron microprobe and the Fe^{3+}/Fe_{tot} ratios were determined using Mössbauer spectroscopy (Dufresne et al., 2015). Additional experiments were conducted with Fe-free basalt glass which was synthesized from chemical grade oxide powders. The powders were ground and mixed before melting at 1500 °C for 10 minutes, quenched, reground and re-melted twice at 1500 °C. The obtained tholeiitic basalt glasses and the Fe-free basalt glass were homogeneous and crystal free. The glass chips were polished on the surface to ¼ μm and washed with methanol to ensure a flat and clean surface (Renggli & King, 2018).

The polished glass chips with diameters of ~2 mm were placed on a Pt-tray which was suspended in a vertical gas mixing furnace at 700 °C for 1 hour and 24 hours respectively and exposed to $SO_{2(g)}$ at a flow rate set to 50 sccm. The four basalt glasses were run in the same experiment to ensure identical run conditions. Before and after the $SO_{2(g)}$ reaction experiment, the furnace was streamed with $Ar_{(g)}$ for approximately two minutes, to remove any atmospheric contamination and to allow thermal equilibration before exposure to $SO_{2(g)}$. The retrieved experimental charges were immediately placed in a desiccator to minimize hydration of the reaction products. For each experimental condition and glass composition three experimental charges were run for different analytical methods. Cross-sections of glasses were obtained by embedding the run products in epoxy resin and cutting the mounds. The cross-sections were polished with diamond paste to a ¼ μm.

4.3.2 Analytical methods

The phases in the surface coatings were identified using a Renishaw 2000 Raman Imaging Microscope at the Research School of Physics and Engineering at the Australian National University. We used a 532 nm laser, focused with a 100x objective lens, with a resulting laser power of 3 mW on the sample and a spot size of ~1 μm. At these conditions the laser may sample the material to a depth of 4 μm, depending on the laser transparency of the analyzed material. The 520.7 cm^{-1} band from a pure Si standard was used to test the alignment of the spectrometer prior to the analysis of the coatings.

The coatings formed by the $SO_{2(g)}$-glass reactions on the basalt glasses were observed by Field Emission Scanning Electron Microscopy (FESEM), using a Hitachi 4300 SE/N

Schottky Field Emission instrument at the Centre for Advanced Microscopy (CAM) at the Australian National University. Backscattered electron (BSE) images were collected, allowing the distinction of the different phases in the coatings and their textural relationships. Due to the rough surfaces of the coatings and the fine grain sizes of some phases in the coatings, quantitative compositional analysis could not be obtained. Instead, we used Energy Dispersive Spectroscopy (EDS) with a 80 mm^2 silicon drift detector to collect qualitative elemental maps from the same areas where the BSE images were recorded. To allow for an efficient element mapping we increased the beam current to 1000 pA by adjusting the condenser lens, and reduced the spectrum processing time by 20%.

In addition to the investigation of the surface coatings we prepared cross-sections through the reacted basalt glasses. During sample preparation the coating was lost from some glass surfaces and Al-rich contamination during polishing cannot be excluded, in particular between the sample and the embedding epoxy resin. The modification features in the reacted glass substrates were analyzed with nanoscale secondary ion mass spectrometry (nanoSIMS) with a CAMECA NanoSIMS 50L instrument at the Centre for Microscopy, Characterisation and Analysis, at the University of Western Australia. The samples were mounted in resin, polished and gold coated. We used a Hyperion (H200) oxygen ion (O^-) source, providing a spot size of 100 nm with a beam current of 12.5 pA and an ion impact energy of 16 keV. Maps of the isotopes ^{23}Na, ^{24}Mg, ^{27}Al, ^{28}Si, ^{40}Ca, ^{48}Ti and ^{56}Fe were collected simultaneously in multicollection mode with a field of view of 50 μm^2 at a resolution of 512 x 512 pixels.

4.4 Results

4.4.1 Mineralogy of the coating

The mineral phases formed in the reaction between $SO_{2(g)}$ and the basaltic glasses were determined using Raman spectroscopy (Figure 4-1). Raman spectra show narrow bands (Figure 4-1a) confirming that well crystallized anhydrite ($CaSO_4$) is present (using band positions reported by Liu et al., 2009). The Fe-rich oxide phase is identified as hematite (Fe_2O_3) (Zoppi et al., 2008), and the Ti-rich phase is the mineral anatase (TiO_2; Tompsett et al., 1995). Hematite occurs as well crystallized large grains with diameters of up to 10 μm in the coatings, but also as very fine-grained hematite is intermixed with Na_2SO_4, such as on the basalt glass pre-equilibrated at NNO+1. The Raman spectrum recorded on this mixture shows bands of hematite and Na_2SO_4 (Figure 4-1a; Hapanowicz and Condrate, 1996). The polymorph of Na_2SO_4 could not be identified unambiguously because of its poor crystallinity and occurrence in a mixture with Fe_2O_3.

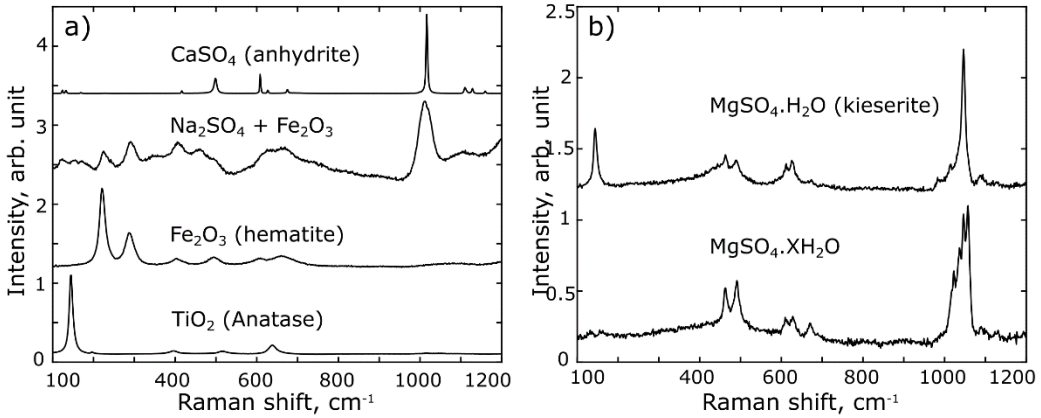

Figure 4-1: Raman spectra recorded on the coatings of the reacted basalt glasses. a) Anhydrite is well crystallized and its Raman spectrum shows sharp bands. Hematite occurs with Na_2SO_4 in a fine-grained mass, and also as well crystallized grains. The Ti-oxide (with some Al and Fe) is identified as anatase. B) The $MgSO_4$ is hydrated to various degrees. Based on the main Raman bands above 1000 cm^{-1} we can identify the phases $MgSO_4 \cdot H_2O$ (kieserite), $MgSO_4 \cdot 2H_2O$ (sanderite) and $MgSO_4 \cdot 3H_2O$ (trihydrate) (Wang et al., 2006).

The magnesium sulfate ($MgSO_4$) occurs in different states of hydration. Using the main Raman SO_4^{2-} stretching modes we can identify three differently hydrated magnesium sulfate phases including $MgSO_4 \cdot H_2O$ (kieserite), $MgSO_4 \cdot 2H_2O$ (sanderite) and $MgSO_4 \cdot 3H_2O$ (trihydrate) (Wang et al., 2006). We have placed the reacted glass samples in a desiccator immediately after taking them out of the gas-mixing furnace. Despite this measure, Raman analysis was under air and so hydration of $MgSO_4$ occurred. This underlines the difficulty in handling samples for the study of gas-solid experiments (Dalby et al., 2018) and the need to use a N_2 or Ar purge during analysis.

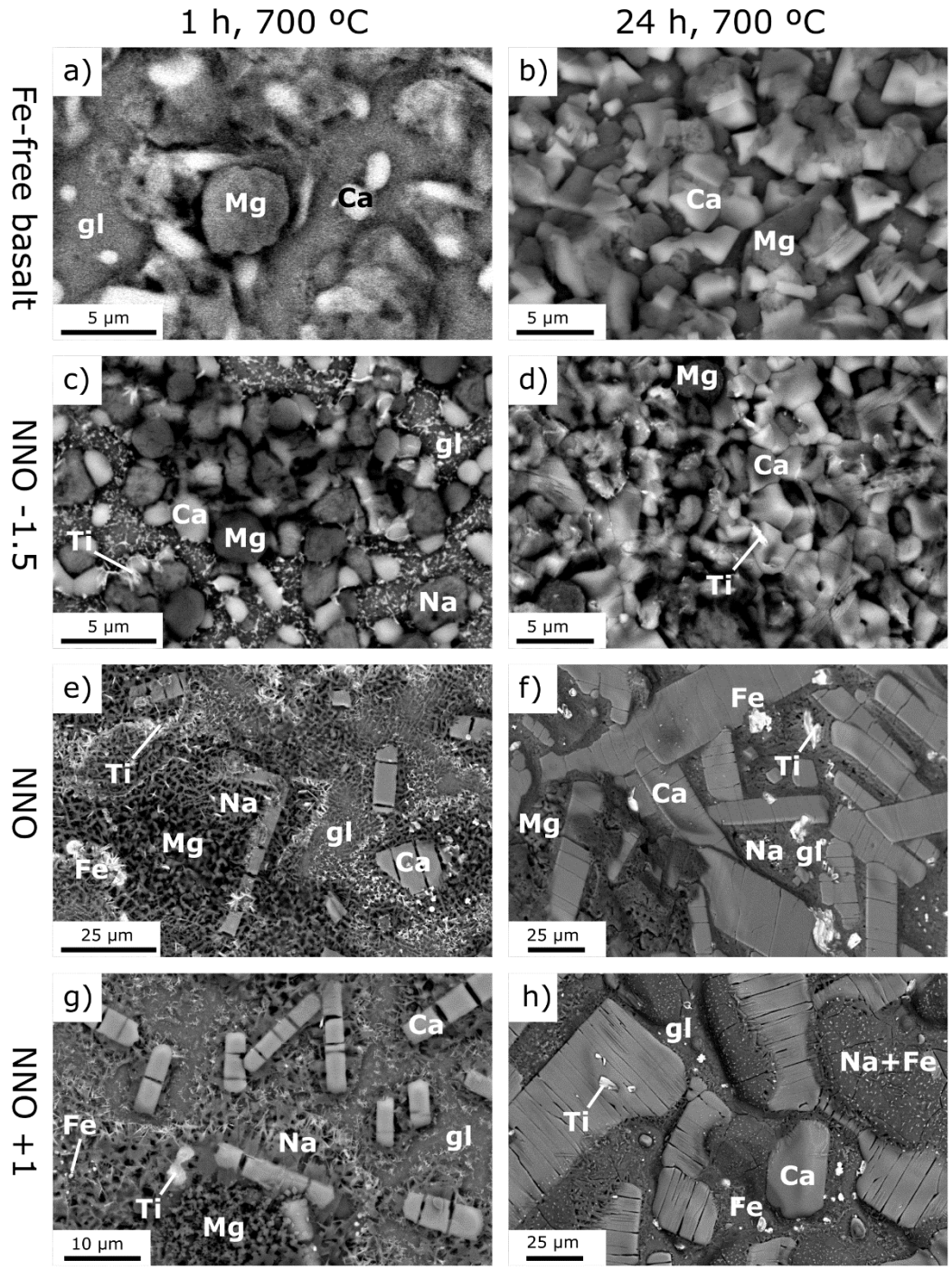

Figure 4-2: Back-scattered electron images of the surface coatings on the basalt glasses reacted with $SO_{2(g)}$ at 700 °C. Element symbols indicate the following phases: Ca = $CaSO_4$; Mg = $MgSO_4$; Na = Na_2SO_4; Fe = Fe_2O_3; Ti = TiO_2; gl = basalt glass substrate. a) Fe-free basalt reacted for 1 h. b) Fe-free basalt reacted for 24 h. c) Tholeiitic basalt pre-equilibrated at NNO-1.5, reacted for 1 h. d) Tholeiitic basalt pre-equilibrated at NNO-1.5, reacted for 24 h. e) Tholeiitic basalt pre-equilibrated at NNO, reacted for 1 h. f) Tholeiitic basalt pre-equilibrated at NNO, reacted for 24 h. g) Tholeiitic basalt pre-equilibrated at NNO+1, reacted for 1 h. h) Tholeiitic basalt pre-equilibrated at NNO+1, reacted for 24 h.

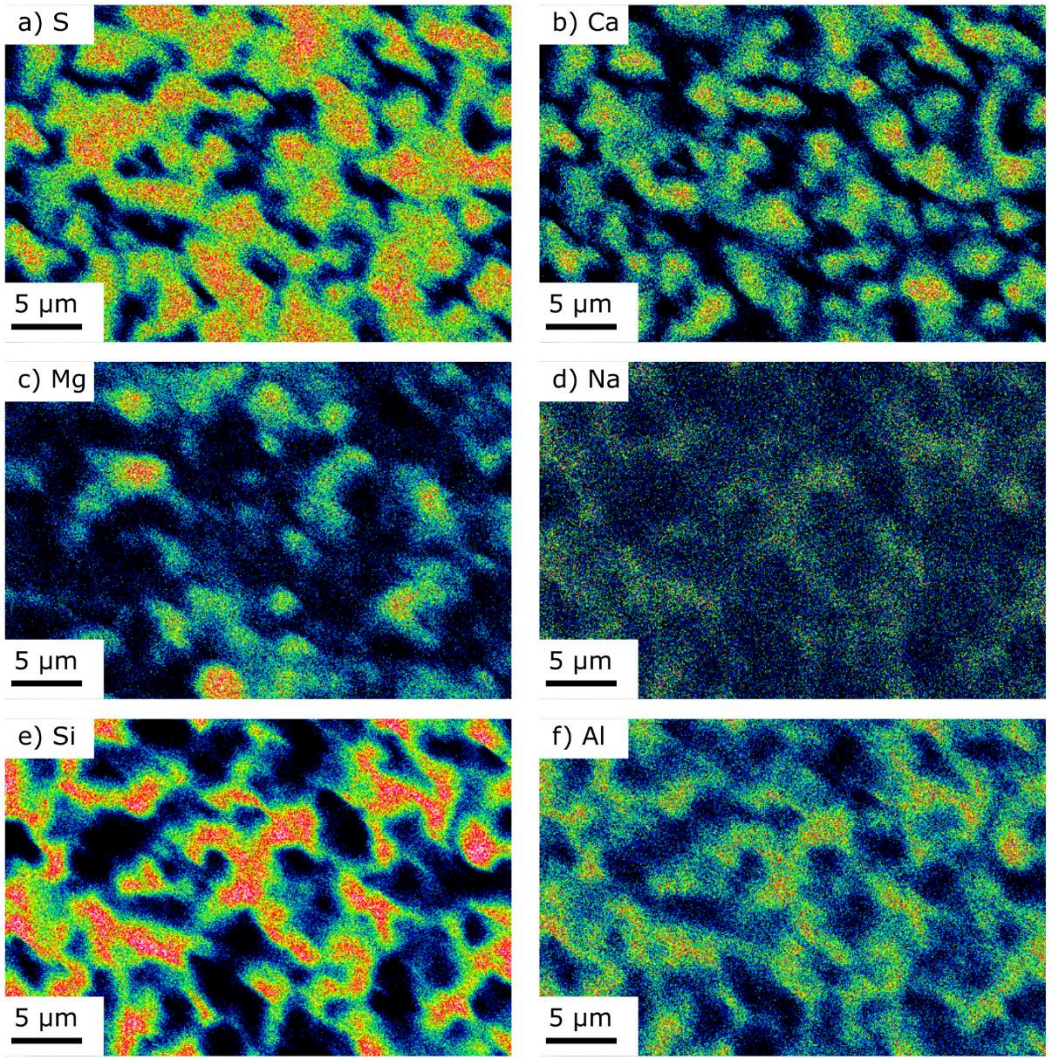

Figure 4-3: EDS maps of the coating on the Fe-free basalt glasses reacted with $SO_{2(g)}$ at 700 °C for 24 h. a) High S-counts indicate the presence of sulfate in the coating. b) Ca correlates with S and forms grains with diameters of less than 5 µm. c) Mg also correlates with S, but not with Ca, suggesting that they form separate sulfate phases. d) Na is not enriched in the coating. e) Si-counts are high where gaps in the coating occur. f) Al correlates with Si and Na, indicating that it remains in the glass substrate.

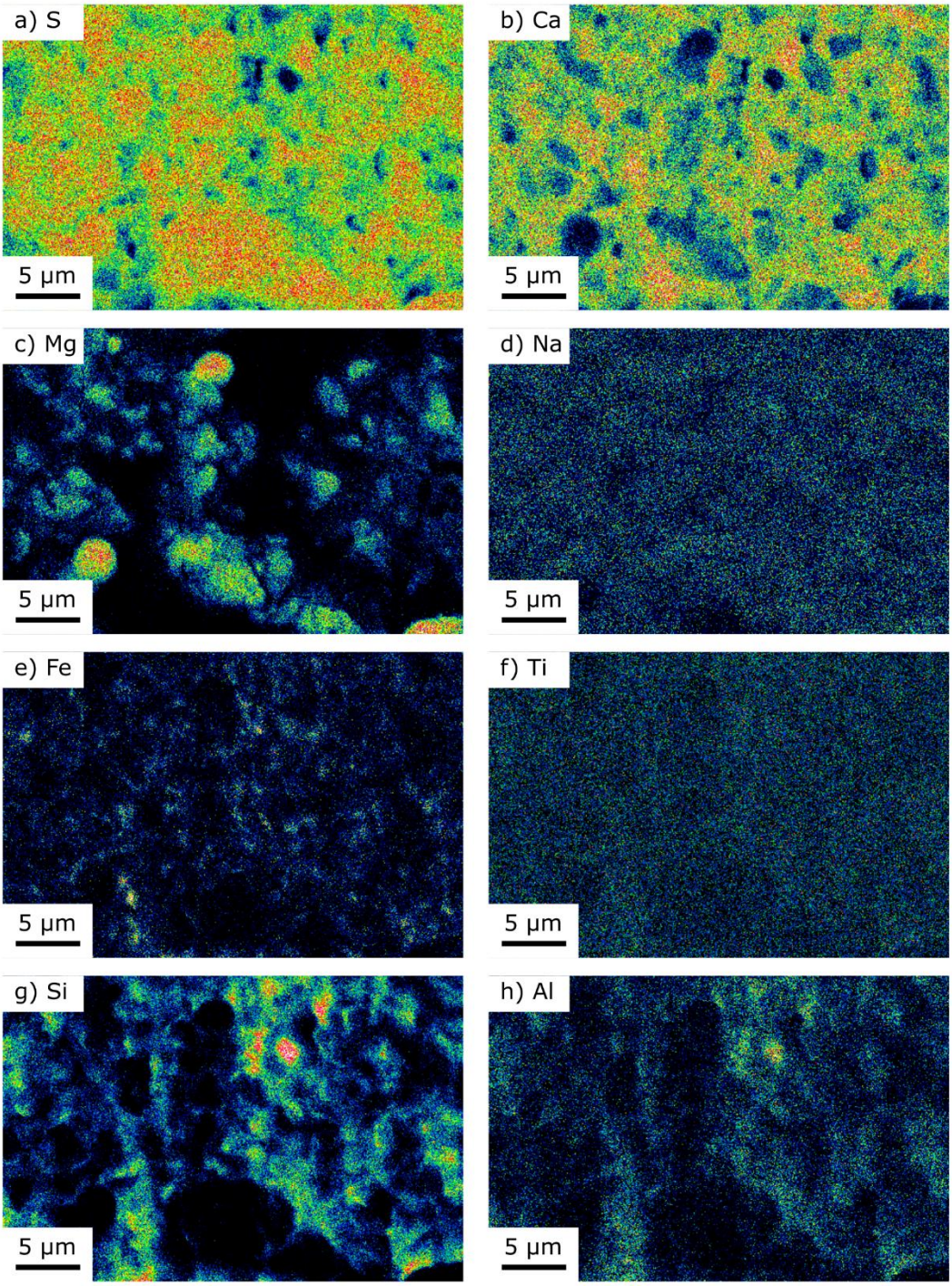

Figure 4-4: EDS surface maps of a tholeiitic basalt glass pre-equilibrated at NNO-1.5 and reacted with $SO_{2(g)}$ at 700 °C for 24 h. a) S b) Ca c) Mg d) Na e) Fe f) Ti g) Si h) Al. Ca and Mg correlate with S but not with each other indicating the presence of two distinct sulfate phases. Fe forms sub-micron sized grains, Na, Ti, Si and Al remain in the glass substrate.

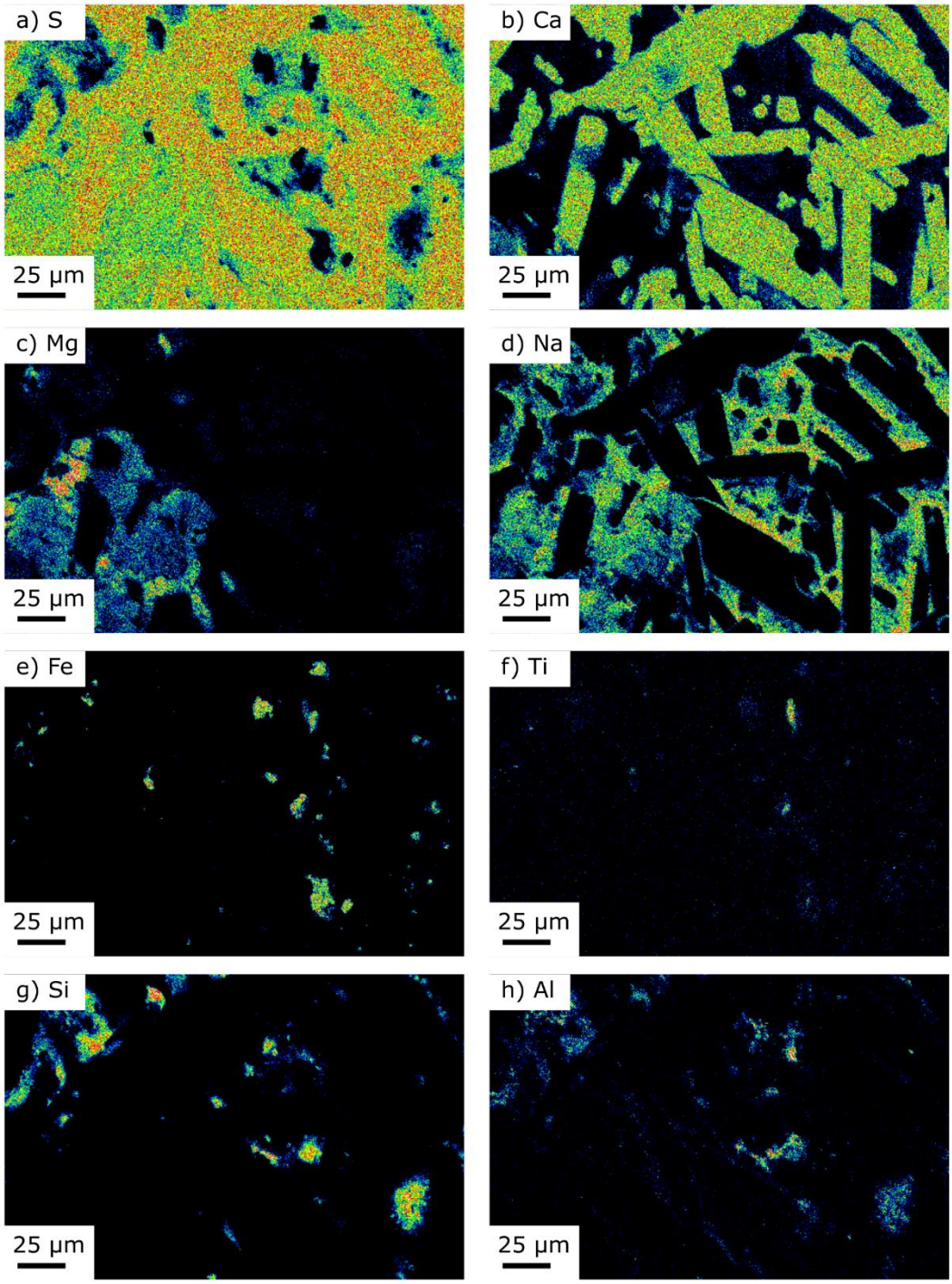

Figure 4-5: EDS surface maps of a tholeiitic basalt glass pre-equilibrated at NNO and reacted with $SO_{2(g)}$ at 700 °C for 24 h. a) S b) Ca c) Mg d) Na e) Fe f) Ti g) Si h) Al. Ca, Mg and Na correlate with S, but form three distinct sulfate phases. Si and Al remain in the glass substrate. Fe forms oxide grains with diameters of up to 20 µm. Some oxide grains are rich in Ti, with som Al and Fe.

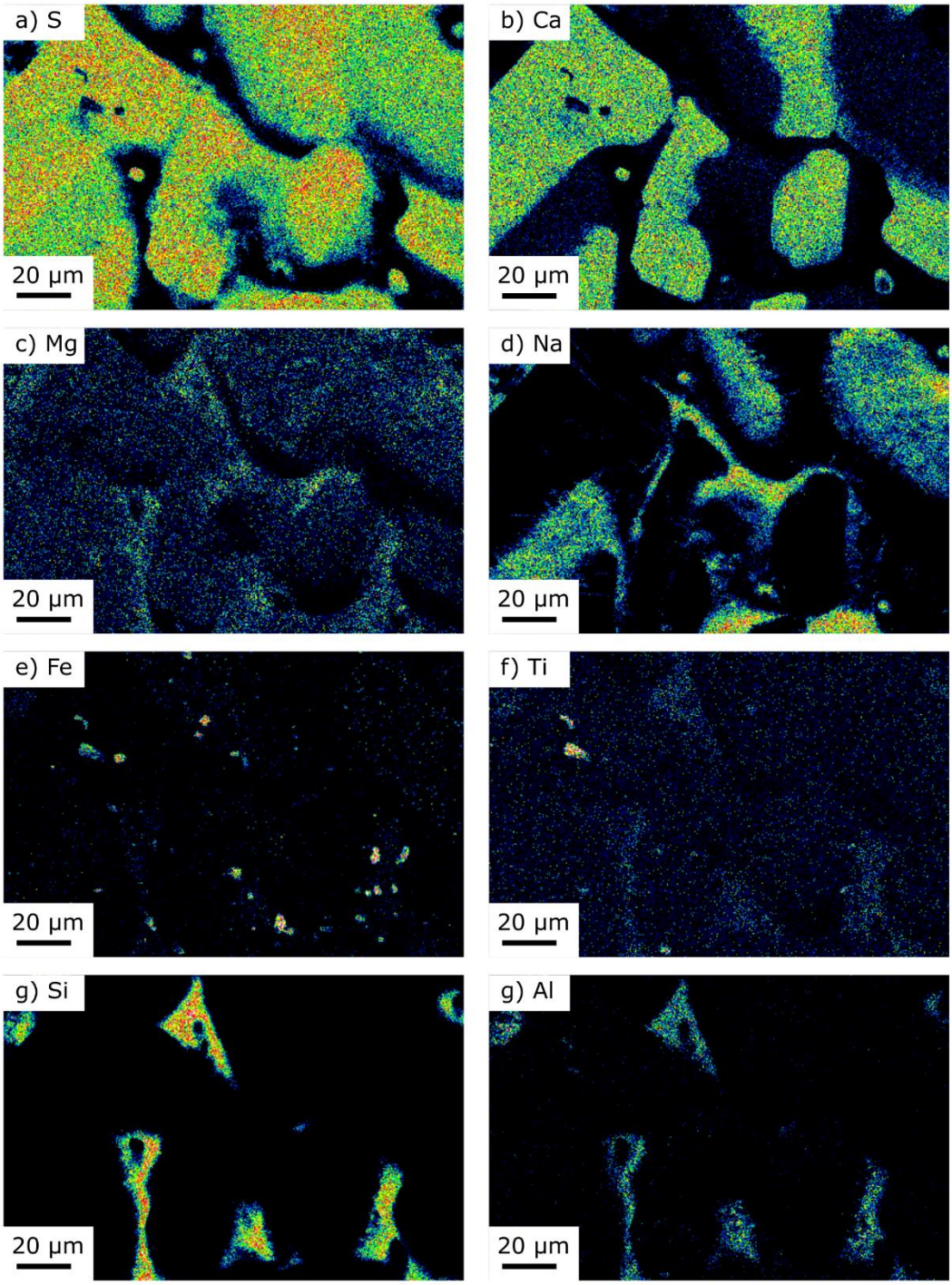

Figure 4-6: EDS surface maps of a tholeiitic basalt glass pre-equilibrated at NNO+1 and reacted with $SO_{2(g)}$ at 700 °C for 24 h. a) S b) Ca c) Mg d) Na e) Fe f) Ti g) Si h) Al. Ca, Mg and Na correlate with S forming sulfate coatings. $CaSO_4$ occurs as large grains, surrounded by fine-grained masses of Na_2SO_4 with some Mg. Fe forms oxide grains with diameters of several microns, and very fine grains associated with the Na_2SO_4. Ti occurs as oxides with some Fe and Al, but predominantly remains in the glass substrate with Si and Al.

4.4.2 Textures and chemistry of the coating

Back-scattered electron (BSE) images allow the distinction of the different phases in the coatings as a function of their densities (Figure 4-2) and energy-dispersive X-ray spectroscopy (EDX) maps of the coatings reveal the distribution of the major chemical elements in the coatings. The electron microscopy images show that the sulfate coatings are mounded on the top of the glass substrates but do not continuously coat the substrates. Gaps in the coatings are evident in areas where high numbers of Si- and Al-counts are measured, which remain in the substrate during the reaction (Figures 4-3, 4-4, 4-5 and 4-6).

The textures of the surface coatings fall into two categories (Figure 4-2). First, the coatings on the Fe-free basalt glass and the reduced tholeiitic basalt glass (NNO-1.5) are fine-grained, and the different phases are approximately equigranular (Figures 4-2a to d). Second, the coatings on the more oxidized tholeiitic basalts (NNO and NNO+1) are dominated by large anhydrite crystals, with lengths extending up to 100 μm (Figures 4-2e to f). Here we discuss the two types of textures separately.

First, on the Fe-free and NNO-1.5 basalts, fine-grained $CaSO_4$ and $MgSO_4$ can be differentiated by their crystal habits (Figure 4-2a to d) and the EDS maps of S, Ca and Mg (Figures 4-3a to c and 4-4a to c). After 1 h, the crystal habit of the $CaSO_4$ is poorly developed (Figure 4-2a and c), but as the grains mature with longer experimental durations (i.e. 24 h) they establish facets (Fe-free basalt, Figure 4-2b) and grain-boundary triple-junctions, with dihedral angles of 120° (NNO-1.5, Figure 4-2d). The $MgSO_4$ grains have rounded shapes, because the grains have taken up variable amounts of water after the experiments (e.g., during transfer from the desiccator to the carbon coater, to the different analytical instruments). In the BSE images (Figure 4-2) the $MgSO_4$ grains can further be identified by their darker grey-shade. The grain sizes of the coatings on the Fe-free basalt and the reduced NNO-1.5 basalt are similar after 1 h and 24 h (Figure 4-2a to d). The coatings on both glass substrates do not contain any Na_2SO_4 (Figures 4-3d and 4-4d).

Second, the coatings on the more oxidized (NNO and NNO+1) tholeiitic basalt are dominated by large elongated $CaSO_4$ crystals with grain sizes of up to 100 μm in length (Figure 4-2e to h). The $CaSO_4$ grains show a perfect cleavage perpendicular to the longest crystal axis (Figures 4-2, 4-5 and 4-6). This cleavage plane corresponds to the (001) plane (Tröger, 2017), and hence the longest dimension of the elongated grains is the crystallographic c-axis. Anhydrite has the largest thermal expansion coefficient along the crystallographic c-axis, with a relative expansion of 2% from room temperature to 700 °C (Evans, 1979). As the $CaSO_4$ crystals cool after removal from the furnace they shrink and the crystals split on the cleavage plains.

Magnesium sulfate surrounds and sometimes overgrows the $CaSO_4$ crystals (Figure 4-5c). On the tholeiitic glass pre-equilibrated at NNO hydrated $MgSO_4$ forms large patches with diameters of up to 200 μm. On the most oxidized tholeiitic basalt glass (NNO+1) the coating in the 1 h experiment contains distinct $MgSO_4$ grains (Appendix), but the coating formed in the 24 h experiment does not contain any $MgSO_4$ (Figure 4-6c). The textural features of $MgSO_4$ were affected by hydration after the experiments (Figure 4-1b).

Sodium sulfate forms fine needles which are commonly twinned and have grain sizes of less than 2 μm (Figure 4-2e to g). On the NNO-glass Na_2SO_4 is mainly observed in-between the $CaSO_4$ crystals and to a lesser degree associated with $MgSO_4$ (Figure 4-5d). On the most oxidized tholeiitic glass (NNO+1) Na_2SO_4 occurs in dense aggregates, which in some cases appear to overgrow the $CaSO_4$ crystals (Figures 4-6d and 4-2h).

Hematite and anatase are clearly observed due to their light gray hues in the BSE images (Figure 4-2) and high numbers of iron and titanium counts in the EDS maps (Figures 4-4, 4-5 and 4-6). Hematite grain sizes range from < 1 μm on the basalt glass pre-equilibrated at NNO-1.5 (Figure 4-4e) to 20 μm on the NNO glass (Figure 4-5e). On the most oxidized glass (NNO+1) sub-micron sized Fe_2O_3 grains are associated with Na_2SO_4 aggregates (Figures 4-6e and 4-2). Anatase is less abundant than hematite and grain sizes range up to 10 μm.

In summary, the coating textures and mineral assemblages on the basalt glasses differ between the Fe-free glass and the most reduced tholeiitic basalt glass (NNO-1.5), and the more oxidized tholeiitic basalt glasses (NNO and NNO+1). The assemblages are summarized in Table 4-2. In the first case the coatings consist of equigranular grains of $CaSO_4$ and $MgSO_4$, with no significant textural difference from 1 h long reaction with $SO_{(g)}$ and 24 h long experiments. In the second case, the coatings are dominated by large $CaSO_4$ crystals, which grow from 1 h to 24 h (Figure 4-2). In these coatings, where $MgSO_4$ and Na_2SO_4 occur (Table 4-2), they infill the space between the large $CaSO_4$ crystals and overgrow these in some places (Figures 4-5b to d and 4-6b and d). This suggests that the Na_2SO_4 and $MgSO_4$ sulfates nucleate or grow, at least partially, after $CaSO_4$. In the case of $MgSO_4$ hydration has likely affected the texture.

Table 4-2: Phases formed by the $SO_{2(g)}$-basalt glass reactions at 700 °C. For each experiment the table lists the phases in the surface coatings as determined with Raman spectroscopy and EDS (Figures 4-1, 4-3, 4-4 and 4-5), as well as crystalline phases in the reacted glass substrates as inferred from nanoSIMS maps (Figures 4-7, 4-8, 4-9 and 4-10).

Time (hours)	1	24
Fe-free basalt	$CaSO_4$, $MgSO_4$, TiO_2 no crystallites	$CaSO_4$, $MgSO_4$, TiO_2 no crystallites
Tholeiitic basalt NNO-1.5	$CaSO_4$, $MgSO_4$, Na_2SO_4, Fe_2O_3 no crystallites	$CaSO_4$, $MgSO_4$, Fe_2O_3 Mg-pyroxene
Tholeiitic basalt NNO0	$CaSO_4$, $MgSO_4$, Na_2SO_4, Fe_2O_3, Fe-Ti-(Al)-oxide no crystallites	$CaSO_4$, $MgSO_4$, Na_2SO_4, Fe_2O_3, Fe-Ti-(Al)-oxide Fe-Na-pyroxene, Mg-pyroxene
Tholeiitic basalt NNO+1	$CaSO_4$, Na_2SO_4, $MgSO_4$, Fe_2O_3, Fe-Ti-(Al)-oxide SiO_2	$CaSO_4$, Na_2SO_4, Fe_2O_3, Fe-Ti-(Al)-oxide SiO_2, Al_2O_3, Fe-Na-pyroxene, Mg-pyroxene

4.4.3 Chemistry of the glass substrate in cross-section

Chemical element maps of cross-sections measured with nanoSIMS reveal crystallites and chemical zones in the reacted basalt glasses (Figures. 4-7, 4-8, 4-9 & 4-10). The nanoSIMS maps do not show absolute concentrations, but relative increases and decreases in count rates, which correlate with the relative concentrations of the elements. Figure 4-11 shows profiles across the nanoSIMS maps, highlighting relative enrichments and depletions in the major elements from the surface to the modified basalt glass substrates.

In the cross-sections mapped with nanoSIMS the coatings are only partially conserved. The loss of the coating likely occurred during embedding in epoxy resin and polishing of the cross-sections. For example, on the Fe-free basalt glass the coating is completely lost (Figure 4-7), whereas it is well-preserved on the most oxidized tholeiitic basalt glass (NNO+1, Figure 4-10). In this case, the nanoSIMS map (Figure 4-10) shows a sulfate coating on the glass surface with a thickness of ~8 μm, predominantly consisting of $CaSO_4$ with some Na. Iron and Ti-oxides are also observed in the cross-section of the coating (Figure 4-10).

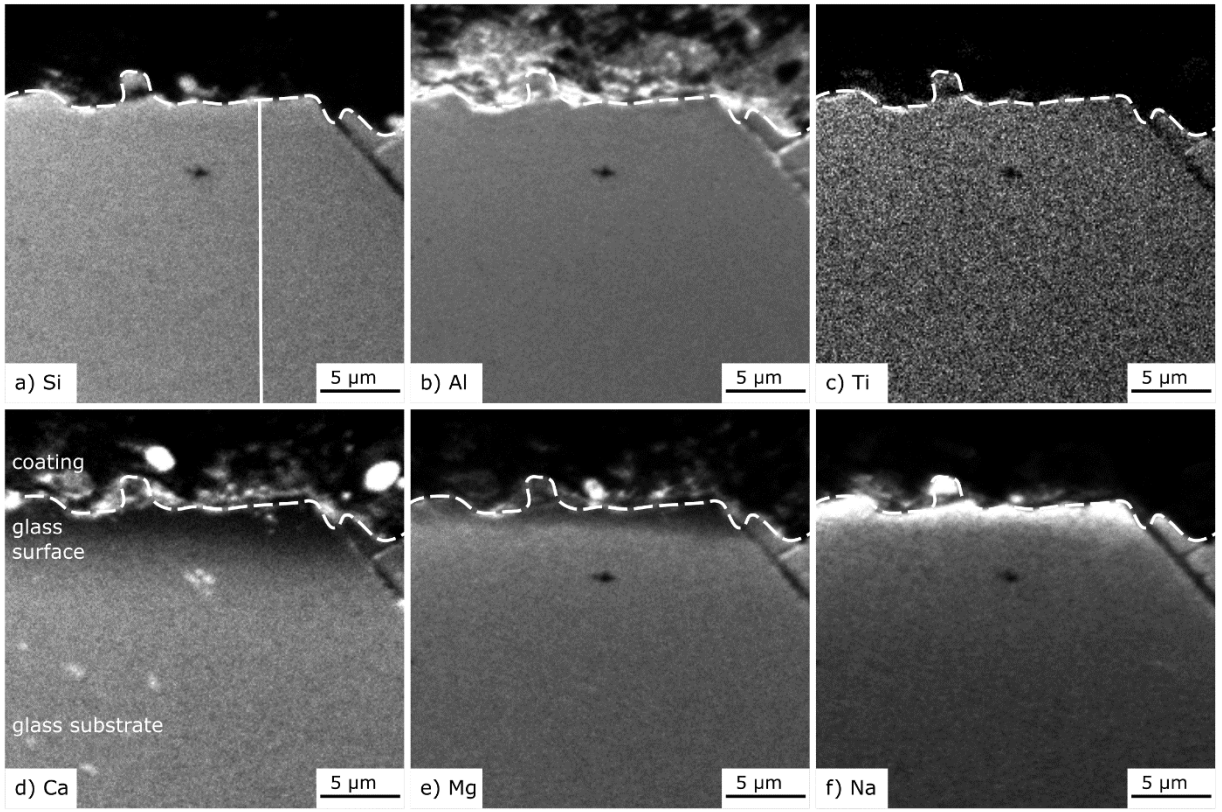

Figure 4-7: NanoSIMS count map of a cross-section through the Fe-free basalt reacted with $SO_{2(g)}$ at 700 °C for 24 h. The stippled line shows the interface below which is the glass substrate. White indicates high count-rates, black indicates low count-rates. a) Si b) Al c) Ti d) Ca e) Mg f) Na. The white line on the Si map indicates the position of the profile shown in Figure 11a

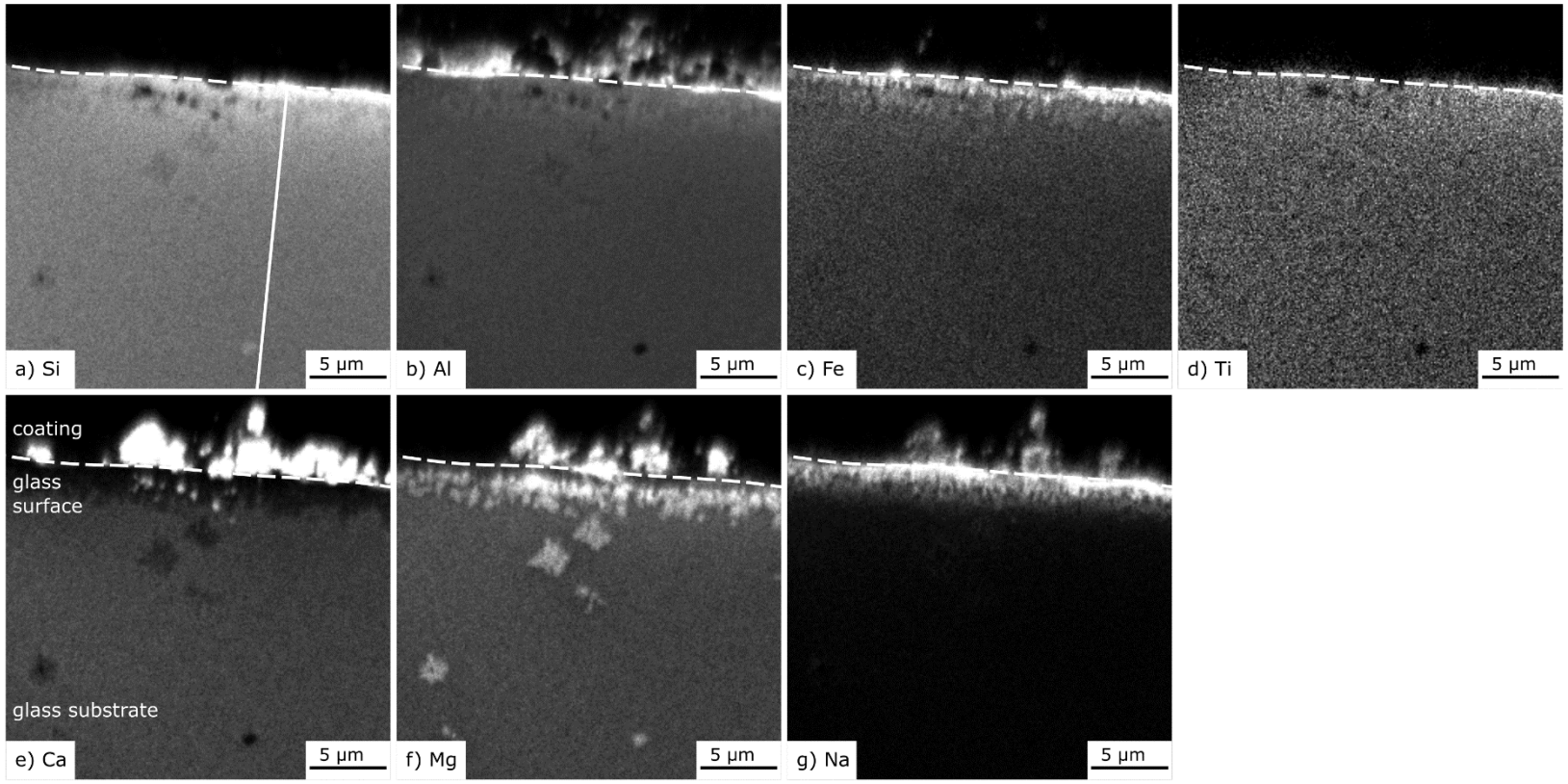

Figure 4-8: NanoSIMS count map of a cross-section through the tholeiitic basalt, pre-equilibrated at NNO-1.5 and reacted with $SO_{2(g)}$ at 700 °C for 24 h. The stippled line shows the interface below which is the glass substrate. White indicates high count-rates, black indicates low count-rates. a) Si b) Al c) Ti d) Ca e) Mg f) Na. The white line on the Si map indicates the position of the profile shown in Figure 11b.

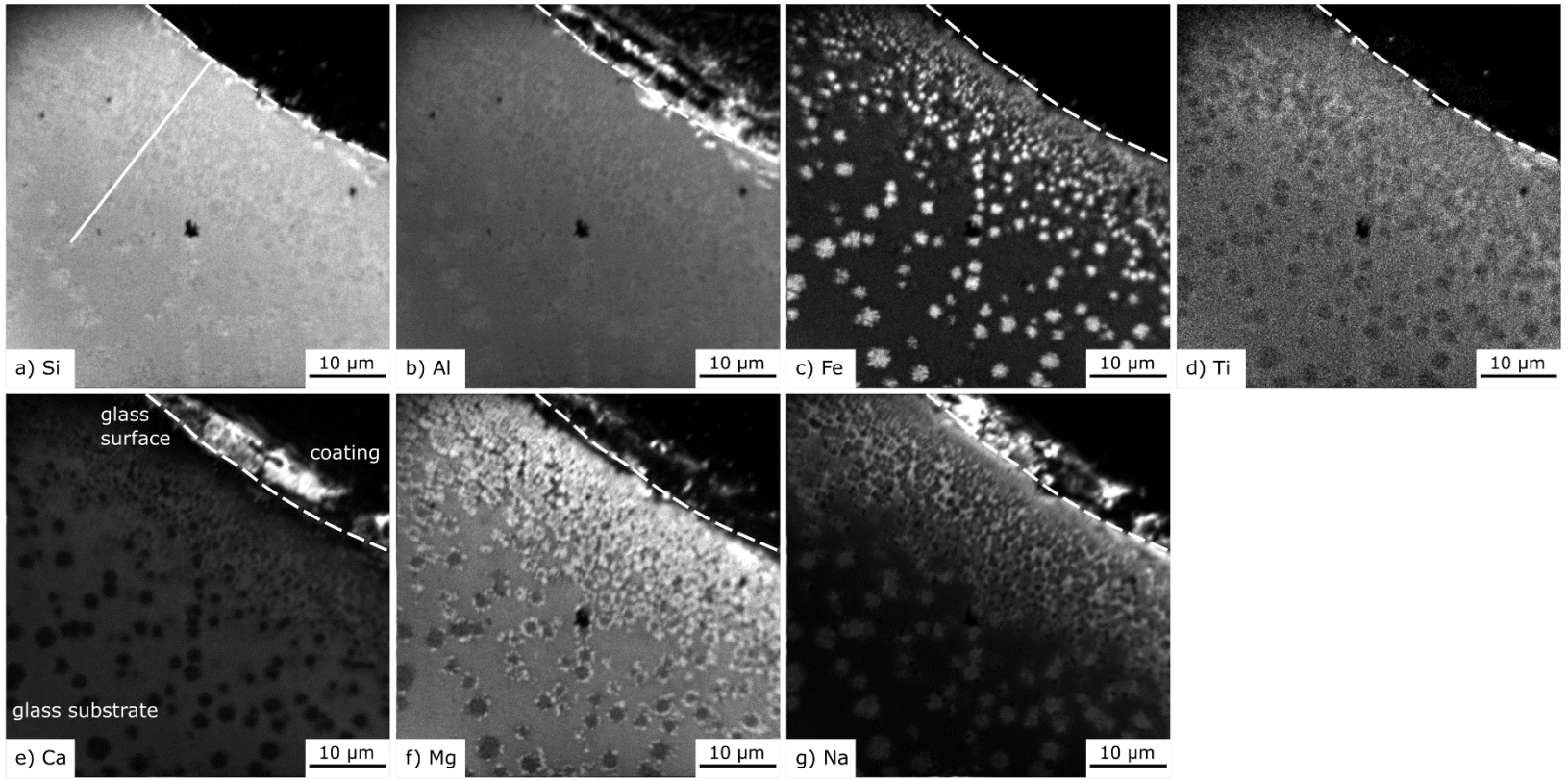

Figure 4-9: NanoSIMS count map of a cross-section through the tholeiitic basalt, pre-equilibrated at NNO and reacted with $SO_{2(g)}$ at 700 °C for 24 h. The stippled line shows the interface below which is the glass substrate. White indicates high count-rates, black indicates low count-rates. a) Si b) Al c) Ti d) Ca e) Mg f) Na. The white line on the Si map indicates the position of the profile shown in Figure 11c.

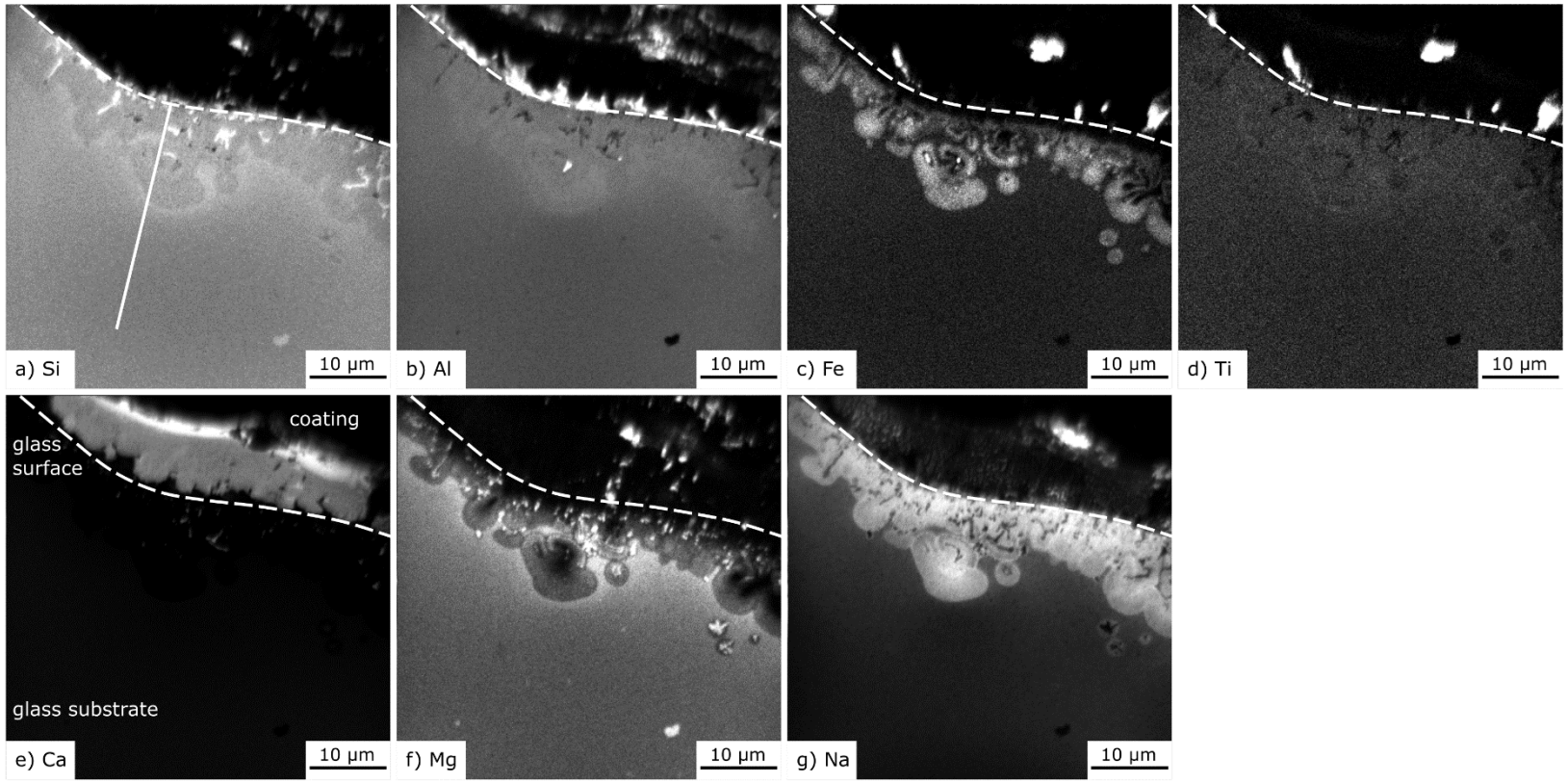

Figure 4-10: NanoSIMS count map of a cross-section through the tholeiitic basalt, pre-equilibrated at NNO+1 and reacted with $SO_{2(g)}$ at 700 °C for 24 h. The stippled line shows the interface below which is the glass substrate. White indicates high count-rates, black indicates low count-rates. a) Si b) Al c) Ti d) Ca e) Mg f) Na. The white line on the Si map indicates the position of the profile shown in Figure 11d.

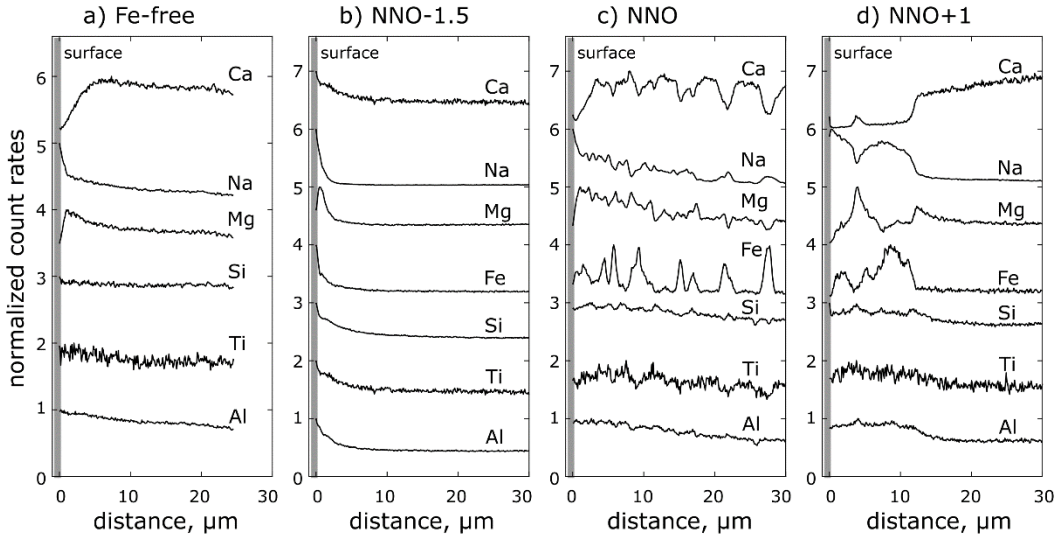

Figure 4-11: Normalized nanoSIMS profiles from the surface into the reacted substrates of the basalt glasses reacted at 700 °C for 24 h. The positions of the profiles are indicated on the Si maps of the respective nanoSIMS analysis (Figures 4-7a, 4-8a, 4-9a and 4-10a). Peaks in the basalt glass substrates indicate the occurrence of crystallites. a) Fe-free basalt; b) NNO-1.5; c) NNO; d) NNO+1.

The Fe-free basalt glass substrate shows the least amount of modification after reaction with $SO_{2(g)}$ for 24 h at 700 °C (Figure 4-7). Calcium and Mg are depleted at the glass surface (Figures 4-7d, 4-7e and 4-11a). The concentration of Ca increases into the glass substrate over a distance of 5 µm, whereas Mg increases occurs over a shorter distance of ~2 µm. Sodium is enriched at the surface to a depth of 2-5 µm (Figure 4-11a). The depletion of Ca and Mg in the glass substrate is in agreement with the observation of $CaSO_4$ and $MgSO_4$ in the sulfate coating, whereas Na_2SO_4 is not observed and hence Na is retained in the near-surface glass substrate. There is no change in Si, Al, and Ti in the glass substrate. No sharp peaks are observed in the major element profiles (Figure 4-11a), which suggests that no crystallites have nucleated on the 100 nm scale.

The tholeiitic glass pre-equilibrated at NNO-1.5 is modified in a similar manner to the Fe-free basalt glass (Figure 4-8). Calcium is depleted at the surface of the glass substrate to a depth of approximately 3 µm (Figure 4-8e) and Na is enriched in the same zone at the glass surface (Figures 4-8g and 4-11b). Mg forms crystallites in the glass substrate to a depth of 20 µm (Figure 4-8f), but the highest density of Mg-rich crystallites occurs within 3 µm of the surface. The largest spherulite crystallites have diameters of up to 2 µm. Silicon and Fe also form crystallites in the glass substrate within 1-3 µm of the surface (Figures 4-8c and 4-8e).

In the reacted tholeiitic glass pre-equilibrated at NNO (Figure 4-9) Ca is depleted at the surface to a depth of <10 µm (Figure 4-9e). In comparison, Na becomes increasingly

enriched towards the glass surface from a depth of 20 μm (Figure 4-9g). Nucleation of Fe-, Na- and Mg-rich spherulites is observed throughout the sample, with decreasing intensity from the surface towards the interior of the glass (Figures 4-9c, 4-9f and 4-11c). The spherulites have Fe-rich cores which also have elevated Na-concentrations. This is evident when comparing Figures 4-9c and 4-9f, where high Fe- and Na count-rates correlate in the glass at a depth of more than 15 μm from the surface. We interpret these larger spherulites with diameters of up to 3 μm as pyroxenes (e.g. $NaFe^{3+}Si_2O_6$, aegirine). They are surrounded by Mg-rich material, which may correspond to $MgSiO_3$ (enstatite or clinoenstatite). Calcium counts are low in the spherulitic crystallites and Si, Al and Ti show minor variations (Figure 4-11c).

The modification of the most oxidized tholeiitic basalt glass (NNO+1) differs from the other glasses in its texture and the occurrence of different nucleated phases (Figure 4-10). Calcium is strongly depleted at the surface to a depth of 12 μm (Figures 4-10e and 4-11d). In a zone of 20 μm from the glass surface mushroom-shaped features are observed. These are highly enriched in Na and Fe and include a number of different crystallites (Figure 4-10c and g). Sodium is enriched throughout the modified zone, whereas Fe is depleted within 1.5 μm of the glass surface and enriched further into the glass (Figures 4-10c and 4-10g). Magnesium is enriched around the mushroom-shaped modification features but is also depleted within ~2 μm from the surface (Figure 4-10f). Crystallites are evident as peaks in the profile (Figure 4-11d) and include Mg-rich spherulites surrounded by Fe- and Na-rich material, Fe-rich crystallites (Figure 4-10c) and SiO_2 needles (Figure 4-10a), and Al-rich material (Figure 4-10b), possibly Al_2O_3. High Al-counts at the surface may be due to contamination during sample polishing.

In summary, the observed modification of the basalt glasses after 24 h of reaction with $SO_{2(g)}$ extends into the glass substrate to a depth of less than 5 μm from the surface in the case of the Fe-free and the NNO-1.5 glasses (Figure 4-11a and b). The more oxidized glasses are modified to a depth ~20 μm (NNO+1) to more than 50 μm (NNO) from the surface (Figure 4-11c and d). The formation of sulfates on the glasses is reflected in a strong depletion of Ca in the near-surface glass substrate in all experiments. Magnesium and Fe are also depleted near the glass surface, whereas Na is enriched near the surface of the glass substrate. Crystallites in the modified basalt glasses are rich in Mg and Fe, with some Na incorporated in the Fe-rich crystallites. We were not able to directly identify the minerals, but the nanoSIMS maps suggest that they are $NaFe^{3+}Si_2O_6$ (aegirine) and $MgSiO_3$ (enstatite or clinoenstatite). In the most intensely modified tholeiitic basalt glass, pre-equilibrated at NNO+1 (Figure 4-10), SiO_2 also occurs as crystallites in the glass substrate.

4.5 Discussion

The reaction of $SO_{2(g)}$ with basaltic glasses forms discontinuous coatings on the glass surface consisting of sulfates ($CaSO_4$, $MgSO_4$ and Na_2SO_4) and oxides (Fe_2O_3 and TiO_2). Overall the sulfate assemblage changes with increasing Fe^{3+}/Fe_{tot} in the pre-equilibrated basalt glasses. On the reacted NNO-1.5 basalt glass the coating consists of $CaSO_4$ and $MgSO_4$. Sodium sulfate appears on the glass pre-equilibrated at NNO together with $CaSO_4$ and $MgSO_4$ and is even more abundant on the NNO+1 basalt glass, where $MgSO_4$ no longer occurs.

The surface products are accompanied by chemical modifications in the reacted basalt glasses which are observed as chemical zones and crystallites that include SiO_2, Fe-Na-rich and Mg-rich pyroxene. We argue that the formation of the phases in the coating and substrate is controlled by the role of the cations (Na^+, Ca^{2+}, Mg^{2+}, $Fe^{2+/3+}$) in the glass structure and their mobility to migrate to the glass surface. Calcium diffusion has previously been suggested as the rate-limiting factor in the reaction between $SO_{2(g)}$-bearing gas and glassy ash, which forms $CaSO_4$ (Ayris et al., 2013; Delmelle et al., 2018). First, we discuss the basaltic glass structure and how it may affect the $SO_{2(g)}$-glass reaction mechanism. We then discuss how the reaction oxidizes the Fe-bearing basalt glasses resulting in an increase of the Fe^{3+}/Fe_{tot} ratio and present a model for the reaction mechanism. Finally, we discuss how the loss of cations (Ca, Mg, Na) to the sulfate coatings affects the normative mineral composition of the reacted basalt glasses.

4.5.1 Role of the glass structure on reaction products

To understand the constraints on reaction pathways and rates we first discuss the structure of basaltic glasses which consists of different building blocks. Si^{4+}, Ti^{4+} and Al^{3+} cations are tetrahedrally (T) coordinated by O^{2-} ions. These tetrahedral building blocks form a network with short- to medium-range order, but no long-range order (Mysen and Richet, 2005). The O^{2-} ions may either bond to two network forming T-cations, forming T-O-T bonds and acting as bridging oxygens (BO), or they may link a T-cation with a network modifying cation (M; e.g., Na^+, K^+, Mg^{2+}, Ca^{2+} and Fe^{2+}), forming T-O-M bonds and acting as non-bridging oxygens (NBO). The number of non-bridging oxygens per tetrahedrally coordinated cation (NBO/T) describes the degree of polymerization of the amorphous network (Mysen and Richet, 2005). Tetrahedrally coordinated Al^{3+} and Fe^{3+} cations further require charge balancing by a mono- or divalent cation as they are negatively charged ($[M^{3+}O_4]^-$). Alkali earths in particular may change their role in the glass structure and act as charge compensators, instead of network modifiers (Neuville and Mysen, 1996; Angeli et al., 2000; Le Losq et al., 2014; Le Losq and Neuville, 2017). In oxidizing Fe-bearing

glass the Fe^{3+}/Fe_{tot} ratio increases and the number of charge compensating cations increases accordingly, which requires some network modifiers to change their role in the glass structure (Cooper et al., 1996).

In the reduced glasses (NNO-1.5 and NNO) the Na^+ concentration is sufficient to charge balance all Fe^{3+} cations ($Fe^{3+}/Na^+ < 1$) (Table 4-1), but not sufficient to charge balance tetrahedrally coordinated Fe^{3+} and Al^{3+} ($(Fe^{3+}+Al^{3+})/Na^+ > 1$). The low K^+ concentrations are also not sufficient to completely charge-balance the tetrahedrally coordinated trivalent cations, so that some divalent cations (Ca^{2+}, Mg^{2+} or Mn^{2+}) are required for charge compensation, in particular with increasing the Fe^{3+}/Fe_{tot} ratio. In the more oxidized glass (NNO+1) the Na^+ concentration is insufficient to charge balance all tetrahedrally coordinated Fe^{3+} and other cations are necessary for charge balance.

The nanoSIMS maps of the cross-section into the modified glass substrate of the reacted tholeiitic basalt pre-equilibrated at NNO+1 (Fig. 4-10) show a correlation of Fe-enrichment and Na-enrichment at the glass surface. In these areas of enrichment, Fe is likely oxidized to Fe^{3+} and charge-compensated by Na^+.

4.5.2 Effect of the initial redox state of the glasses on reaction pathways

Oxidation/reduction mechanisms are important components of gas-solid reactions (Kreider and Lipiński, 2018). The reaction of $SO_{2(g)}$ with Fe-bearing basalt glass is an example of such a process, where a reaction front propagates into the glass where iron is progressively oxidized and the Fe^{3+}/Fe_{tot} ratio increases. Because sulfur is a polyvalent element (S^{2-}, S^-, S^0, S^{4+}, S^{6+}), the redox state of both the gas and solid reactants play a role in the reaction. Here, we assume that the $SO_{2(g)}$ used in the experiments is pure and dissociates at equilibrium to form other gas species including $S_{2(g)}$, $S_{3(g)}$, $SO_{3(g)}$, $SO_{(g)}$, $S_2O_{(g)}$ and $O_{2(g)}$ (Zolotov and Fegley, 1999; Renggli and King, 2018). From a Gibbs Free Energy minimization calculation of the equilibrium dissociation of $SO_{2(g)}$ the oxygen fugacity of the gas can be calculated ($\log fO_2 = -12.1$ at 700 °C), that is 4.2 log units above the NNO-buffer (O'Neill and Pownceby, 1993) at the hematite-magnetite redox buffer (Renggli and King, 2018). Consequently, the $SO_{2(g)}$ reaction with the more reduced tholeiitic basalt glasses (NNO-1.5 to +1) imposes a gradient in the electrochemical environment.

In a dry system this electrochemical potential gradient is most efficiently dissipated by rapid diffusion of electron holes into the oxidizing glass, charge-compensated by the counter-diffusion of monovalent and divalent cations (Cooper et al., 1996; Cook and Cooper, 2000; Cooper, 2018). Multivalent element bearing aluminosilicate glasses act as semiconductors for electron holes, allowing their rapid diffusion. In this oxidation

mechanism, the charge-compensating diffusion of Ca^{2+} and Mg^{2+} is the rate-limiting step. At the glass surface Ca^{2+} and Mg^{2+} form MgO and CaO coatings in such an oxidation

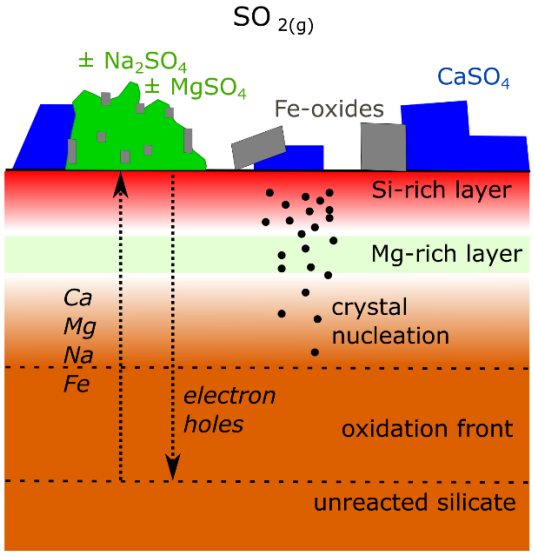

Figure 4-12: Schematic drawing of the reaction mechanism between $SO_{2(g)}$ and Fe-bearing basalt glass. The $SO_{2(g)}$-glass reaction results in the oxidation of Fe in the glass, the formation of sulfates and oxides in the coating and the nucleation of phases including SiO_2 and pyroxenes in the glass substrate.

reaction (Cooper et al., 1996; Cook and Cooper, 2000; Cooper, 2018). Finally, the oxidized Fe^{3+} atoms require charge compensation if they are tetrahedrally coordinated, which results in the development of a Na-front at the oxidation front in the glass (Cook et al., 1990; Cook and Cooper, 2000; Burkhard, 2001).

In the reaction of Fe-bearing basalt glasses with $SO_{2(g)}$ we observe a similar reaction mechanism (Figure 4-12, Renggli and King, 2018). In addition to the sulfate-forming reaction, the overall reaction mechanism is driven by a gradient in the electrochemical potential. Both of these processes result in the diffusion of Ca^{2+} and Mg^{2+} to the glass surface. The $SO_{2(g)}$ reaction further drives the diffusion of Na^{+} and minor amounts of Fe^{3+}, Ti^{4+} and Al^{3+} to the surface. The element maps obtained with nanoSIMS record Na-enrichment in the near-surface glass (Figure 4-11). This Na-enrichment corresponds to the Na-front observed in oxidized basalt glasses (Cook et al., 1990; Cook and Cooper, 2000; Burkhard, 2001; Renggli and King, 2018).

In summary, the reaction of $SO_{2(g)}$ with Fe-bearing basaltic glasses results in the formation of sulfate-rich coatings, and it affects the redox state of the glass. The rate of diffusion of Ca^{2+}, Mg^{2+} and Na^{+} in the basalt glass likely controls the overall reaction rate and hence the formation of sulfate coatings (Renggli et al., in prep.; Ayris et al., 2013; Renggli and King, 2018).

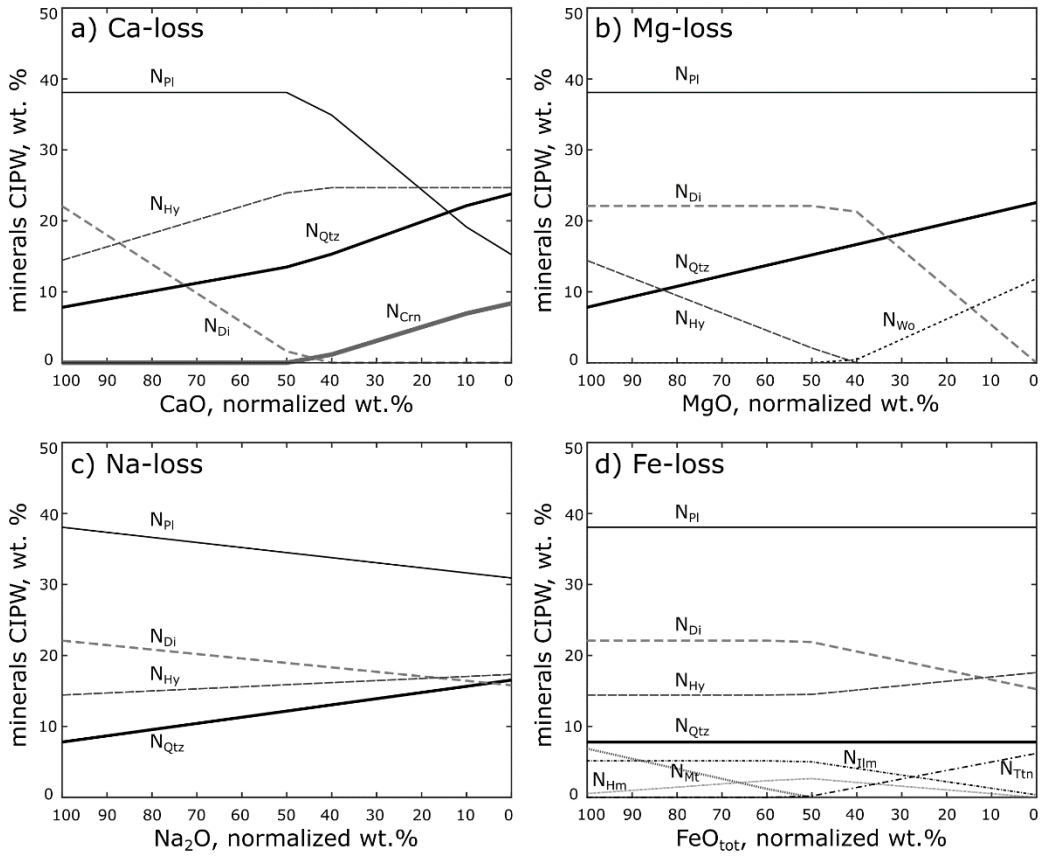

Figure 4-13: Normative mineralogy of the tholeiitic basalt pre-equilibrated at NNO+1 as a function of the loss of a) CaO, b) MgO, c) Na_2O and d) FeO_{tot} from the basaltic glass. The figures only show the minerals with changing abundances. Additional minerals not affected by the reactive cation loss are listed in Table 4-1.

4.5.3 Crystallization in the basalt glasses

The calculation of the normative mineralogy of the basalts (CIPW norm) provides a prediction of relative mineral abundances if the basalt was fully crystallized (Johannsen, 1931). We calculated the normative mineralogy of the unreacted basalts (Table 4-1), to estimate the effect of Ca, Mg, Na and Fe loss from the glass, due to the reaction with $SO_{2(g)}$, on the mineralogy. The evolution of the mineralogy with the loss of these elements is shown in Figure 4-13 for the case of the Fe-bearing basalt pre-equilibrated at NNO+1.

In the Fe-free basalt glass the normative mineralogy consists of plagioclase (N_{Pl}), followed by hypersthene (N_{Hy}), quartz (N_{Qtz}), corundum (N_{Crn}) and rutile (N_{Rt}) (Table 4-1). Decreasing concentrations of Ca and Na (due to their forming sulfate coatings) result in the decrease of N_{Pl}, accompanied by an increase in the abundance of N_{Qtz} and N_{Crn} (Appendix). The loss of Mg results in the decrease in the abundance of N_{Hy} and an increase in N_{Qtz}. The presence of N_{Rt} in the normative mineralogy remains unaffected by the loss of Ca, Na or Mg during the reaction with $SO_{2(g)}$. If all Ca, Na and Mg were completely lost form the Fe-free glass the normative mineralogy would consist of N_{Qtz}, N_{Crn} and N_{Ru}.

The normative mineralogy of the Fe-bearing tholeiitic basalts is dominated by N_{Pl}, followed by the pyroxenes (N_{Hy} and N_{Di}), N_{Qtz}, orthoclase (N_{Or}), ilmenite (N_{Ilm}) and apatite (N_{Ap}). In the glasses pre-equilibrated at NNO-1.5 and NNO the stable Fe-oxide is magnetite (N_{Mag}), whereas hematite (N_{Hem}) occurs with N_{Mag} at NNO+1 (Table 4-1).

To investigate the effect of cation loss on the stability of minerals in the tholeiitic basalt glasses we calculate the normative mineralogy while stepwise removing the sulfate-forming CaO, MgO and Na_2O, as well as FeO_{tot} from the bulk glass composition (Figure 4-13). We show the results of the calculations for the tholeiitic basalt composition pre-equilibrated at NNO+1, representative for all three tholeiitic glasses which exhibit the same trends. The results of the calculations for the other tholeiitic basalt compositions are given in the appendix.

Figures 4-13a, b and c show the phases which are affected by the changes in Ca, Mg and Na concentration, excluding N_{Or}, N_{Ilm}, N_{Mag}, N_{Hem} and N_{Ap}, and Figure 4-13d shows the changes in the normative mineralogy due to the loss of Fe, additionally affecting the N_{Hm}, N_{Mt}, N_{Ilm} and N_{Ttn}. Loss of up to 50 wt.% CaO causes the disappearance of N_{Di} from the normative mineralogy (Figure 4-13a). This is accompanied by increasing abundances of N_{Hy} and N_{Qtz}. After the disappearance of diopside and with ongoing CaO loss the stability of N_{Pl} decreases. Consequently, plagioclase becomes increasingly albitic accompanied by the formation of N_{Crn}. The loss of MgO results first in the disappearance of N_{Hy}, accompanied by an increase in the N_{Qtz} abundance, followed by decreasing abundance of N_{Di} and the formation of N_{Wo}. Sodium oxide loss has a less dramatic effect on the normative mineralogy, mainly resulting in an anorthite-rich plagioclase. In the experiments reacting $SO_{2(g)}$ with tholeiitic basalt glasses we observe Ca-, Mg- and Na-sulfates forming as coatings on the glass surfaces. The complete loss of all three of these elements would result in a normative mineralogy predominantly consisting of N_{Qtz} and N_{Crn}. The calculation of the normative mineralogy does not consider other Al-Si-oxides such as andalusite or mullite, which may replace N_{Crn} and N_{Qtz} in these basalts. Iron loss is modelled by removing Fe^{3+} and Fe^{2+} at a constant Fe^{3+}/Fe_{tot} ratio (Table 4-1) from the glass. Initially, Fe-loss from the basalt glasses results in the disappearance of N_{Mt}, followed by N_{Hm} and N_{Ilm}. The remaining Ti in the bulk compositions is incorporated into N_{Ttn} (Figure 4-13d).

The normative mineral assemblages agree well with our observations of the basalt glasses reacted with $SO_{2(g)}$. The calculations predict that the loss CaO to the sulfate coating is accompanied by a decrease in the abundance of plagioclase and an increase in the abundance of some pyroxenes (Figure 4-13a). In the reacted tholeiitic basalt pre-equilibrated at NNO we observe the formation of Fe-Na-rich spherulites, surrounded by

Mg-rich crystalline material (Figure 4-9) that we interpret as the pyroxenes $NaFe^{3+}Si_2O_6$ (aegirine) and $MgSiO_3$ (enstatite or clinoenstatite), based on the nanoSIMS element maps. Silica is observed in the reacted tholeiitic basalt pre-equilibrated at NNO+1 (Figure 4-10), as predicted for the loss of CaO to the sulfate coating by the normative mineral calculations (Figure 4-13).

4.5.4 Implications for natural systems

The reaction between $SO_{2(g)}$ and Fe-bearing silicate materials occurs in large volcanic eruptions (Ayris et al., 2013; Maters et al., 2016). The most commonly observed sulfate phase on volcanic ash formed via the reaction with $SO_{2(g)}$ is anhydrite (Ayris et al., 2013; Barone et al., 2016). Careful investigation of salts on volcanic ash particles has shown a more diverse assemblage of sulfates. For example, sulfates observed on volcanic ash particles from the Eyjafjallajökull (Iceland) eruption in 2010, determined by leachate analysis, include epsomite ($MgSO_4 \cdot 7H_2O$), melanterite ($FeSO_4$), hydrated thenardite ($Na_2SO_4 \cdot 10H_2O$) and minor arcanite (K_2SO_4) (Gislason et al., 2011). This agrees very well with the range of phases that we observed in the experiments (Figure 4-1). We did not observe K_2SO_4 in our experiments, but its presence on the reacted volcanic ash particles from Eyjafjallajökull may be due to the higher K-concentration in the basalt or sublimation from the volcanic gas (Gislason et al., 2011) compared to our tholeiitic experimental glass compositions. We recommend that the investigation of freshly sampled and unaltered volcanic ash should include mineralogical methods such as Raman spectroscopy to identify the minerals on ash surfaces routinely. This would complement the more commonly applied bulk chemical analysis of materials dissolved from ash surfaces (Delmelle et al., 2018).

The experimental results presented in this study were obtained from reaction experiments with pure $SO_{2(g)}$. As discussed above the effective oxygen fugacity in this gas is in the hematite stability field just above the magnetite-hematite mineral buffer. Consequently, the observed Fe-oxide in the reaction products is Fe_2O_3. Figure 4-14 shows how varying fugacities of $O_{2(g)}$ and $SO_{2(g)}$ affect the stabilities of Fe-oxides, Fe-sulfides, Fe-sulfate and native Fe in the system Fe-S-O. The fugacities fO_2 and fSO_2 vary extensively across different planetary bodies in the solar system. For example, the low oxygen fugacity of a lunar volcanic gas of IW-2 to IW prohibits the stability of Fe-oxides, whereas Fe-sulfides are stable. Similarly, the more reducing conditions on Mercury are favorable to the formation of sulfides in reactions between silicates and S-rich volcanic gases.

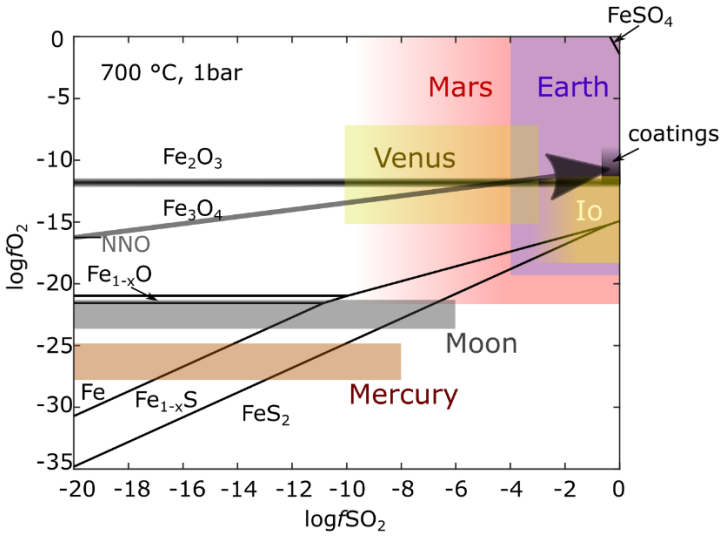

Figure 4-14: Phase relationships in the system Fe-S-O as a function of fSO_2 *and* fO_2 *at 700 °C and 1 bar, modified after Renggli & King (2018). The* $SO_{2(g)}$ *and* $O_{2(g)}$ *fugacities in hot volcanic and atmospheric gases of different planetary bodies are marked in color. Blue: Earth (Carmichael, 1991; Ballhaus, 1993; Oppenheimer et al., 2011); orange: Venus (Fegley et al., 1997; Vandaele et al., 2017); red: Mars (Hirschmann and Withers, 2008; Gaillard and Scaillet, 2009; Gaillard et al., 2013; Franz et al., 2018); yellow: Io (Zolotov and Fegley, 1999; Zolotov and Fegley, 2000); grey: Moon (Rutherford and Papale, 2009; Renggli et al., 2017); brown: Mercury (Kerber et al, 2009; Zolotov, 2011; McCubbin et al., 2012). The long arrow indicates the experimental reaction progress from the pre-equilibrated redox state around NNO to the more oxidized coatings.*

The surface of Mercury is particularly rich in S, with up to 4 wt.% (Nittler et al., 2011). This high S abundance coincides with the occurrence of flood basalts, pyroclastic deposits and compound volcanoes (Kerber et al., 2011; Denevi et al., 2013; Rothery et al., 2013). Sulfur-rich gases and these basaltic rocks were possibly erupted simultaneously, allowing gas-solid reactions, which may have formed a range of different sulfide reaction products which contribute to today's regolith on Mercury. Similarly, a broader range of fO_2 and fSO_2 is necessary in future experiments to investigate gas-solid reactions at conditions pertinent to Venus, Mars and Io (Figure 4-14).

Our experiments revealed a diverse mineral assemblage of phases formed in reactions between $SO_{2(g)}$ and basaltic glasses including $CaSO_4$, $MgSO_4$, Na_2SO_4, Fe_2O_3, TiO_2, pyroxenes and SiO_2 crystallites in the glass substrates. This is in contrast to previous experimental studies, which observed a prevalence of $CaSO_4$ as the sole or dominant reaction product in reactions between $SO_{2(g)}$ and silicate glasses (Renggli et al., in prep.; Ayris et al., 2013). The experiments reveal complex element mobility in glasses by trapping mobile chemical elements in surface coatings and nucleated phases in the modified glasses. To explain what controls the movement of different monovalent and divalent cations to the glass surface in reactions with $SO_{2(g)}$ a better understanding of the complex element mobility in glasses is necessary.

5 SO_2 gas reactions with silicate glasses

This chapter is accepted in *Reviews in Mineralogy and Geochemistry*:

Renggli C.J., King P.L. (2018) SO_2 gas reactions with silicate glasses. Reviews in Mineralogy and Geochemistry, 84, 229–255.

I wrote the majority of this chapter and chose the topics for the discussion. King contributed to the discussion and interpretation, edited and corrected the manuscript.

5.1 Introduction

Sulfur dioxide ($SO_{2(g)}$) is an important gas species in most common volcanic settings on Earth including subduction zones (Shinohara, 2013). The relative abundances of $SO_{2(g)}$ may vary at a volcano over time with the highest rates of $SO_{2(g)}$ emissions occurring during eruptive degassing and lesser amounts emitted continuously during quiescent degassing, resulting in a large total amount of $SO_{2(g)}$ integrated over time of the order of 10 Mt/a (McCormick et al., 2013; Shinohara, 2013; Henley and Hughes, 2016). Much of the emitted $SO_{2(g)}$ is released at high temperatures. For instance, gas mixtures sampled at the highest temperature volcanic vents reach 1085 °C at Erta Ale volcano and these are the most likely to be representative of the volcanic gas phase (de Moor et al., 2013).

$SO_{2(g)}$ is the most abundant of the corrosive gases at volcanoes (Oppenheimer et al., 2014). In the 1970's, thermodynamic models were used to predict that $SO_{2(g)}$ reactions with silicates form sulfate and reduced sulfur (Gooding, 1978; Burnham, 1979). This was later shown experimentally through reactions of silicates and carbonates with $SO_{2(g)}$ (Fegley and Prinn, 1989; Burnett et al., 1997). When $SO_{2(g)}$ reacts with silicates it covalently binds to the solid surface to build up a surface coating (Henley et al., 2015). In this manner, the $SO_{2(g)}$ reaction fundamentally differs from ionic reactions with some of the other species common in volcanic settings such as H_2O-rich fluids (e.g. Oelkers and Schott, 2009) or carbon dioxide (DePaolo and Cole, 2013). Other species common in volcanic gases such as fluorine and chlorine are also important (Delmelle et al., 2018; Henley and Seward, 2018), but sulfur gases have particularly interesting properties because sulfur is a multivalent element. Several valence states are involved in $SO_{2(g)}$ reactions with aluminosilicate glasses (S^{-2}, S^{-1}, S^0, S^{4+} and S^{6+}). These different species add complexity to the reactions because they may affect the valence state of other multivalent cations in the solid (e.g., $Fe^{0/2+/3+}$, $Ti^{3+/4+}$, $Cr^{2+/3+}$, $V^{2+/3+/4+/5+}$, $Eu^{2+/3+}$).

Gaseous sulfur dioxide has been detected on a number of other planetary bodies. For example, on Jupiter's moon, Io, $SO_{2(g)}$ is emitted by large explosive eruptions and contributes to a transient S-rich atmosphere (Pearl et al., 1979; Kumar, 1985; Lellouch et al., 1996; McGrath et al., 2000; Spencer et al., 2000; Doute, 2002; Moses et al., 2002). $SO_{2(g)}$ occurs as a minor volcanogenic gas species in the atmosphere of Venus, where it may play an important role in the alteration of the planet's surface (Zolotov, 2018). On Mars, $SO_{2(g)}$ has not been observed directly, but the regolith and dust are rich in oxidized sulfur (e.g., Berger et al., 2016), suggesting that past volcanic eruptions were rich in $SO_{2(g)}$ (Gaillard and Scaillet, 2009; King and McLennan, 2010). Because $SO_{2(g)}$ dominantly forms in volcanic eruptions, it may be a good proxy for past or ongoing volcanic activity in planetary and exoplanet atmospheres (Hu et al., 2013; Misra et al., 2015). Reactions between gases, including $SO_{2(g)}$, and solids occurring in the solar system are discussed by Zolotov (2018).

In this chapter we discuss observations from gas-solid experiments where $SO_{2(g)}$ is reacted with aluminosilicate glasses. The understanding of $SO_{2(g)}$ reactions with glasses is important because of their ubiquity in volcanic systems (Ayris et al., 2013; Delmelle et al., 2018) and their abundance on planetary surfaces due to impact processes (Schultz and Mustard, 2004). We discuss the chemistry, mineralogy and texture of the reaction products, as well as provide insights into reaction mechanisms.

5.2 Glass properties

Silicate glasses are an ideal substrate material to study gas-silicate reactions because they are amorphous, which avoids complications from mineral orientation effects. To provide context for $SO_{2(g)}$ reactions with glass, we refer the reader to King et al. (2018) for a review of the basic reactions between $SO_{2(g)}$ and silicate minerals.

Aluminosilicate glasses are dominated by Si^{4+} and Al^{3+} cations that are tetrahedrally-coordinated by O^{2-} anions and termed tetrahedral cations (T) (Mysen and Richet, 2005). The T cations (in some cases including Ti^{4+} and Fe^{3+}) form a range of Si-O units (e.g., $[SiO_4]^{4-}$, $[Si_2O_7]^{6-}$, $[Si_6O_{18}]^{12-}$, $[Si_4O_{11}]^{6-}$, $[Si_2O_5]^{2-}$, $[SiO_2]$). These units are polymerized to form a network linked by a distribution of bond lengths and bond angles with a lack of long-range order. Monovalent and divalent cations (e.g., Na^+, K^+, Mg^{2+} and Ca^{2+}) have a role as network modifiers and/or charge compensators and do not contribute to the tetrahedral network (Mysen et al., 1982; Mysen and Richet, 2005).

The structural arrangement of atoms in a silicate glass is of great importance for the physical properties, including structure and degree of polymerization, viscosity, glass

transition temperature and diffusion rates (Dingwell, 2006). The main variable affecting glass properties is the concentration of network-forming cations, the most abundant of which are Si^{4+} and Al^{3+}. Network-forming cations exhibit a low mobility and their self-diffusivities are a function of the melt's viscosity and can be described by the Eyring equation (Dingwell, 1990). Relative to network formers, network modifiers have diffusivities that are orders of magnitude higher (Dingwell, 1990). More recently, the identification of charge compensating cations (e.g. Na, K, Ca) in simple glasses has shown that these elements may move in channels, which allows a more complex element mobility (Le Losq et al., 2017).

Temperature plays an important role in element mobility (Zhang, 2010) and in glasses, the glass transition temperature is a key reference point. The glass transition is the temperature range below which the amorphous structure is locked in and becomes unrelaxed and the material behaves as a solid. As a consequence, configurational changes do not occur on a measurable scale below the glass transition temperature and the energetically most favorable state is not reached (Mysen and Richet, 2005). The glass transition is a function of the relaxation of the network of Si-O units and hence of the lifetime of the bonds (e.g., Webb, 1997). The temperature range from 600 to 850 °C, at which $SO_{2(g)}$ reactions with silicate glasses have been performed experimentally (Table 5-1 and 5-2), is near the glass transitions of these systems (Martens et al., 1987; Knoche et al., 1992). Consequently, minor changes in the temperature conditions may affect the reaction rates and mechanisms considerably when the glass transition is crossed.

5.3 Experimental techniques

Experiments reacting $SO_{2(g)}$ with silicate glasses have been performed with both open and closed systems. Early experiments were performed in closed systems, in respect to the glass, in sealed silica tubes where $SO_{2(g)}$ was produced via the decomposition of $K_2S_2O_8$. The decomposition of this compound forms $SO_{2(g)}$ and $O_{2(g)}$ (Johnson and Burnett, 1993; Li et al., 2010) via Equation 5-1:

$$K_2S_2O_{8(s)} \rightarrow K_2O_{(s\ or\ g)} + 2SO_{2\ (g)} + 1.5O_{2(g)} \qquad \textit{Equation 5-1}$$

In reaction 1, K_2O occurs as either a solid or gas species dependent on temperature and pressure (e.g., Muan and Osborn, 1965). As the sample is cooled, solid K_2O may be deposited in the tube and on the silicate sample. Removal of K_2O as a solid from the experimental system, will tend to favor the reaction:

$$2SO_{2\ (g)} + O_{2(g)} \rightarrow 2SO_{3(g)} \qquad \textit{Equation 5-2}$$

This reaction lowers the fugacity of $SO_{2(g)}$, creating an environment where $SO_{3(g)}$ is an important reactant and the reaction products are changed. Thus, to examine pure $SO_{2(g)}$, it is necessary to trap or remove the $O_{2(g)}$ if the gases are produced via Equation 5-1 (Burnett et al., 1997).

Monitoring of the $SO_{2(g)}/SO_{3(g)}$ in the gas phase is important because $SO_{3(g)}$-mineral reactions follow the general form:

$$SO_{3(g)} + MO\_silicate \rightarrow MSO_4 + silicate \qquad \textit{Equation 5-3}$$

where M is a cation (e.g., Ca, Mg, Na, and Fe) and S remains in the 6+ state. In contrast, in $SO_{2(g)}$-mineral reactions, where S^{4+} in the gas phase disproportionates into 6+ and reduced sulfur (e.g., S^{2-}, a reduced sulfur radical, S^- or S^0), the reaction follows the form (modified after Burnham, 1979):

$$2SO_{2\,(g)} + MO\_silicate \rightarrow MSO_4 + S_{reduced} + silicate(+oxide) \qquad \textit{Equation 5-4}$$

To avoid the issues associated with $K_2S_2O_8$ decomposition, recent experiments used commercial $SO_{2(g)}$ as the gas source (Tables 5-1 & 5-2; King et al., 2018 and references therein). A Gibbs Free Energy minimization calculation reveals that $SO_{2(g)}$ is not pure at equilibrium conditions, even under the assumption that the gas source is pure. We used the software package HSC8 by Outotec, which is based on the JANAF database (Chase, 1998). The most abundant trace gas species in equilibrium with $SO_{2(g)}$ are $SO_{3(g)}$, $SO_{(g)}$ and $S_{2(g)}$ (Figure 5-1). All trace species have abundances of less than 10^{-5} mole fractions in the temperature range relevant to studies involving the reaction of $SO_{2(g)}$ (600-850 °C, see Tables 5-1 & 5-2). The oxygen fugacity of this gas mixture is approximately at the magnetite-hematite buffer in the temperature range relevant to the experiments discussed here. It has been noted that the equilibration of the gas species in this system ($SO_{2(g)}$, $SO_{3(g)}$, $O_{2(g)}$) is relatively slow (Luthra and Worrell, 1979). Therefore, actual abundances of trace gases may be even lower in these experiments because at the high flow rates of 20-50 cm^3 per minute, equilibrium speciation in the gas phase may not be attained. Changes in the composition of the gas during the reaction have not been determined in any experiment and the oxygen fugacities have not been measured.

Solid glass for experiments is best polished prior to reactions with $SO_{2(g)}$ so that the run products are easier to examine and to minimize artefacts. For example, gas-solid reactions are sensitive to the surface area, and so cracks and scratches may result in a higher degree of reaction. Furthermore, irregularities on the surface may act as nucleation points for sulfate formation on the surface (Figure 5-2, Burnett et al., 1997). Additional details on experimental setups are given in King et al. (2018 and references therein).

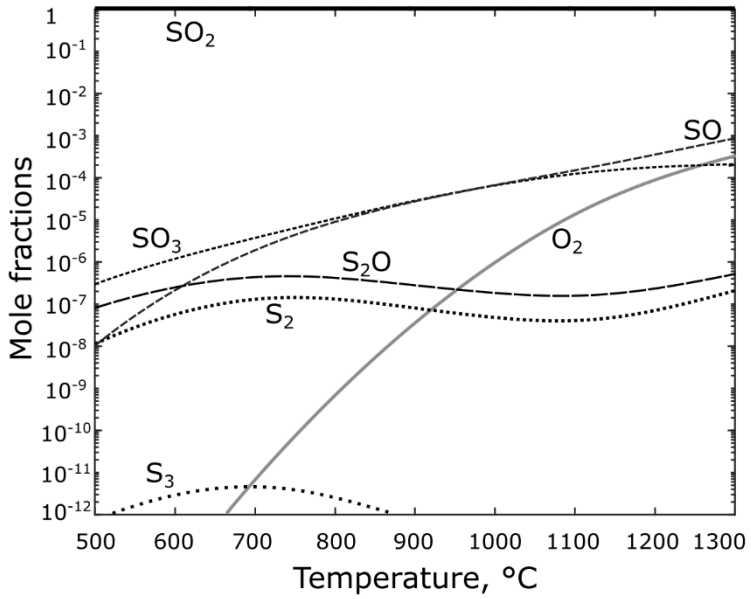

Figure 5-1: Equilibrium speciation of $SO_{2(g)}$ at 1 bar and temperatures from 500 to 1300 °C. The speciation was calculated using a Gibbs Free Energy minimization approach based on the JANAF database (Chase 1998) using the program HSC8 from Outotec. $SO_{2(g)}$ dissociates to $SO_{3(g)}$, $SO_{(g)}$, $O_{2(g)}$ and sulfur allotropes, the most prominent of which are $S_{2(g)}$ and $S_{3(g)}$. The mole fraction of $O_{2(g)}$ is equivalent to its oxygen fugacity (fO_2) under the condition of ideal gas behavior (see also Zolotov & Fegley, 1999).

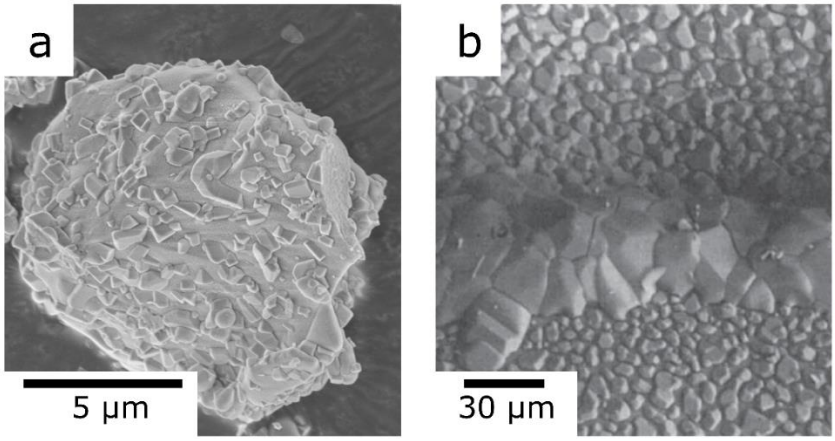

Figure 5-2: Scanning electron microscopy images of surface coatings (view from top) formed in reactions between $SO_{2(g)}$ and glasses. a) Well crystallized platy $CaSO_4$ crystals formed on a tephrite glass reacted for 1 hour at 800 °C with gas mixture of 1% $SO_{2(g)}$, air and He gas (Figure provided by Paul Ayris, Ayris et al., 2013). b) Discontinuously distributed Na_2SO_4 grains on a soda-lime glass reacted with $SO_{2(g)}$ for 21 days at 600 °C. The large crystals cover a scratch in the unreacted glass surface, which resulted in a higher surface area and an associated higher degree of reaction (Used by permission of the American Geophysical Union, from Burnett et al., 1997, Journal of Geophysical Research, Vol. 102, Fig. 5, p. 19378).

Table 5-1: Overview of experiments between $SO_{2(g)}$ and Fe-free glasses and the observed reaction products in the coatings.

	Douglas & Isard 1949	**Johnson & Burnett 1993**	**Burnett et al. 1997**				**Renggli 2018**						**Henley et al. 2015**
Method	SO_2 furnace	sealed glass capsule	sealed glass capsule				SO_2 furnace						SO_2 furnace
Gas source	Gas bottle	$K_2S_2O_8$	$K_2S_2O_8$				Gas bottle						Gas bottle
Gas	0.02-1% SO_2, air, ±water	$SO_2 + O_2$	SO_2				SO_2						SO_2
Temp. °C	300-1000	850	650	750	850		600		700		800		700
Time (h)	1min-2d	168	576	1366	168	624	1	24	1	24	1	24	72
Glass													
Albite							Na_2SO_4						
$Ab_{95}An_5$							$CaSO_4$						
$Ab_{73}An_{27}$													$CaSO_4$
Soda-lime	Na_2SO_4	Na_2SO_4	Na-S		Na_2SO_4								
Albite-orthoclase		K-(Na)-Al-sulfate		Na-S	x	Na-S							
$Ab_{80}An_{10}Di_{10}$		$CaSO_4$, Na_2SO_4 with Ca, K and Al			Na-Ca-sulfate								
Anorthite							$CaSO_4$						
$An_{15}Di_{85}$							$CaSO_4$, $MgSO_4$				$CaSO_4$		
$An_{36}Di_{64}$													
$An_{48}Di_{52}$													
Diopside							$CaSO_4$						
Fe-free basalt									$CaSO_4$, $MgSO_4$				

x: indicates an experiment which did not result in any observed reaction product on the surface of the glass

Table 5-2: Overview of experiments between $SO_{2(g)}$ with Fe-bearting glasses and their reaction products in the coatings

	Johnson & Burnett 1993	**Burnett et al. 1997**		**Ayris et al. 2013**			**This work**	**Palm et al. this volume**
Experimental method	sealed glass capsule	sealed glass capsule		gas-mixing furnace			SO_2 furnace	SO_2 furnace
Gas source	$K_2S_2O_8$	$K_2S_2O_8$		Gas bottle			Gas bottle	Gas bottle
Gas	$SO_2 + O_2$	SO_2		1 mol. % SO_2, 70 mol. % air, 29 mol. % He			SO_2	SO_2
Temperature °C	850	850		0-300	300-600	600-800	700	800
Time (hours)	168	168	624	30s - 1h			24	1
Glass								
Chondrule mesostasis	$CaSO_4$, Na-Mg-Ca-sulfate	$CaSO_4$						
Tephrite				x	$CaSO_4$, Na_2SO_4	$CaSO_4$		
Phonolite				x	$CaSO_4$			
Dacite				x				
Rhyolite				x		$CaSO_4$		
Tholeiitic basalt NNO-1.5							$CaSO_4$, $MgSO_4$, Fe_2O_3	
Tholeiitic basalt NNO0							$CaSO_4$, $MgSO_4$, Na_2SO_4, Fe_2O_3, Fe-Ti-oxide	
Tholeiitic basalt NNO+1							$CaSO_4$, Na_2SO_4, Fe_2O_3, Fe-Ti-oxide	
Alkali basalt IW								Glauberite, $CaSO_4$, Fe_2O_3, Fe_3O_4, Fe-Ti-oxide
Glass + crystals								
Obsidian	K-Na-Al-sulfate, trace Fe	Fe-sulfate						
Kilauea basalt 1971	$CaSO_4$, Na-Ca-Mg-sulfate, trace K, Fe	x						

x: indicates an experiment which did not result in any observed reaction product on the surface of the glass

5.4 $SO_{2(g)}$ reactions with Fe-free silicate glasses

As indicated above, sulfur has many different valence states. This means that there can be considerable complexity in reactions between $SO_{2(g)}$ and multivalent cations, such as Fe, the most abundant multivalent element in most magmatic systems (Schreiber, 1987). We therefore separate our discussion of experiments into either Fe-free or Fe-bearing glasses.

5.4.1 Mineralogy of phases formed on Fe-free glass substrates

Table 5-1 summarizes experiments on $SO_{2(g)}$ reacted with synthetic Fe-free glasses from both the literature and our laboratory. Compositions include glasses in the albite-anorthite-diopside (Ab-An-Di) system, Fe-free basalt, soda-lime (Na-Ca-silicate) glass, and albite-orthoclase glass. Temperature conditions range from 600-850 °C and experimental durations vary considerably from 1 to1366 hours. The run products include Na-, Ca- and/or Mg-sulfates.

The observation and determination of the mineralogy of products formed in $SO_{2(g)}$ experiments is challenging due to small grain sizes (Dalby et al., 2018; Palm et al., 2018). Reaction products may have grain diameters of tens of nanometers, which are far below the resolution of conventional methods such as Raman spectroscopy or energy dispersive X-ray spectroscopy. When the reaction products are thinner than the analytical volume of the method used, the signal includes both the reaction product and the silicate substrate. Such reaction products require high resolution techniques such as transmission electron microscopy, atom probe microscopy, surface sensitive analysis (e.g., X-ray photoelectron spectroscopy) or thin film approaches such as grazing angle techniques or depth profiling (Dalby et al., 2018; Palm et al., 2018).

As the majority of reaction products from $SO_{2(g)}$-silicate reactions are sulfates, a brief overview of sulfate phase relations is necessary (see also King et al., 2018 and references therein). At elevated temperatures, sulfates ultimately decompose into oxides and $SO_{3(g)}$ (Stern, 2001). For example, $MgSO_4$ decomposes at temperatures above 900 °C and $CaSO_4$ above 1200 °C (Rowe et al., 1967; Du, 2000). In addition to thermal decomposition some sulfates may also vaporize at high temperatures (e.g. $Na_2SO_{4(s)} = Na_2SO_{4(g)}$) (Stern and Weise, 1966). At 600-800 °C, at which most $SO_{2(g)}$-reaction experiments have been performed (see Table 5-1 and 5-2), some of the sulfates form limited solid solutions. The degree of solid solubility of Na_2SO_4 in $CaSO_4$ is poorly understood as experimental data is limited. In turn, Na_2SO_4 dissolves up to 35 mol.% of $CaSO_4$ and $Na_2Ca(SO_4)_2$ (glauberite) also forms (Freyer and Voigt, 2003). Similarly, it also dissolves $MgSO_4$ although in a more limited temperature range. Na_2SO_4 and K_2SO_4 form a complete solid solution from 600 to

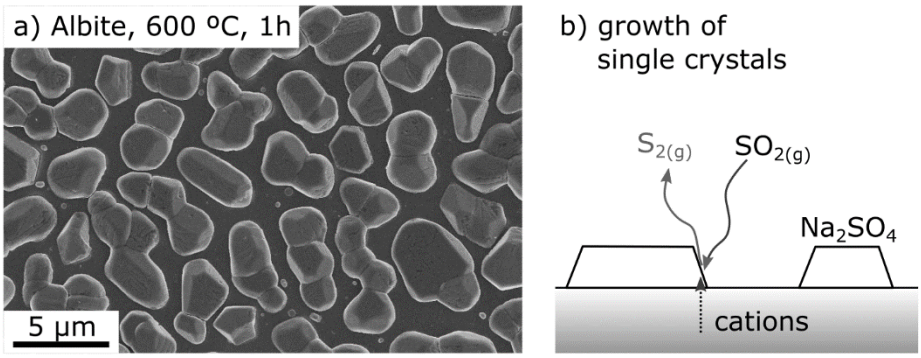

Figure 5-3: Discontinuous sulfate coating on glass surfaces reacted with $SO_{2(g)}$. a) SEM image (view from top) of the discontinuous Na_2SO_4 coating on an albite glass surface reacted with $SO_{2(g)}$ at 600 °C for 1 hour. The sulfate grains show facets. Individual crystals are commonly connected to one or more surrounding grains forming small clusters. b) A schematic cross-section showing how in the case of discontinuous coatings parts of the silicate glass surface remain exposed to the gas phase allowing the reaction to proceed. In this type of reaction, the diffusion of cations in the glass to the surface is the rate controlling mechanism.

800 °C. $CaSO_4$ and $MgSO_4$ do not form solid solutions. Instead, the binary system includes the phase $CaMg_3(SO_4)_4$ (Rowe et al., 1967; Du, 2000); this phase has not been reported in any $SO_{2(g)}$ experiment (Table 5-1). In these experimental studies the reporting of sulfates has generally identified only the pure end-member phases.

The interpretation of sulfate textures formed in $SO_{2(g)}$ reactions can be challenging due to the hydrophilic nature of the materials. Magnesium sulfate in particular readily hydrates, forming a large range of phases with various degrees of hydration (Wang et al., 2006). It is therefore crucial to protect experimental samples from water vapor after the reaction (e.g., in a desiccator or under controlled atmosphere). Even so, sulfates textures may evolve with time during sample storage and hydrate in air (Dalby et al., 2018).

5.4.2 Textures of sulfate coatings on Fe-free glass substrates

The textures of sulfates observed on Fe-free glasses vary strongly with the glass composition and experimental conditions. The sulfates form on the surfaces and are coating the glasses. In the oxidation community these types of reaction products are termed scales (Birks et al., 2006), but we use the term coating, which is consistent with the use in the geological literature. Sulfate surface coatings fall into two distinct categories of continuous and discontinuous coverage. Electron microscopy images of these textures are shown in Figures 5-2, 5-3, 5-4 and 5-5. Discontinuously distributed sulfates commonly display distinct crystal facets (Figure 5-2, 5-3). A secondary electron images of a sulfate texture with discontinuous coverage is shown from an experiment with albite glass (Figure 5-3a, 600 °C, 1hour).

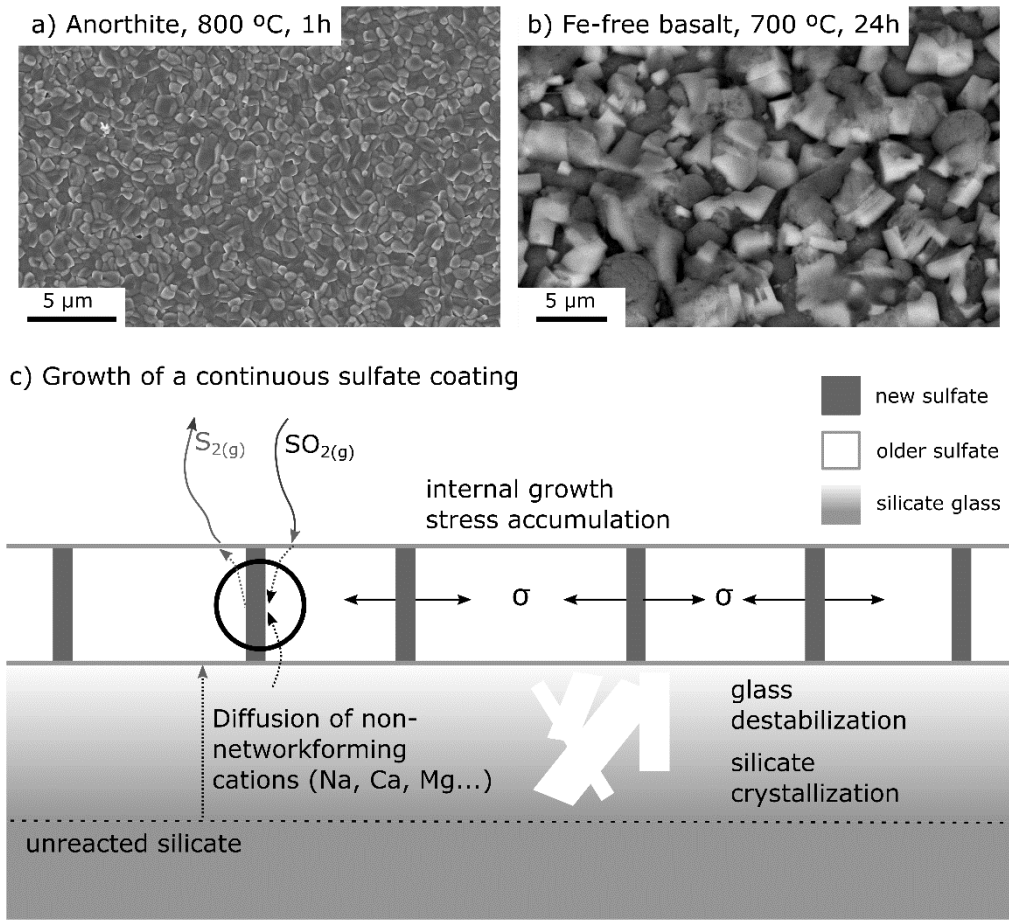

Figure 5-4: Continuous sulfate coatings observed on the surfaces of some Fe-free glasses. a) SEM image of the anhydrite coating on an anorthite glass surface reacted with $SO_{2(g)}$ at 800 °C for 1 hour. b) Backscattered electron image of the coating on an Fe-free basalt glass reacted with $SO_{2(g)}$ at 700 °C for 24 hours. The brighter euhedral grains are anhydrite, whereas the darker material is MgSO4 which was partially hydrated in air after the experiment. c) Schematic drawing of the reaction forming continuous coatings. After initial coating the glass is no longer directly exposed to the gas, such that an additional mechanism is required to transport the gas and/or the cations through the coating for ongoing sulfate formation. When growth occurs within the coating the grains accumulate stress which can result in the deformation of the coating (see Figure 5-5). The outward diffusion of cations results in a depletion in the glass which can cause destabilization, and in some nucleation and crystallization near the surface.

This type of discontinuous coating occurs on albite glasses reacted with $SO_{2(g)}$ at 600-800 °C and experimental durations of 1 hour and 24 hours (Table 5-1). Similarly well-defined sulfate crystals have been observed on soda-lime and obsidian glasses (Burnett et al., 1997). The mechanism of sulfate growth in the case of discontinuous coatings is relatively simple, because the glass surface remains exposed to the gas throughout the reaction as illustrated in Figure 5-3.

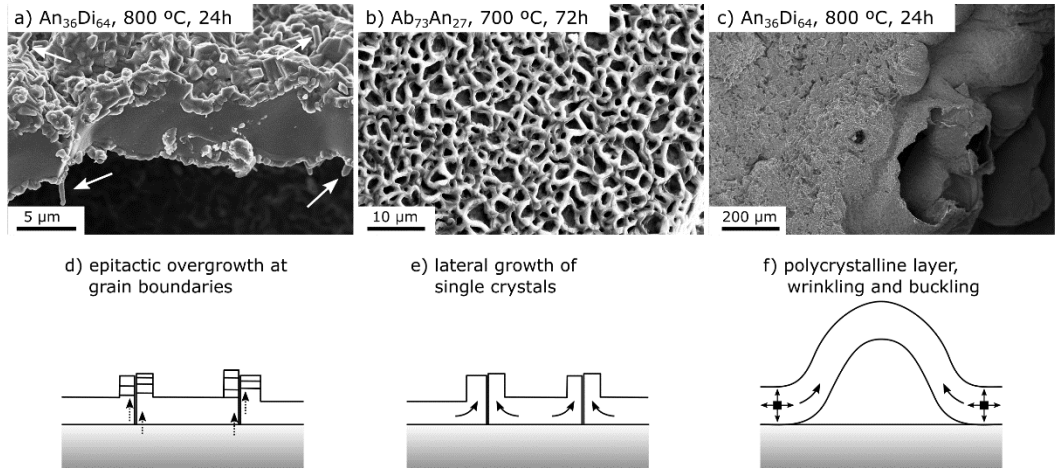

Figure 5-5: Images a, b and c show SEM images of deformed continuous anhydrite coatings on Fe-free glasses. The coatings shown in a and c were formed on the eutectic An_{36}-Di_{64} glass reacted at 800 °C for 24 hours. Image b shows the coating of anhydrite on an $Ab_{73}An_{27}$ glass reacted at 700 °C for 24 hours. The drawings d, e and f schematically represent how the respective textures imaged in a, b and c developed. All of the textures are the result of stress accumulation within the coating due to internal sulfate growth as shown in Figure 5-4. In the first case, whiskers can be formed by epitactic overgrowth at grain boundaries and triple junctions (a and d). In the second case, laterally expanding crystals in the coating have bent upwards at grain boundaries resulting in the imaged "chicken-wire" texture (b and e). A third texture type forms as thick polycrystalline sulfate layers continue to grow they detach from the glass surface and wrinkle and buckle (c and f).

In experiments where the temperatures approach the thermal stability of the sulfates, the individual sulfate "islands" are poorly crystallized and can be polycrystalline and flakey in texture (Johnson and Burnett, 1993). Formed in sealed silica glass tubes, such sulfates may be the product of deposition from the gas phase or the quench product of a sulfate melt (Johnson and Burnett, 1993). In experiments where these textures formed in a gas-furnace under a high $SO_{2(g)}$ flux, and at temperatures below the liquidus temperature of the sulfate, the formation as quench products is not possible and the textures are likely due to very high sulfate nucleation rates which exceed the rates of grain growth.

Continuously-distributed sulfate coatings occur on a range of Fe-free experiments, including Fe-free basalt and glasses in the Ab-An-Di ternary system. Anhydrite is commonly distributed in a single layer of equigranular columnar grains, such as on anorthite glass (Figure 5-4a, 800 °C, 1h). For Fe-free basalts, the surface material consists of a mixture of $CaSO_4$ and $MgSO_4$. The back-scattered electron image (Figure 5-4b) of Fe-free basalt glass (700 °C, 24h) shows areas of darker $MgSO_4$, partially hydrated after the experiment, and rhombohedral anhydrite grains. The textures of the continuous coatings have many similarities with coatings formed during the oxidation in a range of systems, such as aluminum oxide scales on metal alloys (Hsueh and Evans, 1983; Evans et al., 1983;

Tolpygo and Clarke, 1998a, b; Chason et al., 2013). A comparison of the sulfate coatings with extensively studied oxide coatings is valuable as it allows an interpretation of the mechanism that form these coatings.

In experiments where continuous coatings form, the silicate glass is no longer directly exposed to the gas after the initial formation of the sulfate coating. Ongoing reaction requires a transport mechanism through the coating. Consequently, there are three possible growth pathways. First, if the reactive gas diffuses very fast through the sulfate, the reaction occurs at the interface between the sulfate and the silicate glass, below the coating. This type of mechanism commonly occurs during the oxidation of metals, where oxygen migrates through the oxide coating to the interface between the coating and the pristine metal (Evans et al., 1983). If a similar mechanism operates in $SO_{2(g)}$-substrate reactions we would expect a continuous outward displacement of the previously formed sulfate. Such an outward expansion would result in cracks in the coating around edges of the silicate glasses, which are not observed in any experiment. Second, if the cations diffuse rapidly through the coating, growth would occur at the surface interface between the sulfate and the gas. In this case growth would occur continuously across the surface and deformation of the coating would be avoided. This texture has not been observed in any experiments recorded in the literature. In a third possible mechanism, cations and the gas phase migrate at a comparable rate through the sulfate layer. In this case the reaction and growth occur within the sulfate coating, most easily at grain boundaries (Figure 5-4c). This growth mechanism results in the accumulation of stress in the coating. The dissipation of this stress results in three different possible deformation textures (Figure 5-5). First, because transport of cations and $SO_{2(g)}$ most easily occurs along grain boundaries (Figure 5-4c), newly-formed sulfate would accumulate at grain boundaries preferentially (Figure 5-5d). This epitactic overgrowth would continue to such an extent that it results in the formation of protrusions such as whiskers and hillocks. These features are indicated in Figure 5-5a for a reacted eutectic An-Di glass. The formation of whiskers and hillocks extending from coatings is also observed in thin film materials where strain is localized, and the growth of materials is focused outwards by diffusive transport. For example, tin whiskers are commonly observed growing out of intermetallic coatings (Sobiech et al., 2009; Chason et al., 2013). Second, where grains extend laterally and stress is not focused on a small area, individual sulfate crystals can be bent upwards at grain boundaries to form a chicken-wire texture (Figure 5-5b and e) (Tolpygo and Clarke 1998b; Clarke, 2003). Third, entire polycrystalline sulfate layers can wrinkle and buckle due to internal stress and expansion (Figure 5-5c and f). This type of texture occurs when the rate of growth is very high (Clarke, 2003). For example, such a coating is shown in Figure 5-5 with extensively deformed

buckles. Within experimental durations, the volume between the buckled coatings and the substrate is not infilled with additional sulfate material, although this may occur over much longer durations. Similar deformation processes resulting in buckled coatings are observed in oxide coatings formed in gas-alloy reactions (Evans et al., 1983; Clarke, 2003; Birks et al., 2006). The presence of diverse deformation textures formed by continuous sulfate coatings on glasses reacted with $SO_{2(g)}$ (Figure 5-5) strongly implies that these coatings indeed grow internally as illustrated in the schematic drawing in Figure 5-4c. Independent of the mechanisms by which the sulfates grow, the reaction results in a volume increase in the run products. In natural sub-volcanic systems this may result in the filling of veins as the gas passes through and reacts with the surrounding rocks (Henley et al., 2017).

In summary, in the case of continuous sulfate coatings $SO_{2(g)}$ and cations need to migrate into the sulfate coating, where new sulfate forms preferentially at grain boundaries (Figure 5-4). This process results in an increase of the coating volume and commonly causes deformation in the coating. Deformation textures observed in experiments include whiskers, chicken-wire textures, and buckling and wrinkling of the coating (Figure 5-5). The degree of deformation increases with increasing amount of sulfate formed.

5.4.3 Compositional changes in the Fe-free glass substrate

The mineralogical investigation of the coatings formed by reactions of $SO_{2(g)}$ with Fe-free silicate glasses has shown that Ca-sulfates are the dominant reaction products. The observed variation of sulfate phases formed as a function of temperature and relative to the glass transition temperature underlines the importance of the role of the substrate composition on the overall reaction mechanism and reaction rates. For example, the sulfate reaction products have mole% Ca/(Ca+Mg) that generally exceed the mole% Ca/(Ca+Mg) in the reactant anorthite-diopside glasses ($(Ca/(Ca+Mg))_{diopside} = 0.5$, $(Ca/(Ca+Mg))_{anorthte} = 1$). In the anorthite-diopside system at 600 °C the sulfate reaction products are relatively enriched in Ca by 20-40%. At 800 °C, above the glass transition temperatures of all An-Di glasses except for the anorthite endmember, this fractionation effect is much stronger and only minor or trace amounts of Mg are detected in the sulfate reaction products. The mole% Ca/(Ca+Mg) at 800 °C is near 1 in the sulfate formed on all anorthite-diopside glasses. This means that Ca preferentially moves out of the glass to form the sulfates and Mg is relatively retained in the glass, as discussed further below.

The reaction of $SO_{2(g)}$ with a silicate glass requires the mobilization of alkali or alkaline earth metals to form sulfates at the reaction interface. As the relative abundances of Ca and Mg in the sulfate reaction products vary both with temperature relative to the glass transition and also with the composition of the unreacted glasses diffusional transport

mechanisms appear to be important rate controlling factors. The reaction at the surface causes chemical potential gradients which drive mass fluxes. As Ca moves to the surface, additional chemical potential gradients result in the interior of the silicate requiring charge compensation which causes compositional and structural changes, in some cases resulting in crystallization. If the diffusion of Ca is a rate-limiting factor of the overall reaction, then the rate of sulfate formation must also change with experimental duration. This change in the diffusivities of sulfate-forming cations with experimental duration is very poorly constrained and requires future experimental work.

The loss of charge-compensating cations and network-modifying cations from the glass to the surface may require charge balancing. In systems without multivalent elements available to change the valence state to accommodate a change in the electrochemical environment, charge balancing may occur via four different mechanisms. First, anions can co-diffuse with the outward fluxing cations. Second, charge compensation can occur via the counter diffusion of electron holes. Third, charge compensation can occur via the counter diffusion of negatively-charged sulfur. Fourth, Al^{3+} may adapt its coordination and partially become a network-modifier with five- and six-fold coordination (Neuville et al., 2006; Le Losq et al., 2014). There is much work to be done to demonstrate how these different charge balancing mechanisms behave in different materials.

Nucleation and growth of crystallites due to structural changes of the glass induce further chemical potential gradients and affect the diffusivities of the diffusing cations. The interplay of these processes during reactions of $SO_{2(g)}$ with the silicate surface can result in complex textures that reflect the ongoing nature of the reactions and may result in phase assemblages which are out of equilibrium, both in the surface coating and in the silicate. Crystallization in the substrate at the surface, in Fe-free glasses, has only been observed at or near the glass transition temperature. It has been documented in three experiments at 800 °C with diopside glass (T_g = 722 °C), $An_{15}Di_{85}$ glass (T_g = 729 °C) and $An_{48}Di_{52}$ glass (T_g = 760 °C), where diopside crystallized at the interface. When crystallization occurs at the reaction interface the overall reaction rate may be affected significantly and additional variables such as crystal structure, orientation and grain size distribution require consideration in the future (see King et al., 2018).

5.5 $SO_{2(g)}$ reactions with Fe-bearing glasses

5.5.1 Mineralogy of phases formed on Fe-bearing glass substrates

The reaction products formed on Fe-bearing glasses include $CaSO_4$, $MgSO_4$, Na_2SO_4, $Na_2Ca(SO_4)_2$, K_2SO_4, $Al_2(SO_4)_3$, $FeSO_4$, hematite, magnetite and Ti-bearing oxides (Table

5-2). These phases have been determined by a range of direct and indirect methods including SEM, Raman spectroscopy, X-ray photoelectron spectroscopy (XPS), Fourier transform infrared spectroscopy (FTIR), X-ray diffraction (XRD), transmission electron microscopy (TEM), nanoSIMS and leachate solution analysis (Johnson and Burnett, 1993; Burnett et al., 1997; Li et al., 2011; Ayris et al., 2013). Examples of these analyses are described in more detail in Dalby et al. (2018) and Palm et al. (2018).

Early experiments between $SO_{2(g)}$ and Fe-bearing glasses provided variable of results, in part due to Equation 5-2 listed above. Johnson and Burnett (1993) used a 1:1 mixture of $SO_{2(g)}$ and $O_{2(g)}$ that likely formed $SO_{3(g)}$ (Equation 5-2) compared to pure $SO_{2(g)}$ in a sealed silica tube used by Burnett et al. (1997). In the first case, the reaction products include a large range of different sulfates (Ca, Mg, Na, K, Fe and Al) in all three experiments, as summarized in Table 5-2.

The studies by Johnson and Burnett (1993) and Burnett et al. (1997) used the same glasses for their experiments, including a chondrule glass, obsidian and Kilauea basalt (Table 5-2). As described above, the presence of K-sulfate in some experiments by Johnson and Burnett (1993) is likely due to reaction with K from the starting $K_2S_2O_8$ used to produce the gas phase. Burnett et al. (1997) were able to demonstrate the presence of reduced sulfur using photoelectron spectroscopy (XPS) on experimental products of disproportionation reactions with pure $SO_{2(g)}$, but the sulfide phases were not directly determined. The experiments using pure $SO_{2(g)}$ resulted in significantly smaller amounts of reaction products, with $CaSO_4$ on the chondrule glass, very small amounts of Fe-sulfate on the obsidian and no detected reaction products on the Kilauea basalt (Burnett et al., 1997).

Ayris et al. (2013) used a gas mixture which is closer to a naturally occurring mixture in explosive volcanic eruptions, consisting of a small quantity of $SO_{2(g)}$, air and $He_{(g)}$. They used glass substrates with tephrite, phonolite, dacite, and rhyolite compositions. In the 600-800 °C range, $CaSO_4$ is the only phase observed on the surface of any of the glasses (Ayris, 2010; Ayris et al., 2013) (Table 5-2). At 300-600 °C, there was no detected reaction on the rhyolite glass yet the other glasses were coated with $CaSO_4$ and the tephrite glass also had minor amounts of Na_2SO_4. In the 0-300 °C range no reaction products were detected on any of the tested glass compositions after one hour.

On natural glasses, these authors found that the initial rates of reaction are very high, with sulfate detected by leachate analysis on the glass surfaces at 800 °C within 30 seconds. This high rate of $SO_{2(g)}$ uptake in the first minute is due to fast adsorption onto the surface. This is followed by lower reaction rates, which are controlled by diffusive transport of Ca^{2+} from the interior of the glass to the surface. Overall, the amount of reaction increases with the

Ca-concentration in the glass (Ayris et al., 2013). The textures observed by Ayris et al. (2013) on glasses reacted at 800 °C for 1 hour show discontinuously distributed, faceted $CaSO_4$ crystals with diameters ranging from few hundred nanometers to 5 μm. The textures are comparable to those observed on soda-lime, albite and diopside glass (see Figure 5-2 and 5-3; Burnett et al., 1997). The texture in Figure 5-2 also underlines the importance of polishing the glass surface exposed to the reacting gas. The presence of a scratch results in an increasing degree of nucleation and formation of sulfate (Figure 5-2; Burnett et al., 1997).

Li et al. (2010) used the same experimental setup as Johnson and Burnett (1993), conducting experiments with crystalline basalts. At 600 °C they observed $CaSO_4$, whereas at 850 °C they observed an assemblage of $CaSO_4$, $MgSO_4$ and Fe_2O_3 (Li et al., 2010). Similar multi-phase assemblages were observed on basalt glasses reacted with $SO_{2(g)}$ (Table 5-2).

$CaSO_4$ and Na_2SO_4 and Fe_2O_3 were the major products with lesser $MgSO_4$, Fe_3O_4 and Fe-Ti-oxides, in the case of both tholeiitic basalt glasses at 700 °C for 1 hour and 24 hours, and alkali basalt glass at 800 °C for 1 hour (Table 5-2). These tholeiitic basaltic glasses included a series where the Fe^{3+}/Fe^{2+} was set at a range of values by pre-equilibrating the melt at different fO_2 conditions (Dufresne et al., 2015). The unreacted glasses had molar $Fe^{3+}/Fe^{2+} = 0.08$ (pre-equilibrated 1.5 log-units in fO_2 below the Ni-NiO buffer (NNO-1.5)) to 0.54 at one log-unit in fO_2 above the Ni-NiO buffer (NNO+1) (Dufresne et al., 2015).

The coating mineral assemblages depend on the Fe^{3+}/Fe^{2+} ratios in the unreacted glasses, the temperature and the experimental duration. Examples of the textures formed at 700 °C under a stream of $SO_{2(g)}$ for 24 hours are shown in Figure 5-6. In all three examples, $CaSO_4$ is the predominant sulfate phase in the coatings. The glass pre-equilibrated at NNO-1.5 is continuously coated with a mixture of Ca- and Mg-sulfate and very small sub-micron Fe-oxides. In the short experiment of 1 hour, the coating also included some Na_2SO_4. Glasses pre-equilibrated at NNO and NNO+1 show large $CaSO_4$ crystals with lengths of up to 100 μm (Figure 5-6). The coating on the glass pre-equilibrated at NNO further includes dark areas of $MgSO_4$, smaller amounts of Na_2SO_4 and Fe_2O_3 in between the $CaSO_4$ crystals. At NNO+1 the coating includes a fine-grained mixture of Na_2SO_4 and micron-sized hematite

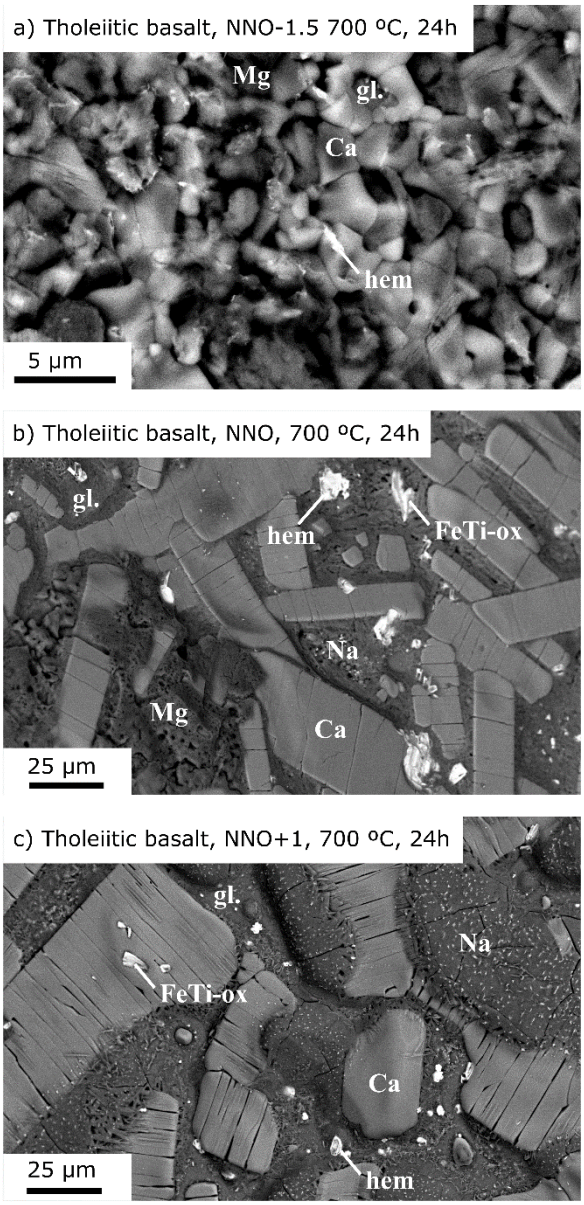

Figure 5-6: Back-scattered electron images of coatings formed on Fe-bearing basaltic glasses which were pre-equilibrated at different fO_2. The textures and assemblages vary considerably as a function of the pre-equilibration. The observed phases are labelled as: gl.: substrate glass; Ca: $CaSO_4$; Mg: $MgSO_4$; Na: Na_2SO_4; hem: Fe_2O_3; FeTi-ox: Fe-Ti-oxide. All three textures are not continuous and in some areas parts of the glass substrate can be observed (gl.). a) Tholeiitic basalt (NNO-1.5, 700 °C, 24h) is coated with $CaSO_4$ (forming brighter crystals, Ca), hydrated $MgSO_4$ (in darker greys, Mg), and sub-micron sized Fe-oxides (hem and FeTi-ox). b) Tholeiitic basalt (NNO, 700 °C, 24h), coated with large columnar $CaSO_4$ (Ca), hydrated $MgSO_4$ (darker grey in the lower left corner of the image, Mg), Na_2SO_4 (Na) in between $CaSO_4$ and mixed into the $MgSO_4$, and Fe_2O_3 (bright white, hem). Some Fe-oxides contain significant amounts of Ti (FeTi-ox). c) Tholeiitic basalt (NNO+1, 700 °C, 24h) coated with large columnar $CaSO_4$ (Ca), fine-grained Na_2SO_4 (Na) mixed with sub-microns sized Fe-oxides, and larger Fe-oxides (hem) including some Fe-Ti-oxides (FeTi-ox). No $MgSO_4$ occurs in this coating.

crystals (Figure 5-6c). Larger oxide crystals also occur, including some Fe-Ti-oxides on the $CaSO_4$ crystals and minor amounts of Al in some Fe-Ti-oxide grains (Figure 5-6). Small grains of $MgSO_4$ were observed on the NNO+1 sample after 1 hour, whereas no $MgSO_4$ was detected after 24 hours.

In addition to Fe_2O_3 the more reduced magnetite (Fe_3O_4) mineral has been observed in the coatings of basalt glasses pre-equilibrated at the iron-wüstite redox buffer (Palm et al., 2018). The dominant sulfate phase in these experiments is $Na_2Ca(SO_4)_2$ (glauberite) with significant amounts of $CaSO_4$. The results from these experiments reacting basalt at 800 °C are described in detail as a case study in the chapter by Palm et al. (2018).

In summary, phase assemblages of the coatings formed by the reaction of $SO_{2(g)}$ with Fe-bearing basalt glasses vary as a function of the composition and the Fe^{3+}/Fe_{total} of the glass prior to the reaction with $SO_{2(g)}$ (Table 5-2). The sulfates observed in the coatings are $CaSO_4$, $MgSO_4$, Na_2SO_4 and $Na_2Ca(SO_4)_2$. The oxides observed in the coatings are hematite, magnetite and Ti-bearing oxides. Future work will be required to determine the mechanisms which control the phases formed in $SO_{2(g)}$ reactions with Fe-bearing basalt glasses.

5.5.2 Textures of sulfate coatings on Fe-bearing glass substrates

All experiments produced by reacting $SO_{2(g)}$ with Fe-bearing glasses have discontinuous coatings (Figure 5-6, Burnett et al., 1997; Ayris et al., 2013). After one hour at 700 °C the coatings cover up to 80% of the surface area of the glass. The coverage increases with time reaching more than 90% after 24 hours. The texture of the sulfate-coating on the tholeiitic basalt pre-equilibrated at NNO-1.5 reacted at 700 °C for 24 hours (Figure 5-6a) is very similar to that on the Fe-free basalt reacted at the same temperature and for the same amount of time (Figure 5-4b). Both figures show backscattered electron images with similar well-crystallized $CaSO_4$ grains with sub- and anhedral Mg-sulfates which partly hydrated after the experiments. Only a few gaps occur in the coatings, exposing the substrate and they are usually surrounded by $CaSO_4$ crystals (Figure 5-6a). The $CaSO_4$ have diameters of less than 2.5 µm.

The coatings on the more oxidized basalts (NNO and NNO+1) reacted at 700 °C for 1 hour and 24 hours share the feature of well crystallized large euhedral anhydrite grains. The large anhydrite grains usually show a distinct cleavage perpendicular to the longest axis of the grains. As anhydrite has the best cleavage in the (001)-plane (Tröger, 2017), the longest axis of the grains in the coatings are the crystallographic c-axis of anhydrite (Figure 5-6).

After one hour, Mg- and Na-sulfates form very fine-grained textures, with grain-sizes of few microns on the glasses pre-equilibrated at NNO and NNO+1. The Mg-sulfates form equant shaped grains, whereas the Na-sulfates have needle-shaped habits which are commonly twinned. The Na-sulfates usually occur as patches surrounding elongated $CaSO_4$ grains. The metal oxides are most frequently found lining the edges of these sulfate patches.

After 24 hours the $CaSO_4$ grains are up to five times larger compared to coatings on 1-hour experiments. Individual crystals of $CaSO_4$ are no longer isolated and there are gaps in-between crystals which are largely filled by other phases. On the glass pre-equilibrated at NNO, Mg-sulfate (where present) occurs in large patches which partially overgrow and surround the $CaSO_4$ grains. The Na_2SO_4 lines the edges of the $CaSO_4$ grains. In this coating, metal oxides reach grain sizes of more than 20 μm (Figure 5-6b). In the coating formed on the most oxidized glass (NNO+1) Na_2SO_4 patches tend to overgrow the $CaSO_4$ grains (Figure 5-6c). The metal oxides are either found as micron-sized needles in the Na_2SO_4 patches, or as large Fe-oxides (commonly Ti-bearing) between sulfates and on top of large $CaSO_4$ grains.

In comparison with the textures observed on Fe-free glasses, the coatings formed by reactions between $SO_{2(g)}$ and Fe-bearing glasses are significantly different. $CaSO_4$ is the dominant phase in most Fe-bearing and Fe-free systems, but the grain morphologies and sizes are very different. On Fe-bearing glasses, $CaSO_4$ forms large grains with diameters of up to tens of microns (Figure 5-2, Figure 5-6), whereas on Fe-free glasses $CaSO_4$ usually forms continuous coatings with small grain sizes of up to several microns (Figure 5-4, Figure 5-5). The large $CaSO_4$ grains in coatings on Fe-bearing glasses are, in some cases, associated with various other phases including sulfates and oxides (Figure 5-6), whereas in other cases $CaSO_4$ remains the only phase detected in the coatings (Table 5-2, Ayris et al., 2013). This diversity of textures and assemblages shows that more work is needed to constrain the processes which control the textures and assemblages formed in reactions between $SO_{2(g)}$ and Fe-bearing aluminosilicate glasses.

5.5.3 Compositional changes in the Fe-bearing glass substrate

Reaction products are also found in the glass substrate in layers or dispersed near the interface with the gas and sulfate coating. For example, chondrule glass substrates produced a region rich in silica and a Na-Ca-Mg-Al silicate, possibly clinopyroxene, in the glass below the $CaSO_4$ coating (Johnson and Burnett, 1993; Burnett et al., 1997). Ayris et al. (2013) used transmission electron microscopy energy-dispersive X-ray spectroscopy (TEM-EDS) to show that the reacted tephrite (Figure 5-2) and phonolite glasses are

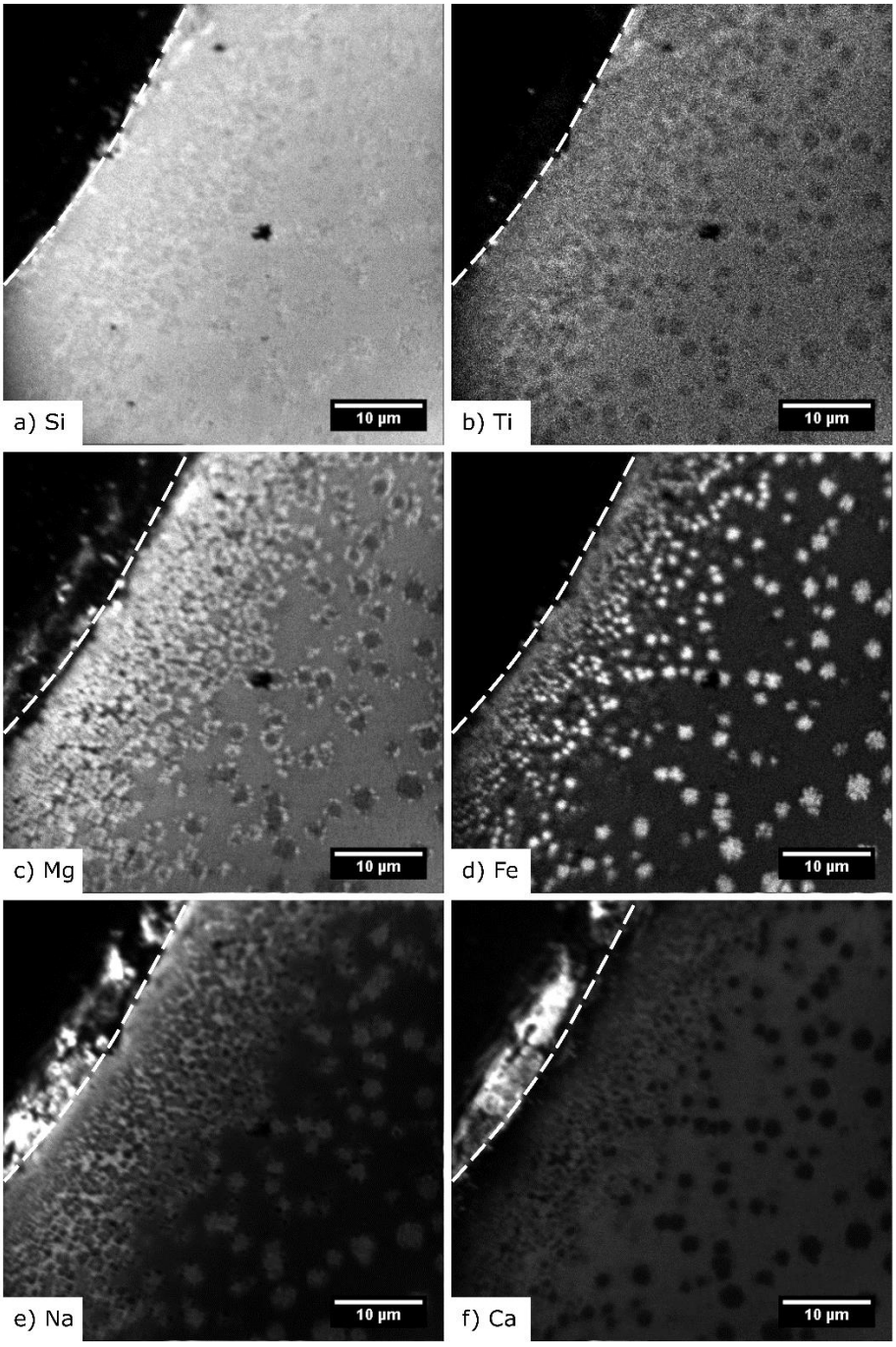

Figure 5-7: NanoSIMS maps of major elements in a cross-section of a tholeiitic basalt (NNO, 700 °C, 24h). The dashed line shows the location of the interface between the basaltic glass to the right and the sulfate coating to the left. a) Si: The network-forming cation remains in the glass and is possibly slightly enriched just beneath the surface, whereas it is not detected in the coating. b) Ti: Ti is not detected in the coating material in this cross-section, even though Ti-bearing Fe-oxides were observed in the coating. c) Mg: Mg is predominantly retained in the glass substrate. Mg-rich zones occur as rings surrounding more depleted Fe-rich nuclei. d) Fe: Fe forms spherulites which are relatively depleted in Ti, Mg and Ca, but slightly enriched in Na. The number of spherulites increases toward the original surface of the glass (dashed line). This cross-section has not sampled a Fe-oxide grain in the coating. e) Na: Na is a major component of the coatings and is also enriched in the substrate towards the surface. f) Ca: Ca is depleted in the glass substrate with decreasing concentrations towards the surface and enriched in the coating.

depleted in Ca near the surface. This depletion supports the assumption that Ca diffusion in the glass is the rate controlling step in the sulfate-forming reaction. The cross-section of the tephrite glass shows the nanometer scale nucleation of a silicate phase, identified as the clinopyroxene augite by X-ray diffraction (Ayris et al., 2013). Palm et al. (2018) also observed the crystallization of clinopyroxene in an alkaline basalt glass reacted with $SO_{2(g)}$ at 800 ºC.

Reactions between tholeiitic basalt glasses and $SO_{2(g)}$ record considerable complexity in these non-equilibrium reactions. For example, a cross-section through the sulfate-rich coating on a tholeiitic basalt glass, pre-equilibrated at the NNO buffer is shown in Figure 5-7. The images are maps of major elements obtained by nanoscale secondary ion mass spectrometry (nano-SIMS, see Palm et al., 2018). The network-forming cations Si and Ti show small or negligible concentration gradients across the interface from the coating into the glass. In some instances, SiO_2 needles form in the reacted glass substrate near the surface. Magnesium and Fe are strongly depleted within the outermost two microns of the glass and show an increase within 20 µm of the surface. The degree of nucleation of Mg- and Fe-rich phases varies considerably between the experiments although consistently crystallization occurs along a gradient of increasing crystal density towards the reaction surface (Figure 5-7). The main sulfate-forming cation is Ca, as reflected by a high relative count rate in the surface layer. The glass substrate is accordingly depleted in Ca. Sodium shows a very different behavior because it partitions into the sulfate coating but is also enriched in the near-surface silicate substrate (Figure 5-7).

5.6 Discussion

In this section, we discuss the reaction mechanisms and possible rate-limiting steps in gas-glass reactions. Since Ayris et al. (2013) found that reactions were most efficient above 600 ºC, we focus the discussion on experiments in the temperature range of 600-800 ºC. First, we discuss the observation from experiments with Fe-free aluminosilicate glasses. Second, we discuss Fe-bearing systems, in which redox reactions play an important role. For this reason, we will examine the variables $SO_{2(g)}$ and $O_{2(g)}$ and their effect on the reaction products in the coatings and the altered glass substrates.

In all experiments recorded in the literature, in which $SO_{2(g)}$ was reacted with Ca-, Mg- and Na-bearing aluminosilicate glasses, the sulfate reaction products are relatively enriched in Ca relative to the unreacted bulk glass composition, hence Ca migrates out of the glass more than Mg. This is the case for both Fe-bearing and Fe-free systems. As pointed out, the sulfates almost entirely consist of $CaSO_4$ on An-Di glasses reacted at 800 ºC, whereas at 600 ºC some $MgSO_4$ is present. $CaSO_4$ has lower Gibbs Free Energies of formation than

$MgSO_4$ from 25 ºC to >1500 ºC, making it a more stable phase. At 600 ºC calculated Gibbs Free Energies of formation are -1558.7 kJ/mol for $CaSO_4$ and -1372.3 kJ/mol for $MgSO_4$, and at 800 ºC they are -1608.5 kJ/mol for $CaSO_4$ and -1418.1 kJ/mol for $MgSO_4$ (Chase, 1998). The differences in the Gibbs Free Energies of formation are -186.4 kJ/mol at 600 ºC and -190.4 kJ/mol at 800 ºC. These data show that $CaSO_4$ is thermodynamically more stable than $MgSO_4$, but the presence of $MgSO_4$ at 600 ºC, and not at 800 ºC, cannot be ascribed to the thermodynamic properties. Thermodynamic properties of the sulfates are discussed in more detail in King et al. (2018 and references therein) and applied to reactions in planetary environments and on Venus in Zolotov (2018).

If the rate-limiting factor is diffusion in the glass substrate, supplying cations to the surface for the formation of sulfate, we can expect that the cation with the larger diffusion coefficient is relatively more abundant in the sulfate reaction products. To our knowledge there is no data on the diffusivities of Ca and Mg in anorthite-diopside glasses, but in albite and jadeite glasses at 800 ºC the tracer diffusivities of the cations follow the order of $D_{Na} > D_{Ca} > D_{Mg}$ (Roselieb and Jambon, 2002). The same relationship likely holds for the compositionally similar anorthite-diopside glasses and diffusivities in the glass follow $D_{Ca^{2+}}^{glass} > D_{Mg^{2+}}^{glass}$. The enrichment of Ca in the sulfate compared to Mg appears to depend on the temperature, relative to the glass transition, with a higher mobility for Ca than Mg. This suggests that the substrate properties control the supply of cations and the amount of reaction products formed. Further work is needed to unravel the relative mobilities of the sulfate-forming cations as a function of temperature, composition and properties of the reactants.

We posit that network-modifying cations which are not charge-compensating are the most easily mobilized as a function of temperature or due to chemical potential gradients, as imposed by gradients in gas-solid and redox reactions. In the absence of systematic studies on the relative diffusivities of Ca and Mg in aluminosilicate glasses we draw on our experimental results. The high relative mobility of Ca indicates that it is less strongly bound in the glass aluminosilicate network than Mg, or that it is more readily mobilized by reaction with $SO_{2(g)}$. This distinction may be explained by the difference in the ionic field strengths of the cations. The ionic field strength is the ratio of the valence of the cation over the squared effective ionic radius for a given coordination number. The calculated ionic field strengths for 6-fold oxygen coordination are 3.86 for Mg and 2 for Ca (Shannon, 1976), which suggests that Mg may form stronger bonds with non-bridging oxygens and is more likely to be retained in the glass to charge compensate Al^{3+} and Fe^{3+} cations. This

interpretation remains speculative and will require further experimental work on simple glasses in the future.

5.6.1 Role of the fugacities of $SO_{2(g)}$ and $O_{2(g)}$ on reactions with silicate glasses

The reaction between $SO_{2(g)}$ and silicate glasses is thermodynamically expected to form sulfates and sulfides due to the disproportionation of S^{4+} in the gas molecule to S^{6+} in the sulfate and S^{2-} in a sulfide or gas phase (Equation 5-4). However, the description of the experimental reaction products from a range of different studies has shown that sulfides are rarely observed (only with XPS), both in Fe-free and Fe-bearing systems. Fe occurs in hematite in experiments with tholeiitic basalts (Figure 5-6), thus a high oxygen fugacity seems to be a plausible mechanism, prohibiting the formation of sulfides. If the reacting $SO_{2(g)}$ is in equilibrium, the speciation calculation shown in Figure 5-1 can be used to establish the oxygen fugacity (fO_2) of the gas phase ($\log fO_2$ = -12.1 at 700 °C), assuming that the gases mix in an ideal manner. This calculated value is uncertain due to high gas flow rates (up to 50 standard cm^3 per minute) which likely ensures that $SO_{2(g)}$ remains the dominant species and $\log fO_2$ may be lower. Second, the zone in the furnace at which the experimental temperature of 700 °C is reached is small, so that equilibrium in the gas is unlikely.

Understanding the fO_2 in Fe-bearing experiments is of importance because this variable controls the stability of different Fe-oxide phases. The phase relationship in the system Fe-S-O is commonly shown as a function of fO_2 and fS_2 (Hall, 1986). Here instead we calculate the phase relations using thermodynamic data (Chase, 1998) to recast the relationship as a function of fSO_2 and $fO_{2(g)}$ (Figure 5-8). It should be noted that the thermodynamic calculations assume activities of unity in both the reactant and the product. This is not the case and results in uncertainties in applying the experimental results to the calculated phase boundaries.

The Ni-NiO fO_2-buffer (NNO) is shown in Figure 5-8, at $\log fO_2$=-16.3 (O'Neill and Pownceby, 1993). This is 4.7 orders of magnitude below the fO_2 of the calculated magnetite-hematite buffer above which the oxides are placed in the coatings of the reacted tholeiitic basalt glasses pre-equilibrated near NNO (Figure 5-8). An even greater overall oxidation is required in the reaction of $SO_{2(g)}$ with alkali basalt glasses pre-equilibrated at the iron-wüstite buffer, where both magnetite and hematite were observed in the coatings (see Palm et al., 2018).

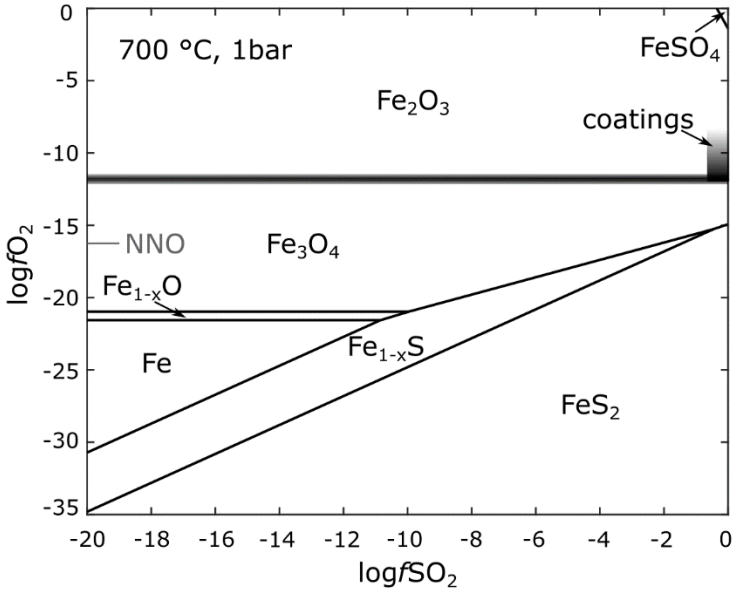

Figure 5-8: Phase relationships in the system Fe-S-O as a function of fSO_2 and fO_2 at 700 °C and 1 bar. Fe-phases observed in coatings of $SO_{2(g)}$ experiments are Fe_2O_3 in most cases and assemblages including both Fe_2O_3 and Fe_3O_4 (Palm et al. 2018) as indicated by the box at $logfSO_2$ near 0. The figure also shows the $logfO_2$ of the NNO redox buffer relative to which some of the reacted basalt glasses were pre-equilibrated. The geometric relationship of the phase boundaries remains constant with temperature. At 700 °C and 1 bar the fugacities of minor gas species in equilibrium with $SO_{2(g)}$ (see Figure 5-1) are $logfO_2$=-12.1, $logfS_2$=-7, $logfS_3$=-11.4, $logfSO_3$=-5.7, $logfSO$=-6.1 and $logfS_2O$=-6.5. The calculations were made using the package HSC8 by Outotec based on the JANAF database (Chase 1998).

Therefore, $SO_{2(g)}$ reactions with Fe-bearing silicate glasses are characterized by chemical potential gradients imposed by the sulfate-forming reaction (Equation 5-4) and by redox reactions (Figure 5-8). This combination in gradients creates a system which is highly out of equilibrium, forcing the reaction to be more effective.

Burnett et al. (1997) were the only authors who reported the observation of Fe-sulfate, on an obsidian sample reacted with $SO_{2(g)}$ at 850 °C, based on XPS spectra and optical microscopy. In a reaction with pure $SO_{2(g)}$ Fe-sulfates are not predicted thermodynamically (Figure 5-8). Overall, the reaction with obsidian produced very small amounts of reaction product on the surface, likely due to the low concentrations of Na_2O (3.80 wt.%), CaO (0.52 wt.%) and FeO (1.02 wt.%), and the high concentrations of Al_2O_3 (12.32 wt.%) and SiO_2 (76.45 wt.%) (Burnett et al., 1997). As traces of the same Fe-bearing phase were observed in an Fe-free experiment with an Ab-An-Di glass, where the observation was interpreted as a contamination (Burnett et al., 1997), the same contamination may also explain the observation on the obsidian sample.

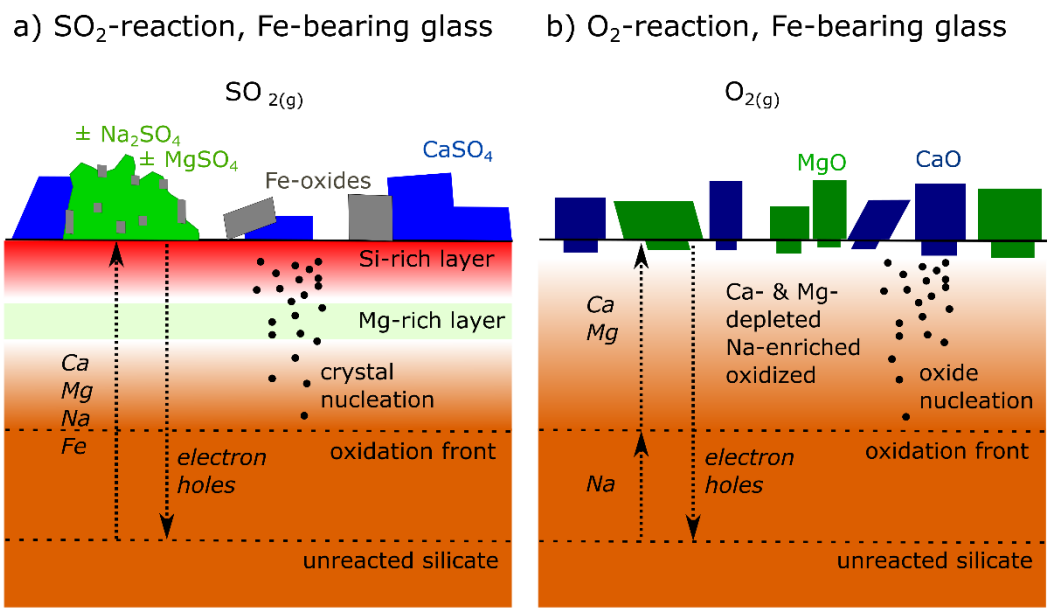

Figure 5-9: Schematic drawings of the reaction between gases and Fe-bearing silicate glasses at 700 °C and 1 bar. a) $SO_{2(g)}$ reaction results in the formation of sulfate and oxide coatings. The oxidation of Fe in the glass occurs via the inward diffusion of electron holes and the outward diffusion of alkali and alkaline earth cations, forming the sulfates. The glass subsurface is relatively enriched in Si and Al (network-forming cations) due to the diffusive loss of other cations. The change in the chemical composition of the glass results in the crystal nucleation near the glass surface. b) $O_{2(g)}$ reaction with Fe-bearing silicate glasses requires the outward diffusion of alkaline earths and inward diffusion of electron holes. Na diffuses into the oxidizing surface layer to stabilize tetrahedrally coordinated ferric iron. Insufficient charge balancing of ferric iron can result in the destabilization of the glass and the nucleation of oxides and silicates (Cook et al. 1990; Cooper et al. 1996b, a; Cook and Cooper 2000; Burkhard 2001).

Iron is the most abundant multivalent cation in natural aluminosilicates. In glasses and melts the redox state of iron affects its coordination state in the amorphous network and physical properties including viscosity and liquidus temperatures (Farges et al., 2004; Wilke, 2005). As indicated above, $SO_{2(g)}$ reactions with Fe-bearing aluminosilicate glasses result in the formation of Fe-oxides in the coatings and also affect the redox state of Fe in the glass substrates. With ongoing reaction physical properties of the glasses affected by the redox state of iron are expected to change accordingly. Therefore, it is important to investigate the mechanism of oxidation here.

The oxidation of Fe^{2+} in a silicate melt or glass may occur via several different kinetic pathways. The pathway which reduces the chemical potential gradient of oxygen the fastest is the dominant mechanism for Fe^{2+} oxidation. In hydrogen-bearing systems the diffusion rate of free H_2 is very high. The hydrogen is bound in the form OH-groups following the oxidation reaction of ferrous to ferric iron (Gaillard et al., 2003). When studying reactions between gases and Fe-bearing glasses it is therefore important to determine if hydrogen is present in the system, as it can significantly affect redox reactions.

In a hydrogen-free system, three redox pathways are possible. First, molecular O_2 may diffuse through the glass to increase the cation/oxygen ratio, or ionic O^{2-} and charge-compensating electron holes can co-diffuse to decrease the chemical potential gradient (Magnien et al., 2008; Wendlandt, 1991). In both cases the cation/oxygen ratio changes in response to the redox gradient. Second, divalent and monovalent cations move to the surface, balanced by the counter-diffusion of electron holes ($h^{\cdot}$) (Figure 5-9b) (Magnien et al., 2008). It has been shown that molecular and ionic oxygen diffusion is very slow in super-cooled melts and aluminosilicate glasses (Cook et al., 1990; Cooper et al., 1996b, a; Magnien et al., 2008; Cochain et al., 2013; Cooper, 2018). For example, there is negligible uptake of atmospheric oxygen by oxidizing and reheating Kilauea basalt glasses at temperatures below 1200 °C (Burkhard, 2001). The third pathway dominates when the diffusivities (*D*) of monovalent/divalent cations and electron holes are considerably faster than the diffusivities of molecular and ionic oxygen, and if the system is hydrogen-free (subscripts denote diffusing species):

$$D_{O_2}, D_{O^{2-}} \ll D_{M^+}, D_{M^{2+}} \ll D_{h^{\cdot}} \qquad \textit{Equation 5-5}$$

In the case of oxidation of crystalline oxides, for which the same principle of cation diffusion is valid, the diffusion of monovalent and divalent cations to the surface is charge-balanced by the inward diffusion of cation vacancies, particularly along dislocations (Schmalzried, 1983; Ostyn et al., 1984; Schmalzried and Backhaus-Ricoult, 1993). In crystalline materials electron holes are the equivalent of Fe^{3+} cations occupying the sites of Fe^{2+} cations (Cooper et al., 1996a; Cooper, 2018).

In aluminosilicate glasses with multivalent transition metals electron holes are mobile. For example, Fe^{2+} easily releases an electron, or in other words takes up an electron hole. The material behaves like a semiconductor for electron holes, as they can jump between transition metals almost instantaneously (Cooper et al., 1996a; Cook and Cooper; 2000; Cooper, 2018). Due to this high mobility, electron holes do not create an electrochemical potential gradient and their flux is not rate-limiting. The chemical potential gradient of oxygen from the surface to the interior results in the flux of monovalent and divalent cations to the surface, expressed as:

$$j_{M^{2+}} = \frac{c_{M^{2+}} D_{M^{2+}}}{2RT} \cdot \frac{d\mu_{O_2}}{d\xi} \qquad \textit{Equation 5-6}$$

where $j_{M^{2+}}$ is the flux of divalent cations to the surface, $c_{M^{2+}}$ is its concentration, $D_{M^{2+}}$ is the self-diffusion coefficient, R is the gas constant, T is temperature in K and $\frac{d\mu_{O_2}}{d\xi}$ is the chemical potential gradient of oxygen with ξ being the distance variable (Cooper et al., 1996a; Cook and Cooper, 2000; Cooper, 2018). This relationship is fundamental for the

oxidation mechanism and shows the dependence of cation diffusion on the chemical potential gradient of oxygen (Cooper et al., 1996a; Cook and Cooper. 2000; Cooper, 2018). As the major element abundance in the oxidizing surface layer is changed by the loss of cations to the surface, the physical properties of the silicate change also. Consequently, the diffusion coefficients are not constant with time (Schmalzried. 1983).

A significant property of the reaction morphology of the oxidation of silicate glasses and super-cooled melts is the nucleation of oxides between the surface and the oxidation front if tetrahedrally coordinated Fe^{3+} is not sufficiently charge compensated (Figure 5-9b; Cook et al., 1990; Cooper et al., 1996b; Cook and Cooper. 2000). If, for example, sufficient Na is available as a charge compensator, nucleation of oxides in the glass is avoided. This is observed as an enrichment of Na in the oxidized glass layer. In this case, the oxidation front coincides with a Na-front (Cook et al., 1990; Cook and Cooper. 2000; Burkhard. 2001). In the absence of sufficient charge compensating alkalis the glass structure is no longer stable and oxides nucleate homogeneously (Cooper et al., 1996a, b; Cook and Cooper. 2000; Cooper, 2018). The nanoSIMS maps (Figure 5-7) of a cross section through a tholeiitic basaltic glass pre-equilibrated at the NNO oxide buffer and reacted for 24 hours at 700 °C show such an enrichment of Na near the surface in the glass substrate. The Na enrichment was not sufficient to charge-balance the oxidizing and reacting glass, which resulted in the nucleation of Fe-rich spherulites, surrounded by Mg-rich phases (Figure 5-7).

The reaction mechanism of $SO_{2(g)}$ with Fe-bearing silicate glasses and supercooled melts is comparable with that of oxidation. In both cases divalent cations diffuse to the surface due to a chemical potential gradient (Figure 5-9). In the case of the $SO_{2(g)}$ reaction (Figure 5-9a) gradients in fSO_2, fS_2 and other gas species (see Figure 5-1) occur in addition to a gradient in fO_2. In the absence of S-bearing species diffusing divalent cations (Ca and Mg) form oxides near the surface (Cooper et al., 1996a; Cook and Cooper, 2000; Cooper, 2018). In the presence of $SO_{2(g)}$ the cations react to form sulfates and oxides. Due to the high fSO_2 of the experimental gas (Figure 5-1 and 5-8) it is likely that the cation diffusion is predominantly due to the driving force of the reaction in Equation 5-3 and only secondarily due to the effect of oxidation as described by Cooper et al., (1996a). The relative importance of these mechanisms remains to be determined experimentally.

5.6.2 Reaction rates

The depletion of cations in the glass substrate, due to the formation of sulfates and oxides on the surface, can result in the destabilization of the glass, resulting in the nucleation and crystallization of oxide and silicate phases (Figure 5-4 and 5-9). Crystal growth can impose additional chemical potential gradients and affect the mobility of cations in the glass and

their availability to form surface coatings. Crystallization near the surface can also act as a barrier for further diffusion of cations to the surface, and thus become reaction limiting.

The rate at which the reaction between $SO_{2(g)}$ or $O_{2(g)}$ with a glass occurs can be described by three different rate laws, depending on which mechanism is rate-limiting. First, if the surface reaction is rate-limiting, then the law is linear and the rate is independent of time. This initial chemisorption reaction (Henley et al., 2015) is not likely the rate controlling mechanism because experimental work has shown that significant amounts of sulfate form almost instantaneously within few minutes (Ayris et al., 2013). Second, if the reaction occurs at low temperature resulting in a very thin oxide layer, it follows a logarithmic law, which is not the case in high-temperature gas-solid reactions either. Third, if the reaction is diffusion controlled (Figure 5-4 and 5-9) and the transport mechanisms are rate-limiting, the rate follows a parabolic law and is inversely proportional to the square root of time (Birks et al., 2006):

$$\frac{d\xi}{dt} = \frac{k'}{\xi} \qquad \textit{Equation 5-7}$$

Integrated:

$$\xi = \sqrt{2k't} \qquad \textit{Equation 5-8}$$

where k' is the parabolic rate constant. The parabolic rate constant is an intrinsic property dependent on the cation flux, composition, concentration gradient, thermodynamic driving force and temperature and is derived experimentally (Pieraggi, 1987; Cooper et al., 1996a; Monceau and Pieraggi, 1998; Birks et al., 2006; Cooper, 2018).

The rates of sulfate formation have been determined by leaching the coatings in solution and measuring the concentration of the leached material as a function of the amounts of reacted solids. Ayris et al. (2013) measured the molar amount of sulfur as a function of the weight of reacted volcanic ash. After initial $SO_{2(g)}$ adsorption, the formation of $CaSO_4$ is limited by the diffusion of Ca from within the ash particles to the surface. Accordingly, they calculate a diffusion coefficient for Ca^{2+} ($D_{Ca^{2+}}^{glass}$) assuming constant diffusion rates and solving Fick's first law of diffusion for ideal spherical ash particles (Ayris et al., 2013). Diffusion rates are greatest in the tephrite glass ($D_{Ca^{2+}}^{tephrite\ gl.} = 6.5 \times 10^{-14}$), followed by phonolite glass ($D_{Ca^{2+}}^{phonolite\ gl.} = 1.8 \times 10^{-12}$), dacite glass ($D_{Ca^{2+}}^{dacite\ gl.} = 3.7 \times 10^{-13}$) and rhyolite glass ($D_{Ca^{2+}}^{rhyolite\ gl.} = 8.7 \times 10^{-13}$). These diffusion coefficients apply to the first minutes of the reaction after $SO_{2(g)}$ adsorbs onto Ca-O surface sites.

As the reaction proceeds, between $SO_{2(g)}$ and silicate glasses, significant amounts of sulfate can be formed. Consequently, the glasses become increasingly depleted in Ca, Mg or Na,

depending on the system. As the network-forming cations (Si, Al) are not extracted by the reaction, the glass becomes increasingly Si- and Al-rich. This change in the chemical composition within the near-surface glass affects the rates at which the divalent and monovalent cations can diffuse and be extracted. For example, the rate of sulfate formation in reactions between $SO_{2(g)}$ and silicate glasses in the anorthite-diopside system is an order of magnitude higher within the first hour of reaction compared to the following 23 hours. As pointed out in the context of the oxidation of metal alloys (Schmalzried, 1983), diffusion coefficients are not constant in these systems and evolve with time. Furthermore, $SO_{2(g)}$-silicate glass reactions frequently result in the nucleation of crystallites in the sub-surface glass. This has been observed in Fe-free and Fe-bearing glass of a various compositions as indicated in Figures 5-4, 5-7 and 5-9 (Ayris et al., 2013). It is for these reasons, that none of the rate laws, including parabolic rate laws, sufficiently describe the reaction rates of $SO_{2(g)}$ with silicate glasses. Future work needs to develop kinetic models that encapsulate the complexity of the reaction mechanisms.

5.7 Summary and outlook

In summary, reactions between $SO_{2(g)}$ and silicate glasses with diverse compositions have been observed to form significant amounts of sulfate over short time frames of few minutes to an hour at 600-800 °C (Ayris et al., 2013; Delmelle et al., 2018). In Ca-bearing systems, the reaction products primarily consist of $CaSO_4$ coatings on the glass surfaces and associated Ca-depleted glass substrates. In the presence of other di- and monovalent cations, in particular Na and Mg, Ca remains the main sulfate-forming cation. Other sulfates, including $MgSO_4$, Na_2SO_4 and $Na_2Ca(SO_4)_2$ have been observed in some experiments, but they usually occur in lesser abundance than $CaSO_4$. Experimental studies with natural volcanic ash samples, synthetic Fe-free glasses and natural Fe-bearing glasses collectively suggest that the reaction rates and compositions of the reaction products are a function of the physical properties of the reacting glasses, and in particular the mobility of different cations in the glasses. In Al^{3+}- and Fe^{3+}-bearing systems some monovalent and divalent cations are preferentially retained in the glass to charge-balance the tetrahedrally coordinated Al^{3+} and Fe^{3+}. Calcium appears to be less strongly bound to the amorphous network than Mg and Na and is more easily mobilized to form $CaSO_4$ coatings. The reactions are further complicated where $Fe^{3+}{}_{tot}$ increases (Fe^{2+} is oxidized to Fe^{3+}) with time due to oxidation, gradually requiring more charge compensation.

The complexities underline the importance of future experimental investigations. In particular, reaction rates at different stages of the reaction remain under-determined. Another open question relates to what physicochemical properties and mechanisms control

the mobility or retention of alkali and alkaline earth metals in the aluminosilicate glasses. Recently, Le Losq et al. (2017) have shown that percolation channels control the mobility of alkali metals in aluminosilicate glasses and melts. Similar structural properties may also control the mobility of alkaline earth metals in aluminosilicate glasses, and their transport to the surface to form sulfates as described in this chapter. A better understanding of these structural properties is of fundamental importance for the interpretation of reactions between aluminosilicate glasses and reactive gas species such as $SO_{2(g)}$.

Experimental observations summarized in this chapter were all made at room temperature. However, a number of these observations may be affected by the cooling paths of the samples at the end of the experiments. For example, the nucleation of crystalline phases near the reacting surface may occur during quench. Furthermore, some salts formed in these experiments can go through phase transitions as they are cooled to lower temperatures (e.g. Na_2SO_4). Others such as $MgSO_4$ are prone to hydration or may recrystallize at room temperatures. These mechanisms may result in textural, mineralogical and chemical changes between experiment and analysis. Experiments investigating gas-solid reactions *in situ* are therefore essential to better constrain these secondary processes.

In systems which contain multivalent elements, in particular Fe, the oxygen fugacity is an important variable. It varies in the glasses during the reactions, but also in the gas phase and in the resulting coatings. Future interpretations would benefit from fO_2 monitoring during experiments and the understanding of the reactions will improve with the determination of Fe^{3+}/Fe^{2+} and S^{6+}/S^{2-} across the reaction interface after the experiments, for example with XANES, which additionally provides information about the coordination of Fe in the glasses (Wilke et al., 2007 and 2011).

6 Conclusions

This chapter provides a brief summary of the research presented in this thesis. The main conclusions and their implications are discussed. Finally, I discuss some implications for planetary volcanism and highlight where more research is needed.

6.1 Volcanic gases on Earth and on the Moon

On Earth, volcanic gases can be observed and sampled in situ or by remote using spectroscopic data. The composition of volcanic gases sampled at the surface is accordingly well constrained. This is not the case for past volcanism on the Moon, where volcanic activity peaked before 3 Ga (Heiken et al., 1991). Nevertheless, ancient well preserved volcanic materials, such as the ~3.6 Ga old orange and green glasses on the Moon (Heiken et al., 1991), can keep a record of the composition of volcanic gases from long extinct volcanic activity. I used volatile abundances measured in lunar pyroclastic glasses (Saal et al., 2008; Wetzel et al., 2015) to calculate the bulk composition of lunar volcanic gas.

Compared to a terrestrial volcanic gas, such as from Erta Volcano in Ethiopia (Zelenski et al., 2013; de Moor et al., 2013), the lunar gas is three times richer in C and up to 10 times richer in S, whereas it has lower H and Cl concentrations (Table 2-1). The lunar volcanic gas is significantly more reduced at an oxygen fugacity (fO_2) of approximately two orders of magnitude below the iron-wüstite buffer (IW-2), whereas the volcanic gas from Erta Ale has an oxygen fugacity of IW+3.6. Furthermore, the lunar gas was emitted at significantly higher temperatures above the liquidus temperature of the orange and green picritic glasses (1448 °C; Delano, 1990), whereas the gas from Erta Ale was sampled at 1084 °C (Zelenski et al., 2013; de Moor et al., 2013).

My thermochemical calculations show that such a lunar volcanic gas is dominated by a range of different species, including near-equal abundances of $CO_{(g)}$, $S_{2(g)}$ and $H_{2(g)}$ at emission conditions of 1450 °C and 0.1 bar and during decompression and cooling to conditions at < 800 °C and 10^{-6} bar (Figure 2-2). This is in contrast to previous studies suggesting that lunar volcanic gas was predominantly consisting of $CO_{(g)}$ (Fegley, 1991; Fogel and Rutherford, 1995; Sutton et al., 2005; Rutherford and Papale, 2009; Nicholis and Rutherford, 2009; Elkins-Tanton and Grove, 2011). Sulfur dioxide is the third most abundant gas species in the volcanic gas from Erta Ale, whereas it has a very low abundance in the lunar volcanic gas with 1.5 x 10^{-6} mole fractions at 1000 °C and 1 bar.

The diverse range of hydrogen species in the lunar gas ($H_{2(g)}$, $HF_{(g)}$, $HCl_{(g)}$, $H_2S_{(g)}$ and $H_2S_{2(g)}$) suggests that a similar diverse range of species may occur as diffusing species in

the picritic glasses and melts. As these species have variable diffusivities the simple modeling of hydrogen diffusion in the picritic glasses and melts as H_2 or H_2O may not be accurate.

In addition to the speciation of the main volatile elements (H, O, C, Cl, S and F) in the volcanic gases from the Moon and Erta Ale, I calculated the speciation of the metals Zn, Ni, Ga, Pb, Cu and Fe in these gases (Figures 2-3, 2-4, 9-1, 9-2, 9-3 and 9-5). The metals are transported in the gas as chlorides, sulfides and elemental gas species. In comparison, the terrestrial volcanic gas from Erta Ale can transport larger amounts of all six investigated metals (Figure 2-5). This is mainly due to the three times higher concentration of Cl in the volcanic gas from Erta Ale, which increases the abundance of metal-chloride gas species. The metals are deposited from the lunar volcanic gas mainly as sulfides and native metals (Figure 2-3), whereas the metal phases deposited from the Erta Ale volcanic gas also include oxides and some chlorides (Figure 2-4). This is in good agreement with observations of sulfide and native metal coatings orange and green glass beads (McKay and Wentworth, 1992), as well as from fumarole deposits at Erta Ale volcano (Zelenski et al., 2013).

6.2 Gas-solid reactions between $SO_{2(g)}$ and basalt glasses

6.2.1 Summary of experimental results

Experiments reacting $SO_{2(g)}$ with Fe-free and Fe-bearing basaltic glasses at 600 – 800 °C show a near-prevalence of anhydrite ($CaSO_4$) as the dominant coating phase formed on the glasses. This observation is in agreement with Ayris et al. (2013), who exclusively observed $CaSO_4$ on phonolite, dacite and rhyolite glasses reacted with $SO_{2(g)}$ at 300 – 800 °C, with only very minor amounts of Na_2SO_4 together with $CaSO_4$ on a tephrite glass reacted with $SO_{2(g)}$ at 300 – 600 °C. In my experiments I observe a more complex and diverse range of reaction products in the coatings including $CaSO_4$, $MgSO_4$, Na_2SO_4, Fe_2O_3 and Fe-Ti-oxide.

6.2.1.1 Experiments with Fe-free glasses

First, experiments with Fe-free glasses in the system Anorthite-Diopside reveal that not only the glass composition and the abundance of Ca in the glass control the formation of sulfate coatings, but also that the temperature and the glass properties play an essential role. Below the glass transition temperature (T_g) the total amount of sulfate formed increases with the abundance of anorthite component in the glass. Above T_g at 800 °C, the amount of sulfate increases with decreasing $T_l - T_g$, where T_l is the liquidus temperature. Hence, the eutectic glass is reacted the fastest and forms the largest amount of sulfate in the coating

(Figure 3-10). The rate of reaction is controlled by the mobility of the sulfate-forming cations in the glass, which changes at T_g.

The temperature also controls the composition of the sulfate, $X_{Ca}^{sulfate}$. The following two relationships are observed:

1) $X_{Ca}^{sulfate} > X_{Ca}^{glass}$

2) $X_{Ca,800\,°C}^{sulfate} > X_{Ca,600\,°C}^{sulfate}$

Significant amounts of Mg-sulfate are only observed at 600 °C (below T_g), whereas at 800 °C the sulfate almost exclusively consists of anhydrite. Finally, Na_2SO_4 was only observed on the albite endmember glass in the Fe-free experiments.

6.2.1.2 Experiments with Fe-bearing glasses

The Fe-bearing tholeiitic basalt glasses are pre-equilibrated at oxygen fugacities relative to the Ni-NiO buffer (NNO) of NNO-1.5, NNO and NNO+1. The reaction products in experiments with $SO_{2(g)}$ at 700 °C show a dependency of the reaction products on the Fe^{3+}/Fe_{tot} ratio. In these experiments $CaSO_4$ is always accompanied by either $MgSO_4$, Na_2SO_4 or both. With increasing Fe^{3+}/Fe_{tot} the abundance of the sulfates shifts. In the case of the NNO-1.5 experiment the coating consists of $CaSO_4$ and $MgSO_4$, at NNO the coating consists of $CaSO_4$, $MgSO_4$ and Na_2SO_4, and at NNO+1 the coating consists of $CaSO_4$ and Na_2SO_4, lacking $MgSO_4$.

I propose that the formation of these different sulfates is controlled by the role which the cations have in the glass structure. Tetrahedrally coordinated Fe^{3+} and Al^{3+} in the basalt glasses require charge balancing by di- or monovalent cations. As the tholeiitic glasses are reacted with $SO_{2(g)}$ the Fe^{3+}/Fe_{tot} ratio increases, requiring more charge compensation. The degree of oxidation is the largest in the case of the glass pre-equilibrated at NNO-1.5. In this case, Na remains in the glass as a charge compensating cation.

The oxidation of the glass is an important part of the reaction with $SO_{2(g)}$. The outward diffusion of the sulfate-forming cations is charge balanced by the inward diffusion of electron holes (Figure 5-9). Iron oxidizes from Fe^{2+} to Fe^{3+}, which may change the role in the glass structure from a network modifying cation to a tetrahedrally coordinated network forming cation. Accordingly, an alkali or alkaline earth metal is required as a charge balancing cation. This is observed in some experiments where Fe and Na are correlated in the modified and oxidized zone of the basalt glass.

6.2.2 Implications

Fast $SO_{2(g)}$ scavenging by the reaction with aluminosilicates occurs primarily at high temperature above T_g. This limits the temperature window in which $SO_{2(g)}$ can be scavenged in large explosive eruptions onto volcanic ash particles to a minimum of 600 °C depending on the glass composition (Figure 1-2). It is not possible to estimate the amount of potential $SO_{2(g)}$ scavenging onto glassy volcanic ash based on the concentration of Ca. The degree of reaction and the reaction products depend on the structure of the reacted silicates and the structural role of the sulfate-forming cations (Ca, Mg, Na) in the silicate.

The experimental results show that the reaction of $SO_{2(g)}$ with basaltic glasses can mobilize several major elements including Ca, Mg, Na, Fe and Ti. Where silicates are exposed to $SO_{2(g)}$ at high temperature for longer periods of time or repeatedly, the silicates can become significantly depleted in these elements. Such a process occurs in the subvolcanic environment (Figure 1-2), where large volumes of reactive gas can alter rocks significantly, resulting in compositions which are highly enriched in SiO_2 and Al_2O_3.

As outlined in the introduction, basaltic rocks and high temperature $SO_{2(g)}$ play or have played significant roles in the volcanic processes on Mars, Venus and Io. Remote sensing and robotic missions to these planetary bodies should therefore look for traces of such gas-solid reaction products. For example, on Io high abundance of Na and S on the planetary surface has been suggested to be the product of the reaction between $SO_{2(g)}$ and silicate materials (Johnson and Burnett, 1993; Burnett et al., 1997). The experimental results presented here suggest that these Na-S rich materials may be the reaction product of $SO_{2(g)}$ and a moderately oxidized basalt. The formation of Na_2SO_4 as a reaction product does not require uncommonly high Na-concentrations in the reactant. It may form where Na is not retained in the glass as a charge compensating cation.

6.3 Future work

It is important to better quantify the diffusivities of volatile species in silicate melts and glasses. Depending on the speciation the diffusivities vary and hence affect the estimation of volatile loss from a glass or melt to the gas phase such as in the case of lunar volatiles. Future experiments may also address how the metals are complexed by volatile elements (H, S, Cl and F) in the gas phase, and how this complexation affects the volatility and degassing behavior of trace metals from silicate melts at lunar and terrestrial conditions. Volcanic gases are a major component of global volatile and metal cycles, linking the Earth's sub-surface with the atmosphere and hydrosphere. There is some evidence to indicate that transport of metals in the gas phase may control isotopic fractionation of metals from melts. Gannoun et al. (2015) show that radiogenic Re is more volatile than non-radiogenic Os, resulting in isotopic fractionation during magmatic degassing.

Experimental quantification of metal degassing, and associated isotopic fractionation, is of importance for models concerned with the rate and mechanisms of ore deposit formation and the impact of toxic metals on the environment in volcanically active regions, but also the isotopic evolution of magma systems with gases. Similarly, such experiments are required for volcanic conditions on the Moon and the other terrestrial planets Mercury, Venus and Mars.

All gas-solid experiments presented here were conducted with $SO_{2(g)}$ without controlling the fO_2. Gibbs Free Energy minimization calculations suggest that the resulting fO_2 in these experiments is just above the magnetite-hematite buffer in the stability field of hematite. These are appropriate conditions for fO_2 and fSO_2 conditions on Earth, but not for conditions as they occur or occurred on other terrestrial planetary bodies in the solar system (Figure 4-14).

To constrain the mineralogy of phases formed via the reaction of volcanic gases and silicates it is crucial to control additional variables such as fO_2 in future experiments. This will allow predictions about mineral phases on the surfaces of other planetary bodies with active volcanism or volcanic histories including Mars, Mercury, Venus, Io and the Moon.

To improve the understanding of the reaction mechanisms future experiments will greatly benefit form in situ analysis. In situ experiments will improve the time resolution providing insight into how the reaction rates evolve. The extensive chemical alteration of the reacted glasses affects the diffusive mobility of the cations in the glass, resulting in a nonconstant reaction rate.

The experiments show that the role of the alkali and alkaline earth metals in the glass structure affects their potential incorporation into sulfate reaction products. A better understanding of the role of these elements in the structure of glasses and the mechanisms and rates at which they diffuse in the glasses will significantly improve the interpretation and predictability of gas-solid reactions between glasses and gases such as $SO_{2(g)}$.

Finally, some of the major elements preferentially partition into the sulfate and oxide reaction products (e.g. Ca, Mg, Na, Fe, Ti), whereas others are retained in the altered glass (e.g. Si, Al). A similar chemical fractionation may affect the distribution of trace elements (Palm et al., 2018). This is of particular importance for chemical systems which are used for age dating such as Rb-Sr, U-Pb, Sm-Nd or K-Ca. For example, in a preliminary study, Palm et al. (2018) have shown that Pb partitions into the sulfate-oxide coating in the reaction between a basalt glass and $SO_{2(g)}$ at 700 °C, whereas U is retained in the glass. Additional experimental work on the partitioning of major and trace elements in gas-solid reactions is therefore required.

7 References

Africano F., Rompaey G. V., Bernard A. and Guern F. L. (2002) Deposition of trace elements from high temperature gases of Satsuma-Iwojima volcano. *Earth Planets Space* **54**, 275–286.

Aiuppa A., Dongarrà G., Valenza M., Federico C. and Pecoraino G. (2004) Degassing of trace volatile metals during the 2001 eruption of Etna. In *Volcanism and the Earth's Atmosphere* (eds. A. Robock and C. Oppenheimer). American Geophysical Union. pp. 41–54.

Aiuppa A., Federico C., Giudice G., Giuffrida G., Guida R., Gurrieri S., Liuzzo M., Moretti R. and Papale P. (2009) The 2007 eruption of Stromboli volcano: Insights from real-time measurement of the volcanic gas plume CO_2/SO_2 ratio. *J. Volcanol. Geotherm. Res.* **182**, 221–230.

Allard P., Aiuppa A., Bani P., Métrich N., Bertagnini A., Gauthier P.-J., Shinohara H., Sawyer G., Parello F., Bagnato E., Pelletier B. and Garaebiti E. (2016) Prodigious emission rates and magma degassing budget of major, trace and radioactive volatile species from Ambrym basaltic volcano, Vanuatu island Arc. *J. Volcanol. Geotherm. Res.* **322**, 119–143.

Allard P., Carbonnelle J., Métrich N., Loyer H. and Zettwoog P. (1994) Sulphur output and magma degassing budget of Stromboli volcano. *Nature* **368**, 326–330.

Allen D. and Hayhurst A. N. (1996) Reaction between gaseous sulfur dioxide and solid calcium oxide mechanism and kinetics. *J. Chem. Soc. Faraday Trans.* **92**, 1227–1238.

Alletti M., Baker D. R. and Freda C. (2007) Halogen diffusion in a basaltic melt. *Geochim. Cosmochim. Acta* **71**, 3570–3580.

Andersen A. and Kofstad P. (1984) The reaction of Ni-20Cr with SO_2 at 600-900 °C. *Corros. Sci.* **24**, 731–743.

Angeli F., Delaye J.-M., Charpentier T., Petit J.-C., Ghaleb D. and Faucon P. (2000) Influence of glass chemical composition on the Na–O bond distance: a ^{23}Na 3Q-MAS NMR and molecular dynamics study. *J. Non-Cryst. Solids* **276**, 132–144.

Armstrong L. S., Hirschmann M. M., Stanley B. D., Falksen E. G. and Jacobsen S. D. (2015) Speciation and solubility of reduced C–O–H–N volatiles in mafic melt: Implications for volcanism, atmospheric evolution, and deep volatile cycles in the terrestrial planets. *Geochim. Cosmochim. Acta* **171**, 283–302.

Arndt J. and von Engelhardt W. (1987) Formation of Apollo 17 orange and black glass beads. *J. Geophys. Res. Solid Earth* **92**, E372–E376.

Arndt J., von Engelhardt W., Gonzalez-Cabeza I. and Meier B. (1984) Formation of Apollo 15 green glass beads. *J. Geophys. Res. Solid Earth* **89**, C225–C232.

Ayris P. M. (2010) High temperature SO_2 chemisorption on model systems. Implications for in-plume processes. PhD thesis, York UK, Universityof York.

Ayris P. M. and Delmelle P. (2012) The immediate environmental effects of tephra emission. *Bull. Volcanol.* **74**, 1905–1936.

Ayris P. M., Delmelle P., Cimarelli C., Maters E. C., Suzuki Y. J. and Dingwell D. B. (2014) HCl uptake by volcanic ash in the high temperature eruption plume: Mechanistic insights. *Geochim. Cosmochim. Acta* **144**, 188–201.

Ayris P. M., Delmelle P., Pereira B., Maters E. C., Damby D. E., Durant A. J. and Dingwell D. B. (2015) Spatial analysis of Mount St. Helens tephra leachate compositions: implications for future sampling strategies. *Bull. Volcanol.* **77**, 1–17.

Ayris P. M., Lee A. F., Wilson K., Kueppers U., Dingwell D. B. and Delmelle P. (2013) SO_2 sequestration in large volcanic eruptions: High-temperature scavenging by tephra. *Geochim. Cosmochim. Acta* **110**, 58–69.

Balic-Zunic T., Garavelli A., Jakobsson S. P., Jonasson K., Katerinopoulos A., Kyriakopoulos K. and Acquafredda P. (2016) Fumarolic minerals: An overview of active european volcanoes. In *Updates in Volcanology - From Volcano Modelling to Volcano Geology* (ed. K. Nemeth). InTech.

Ballhaus C. (1993) Redox states of lithospheric and asthenospheric upper mantle. *Contrib. Mineral. Petrol.* **114**, 331–348.

Baltrusaitis J., Cwiertny D. M. and Grassian V. H. (2007) Adsorption of sulfur dioxide on hematite and goethite particle surfaces. *Phys. Chem. Chem. Phys.* **9**, 5542.

Barnes J. J., Franchi I. A., Anand M., Tartèse R., Starkey N. A., Koike M., Sano Y. and Russell S. S. (2013) Accurate and precise measurements of the D/H ratio and hydroxyl content in lunar apatites using NanoSIMS. *Chem. Geol.* **337**–**338**, 48–55.

Barone G., Mazzoleni P., Corsaro R. A., Costagliola P., Di Benedetto F., Ciliberto E., Gimeno D., Bongiorno C. and Spinella C. (2016) Nanoscale surface modification of Mt. Etna volcanic ashes. *Geochim. Cosmochim. Acta* **174**, 70–84.

Basalt Volcanism Study Project (1981) *Basaltic Volcanism on the Terrestrial Planets*. Pergamon, New York, 1286 pp.

Bastow B. D., Wood G. C. and Whittle D. P. (1981) Morphologies of uniform adherent scales on binary alloys. *Oxid. Met.* **16**, 1–28.

Beatty J. K., Petersen C. C. and Chaikin A. (1999) *The New Solar System*, Cambridge University Press, Cambridge, UK.

Behrens H. (1992) Na and Ca tracer diffusion in plagioclase glasses and supercooled melts. *Chem. Geol.* **96**, 267–275.

Behrens H. and Gaillard F. (2006) Geochemical aspects of melts: volatiles and redox behavior. *Elements* **2**, 275–280.

Behrens H. and Stelling J. (2011) Diffusion and redox reactions of sulfur in silicate melts. *Rev. Mineral. Geochem.* **73**, 79–111.

Bell A. S., Shearer C., de Moor J. M. and Provencio P. (2015) Using the sulfide replacement petrology in lunar breccia 67915 to construct a thermodynamic model of S-bearing fluid in the lunar crust. *Geochim. Cosmochim. Acta* **171**, 50–60.

Berger J. A., Schmidt M. E., Gellert R., Campbell J. L., King P. L., Flemming R. L., Ming D. W., Clark B. C., Pradler I., VanBommel S. J. V., Minitti M. E., Fairén A. G., Boyd N. I., Thompson L. M., Perrett G. M., Elliott B. E. and Desouza E. (2016) A global Mars dust composition refined by the Alpha-Particle X-ray Spectrometer in Gale Crater. *Geophys. Res. Lett.* **43**, 2015GL066675.

Birks N., Meier G. H. and Pettit F. S. (2006) *Introduction to the High-Temperature Oxidation of Metals*., Cambridge University Press, Cambridge, UK; New York.

Blaney D. L., Johnson T. V., Matson D. L. and Veeder G. J. (1995) Volcanic eruptions on Io: Heat flow, resurfacing, and lava composition. *Icarus* **113**, 220–225.

Bluth G. J. S., Doiron S. D., Schnetzler C. C., Krueger A. J. and Walter L. S. (1992) Global tracking of the SO_2 clouds from the June, 1991 Mount Pinatubo eruptions. *Geophys. Res. Lett.* **19**, 151–154.

Brunauer S., Emmett P. H. and Teller E. (1938) Adsorption of gases in multimolecular layers. *J. Am. Chem. Soc.* **60**, 309–319.

Burkhard D. J. M. (2001) Crystallization and oxidation of Kilauea basalt glass: Processes during reheating experiments. *J. Petrol.* **42**, 507–527.

Burnett D. S., Goreva J., Epstein S., Haldemann S. L. and Johnson A. R. (1997) SO_2-rock interaction on Io. Interaction with pure SO2. *J. Geophys. Res. Atmospheres* **102**, 19371–19382.

Burnham C. W. (1979) Magmas and hydrothermal fluids. In *Geochemistry of Hydrothermal Ore Deposits* (ed. H. L. Barnes). pp. 71–136.

Butler P. Jr. (1978) Recognition of lunar glass droplets produced directly from endogenous liquids: The evidence from S-Zn coations. *Proc. Lunar Sci. Conf.* **9**, 1459–1471.

Butler P. and Meyer C. (1976) Sulfur prevails in coatings on glass droplets - Apollo 15 green and brown glasses and Apollo 17 orange and black (devitrified) glasses. *Proc. Lunar Sci. Conf.* **7**, 1561–1581.

Cailleteau C., Angeli F., Devreux F., Gin S., Jestin J., Jollivet P. and Spalla O. (2008) Insight into silicate-glass corrosion mechanisms. *Nat. Mater.* **7**, 978–983.

Carmichael I. S. (1991) The redox states of basic and silicic magmas: a reflection of their source regions? *Contrib. Mineral. Petrol.* **106**, 129–141.

Carr M. H. (1986) Silicate volcanism on Io. *J. Geophys. Res. Solid Earth* **91**, 3521–3532.

Casanova I. and Aulesa V. (2000) Construction Materials from In-Situ Resources on the Moon and Mars. In *Space 2000* American Society of Civil Engineers. pp. 638–644.

Chase M. W. (1998) *NIST-JANAF Thermochemical Tables*. 4th ed., Physical and Chemical Reference Data.

Chason E., Jadhav N., Pei F., Buchovecky E. and Bower A. (2013) Growth of whiskers from Sn surfaces: Driving forces and growth mechanisms. *Prog. Surf. Sci.* **88**, 103–131.

Chen Y., Zhang Y., Liu Y., Guan Y., Eiler J. and Stolper E. M. (2015) Water, fluorine, and sulfur concentrations in the lunar mantle. *Earth Planet. Sci. Lett.* **427**, 37–46.

Choi B.-K. and Lockwood D. J. (2005) Peculiarities of the structural phase transitions in Na_2SO_4(V): a Raman scattering study. *J. Phys. Condens. Matter* **17**, 6095.

Chou C.-L., Boynton W. V., Sundberg L. L. and Wasson J. T. (1975) Volatiles on the surface of Apollo 15 green glass and trace-element distributions among Apollo 15 soils. *Proc. Lunar Sci. Conf.* **6**, 1701–1727.

Cirlin E. H. and Housley R. M. (1979) Scanning Auger Microprobe and atomic absorption studies of lunar volcanic volatiles. *Proc. Lunar Sci. Conf.* **10**, 341–354.

Clanton U. S., McKay D. S., Waits G. and Fuhrman R. (1978) Sublimate morphology on 74001 and 74002 orange and black glassy droplets. *Proc. Lunar Sci. Conf.* **9**, 1945–1957.

Clarke D. R. (2003) The lateral growth strain accompanying the formation of a thermally grown oxide. *Acta Mater.* **51**, 1393–1407.

Cochain B., Pinet O. and Richet P. (2013) Diffusion of sodium ions driven by charge compensation as the rate-limiting step of internal redox reactions. *J. Non-Cryst. Solids* **365**, 23–26.

Colson R. O. (1992) Mineralization on the Moon?: Theoretical Considerations of Apollo 16 "Rusty Rocks," Sulfide Replacement in 67016, and Surface-Correlated Volatiles on Lunar Volcanic Glass. *Proc. Lunar Planet. Sci.* **22**, 427–436.

Cook G. B. and Cooper R. F. (2000) Iron concentration and the physical processes of dynamic oxidation in an alkaline earth aluminosilicate glass. *Am. Mineral.* **85**, 397–406.

Cook G. B., Cooper R. F. and Wu T. (1990) Chemical diffusion and crystalline nucleation during oxidation of ferrous iron-bearing magnesium aluminosilicate glass. *J. Non-Cryst. Solids* **120**, 207–222.

Cooper R. F. (2018) Redox thermodynamics and kinetics in silicate melts and glasses - and related morphology/texture. In *Encyclopedia of Glass Science, Technology, History and Culture* (ed. P. Richet). Wiley/American Ceramic Society, New York.

Cooper R. F., Fanselow J. B. and Poker D. B. (1996a) The mechanism of oxidation of a basaltic glass: Chemical diffusion of network-modifying cations. *Geochim. Cosmochim. Acta* **60**, 3253–3265.

Cooper R. F., Fanselow J. B., Weber J. K. R., Merkley D. R. and Poker D. B. (1996b) Dynamics of oxidation of a Fe^{2+}-bearing aluminosilicate (basaltic) melt. *Science* **274**, 1173–1176.

Crank J. (1975) *The Mathematics of Diffusion*. 2nd ed., Clarendon Press, Oxford, UK.

Crawford I. A. (2015) Lunar resources A review. *Prog. Phys. Geogr.* **39**, 137–167.

Dalby K. N., Berger J. A., Brand H. E. A., Cairney J. M., Eder K., Eggins S. M., Herring A., Hervig R. L., Krieder P. B., Mernagh T. P., Palm A. B., Renggli C. J., Troitzsch U., Yue L. and King P. L. (2018) Analytical techniques for probing gases and

small-scale layers that preserve information on gas-solid interactions. *Rev. Mineral. Geochem.* **84**, 103–175.

Davies A. G., Keszthelyi L. P. and Harris A. J. L. (2010) The thermal signature of volcanic eruptions on Io and Earth. *J. Volcanol. Geotherm. Res.* **194**, 75–99.

Delano J. W. (1990) Buoyancy-driven melt segregation in the Earth's Moon. I - Numerical results. *Proc. Lunar Sci. Conf.* **20**, 3–12.

Delmelle P., Lambert M., Dufrêne Y., Gerin P. and Óskarsson N. (2007) Gas/aerosol–ash interaction in volcanic plumes: New insights from surface analyses of fine ash particles. *Earth Planet. Sci. Lett.* **259**, 159–170.

Delmelle P. and Stix J. (2000) Volcanic gases. In *Encyclopedia of Volcanoes* Academic Press. pp. 803–815.

Delmelle P., Wadsworth F. B., Maters E. C. and Ayris P. M. (2018) High temperature uptake of volcanic gases on ash in eruption plumes. *Rev. Mineral. Geochem.* **84**, 285–308.

Demény A., Vennemann T. W., Harangi S., Homonnay Z. and Fórizs I. (2006) H_2O-δD-FeIII relations of dehydrogenation and dehydration processes in magmatic amphiboles. *Rapid Commun. Mass Spectrom.* **20**, 919–925.

Denevi B. W., Ernst C. M., Meyer H. M., Robinson M. S., Murchie S. L., Whitten J. L., Head J. W., Watters T. R., Solomon S. C., Ostrach L. R., Chapman C. R., Byrne P. K., Klimczak C. and Peplowski P. N. (2013) The distribution and origin of smooth plains on Mercury. *J. Geophys. Res. Planets* **118**, 891–907.

DePaolo D. J. and Cole D. R. (2013) Geochemistry of geologic carbon sequestration: An overview. *Rev. Mineral. Geochem.* **77**, 1–14.

Dingwell D. B. (1990) Effects of structural relaxation on cationic tracer diffusion in silicate melts. *Chem. Geol.* **82**, 209–216.

Douglas R. W. and Isard J. O. (1949) The action of water and of sulphur dioxide on glass surfaces. *J. Soc. Glass Technol.* **33**, 289–355.

Doute S. (2002) Dynamics and evolution of SO_2 gas condensation around Prometheus-like volcanic plumes on Io as seen by the near infrared mapping spectrometer. *Icarus* **158**, 460–482.

Du H. (2000) Thermodynamic assessment of the K_2SO_4-Na_2SO_4-$MgSO_4$-$CaSO_4$ system. *J. Phase Equilibria* **21**, 6–18.

Dufresne C. D. M., King P. L., Dyar M. D. and Dalby K. N. (2015) Effect of SiO_2, total FeO, Fe^{3+}/Fe^{2+}, and alkali elements in basaltic glasses on mid-infrared. *Am. Mineral.* **94**, 1580–1590.

Elkins-Tanton L. T., Chatterjee N. and Grove T. L. (2003) Magmatic processes that produced lunar fire fountains. *Geophys. Res. Lett.* **30**, 1513–1516.

Elkins-Tanton L. T. and Grove T. L. (2011) Water (hydrogen) in the lunar mantle: Results from petrology and magma ocean modeling. *Earth Planet. Sci. Lett.* **307**, 173–179.

Evans A. G., Crumley G. B. and Demaray R. E. (1983) On the mechanical behavior of brittle coatings and layers. *Oxid. Met.* **20**, 193–216.

Evans Jr. H. T. (1979) The thermal expansion of anhydrite to 1000 °C. *Phys. Chem. Miner.* **4**, 7782.

Farges F., Lefrère Y., Rossano S., Berthereau A., Calas G. and Brown G. E. (2004) The effect of redox state on the local structural environment of iron in silicate glasses: a combined XAFS spectroscopy, molecular dynamics, and bond valence study. *J. Non-Cryst. Solids* **344**, 176–188.

Fegley B. (1992) Lunar volcanic gases: the predicted presence of chlorofluorocarbon gases. *Lunar Planet. Sci. Conf.* **23**, 347–348.

Fegley B. (2006) *Practical Chemical Thermodynamics for Geoscientists*., Academic Pr Inc, Amsterdam.

Fegley B. (1991) Thermodynamic models of the chemistry of lunar volcanic gases. *Geophys. Res. Lett.* **18**, 2073–2076.

Fegley B. and Prinn R. G. (1989) Estimation of the rate of volcanism on Venus from reaction rate measurements. *Nature* **337**, 55–58.

Fegley B. and Swindle T. D. (1993) Lunar volatiles: implications for Lunar resource utilization. In *Resources of Near-Earth Space* (eds. J. S. Lewis, M. S. Matthews, and M. L. Guerrieri). University of Arizona, Tuscon, AZ. pp. 367–426.

Fegley B. and Zolotov M. Y. (2000) Chemistry of sodium, potassium, and chlorine in volcanic gases on Io. *Icarus* **148**, 193–210.

Fegley B., Zolotov M. Y. and Lodders K. (1997) The oxidation state of the lower atmosphere and surface of Venus. *Icarus* **125**, 416–439.

Fischer T. P., Morrissey M. M., Marta Lucía Calvache V., Diego Gòmez M., Roberto Torres C., Stix J. and Williams S. N. (1994) Correlations between SO2 flux and long-period seismicity at Galeras volcano. *Nature* **368**, 135–137.

Fogel R. A. and Rutherford M. J. (1995) Magmatic volatiles in primitive lunar glasses: I. FTIR and EPMA analyses of Apollo 15 green and yellow glasses and revision of the volatile-assisted fire-fountain theory. *Geochim. Cosmochim. Acta* **59**, 201–215.

Franz H. B., King P. L. and Gaillard F. (2018) Sulfur on Mars from the atmosphere to the core. In *Volatiles in the Martian Crust* (eds. J. Filiberto and S. P. Schwenzer). Elsevier.

Freyer D. and Voigt W. (2003) Crystallization and phase stability of $CaSO_4$ and $CaSO_4$ - based salts. *Monatshefte Für Chem. Chem. Mon.* **134**, 693–719.

Freyer D., Voigt W. and Köhnke K. (1998) The phase diagram of the system Na_2SO_4 - $CaSO_4$. *Eur. J. Solid State Inorg. Chem.* **35**, 595–606.

Gaddis L. R., Pieters C. M. and Hawke B. R. (1985) Remote sensing of lunar pyroclastic mantling deposits. *Icarus* **61**, 461–489.

Gaddis L. R., Staid M. I., Tyburczy J. A., Hawke B. R. and Petro N. E. (2003) Compositional analyses of lunar pyroclastic deposits. *Icarus* **161**, 262–280.

Gaillard F. and Scaillet B. (2009) The sulfur content of volcanic gases on Mars. *Earth Planet. Sci. Lett.* **279**, 34–43.

Gaillard F., Schmidt B., Mackwell S. and McCammon C. (2003) Rate of hydrogen–iron redox exchange in silicate melts and glasses. *Geochim. Cosmochim. Acta* **67**, 2427–2441.

Gannoun A., Vlastélic I. and Schiano P. (2015) Escape of unradiogenic osmium during sub-aerial lava degassing: Evidence from fumarolic deposits, Piton de la Fournaise, Réunion Island. *Geochim. Cosmochim. Acta* **166**, 312–326.

Gao Y. and Chen D. (2006) Heterogeneous reactions of sulfur dioxide on dust. *Sci. China Ser. B* **49**, 273–280.

Gesmundo F., Asmundis C. de and Nanni P. (1983) The corrosion of nickel in 1 atm of pure SO_2 at 600–1000 °C and the mechanism of formation of the two-layered scales. *Oxid. Met.* **20**, 217–240.

Gilewicz-Wolter J. (1988) Studies of the mechanism of reaction of nickel with SO_2. *Oxid. Met.* **29**, 225–238.

Gilewicz-Wolter J., Żurek Z. and Dudała J. (2004) Corrosion of manganese in sulfur dioxide at high temperatures. *Solid State Ion.* **170**, 287–295.

Giordano D., Russell J. K. and Dingwell D. B. (2008) Viscosity of magmatic liquids: A model. *Earth Planet. Sci. Lett.* **271**, 123–134.

Gislason S. R., Hassenkam T., Nedel S., Bovet N., Eiriksdottir E. S., Alfredsson H. A., Hem C. P., Balogh Z. I., Dideriksen K., Oskarsson N., Sigfusson B., Larsen G. and Stipp S. L. S. (2011) Characterization of Eyjafjallajökull volcanic ash particles and a protocol for rapid risk assessment. *Proc. Natl. Acad. Sci.* **108**, 7307–7312.

Glaze L. S. (1999) Transport of SO_2 by explosive volcanism on Venus. *J. Geophys. Res. Planets* **104**, 18899–18906.

Gooding J. L. (1978) Chemical weathering on Mars thermodynamic stabilities of primary minerals (and their alteration products) from mafic igneous rocks. *Icarus* **33**, 483–513.

Goodrich C. A., Scott E. R. D. and Fioretti A. M. (2004) Ureilitic breccias: clues to the petrologic structure and impact disruption of the ureilite parent asteroid. *Chem. Erde - Geochem.* **64**, 283–327.

Grabowsky S., Luger P., Buschmann J., Schneider T., Schirmeister T., Sobolev A. N. and Jayatilaka D. (2012) The significance of ionic bonding in sulfur dioxide: Bond orders from X-ray diffraction data. *Angew. Chem. Int. Ed.* **51**, 6776–6779.

Greenwood J. P., Itoh S., Sakamoto N., Warren P., Taylor L. and Yurimoto H. (2011) Hydrogen isotope ratios in lunar rocks indicate delivery of cometary water to the Moon. *Nat. Geosci.* **4**, 79–82.

Hall A. J. (1986) Pyrite-pyrrhotine redox reactions in nature. *Miner. Mag* **50**, 223–229.

Halmer M. M., Schmincke H.-U. and Graf H.-F. (2002) The annual volcanic gas input into the atmosphere, in particular into the stratosphere: a global data set for the past 100 years. *J. Volcanol. Geotherm. Res.* **115**, 511–528.

Hammond J. O. S., Kendall J.-M., Stuart G. W., Keir D., Ebinger C., Ayele A. and Belachew M. (2011) The nature of the crust beneath the Afar triple junction: Evidence from receiver functions. *Geochem. Geophys. Geosystems* **12**, Q12004.

Hapanowicz R. P. and Condrate R. A. (1996a) High-temperature Raman spectral investigation of sodium sulfate. *Spectrosc. Lett.* **29**, 133–141.

Hapanowicz R. P. and Condrate S. R. A. (1996b) Raman spectral investigation of sulfate inclusions in sodium calcium silicate glasses. *J. Solid State Chem.* **123**, 183–185.

Haskin L. A., Colson R. O., Vaniman D. T. and Gillett S. L. (1993) A geochemical assessment of possible lunar ore formation. In *Resources of near-earth space* pp. 17–50.

Hauri E. H., Saal A. E., Rutherford M. J. and Van Orman J. A. (2015) Water in the Moon's interior: Truth and consequences. *Earth Planet. Sci. Lett.* **409**, 252–264.

Head J. W. (1976) Lunar volcanism in space and time. *Rev. Geophys.* **14**, 265–300.

Head J. W. and Wilson L. (1992) Lunar mare volcanism: Stratigraphy, eruption conditions, and the evolution of secondary crusts. *Geochim. Cosmochim. Acta* **56**, 2155–2175.

Head J. W., Wilson L. and Weitz C. M. (2002) Dark ring in southwestern Orientale Basin: Origin as a single pyroclastic eruption. *J. Geophys. Res. Planets* **107**, 1–1.

Heiken G. H., McKay D. S. and Brown R. W. (1974) Lunar deposits of possible pyroclastic origin. *Geochim. Cosmochim. Acta* **38**, 1703–1718.

Heiken G., Vaniman D. and French B. M. eds. (1991) *Lunar Sourcebook: A User's Guide To The Moon*., Cambridge University Press, Cambridge [England] ; New York.

Henderson G. S. (2005) The structure of silicate melts: a glass perspective. *Can. Mineral.* **43**, 1921–1958.

Henley R. W. and Berger B. R. (2013) Nature's refineries – Metals and metalloids in arc volcanoes. *Earth-Sci. Rev.* **125**, 146–170.

Henley R. W., Brink F. J., King P. L., Leys C., Ganguly J., Mernagh T., Middleton J., Renggli C. J., Sieber M., Troitzsch U. and Turner M. (2017) High temperature gas–solid reactions in calc–silicate Cu–Au skarn formation; Ertsberg, Papua Province, Indonesia. *Contrib. Mineral. Petrol.* **172**, 106.

Henley R. W. and Hughes G. O. (2016) SO_2 flux and the thermal power of volcanic eruptions. *J. Volcanol. Geotherm. Res.* **324**, 190–199.

Henley R. W., King P. L., Wykes J. L., Renggli C. J., Brink F. J., Clark D. A. and Troitzsch U. (2015) Porphyry copper deposit formation by sub-volcanic sulphur dioxide flux and chemisorption. *Nat. Geosci.* **8**, 210–215.

Henley R. W. and McNabb A. (1978) Magmatic vapor plumes and ground-water interaction in porphyry copper emplacement. *Econ. Geol.* **73**, 1–20.

Henley R. W. and Seward T. M. (2018) Gas-solid reactions and reactive mass transport in volcanic systems. *Rev. Mineral. Geochem.* **84**, 309–349.

Hinkley T. K., Lamothe P. J., Wilson S. A., Finnegan D. L. and Gerlach T. M. (1999) Metal emissions from Kilauea, and a suggested revision of the estimated worldwide metal output by quiescent degassing of volcanoes. *Earth Planet. Sci. Lett.* **170**, 315–325.

Hirschmann M. M. and Withers A. C. (2008) Ventilation of CO_2 from a reduced mantle and consequences for the early Martian greenhouse. *Earth Planet. Sci. Lett.* **270**, 147–155.

Hirschmann M. M., Withers A. C., Ardia P. and Foley N. T. (2012) Solubility of molecular hydrogen in silicate melts and consequences for volatile evolution of terrestrial planets. *Earth Planet. Sci. Lett.* **345**–**348**, 38–48.

Holloway J. R. and Burnham C. W. (1972) Melting relations of basalt with equilibrium water pressure less than total pressure. *J. Petrol.* **13**, 1–29.

Hsueh C. H. and Evans A. G. (1983) Oxidation induced stresses and some effects on the behavior of oxide films. *J. Appl. Phys.* **54**, 6672–6686.

Hu G., Dam-Johansen K., Wedel S. and Peter Hansen J. (2006) Review of the direct sulfation reaction of limestone. *Prog. Energy Combust. Sci.* **32**, 386–407.

Hu R., Seager S. and Bains W. (2013) Photochemistry in terrestrial exoplanet atmospheres. II. H_2S and SO_2 photochemistry in anoxic atmospheres. *Astrophys. J.* **769**, 6.

Johannsen A. (1931) *A Descriptive Petrography of the Igneous Rocks: Introduction, textures, classifications and glossary*., University of Chicago Press, US.

Johnson M. L. and Burnett D. S. (1993) SO_2-rock interaction on Io: Reaction under highly oxidizing conditions. *J. Geophys. Res.* **98**, 1223–1230.

Kerber L., Head J. W., Blewett D. T., Solomon S. C., Wilson L., Murchie S. L., Robinson M. S., Denevi B. W. and Domingue D. L. (2011) The global distribution of pyroclastic deposits on Mercury: The view from MESSENGER flybys 1–3. *Planet. Space Sci.* **59**, 1895–1909.

Kerber L., Head J. W., Solomon S. C., Murchie S. L., Blewett D. T. and Wilson L. (2009) Explosive volcanic eruptions on Mercury: Eruption conditions, magma volatile content, and implications for interior volatile abundances. *Earth Planet. Sci. Lett.* **285**, 263–271.

Kieffer S. W. (1982) Dynamics and thermodynamics of volcanic eruptions - Implications for the plumes on Io. In *Satellites of Jupiter* Satellites of Jupiter. pp. 647–723.

Kieffer S. W. and Sturtevant B. (1984) Laboratory studies of volcanic jets. *J. Geophys. Res. Solid Earth* **89**, 8253–8268.

King P. L., Wheeler V. W., Renggli C. J., Palm A. B., Wilson S. A., Harrison A. L., Morgan B., Nekvasil H., Troitzsch U., Mernagh T. P., Yue L., Bayon A., DiFrancesco N.J., Baile R., Kreider P. and Lipiński W (2018) Experimental approaches and theoretical aspects of gas-solid reactions with case studies. *Rev. Mineral. Geochem.* **84**, 1–56.

King P. L. and Holloway J. R. (2002) CO_2 solubility and speciation in intermediate (andesitic) melts: the role of H2O and composition. *Geochim. Cosmochim. Acta* **66**, 1627–1640.

King P. L. and McLennan S. M. (2010) Sulfur on Mars. *Elements* **6**, 107–112.

Knoche R., Dingwell D. B. and Webb S. L. (1992) Non-linear temperature dependence of liquid volumes in the system albite-anorthite-diopside. *Contrib. Mineral. Petrol.* **111**, 61–73.

Kreider P. and Lipiński W. (2018) High-temperature gas-solid heterogenous reactions in industrial processes. *Rev. Mineral. Geochem.* **84**, 499–514.

Kubicki J.D. and Watts H.D. (2018) Reaction mechanisms and solid-gas phase reactions: Theory and density functional theory simulations. *Rev. Mineral. Geochem.* **84**, 85–101.

Kumar S. (1985) The SO_2 atmosphere and ionosphere of Io: Ion chemistry, atmospheric escape, and models corresponding to the Pioneer 10 radio occultation measurements. *Icarus* **61**, 101–123.

Le Cloarec M. F., Allard P., Ardouin B., Giggenbach W. F. and Sheppard D. S. (1992) Radioactive isotopes and trace elements in gaseous emissions from White Island, New Zealand. *Earth Planet. Sci. Lett.* **108**, 19–28.

Le Losq C. and Neuville D. R. (2017) Molecular structure, configurational entropy and viscosity of silicate melts: Link through the Adam and Gibbs theory of viscous flow. *J. Non-Cryst. Solids* **463**, 175–188.

Le Losq C., Neuville D. R., Florian P., Henderson G. S. and Massiot D. (2014) The role of Al3+ on rheology and structural changes in sodium silicate and aluminosilicate glasses and melts. *Geochim. Cosmochim. Acta* **126**, 495–517.

Lee R. J., King P. L. and Ramsey M. S. (2010) Spectral analysis of synthetic quartzofeldspathic glasses using laboratory thermal infrared spectroscopy. *J. Geophys. Res.* **115**.

Lellouch E., Strobel D. F., Belton M. J. S., Summers M. E., Paubert G. and Moreno R. (1996) Detection of Sulfur Monoxide in Io's Atmosphere. *Astrophys. J. Lett.* **459**, L107.

Li E. Y., Chareev, D. A., Shilobreeva, S. N., Grichuk, D. V. and Tyutyunnik, O. A. (2010) Experimental study of sulfur dioxide interaction with silicates and aluminosilicates at temperatures of 650 and 850°C. *Geochem. Int.* **48**, 1039–1046.

Li E. Y., Grichuk D. V., Shilobreeva S. N. and Chareev D. A. (2011) Interaction between (alumino)silicates and SO_2-containing gas: experiment and thermodynamic model. *Vestn. Otd. Nauk O Zemle RAN* **3**, 1–7.

Lide D. R. (2010) *CRC Handbook of Chemistry and Physics, 90th Edition (Internet Version 2010)*. 90th ed., CRC Press/Taylor and Francis, Boca Raton, FL.

Liu Y., Wang A. and Freemen J. J. (2009) Raman, MIR, and NIR spectroscopic study of calcium sulfates: gypsum, bassanite, and anhydrite. *Lunar Planet. Sci. Conf.* **40**, 2128.

Lopes R. M. C. and Spencer J. R. (2007) *Io after Galileo: A New View of Jupiter's Volcanic Moon*. Springer; Praxis Publishing, Berlin ; New York : Chichester, UK.

Lopes-Gautier R., Douté S., Smythe W. D., Kamp L. W., Carlson R. W., Davies A. G., Leader F. E., McEwen A. S., Geissler P. E., Kieffer S. W., Keszthelyi L., Barbinis E., Mehlman R., Segura M., Shirley J. and Soderblom L. A. (2000) A close-up look at Io from Galileo's near-infrared mapping spectrometer. *Science* **288**, 1201–1204.

Luthra K. L. and Worrell W. L. (1978) Simultaneous sulfidation-oxidation of nickel at 603°C in argon-SO_2 atmospheres. *Metall. Trans. A* **9**, 1055–1061.

Magnien V., Neuville D. R., Cormier L., Roux J., Hazemann J.-L., de Ligny D., Pascarelli S., Vickridge I., Pinet O. and Richet P. (2008) Kinetics and mechanisms of iron redox reactions in silicate melts: The effects of temperature and alkali cations. *Geochim. Cosmochim. Acta* **72**, 2157–2168.

Martens R. M., Rosenhauer M., Büttner H. and von Gehlen K. (1987) Heat capacity and kinetic parameters in the glass transformation interval of diopside, anorthite and albite glass. *Chem. Geol.* **62**, 49–70.

Mastin L. G. and Ghiorso M. S. (2001) Adiabatic temperature changes of magma–gas mixtures during ascent and eruption. *Contrib. Mineral. Petrol.* **141**, 307–321.

Maters E. C., Delmelle P. and Gunnlaugsson H. P. (2017) Controls on iron mobilisation from volcanic ash at low pH: Insights from dissolution experiments and Mössbauer spectroscopy. *Chem. Geol.* **449**, 73–81.

Maters E. C., Delmelle P., Rossi M. J., Ayris P. M. and Bernard A. (2016) Controls on the surface chemical reactivity of volcanic ash investigated with probe gases. *Earth Planet. Sci. Lett.* **450**, 254–262.

Mather T. A., Witt M. L. I., Pyle D. M., Quayle B. M., Aiuppa A., Bagnato E., Martin R. S., Sims K. W. W., Edmonds M., Sutton A. J. and Ilyinskaya E. (2012) Halogens and trace metal emissions from the ongoing 2008 summit eruption of Kīlauea volcano, Hawai`i. *Geochim. Cosmochim. Acta* **83**, 292–323.

McCanta M. C., Dyar M. D., Rutherford M. J., Lanzirotti A., Sutton S. R. and Thomson B. J. (2017) In situ measurement of ferric iron in lunar glass beads using Fe-XAS. *Icarus* **285**, 95–102.

McCormick B. T., Edmonds M., Mather T. A., Campion R., Hayer C. S. L., Thomas H. E. and Carn S. A. (2013) Volcano monitoring applications of the Ozone Monitoring Instrument. *Geol. Soc. Lond. Spec. Publ.* **380**, 259–291.

McCubbin F. M., Riner M. A., Vander Kaaden K. E. and Burkemper L. K. (2012) Is Mercury a volatile-rich planet? *Geophys. Res. Lett.* **39**, L09202.

McEwen A. S., Keszthelyi L., Spencer J. R., Schubert G., Matson D. L., Lopes-Gautier R., Klaasen K. P., Johnson T. V., Head J. W., Geissler P., Fagents S., Davies A. G., Carr M. H., Breneman H. H. and Belton M. J. S. (1998) High-temperature silicate volcanism on Jupiter's moon Io. *Science* **281**, 87–90.

McGetchin T. R. and Head J. W. (1973) Lunar cinder cones. *Science* **180**, 68–71.

McGrath M. A., Belton M. J. S., Spencer J. R. and Sartoretti P. (2000) Spatially Resolved Spectroscopy of Io's Pele Plume and SO_2 Atmosphere. *Icarus* **146**, 476–493.

McKay D. S. and Wentworth S. J. (1992) Morphology and composition of condensates on Apollo 17 orange and black glass. *LPI Tech. Rep.* **92**–**09**, 31–36.

McKay D. S., Wentworth S. J., Thomas-Keprta K. L., Ross K. and Clemett S. J. (2010) Volcanic coatings on picritic Apollo 17 glasses: submicrometer-deposits of Fe-, Cr-metal. In Lunar and Planetary Science Conference. p. 2509.

McSween H. Y., Ruff S. W., Morris R. V., Bell J. F., Herkenhoff K., Gellert R., Stockstill K. R., Tornabene L. L., Squyres S. W., Crisp J. A., Christensen P. R., McCoy T. J., Mittlefehldt D. W. and Schmidt M. (2006) Alkaline volcanic rocks from the Columbia Hills, Gusev crater, Mars. *J. Geophys. Res. Planets* **111**, E09S91.

McSween H. Y., Taylor G. J. and Wyatt M. B. (2009) Elemental Composition of the Martian Crust. *Science* **324**, 736–739.

Mernagh T. P., King P. L., McMillan P. F., Berger J. A. and Dalby K. N. (2018) Using infrared and Raman spectroscopy to analyze gas-solid reactions. *Rev. Mineral. Geochem.* **84**, 177–228.

Meyer C., McKay D. S., Anderson D. H. and Butler Jr. P. (1975) The source of sublimates on the Apollo 15 green and Apollo 17 orange glass samples. *Proc. Lunar Sci. Conf.* **6**, 1673–1699.

Misra A., Krissansen-Totton J., Koehler M. C. and Sholes S. (2015) Transient sulfate aerosols as a signature of exoplanet volcanism. *Astrobiology* **15**, 462–477.

Monceau D. and Pieraggi B. (1998) Determination of parabolic rate constants from a local analysis of mass-gain curves. *Oxid. Met.* **50**, 477–493.

de Moor J. M., Fischer T. P., Sharp Z. D., King P. L., Wilke M., Botcharnikov R. E., Cottrell E., Zelenski M., Marty B., Klimm K., Rivard C., Ayalew D., Ramirez C. and Kelley K. A. (2013) Sulfur degassing at Erta Ale (Ethiopia) and Masaya (Nicaragua) volcanoes: Implications for degassing processes and oxygen fugacities of basaltic systems. *Geochem. Geophys. Geosystems* **14**, 4076–4108.

Moretti R., Papale P. and Ottonello G. (2003) A model for the saturation of C-O-H-S fluids in silicate melts. *Geol. Soc. Lond. Spec. Publ.* **213**, 81–101.

Mori Toshiya, Shinohara H., Kazahaya K., Hirabayashi J., Matsushima T., Mori Takehiko, Ohwada M., Odai M., Iino H. and Miyashita M. (2013) Time-averaged SO_2 fluxes of subduction-zone volcanoes: Example of a 32-year exhaustive survey for Japanese volcanoes. *J. Geophys. Res. Atmospheres* **118**, 8662–8674.

Morse S. A. (1980) *Basalts and Phase Diagrams*., Springer New York, New York, NY.

Moses J. I., Zolotov M. Y. and Fegley Jr. B. (2002) Photochemistry of a Volcanically Driven Atmosphere on Io: Sulfur and Oxygen Species from a Pele-Type Eruption. *Icarus* **156**, 76–106.

Moynier F., Albarède F. and Herzog G. F. (2006) Isotopic composition of zinc, copper, and iron in lunar samples. *Geochim. Cosmochim. Acta* **70**, 6103–6117.

Muan A. and Osborn E. F. (1965) *Phase equilibria among oxides in steelmaking*., Addison-Wesley Pub. Co.

Mueller S. B., Ayris P. M., Wadsworth F. B., Kueppers U., Casas A. S., Delmelle P., Taddeucci J., Jacob M. and Dingwell D. B. (2017) Ash aggregation enhanced by deposition and redistribution of salt on the surface of volcanic ash in eruption plumes. *Sci. Rep.* **7**, 45762.

Muenow D. W., Keil K. and Wilson L. (1992) High-temperature mass spectrometric degassing of enstatite chondrites: Implications for pyroclastic volcanism on the aubrite parent body. *Geochim. Cosmochim. Acta* **56**, 4267–4280.

Mysen B. O. and Richet P. (2005) *Silicate Glasses and Melts: Properties and Structure*., Elsevier, Amsterdam; Boston.

Mysen B. O., Virgo D. and Seifert F. A. (1982) The structure of silicate melts: Implications for chemical and physical properties of natural magma. *Rev. Geophys.* **20**, 353–383.

Neuville D. R., Cormier L. and Massiot D. (2006) Al coordination and speciation in calcium aluminosilicate glasses: Effects of composition determined by ^{27}Al MQ-MAS NMR and Raman spectroscopy. *Chem. Geol.* **229**, 173–185.

Neuville D. R. and Mysen B. O. (1996) Role of aluminium in the silicate network: In situ, high-temperature study of glasses and melts on the join SiO_2-$NaAlO_2$. *Geochim. Cosmochim. Acta* **60**, 1727–1737.

Newcombe M. E., Brett A., Beckett J. R., Baker M. B., Newman S., Guan Y., Eiler J. M. and Stolper E. M. (2017) Solubility of water in lunar basalt at low pH_2O. *Geochim. Cosmochim. Acta* **200**, 330–352.

Nicholis M. G. and Rutherford M. J. (2009) Graphite oxidation in the Apollo 17 orange glass magma: Implications for the generation of a lunar volcanic gas phase. *Geochim. Cosmochim. Acta* **73**, 5905–5917.

Nimmo F. and McKenzie D. (1998) Volcanism and tectonics on Venus. *Annu. Rev. Earth Planet. Sci.* **26**, 23–51.

Nittler L. R., Starr R. D., Weider S. Z., McCoy T. J., Boynton W. V., Ebel D. S., Ernst C. M., Evans L. G., Goldsten J. O., Hamara D. K., Lawrence D. J., McNutt R. L., Schlemm C. E., Solomon S. C. and Sprague A. L. (2011) The major-element composition of Mercury's surface from MESSENGER X-ray spectrometry. *Science* **333**, 1847–1850.

Nriagu J. O. (1989) A global assessment of natural sources of atmospheric trace metals. *Nature* **338**, 47–49.

Oelkers E. H. and Schott J. eds. (2009) Thermodynamics and Kinetics of Water-Rock Interaction. *Rev. Mineral. Geochem.* **70**.

O'Neill H. S. C. (1988) Systems Fe-O and Cu-O: thermodynamic data for the equilibria Fe-'FeO', Fe-Fe_3O_4,'FeO'-Fe_3O_4, Fe_3O_4-Fe_2O_3, Cu-Cu_2O, and Cu_2O-CuO from emf measurements. *Amer Miner.* **73**, 470–486.

O'Neill H. S. C. and Pownceby M. I. (1993) Thermodynamic data from redox reactions at high temperatures. I. An experimental and theoretical assessment of the electrochemical method using stabilized zirconia electrolytes, with revised values for the Fe-"FeO", Co-CoO, Ni-NiO and Cu-Cu_2O oxygen buffers, and new data for the W-WO_2 buffer. *Contrib. Mineral. Petrol.* **114**, 296–314.

Oppenheimer C., Fischer T. P. and Scaillet B. (2014) 4.4 - Volcanic degassing: Process and impact. In *Treatise on Geochemistry (Second Edition)* (eds. H. D. Holland and K. K. Turekian). Elsevier, Oxford. pp. 111–179.

Oppenheimer C., Scaillet B. and Martin R. S. (2011) Sulfur degassing from volcanoes: Source conditions, surveillance, plume chemistry and Earth system impacts. *Rev. Mineral. Geochem.* **73**, 363–421.

Óskarsson N. (1980) The interaction between volcanic gases and tephra: fluorine adhering to tephra of the 1970 Hekla eruption. *J. Volcanol. Geotherm. Res.* **8**, 251–266.

Ostyn K. m., Carter C. b., Koehne M., Falke H. and Schmalzried H. (1984) Internal reactions in oxide solid solutions. *J. Am. Ceram. Soc.* **67**, 679–685.

Palm A. B., King P. L., Renggli C. J., Hervig R. L., Dalby K. N., Herring A., Mernagh T. P., Eggins S. M., Troitzsch U., Beeching L., Kinsley L. and Guagliardo P. (2018) Unravelling the consequences of SO_2-basalt reactions for geochemical fractionation and mineral formation. *Rev. Mineral. Geochem.* **84**, 257–283.

Paniello R. C., Day J. M. D. and Moynier F. (2012) Zinc isotopic evidence for the origin of the Moon. *Nature* **490**, 376–379.

Pardini F., Burton M., de' Michieli Vitturi M., Corradini S., Salerno G., Merucci L. and Di Grazia G. (2017) Retrieval and intercomparison of volcanic SO_2 injection height and eruption time from satellite maps and ground-based observations. *J. Volcanol. Geotherm. Res.* **331**, 79–91.

Pearl J., Hanel R., Kunde V., Maguire W., Fox K., Gupta S., Ponnamperuma C. and Raulin F. (1979) Identification of gaseous SO_2 and new upper limits for other gases on Io. *Nature* **280**, 755–758.

Pieraggi B. (1987) Calculations of parabolic reaction rate constants. *Oxid. Met.* **27**, 177–185.

Pierazzo E., Hahmann A. N. and Sloan L. C. (2003) Chicxulub and Climate: Radiative Perturbations of Impact-Produced S-Bearing Gases. *Astrobiology* **3**, 99–118.

Renggli C. J. and King P. L. (2018) SO_2 gas reactions with silicate glasses. *Rev. Mineral. Geochem.*, 229–255.

Renggli C. J., King P. L., Henley R. W. and Norman M. D. (2017) Volcanic gas composition, metal dispersion and deposition during explosive volcanic eruptions on the Moon. *Geochim. Cosmochim. Acta* **206**, 296–311.

Righter K. and Drake M. J. (1996) Core formation in Earth's Moon, Mars, and Vesta. *Icarus* **124**, 513–529.

Robie R. A. and Hemingway B. S. (1995) *Thermodynamic Properties of Minerals and Related Substances at 298.15 K and 1 bar (10^5 pascals) Pressure and at Higher Temperatures*., United States Geological Survey.

Robock A., Ammann C. M., Oman L., Shindell D., Levis S. and Stenchikov G. (2009) Did the Toba volcanic eruption of ~74 ka b.p. produce widespread glaciation? *J. Geophys. Res. Atmospheres* **114**, D10107.

Roine A. (2015) *Outotec HSC Chemistry 8.1*., Outotec Research Center, Finland.

Rose W. I. (1977) Scavenging of volcanic aerosol by ash: Atmospheric and volcanologic implications. *Geology* **5**, 621.

Roselieb K. and Jambon A. (2002) Tracer diffusion of Mg, Ca, Sr, and Ba in Na-aluminosilicate melts. *Geochim. Cosmochim. Acta* **66**, 109–123.

Rothery D. A., Thomas R. J. and Kerber L. (2013) Prolonged eruptive history of a compound volcano on Mercury: volcanic and tectonic implications. *Earth Planet. Sci. Lett.* **385**, 59–67.

Rowe J. J., Morey G. W. and Silber C. C. (1967) The ternary system K_2SO_4-$MgSO_4$-$CaSO_4$. *J. Inorg. Nucl. Chem.* **29**, 925–942.

Russell J. K. and Giordano D. (2005) A model for silicate melt viscosity in the system $CaMgSi_2O_6$-$CaAl_2Si_2O_8$-$NaAlSi_3O_8$. *Geochim. Cosmochim. Acta* **69**, 5333–5349.

Rutherford M. J. and Papale P. (2009) Origin of basalt fire-fountain eruptions on Earth versus the Moon. *Geology* **37**, 219–222.

Ryan M. P. and Sammis C. G. (1981) The glass transition in basalt. *J. Geophys. Res.* **86**, 9519–9535.

Saal A. E., Hauri E. H., Cascio M. L., Van Orman J. A., Rutherford M. C. and Cooper R. F. (2008) Volatile content of lunar volcanic glasses and the presence of water in the Moon's interior. *Nature* **454**, 192–195.

Saal A. E., Hauri E. H., Langmuir C. H. and Perfit M. R. (2002) Vapour undersaturation in primitive mid-ocean-ridge basalt and the volatile content of Earth's upper mantle. *Nature* **419**, 451–455.

Saal A. E., Hauri E. H., Van Orman J. A. and Rutherford M. J. (2013) Hydrogen isotopes in lunar volcanic glasses and melt inclusions reveal a carbonaceous chondrite heritage. *Science* **340**, 1317–1320.

Schaefer L. and Fegley B. (2004) A thermodynamic model of high temperature lava vaporization on Io. *Icarus* **169**, 216–241.

Schaefer L. and Fegley B. (2005a) Alkali and halogen chemistry in volcanic gases on Io. *Icarus* **173**, 454–468.

Schaefer L. and Fegley B. (2005b) Silicon tetrafluoride on Io. *Icarus* **179**, 252–258.

Schaeffer H. A., Stengel M. and Mecha J. (1986) Dealkalization of glass surfaces utilizing HCI gas. *J. Non-Cryst. Solids* **80**, 400–404.

Schmalzried H. (1983) Internal and external oxidation of nonmetallic compounds and solid solutions (I). *Berichte Bunsenges. Für Phys. Chem.* **87**, 551–558.

Schmalzried H. and Backhaus-Ricoult M. (1993) Internal solid state reactions. *Prog. Solid State Chem.* **22**, 1–57.

Schreiber H. D. (1987) An electrochemical series of redox couples in silicate melts: A review and applications to geochemistry. *J. Geophys. Res. Solid Earth* **92**, 9225–9232.

Schultz P. H. and Mustard J. F. (2004) Impact melts and glasses on Mars. *J. Geophys. Res. Planets* **109**, E01001.

Shannon R. (1976) Revised effective ionic radii and systematic studies of interatomic distances in halides and chalcogenides. *Acta Crystallogr. A* **32**, 751–767.

Sharp Z. D., McCubbin F. M. and Shearer C. K. (2013) A hydrogen-based oxidation mechanism relevant to planetary formation. *Earth Planet. Sci. Lett.* **380**, 88–97.

Shearer C. K., Burger P. V., Guan Y., Papike J. J., Sutton S. R. and Atudorei N.-V. (2012) Origin of sulfide replacement textures in lunar breccias. Implications for vapor element transport in the lunar crust. *Geochim. Cosmochim. Acta* **83**, 138–158.

Shinohara H. (2013) Volatile flux from subduction zone volcanoes: Insights from a detailed evaluation of the fluxes from volcanoes in Japan. *J. Volcanol. Geotherm. Res.* **268**, 46–63.

Sigurdsson H., D'Hondt S. and Carey S. (1992) The impact of the Cretaceous/Tertiary bolide on evaporite terrane and generation of major sulfuric acid aerosol. *Earth Planet. Sci. Lett.* **109**, 543–559.

Sobiech M., Wohlschlögel M., Welzel U., Mittemeijer E. J., Hügel W., Seekamp A., Liu W. and Ice G. E. (2009) Local, submicron, strain gradients as the cause of Sn whisker growth. *Appl. Phys. Lett.* **94**, 221901.

Spencer J. R., Jessup K. L., McGrath M. A., Ballester G. E. and Yelle R. (2000) Discovery of Gaseous S_2 in Io's Pele Plume. *Science* **288**, 1208–1210.

Stern K. H. and Weise E. L. (1966) *High temperature properties and decomposition of inorganic salts. Part 1. Sulfates*., National Bureau of Standards.

Strobel D. F. and Wolven B. C. (2001) The atmosphere of Io: Abundances and sources of sulfur dioxide and atomic hydrogen. *Astrophys. Space Sci.* **277**, 271–287.

Sucov E. W. and Gorman R. R. (1965) Interdiffusion of calcium in soda-lime-silica glass at 880° to 1308°C. *J. Am. Ceram. Soc.* **48**, 426–429.

Suo Z. (1995) Wrinkling of the oxide scale on an aluminum-containing alloy at high temperatures. *J. Mech. Phys. Solids* **43**, 829–846.

Sutton S. R., Karner J., Papike J., Delaney J. S., Shearer C., Newville M., Eng P., Rivers M. and Dyar M. D. (2005) Vanadium K edge XANES of synthetic and natural basaltic glasses and application to microscale oxygen barometry. *Geochim. Cosmochim. Acta* **69**, 2333–2348.

Symonds R. B. and Reed M. H. (1993) Calculation of multicomponent chemical equilibria in gas-solid-liquid systems; calculation methods, thermochemical data, and applications to studies of high-temperature volcanic gases with examples from Mount St. Helens. *Am. J. Sci.* **293**, 758–864.

Symonds R. B., Reed M. H. and Rose W. I. (1992) Origin, speciation, and fluxes of trace-element gases at Augustine volcano, Alaska: Insights into magma degassing and fumarolic processes. *Geochim. Cosmochim. Acta* **56**, 633–657.

Symonds R. B., Rose W. I., Gerlach T. M., Briggs P. H. and Harmon R. S. (1990) Evaluation of gases, condensates, and SO_2 emissions from Augustine volcano, Alaska: the degassing of a Cl-rich volcanic system. *Bull. Volcanol.* **52**, 355–374.

Symonds R. B., Rose W. I., Reed M. H., Lichte F. E. and Finnegan D. L. (1987) Volatilization, transport and sublimation of metallic and non-metallic elements in high temperature gases at Merapi Volcano, Indonesia. *Geochim. Cosmochim. Acta* **51**, 2083–2101.

Szekely J., Evans J. W. and Sohn H. Y. (1976) *Gas-Solid Reactions*. Academic Press, New York.

Tauber P. and Arndt J. (1987) The relationship between viscosity and temperature in the system anorthite-diopside. *Chem. Geol.* **62**, 71–81.

Taylor G. J., Keil K., McCoy T., Haack H. and Scott E. R. D. (1993) Asteroid differentiation - Pyroclastic volcanism to magma oceans. *Meteoritics* **28**, 34–52.

Taylor G. J. and Martel L. M. V. (2003) Lunar prospecting. *Adv. Space Res.* **31**, 2403–2412.

Taylor S. R. and McLennan S. (2009) *Planetary Crusts: Their Composition, Origin and Evolution*. Cambridge University Press, Cambridge, UK.

Thomas-Keprta K. L., Clemett S. J., Berger E. L., Rahman Z., McKay D. S., Gibson E. K. and Wentworth S. J. (2014) Vesicles in Apollo 15 green glasses: The nature of ancient lunar gases. In Lunar and Planetary Science Conference. p. 2507.

Thomson G. W. (1946) The Antoine Equation for vapor-pressure data. *Chem. Rev.* **38**, 1–39.

Tolpygo V. K and Clarke D. R. (1998) Wrinkling of α-alumina films grown by oxidation—II. Oxide separation and failure. *Acta Mater.* **46**, 5167–5174.

Tolpygo V. K. and Clarke D. R. (1998) Wrinkling of α-alumina films grown by thermal oxidation—I. Quantitative studies on single crystals of Fe–Cr–Al alloy. *Acta Mater.* **46**, 5153–5166.

Tompsett G. A., Bowmaker G. A., Cooney R. P., Metson J. B., Rodgers K. A. and Seakins J. M. (1995) The Raman spectrum of brookite, TiO_2 (Pbca, Z = 8). *J. Raman Spectrosc.* **26**, 57–62.

Treiman A. H. (2007) Geochemistry of Venus' surface: Current limitations as future opportunities. In *Exploring Venus as a Terrestrial Planet* (eds. L. W. Esposito, E. R. Stofan, and T. E. Cravens). American Geophysical Union. pp. 7–22.

Tröger W. E. (2017) *Optische Bestimmung der gesteinsbildenden Minerale Teil I.: Bestimmungstabellen*. eds. H. U. Bambauer, F. Taborszky, and H. Dieter, Schweizerbart Science Publishers, Stuttgart, Germany.

Vandaele A. C., Korablev O., Belyaev D., Chamberlain S., Evdokimova D., Encrenaz T., Esposito L., Jessup K. L., Lefèvre F., Limaye S., Mahieux A., Marcq E., Mills F. P., Montmessin F., Parkinson C. D., Robert S., Roman T., Sandor B., Stolzenbach A., Wilson C. and Wilquet V. (2017) Sulfur dioxide in the Venus Atmosphere: II. Spatial and temporal variability. *Icarus* **295**, 1–15.

Vita F., Inguaggiato S., Bobrowski N., Calderone L., Galle B. and Parello F. (2012) Continuous SO_2 flux measurements for Vulcano Island, Italy. *Ann. Geophys.* **55**.

Wahrenberger C., Seward T. M. and Dietrich V. (2002) Volatile trace-element transport in high-temperature gases from Kudriavy volcano (Iturup, Kurile Islands, Russia). *Geochem. Soc. Spec. Publ.* **7**, 307–327.

Wang A., Freeman J. J., Jolliff B. L. and Chou I.-M. (2006) Sulfates on Mars: A systematic Raman spectroscopic study of hydration states of magnesium sulfates. *Geochim. Cosmochim. Acta* **70**, 6118–6135.

Waqif M., Mohammed Saad A., Bensitel M., Bachelier J., Saur O. and Lavalley J.-C. (1992) Comparative study of SO_2 adsorption on metal oxides. *J. Chem. Soc. Faraday Trans.* **88**, 2931–2936.

Warren P. H. and Kallemeyn G. W. (1992) Explosive volcanism and the graphite-oxygen fugacity buffer on the parent asteroid(s) of the ureilite meteorites. *Icarus* **100**, 110–126.

Wasson J. T., Boynton W. V., Kallemeyn G. W., Sundberg L. L. and Wai C. M. (1976) Volatile compounds released during lunar lava fountaining. *Proc. Lunar Sci. Conf.* **7**, 1583–1595.

Webb S. (1997) Silicate melts: Relaxation, rheology, and the glass transition. *Rev. Geophys.* **35**, 191–218.

Weitz C. M., Head J. W. and Pieters C. M. (1998) Lunar regional dark mantle deposits: Geologic, multispectral, and modeling studies. *J. Geophys. Res. Planets* **103**, 22725–22759.

Weitz C. M., Rutherford M. J., Head III J. W. and McKay D. S. (1999) Ascent and eruption of a lunar high-titanium magma as inferred from the petrology of the 74001/2 drill core. *Meteorit. Planet. Sci.* **34**, 527–540.

Wendlandt R. F. (1991) Oxygen diffusion in basalt and andesite melts: experimental results and discussion of chemical versus tracer diffusion. *Contrib. Mineral. Petrol.* **108**, 463–471.

Wentworth S. J., Thomas-Keprta K. L., Clemett S. J. and McKay D. S. (2008) Surface Coatings on Apollo 15 Volcanic Glass Beads. *Proc. Lunar Planet. Sci. Conf.* **39**, 2529.

Wetzel D. T., Hauri E. H., Saal A. E. and Rutherford M. J. (2015) Carbon content and degassing history of the lunar volcanic glasses. *Nat. Geosci.* **8**, 755–758.

Wildenschild D. and Sheppard A. P. (2013) X-ray imaging and analysis techniques for quantifying pore-scale structure and processes in subsurface porous medium systems. *Adv. Water Resour.* **51**, 217–246.

Wilke M. (2005) Fe in magma-An overview. *Ann. Geophys.* **48**, 609–617.

Wilke M., Farges F., Partzsch G. M., Schmidt C. and Behrens H. (2007) Speciation of Fe in silicate glasses and melts by in-situ XANES spectroscopy. *Am. Mineral.* **92**, 44–56.

Wilke M., Klimm K. and Kohn S. C. (2011) Spectroscopic studies on sulfur speciation in synthetic and natural glasses. *Rev. Mineral. Geochem.* **73**, 41–78.

Williams D. A., Keszthelyi L. P., Crown D. A., Yff J. A., Jaeger W. L., Schenk P. M., Geissler P. E. and Becker T. L. (2011) Volcanism on Io: New insights from global geologic mapping. *Icarus* **214**, 91–112.

Wilson L. (2003) Deep generation of magmatic gas on the Moon and implications for pyroclastic eruptions. *Geophys. Res. Lett.* **30**.

Wilson L. and Head J. W. (1981) Ascent and eruption of basaltic magma on the Earth and Moon. *J. Geophys. Res. Solid Earth* **86**, 2971–3001.

Wilson L. and Head J. W. (2017) Generation, ascent and eruption of magma on the Moon: New insights into source depths, magma supply, intrusions and effusive/explosive eruptions (Part 1: Theory). *Icarus* **283**, 146–175.

Wilson L. and Keil K. (1991) Consequences of explosive eruptions on small Solar System bodies: the case of the missing basalts on the aubrite parent body. *Earth Planet. Sci. Lett.* **104**, 505–512.

Wilson L. and Keil K. (1997) The fate of pyroclasts produced in explosive eruptions on the asteroid 4 Vesta. *Meteorit. Planet. Sci.* **32**, 813–823.

Wylen G. J. V. and Sonntag R. E. (1986) *Fundamentals of Classical Thermodynamics*. 3rd ed., John Wiley & Sons Inc., New York.

Yudovskaya M. A., Tessalina S., Distler V. V., Chaplygin I. V., Chugaev A. V. and Dikov Y. P. (2008) Behavior of highly-siderophile elements during magma degassing: A case study at the Kudryavy volcano. *Chem. Geol.* **248**, 318–341.

Zelenski M. E., Fischer T. P., de Moor J. M., Marty B., Zimmermann L., Ayalew D., Nekrasov A. N. and Karandashev V. K. (2013) Trace elements in the gas emissions from the Erta Ale volcano, Afar, Ethiopia. *Chem. Geol.* **357**, 95–116.

Zhang J., Goldstein D. B., Varghese P. L., Gimelshein N. E., Gimelshein S. F. and Levin D. A. (2003) Simulation of gas dynamics and radiation in volcanic plumes on Io. *Icarus* **163**, 182–197.

Zhang J., Goldstein D. B., Varghese P. L., Trafton L., Moore C. and Miki K. (2004) Numerical modeling of Ionian volcanic plumes with entrained particulates. *Icarus* **172**, 479–502.

Zhang Y. (2010) Diffusion in minerals and melts: Theoretical background. *Rev. Mineral. Geochem.* **72**, 5–59.

Zhang Y. (2011) “Water” in lunar basalts: The role of molecular hydrogen (H_2), especially in the diffusion of the H component. *Lunar Planet. Sci. Conf.* **42**, 1957.

Zolotov M. Y. (2018) Gas-solid interactions on Venus and other solar system bodies. *Rev. Mineral. Geochem.* **84**, 351–392.

Zolotov M. Y. (2011) On the chemistry of mantle and magmatic volatiles on Mercury. *Icarus* **212**, 24–41.

Zolotov M. Y. and Fegley B. (2001) Chemistry and vent pressure of very high-temperature gases emitted from Pele Volcano on Io. *Lunar Planet. Sci. Conf.* **32**, 1474.

Zolotov M. Y. and Fegley B. (2000) Eruption conditions of Pele Volcano on Io inferred from chemistry of its volcanic plume. *Geophys. Res. Lett.* **27**, 2789–2792.

Zolotov M. Y. and Fegley B. (1999) Oxidation state of volcanic gases and the interior of Io. *Icarus* **141**, 40–52.

Zolotov M. Y. and Fegley B. (1998) Volcanic production of sulfur monoxide (SO) on Io. *Icarus* **132**, 431–434.

Zolotov M. Y., Sprague A. L., Hauck S. A., Nittler L. R., Solomon S. C. and Weider S. Z. (2013) The redox state, FeO content, and origin of sulfur-rich magmas on Mercury. *J. Geophys. Res. Planets* **118**, 138–146.

Zoppi A., Lofrumento C., Castellucci E. M. and Sciau P. (2008) Al-for-Fe substitution in hematite: the effect of low Al concentrations in the Raman spectrum of Fe_2O_3. *J. Raman Spectrosc.* **39**, 40–46.

8 Appendix to Chapter 2

Gibbs Free Energy minimization calculations were performed using the software HSC8 (Outotec, 2015). The thermochemical data includes temperature conditions from 50 to 20000 K for gas, solid and liquid phases. The heat capacities are described by the polynomial:

$$C_p(T) = A + BT * 10^{-3} + CT^{-2} * 10^5 + DT^2 * 10^{-6}$$

Where A, B, C and D are numerical coefficients. The pressure conditions were modelled assuming ideal gas behavior. The species included in the model and the reference from where the HSC8 sources the thermochemical data are given in the table below.

The HSC software accesses its uses its database my taking the most recent reliable thermodynamic data and where disagreements between different sources are found, the data is further evaluated (Outotec, 2015).

Species included in the thermochemical model and temperature ranges over which the thermochemical data is available from the references given as abbreviations and full references below. T-conditions outside the defined range are extrapolated by the software according to the polynomial given above.

Species	Tmin (K)	Tmax (K)	P	References					
CO(g)	200	20000	g	Barin 89	Frenkel 94	Burcat 14	Belov 99		
CO_2(g)	50	10000	g	Barin 93	Frenkel 94	Glushko 94	Landolt 99		
HCl(g)	50	6000	g	Barin 93	Frenkel 94	Glushko 94	Landolt 99		
H_2O(g)	298.15	20000	g	JANAF 85	Glushko 94	Landolt 01			
OH(g)	298.15	20000	g	Ponomarev 08	Ruscic 05	Glushko 94	Landolt 01		
H_2(g)	50	20000	g	JANAF 85	Frenkel 94	Nasa 93			
Cl_2(g)	100	10000	g	JANAF 98	Landolt 99	JANAF 85			
ClO(g)	50	6000	g	Barin 93	Landolt 99	Glushko 94			
O_2(g)	100	20000	g	Barin 93	Frenkel 94	Nasa 93	Landolt 99		
N_2(g)	100	20000	g	JANAF 85	Nasa 93				
F_2(g)	50	10000	g	Landolt 99	Barin 93	Frenkel 94			
CCl_4(g)	100	6000	g	JANAF 98	Knacke 91	Frenkel 94	Landolt 99	Glushko 94	
$CClF_3$(g)	100	6000	g	Ruscic 98	JANAF 98	Frenkel 94	Landolt 99		
CCl_2F_2(g)	50	6000	g	Perrot 08	JANAF 98	Binnewies 02			
CCl_3F(g)	50	6000	g	JANAF 98	Binnewies 02	Glushko 94	Landolt 99		
CF_2(g)	50	6000	g	Belov 99	Cioslowski 00	Barin 93	JANAF 85	Landolt 99	
CF_3(g)	50	6000	g	Ponomarev 08	Belov 99	Barin 89	JANAF 85	Landolt 99	
CF_4(g)	50	6000	g	Barin 77	Landolt 99	Glushko 94			
HF(g)	50	10000	g	Barin 93	Landolt 00	Glushko 94			
C_2Cl_2(g)	100	6000	g	Zhu 02	Barin 93	JANAF 85	JANAF 98		
C_2Cl(g)	298.15	6000	g	Zhu 02	Barin 93	Glushko 94	Landolt 99		
H(g)	100	20000	g	JANAF 85	Belov 99	Nasa 99			
O(g)	50	20000	g	Barin 89	Frenkel 94	Belov 99			
C(g)	100	20000	g	Landolt 99	Barin 77	Belov 99	Nasa 99		
Cl(g)	100	20000	g	Knacke 91	Frenkel 94	Landolt 99	Nasa 99		
F(g)	100	20000	g	Barin 89	Frenkel 94	Landolt 99	Nasa 99		
N(g)	100	20000	g	JANAF 85	Nasa 99	Belov 99			
S(g)	100	20000	g	Landolt 99	Patnaik 03	Barin 89	Frenkel 94	Nasa 99	
COS(g)	100	6000	g	Perrot 08	JANAF 98	Binnewies 02	Barin 93	Glushko 04	Landolt 99
CS(g)	200	6000	g	Burcat 14	Perrot 08	Glushko 94	Landolt 99		
CS_2(g)	100	6000	g	JANAF 98	Barin 93	Glushko 94	Landolt 99		
H_2S(g)	50	6000	g	Barin 89	Frenkel 94	Glushko 94	Landolt 01		
S_2(g)	50	6000	g	Knacke 91	Frenkel 94	Landolt 99			
S_3(g)	50	6000	g	Barin 93	Frenkel 94	Landolt 99			
S_4(g)	50	6000	g	Belov 99	Frenkel 94	JANAF 98	Binnewies 02		
S_5(g)	298.15	6000	g	Belov 99	JANAF 98	Binnewies 02	Landolt 99		
S_6(g)	50	6000	g	Belov 99	Barin 93	JANAF 98	Binnewies 02	Frenkel 94	Landolt 99
S_7(g)	50	6000	g	Belov 99	JANAF 98	Binnewies 02	Landolt 99	Frenkel 94	Barin 89

Species	Tmin (K)	Tmax (K)	P	References					
S_8(g)	50	6000	g	Belov 99	JANAF 98	Binnewies 02	Landolt 99	Frenkel 94	
SO(g)	50	6000	g	Barin 89	Frenkel 94	Landolt 01	Glushko 94		
SCl(g)	100	6000	g	JANAF 98	Barin 93	JANAF 85	Landolt 99		
SO_3(g)	298.15	6000	g	Barin 89	Frenkel 94	Belov 99			
SN(g)	298.15	6000	g	Glushko 94	Landolt 01	JANAF 98			
SO_2(g)	50	5000	g	Barin 93	Frenkel 94				
S_2O(g)	100	4000	g	JANAF 98	Barin 89	Landolt 01			
SCl_2(g)	100	6000	g	JANAF 98	Knacke 91	JANAF 85	Landolt 99		
SF(g)	100	6000	g	Ponomarev 08	JANAF 98	Binnewies 02	Landolt 00		
SF_2(g)	100	6000	g	Belov 99	Cioslowski 00	JANAF 98	Binnewies 02	Glushko 94	Landolt 00
SF_3(g)	100	6000	g	Belov 99	JANAF 98	Binnewies 02	Glushko 94	Landolt 00	
Zn(g)	100	20000	g	Landolt 99	JANAF 98	Bard 85	Nasa 99		
ZnS(g)	298.15	6000	g	Barin 77	Glushko 96	Landolt 01			
ZnCl(g)	298.15	6000	g	Glushko 96	Landolt 99				
$ZnCl_2$(g)	298.15	6000	g	Barin 93	Patnaik 03	Glushko 96	Landolt 99		
ZnO(g)	298.15	6000	g	Glushko 96	Landolt 01				
ZnF(g)	298.15	6000	g	Glushko 96	Landolt 00				
ZnF_2(g)	298.15	6000	g	Barin 93	Glushko 96	Landolt 00			
ZnH(g)	298.15	6000	g	Glushko 96	Landolt 01				
Zn	100	6000	s & l	Barin 77	Nasa 93	JANAF 98			
ZnS_{sph}	298.15	3000	s & l	Barin 77	Glushko 94	Mullin 93	Landolt 01		
ZnS_{wu}	298.15	2500	s & l	Barin 89	Patnaik 03	Glushko 96	Landolt 01		
$ZnCl_2$	298.15	2000	s & l	Barin 89	Glushko 96	Landolt 99			
ZnO	298.15	4000	s & l	Barin 93	Patnaik 03	Glushko 96	Landolt 01		
ZnF_2	298.15	3500	s & l	Barin 89	Glushko 96	Landolt 00			
Ni(g)	100	20000	g	Landolt 99	JANAF 98	Binnewies 02	Nasa 99		
NiS(g)	298.15	6000	g	Belov 99	JANAF 85				
NiCl(g)	100	6000	g	JANAF 98	Binnewies 02	Landolt 99			
$NiCl_2$(g)	100	6000	g	JANAF 98	Barin 93	Glushko 96	Landolt 99		
$NiCl_3$(g)	298.15	6000	g	Glushko 96	Landolt 00				
NiO(g)	298.15	6000	g	Knacke 91	Glushko 96	Landolt 01			
NiF(g)	298.15	6000	g	Belov 99	Glushko 94	Landolt 00			
NiF_2(g)	298.15	6000	g	Knacke 91	Glushko 96	Landolt 00			
Ni	100	6000	s & l	Landolt 99	Barin 77	Nasa 93			
NiS	298.15	833	s	Barin 77					
NiS_2	298.15	2000	s & l	Barin 89					
$NiCl_2$	100	2000	s & l	JANAF 98	Glushko 96	Archer 99c	Landolt 99		
NiO	298.15	4000	s & l	Barin 89	SGTE 99	Landolt 01			

Species	Tmin (K)	Tmax (K)	P	References					
NiF_2	298.15	3000	s & l	Gamsjaeger 05					
Ga(g)	100	10000	g	JANAF 98	Landolt 99	Barin 93			
Ga_2S(g)	298.15	2000	g	Barin 77					
GaCl(g)	298.15	6000	g	Glushko 94	Landolt 99				
$GaCl_2$(g)	298.15	6000	g	Glushko 94	Landolt 99				
$GaCl_3$(g)	298.15	6000	g	Barin 89	Glushko 94	Landolt 00			
GaO(g)	298.15	6000	g	Yaws 06	Glushko 94	Landolt 00			
Ga	298.15	4000	s & l	Landolt 99	Barin 77				
GaS	298.15	1288	s	Barin 77	Knacke 91	Binnewies 02			
Ga_2S_3	298.15	1393	s	Knacke 91	Binnewies 02				
$GaCl_3$	298.15	500	s & l	Barin 77	Patnaik 03	Landolt 99	Barin 93	Landolt 00	
Ga_2O	298.15	1000	s & l	Bard 85	Ruzinov 75				
Ga_2O_3	298.15	4000	s & l	Barin 89	Patnaik 03	Glushko 94	Landolt 00		
Pb(g)	100	20000	g	Barin 89	Nasa 99	Gurvich 90			
PbS(g)	298.15	6000	g	Barin 93	JANAF 98	Binnewies 02	Glushko 94	Landolt 01	
PbS_2(g)	298.15	6000	g	Glushko 94	Landolt 01				
PbCl(g)	100	6000	g	JANAF 98	Glushko 94	Landolt 99			
$PbCl_2$(g)	100	6000	g	JANAF 98	Binnewies 02	Glushko 94	Landolt 99		
$PbCl_3$(g)	298.15	6000	g	Gurvich 90					
$PbCl_4$(g)	298.15	6000	g	Yaws 06	Knacke 91	JANAF 98	Binnewies 02	Gurvich 90	Barin 89
PbO(g)	298.15	6000	g	Glushko 94	JANAF 98	Binnewies 02	Landolt 01		
PbF(g)	298.15	6000	g	JANAF 98	Binnewies 02	Landolt 00	Glushko 94		
Pb	100	3600	s & l	Barin 77	Nasa 93				
PbS	298.15	3000	s & l	Glushko 94	Patnaik 03	JANAF 98	Binnewies 02	Landolt 01	
$PbCl_2$	298.15	2300	s & l	Barin 93	JANAF 98	Mullin 93	Gurvich 90		
PbO	298.15	2000	s & l	Barin 93	Gurvich 90				
PbO_2	298.15	1200	s	Patnaik 03	Knacke 91	Binnewies 02			
Pb_2O_3	298.15	1000	s	Gurvich 90	Lamoreaux 87				
Pb_3O_4	298.15	2000	s	Barin 89	SGTE 94	Landolt 01			
PbF_2	298.15	3200	s & l	Barin 93	Glushko 94	Landolt 00			
Cu(g)	100	20000	g	Landolt 99	Bard 85	Nasa 99			
Cu_2(g)	298.15	6000	g	Landolt 99	JANAF 98	Binnewies 02			
CuS(g)	298.15	6000	g	Knacke 91	Glushko 96	Landolt 00			
Cu_2S(g)	298.15	6000	g	THDA 94	Landolt 00				
CuCl(g)	100	6000	g	JANAF 98	Binnewies 02	Knacke 91	Glushko 94	Landolt 99	
$CuCl_2$(g)	298.15	6000	g	CRC 94	Glushko 96	Landolt 99			
CuO(g)	100	6000	g	JANAF 98	Binnewies 02	Barin 89	Glushko 96	Landolt 00	

Species	Tmin (K)	Tmax (K)	P	References				
CuF(g)	100	6000	g	JANAF 98	Binnewies 02	Knacke 91	Glushko 96	Landolt 00
Cu	100	6000	s & l	Landolt 99	Knacke 91	Nasa 93		
CuS	298.15	1000	s	Knacke 91	Patnaik 03	Glushko 96		
Cu_2S	298.15	3000	s & l	Belov 99	Barin 89	SGTE 94	Landolt 00	
CuCl	298.15	4000	s & l	Barin 93	Patnaik 03	Glushko 94	Landolt 99	
$CuCl_2$	298.15	3000	s & l	Polyachenok 09	Barin 89	Glushko 96		
CuO	298.15	3000	s & l	Knacke 91	Patnaik 03	Glushko 96	Landolt 00	
Cu_2O	298.15	4000	s & l	Knacke 91	Holland 11	Patnaik 03	Glushko 96	Landolt 00
CuF	298.15	2000	s	JANAF 98	Binnewies 02	Glushko 96	Landolt 00	
Fe(g)	100	20000	g	JANAF 98	Landolt 99	Barin 89	Nasa 99	
FeS(g)	298.15	6000	g	JANAF 98	Binnewies 02	Glushko 96	Landolt 00	
FeCl(g)	100	6000	g	JANAF 98	Binnewies 02	Glushko 94	Landolt 99	
$FeCl_2$(g)	100	6000	g	JANAF 98	Binnewies 02	Barin 89	Glushko 94	Landolt 99
$FeCl_3$(g)	100	6000	g	JANAF 98	Binnewies 02	Knacke 91	Glushko 94	Landolt 00
Fe_2Cl_4(g)	298.15	6000	g	JANAF 98	Binnewies 02	Glushko 96	Landolt 00	
Fe_2Cl_6(g)	100	6000	g	JANAF 98	Barin 89	JANAF 85	Landolt 00	
FeO(g)	298.15	6000	g	JANAF 98	Binnewies 02	Barin 89	Glushko 96	Landolt 00
FeO_2(g)	298.15	6000	g	Belov 99	Glushko 96	Landolt 00		
FeF(g)	298.15	6000	g	JANAF 98	Binnewies 02	Glushko 96	Landolt 00	
FeF_2(g)	100	6000	g	JANAF 98	Binnewies 02	Barin 89	Glushko 96	Landolt 00
FeF_3(g)	100	6000	g	JANAF 98	Binnewies 02	Knacke 91	Glushko 96	Landolt 00
Fe_2F_4(g)	298.15	6000	g	Glushko 96	Landolt 00			
Fe_2F_6(g)	298.15	6000	g	Glushko 96	Landolt 00			
Fe	100	4000	s & l	JANAF 98	Landolt 99	Nasa 93	Knacke 91	
FeS	100	3800	s & l	Holland 11	JANAF 98	Patnaik 03	Barin 93	
FeS_2	298.15	1500	s	Holland 11	Patnaik 03	JANAF 98	Binnewies 02	
Fe_2S	298.15	300	s	Waldner 04				
Fe_2S_3	298.15	398	s	Phillips 88				
$FeCl_2$	100	3000	s & l	JANAF 98	Knacke 91	Mullin 93	Glushko 96	Landolt 99
$FeCl_3$	100	2000	s & l	Patnaik 03	JANAF 98	Barin 93	Glushko 96	Landolt 00
FeO	298.15	5000	s & l	Fabri 10	Patnaik 03	Landolt 99	JANAF 85	Landolt 00
Fe_2O_3	298.15	4000	s	Fabri 10	Barin 93	Robie 95	Glushko 96	Landolt 00
$Fe_2O_3*H_2O$	298.15	400	s	Barin 77	THDA 94	Landolt 00		

Species	Tmin (K)	Tmax (K)	P	References				
FeF_2	100	4000	s & l	Patnaik 03	JANAF 98	Binnewies 02	Glushko 96	Landolt 00
FeF_3	298.15	2000	s & l	Barin 93	Glushko 96	Landolt 00	Belov 99	

Abbreviation	Data References from Outotec (2015) *HSC Chemistry software.*
Archer 99c	Archer, D.G., Thermodynamic Properties of Import to Environmental Processes and Remediation. II. Previous Thermodynamic Property Values for Nickel and Some of its compounds, J. Phys. Chem. Ref. Data, Vol. 28, No. 5, pp. 1485-1507, 1999.
Bard 85	Bard A. J., Parsons R., Jordan J., Standard potentials in aqueous solution, Marcel Dekker Inc., New York, 1985.
Barin 77	Barin I., Knacke O., Kubaschewski O., Thermochemical properties of inorganic substances, Supplement, Springer-Verlag, Berlin, 861, 1977.
Barin 89	Barin I: Thermochemical Data of Pure Substances, VCH Verlags Gesellschaft, Weinheim, 1989.
Barin 93	Barin I: Thermochemical Data of Pure Substances, Part I & 2, VCH Verlags Gesellschaft, Weinheim, 1993.
Belov 99	Belov, G., Iorish, V., Yungman, V., IVTANTHERMO - database on thermodynamic properties and related software, Calphad 23(2) (1999) 173-180.
Binnewies 02	Binnewies, M., Milke, E., Thermochemical Data of Elements and Compounds, 2nd edition, Wiley-VCH, Weinheim, 2002.
Burcat 14	Goos, E., Burcat, A., Ruscic, B., "Extended Third Millennium Ideal Gas and Condensed Phase Thermochemical Database for Combustion with Updates from Active Thermochemical Tables". Update of "Third Millennium Ideal Gas and Condensed Phase Thermochemical Database for Combustion with Updates from Active Thermochemical Tables": Burcat, A., Ruscic, B., Report ANL 05/20 and TAE 960 Technion-IIT, Aerospace Engineering, and Argonne National Laboratory, Chemistry Division, September 2005.
Cioslowski 00	Cioslowski, J., Schimeczek, M., Liu, G., Stoyanov, V., A set of standard enthalpies of formation for benchmarking, calibration, and parametrization of electronic structure methods, Journal of Chemical Physics 113(21) (2000) 9377-9389.
CRC 94	CRC Handbook of Chemistry and Physics, 74th edition, CRC press.,1994.
Fabri 10	Fabrichnaya, O., Saxena, S. K., Richet, P., Westrum, E. F., Thermodynamic Data, Models and Phase Diagrams in Multicomponent Oxide Systems: An Assessment for Materials and Planetary Scientists Based on Calorimetric, Volumetric and Phase Equilibrium Data, Springer-Verlag, Berlin 2010.
Frenkel 94	Frenkel, M. , Kabo, G. J. , Marsh, K. N. , Roganov, G. N. , Wilhoit, R. C. , Thermodynamics of organic compounds in the gas state, Vol. 1 & 2, 1994
Gamsjaeger 05	Gamsjäger Heinz, Chemical Thermodynamics of Nickel, Chemical Thermodynamics vol. 6, pp. 43-72, Elsevier B.V., Amsterdam, 2005.
Glushko 94	Glushko Thermocenter of the Russian Academy of Sciences, IVTAN Association, Izhorskaya 13/19, 127412 Moscow, Russia, 1994.
Glushko 96	Glushko Thermocenter of the Russian Academy of Sciences, IVTAN Association, Izhorskaya 13/19, 127412 Moscow, Russia, 1996.
Gurvich 90	Gurvich, L.V., Veitz, I.V., et al. Thermodynamic Properties of Individual Substances. Fourth edition in 5 volumes, Hemisphere Pub Co. NY, L., Vol 1 in 2 parts, 1989.
Holland 11	Holland, T. J. B., Powell, R., An improved and extended internally consistent thermodynamic dataset for phases of petrological interest, involving a new equation of state for solids, Journal of Metamorphic Geology 29 (2011) 333-383.
JANAF 85	JANAF Thermochemical Tables, 3rd ed., M.W. Chase, et. al.., eds., J. of Phys. and Chem. Ref. Data, Vol.14 , Suppl.1, pp. 1-1856, 1985.
JANAF 85	Chase M. W., Jr., Davies C. A., Downey J. R., Jr., Frurip D. Journal, McDonald R. A., Syverud A. N., JANAF thermochemical tables third edition part II, Cr-Zr, J. of Phys. and Chem. Ref. Data, Vol.14, No.1, pp.927-1856, 1985.
JANAF 98	Chase Malcolm, NIST-JANAF, Thermochemical Tables - Fourth Edition, J. of Phys. and Chem. Ref. Data, Mononograph No. 9, 1998.
Knacke 91	Knacke O., Kubaschewski O., Hesselman K., Thermochemical properties of inorganic substances, 2nd ed., Springer-Verlag, Berlin, pp.1-2412, 1991. (KKH 91).

Abbreviation	Data References from Outotec (2015) *HSC Chemistry software.*
Lamoreaux 87	Lamoreaux, R.H.,Hildenbrand, D.L., Brewer, L. High Temperature Vaporization Behavior of Oxides II.Oxides of Be, Mg, Ca, Sr, Ba, B, Al, Ga, In, Tl, Si, Ge, Sn, Pb, Zn, Cd, and Hg. J. of Phys. and Chem. Ref. Data,Vol.16,No.3,pp.419-443, 1987.
Landolt 99	Landolt-Börnstein: Thermodynamic Properties of Inorganic Materials, Scientific Group Thermodata Europe (SGTE), Springer-Verlag, Berlin-Heidelberg, 1999.
Landolt 00	Landolt-Börnstein: Thermodynamic Properties of Inorganic Materials, Scientific Group Thermodata Europe (SGTE), Springer-Verlag, Berlin-Heidelberg, 2000.
Landolt 01	Landolt-Börnstein: Thermodynamic Properties of Inorganic Materials, Scientific Group Thermodata Europe (SGTE), Springer-Verlag, Berlin-Heidelberg, 2001.
Mullin 93	Mullin, J.W., Crystallization, Third Edition, Butterworth-Heinemann; a division of Reed Educational and Professional Publishing Ltd, Great Britain, 1993.
Nasa 93	Thermodynamic Data for Fifty Reference Elements, NASA-TP-3287, N93-19977, 1993, 240 pages.
Nasa 99	Thermodynamic Data to 20 000 K for Monatomic Gases, NASA/TP-1999-208523, 1999, 375 pages.
Patnaik 03	Patnaik, P. Handbook of Inorganic Chemicals, McGraw-Hill, New York, 2003.
Perrot 08	Perrot, P., Propriétés thermodynamiques des composés organiques, Techniques de l'ingenieur Constantes physico-chimiques, (2008) K5(K620), pp. K620v2.1-K620v2.22.
Phillips 88	Thermodynamic Tables for Nuclear Waste Isolation. Prepared by S. L. Philips, F. V. Hale, L. F. Silvester, Lawrence Berkely Laboratory M. D. Siegel, Sandia National Laboratories, 182, 1988.
Polyachenok 09	Polyachenok, O. G., Dudkina, E. N., Polyachenok, L. D., Thermal stability and thermodynamics of copper(II) chloride dihydrate, J. Chem. Thermodynamics 41 (2009) 74-79.
Ponomarev 08	Ponomarev, D., Takhistov, V., Slayden, S., Liebman, J., Thermochemistry of organic, elementorganic and inorganic species. Part XX. Enthalpies of formation for free radicals of main group elements' halogenides, Journal of Molecular Structure 876 (2008) 15-33.
Ponomarev 08	Ponomarev, D., Takhistov, V., Slayden, S., Liebman, J., Thermochemistry of organic, elementorganic and inorganic species. Part XXI. Enthalpies of formation for bi- and triradicals of main group elements' halogenides, Journal of Molecular Structure 876 (2008) 34-55.
Robie 95	Robie, R. A., Hemingway, B. S., Thermodynamic Properties of Minerals and Related Substances at 298.15 K and 1 Bar (105 Pascals) Pressure and at Higher Temperatures, U.S. Geological Survey Bulletin 2131, 1995, 461 p.
Ruscic 98	Ruscic, B., Michael, J. V., Redfern, p. C., Curtiss, L. C., Raghavachari, K., Simultaneous Adjustment of Experimentally Based Enthalpies of Formation of CF3X, X = nil, H, Cl, Br, I, CF3, CN, and a Probe of G3 Theory, J. Phys. Chem. A 102 (1998) 10889-10899.
Ruscic 05	Ruscic, B., Boggs, J. E., Burcat, A., Császár, A. G., Demaison, J., Janoschek, R., Martin, J. M. L., Morton, M. L., Rossi, M. J., Stanton, J. F., Szalay, P. G., Westmoreland, P. R., Zabel, F., Bérces, T., IUPAC Critical Evaluation of Thermochemical Properties of Selected Radicals. Part I, J. Phys. Chem. Ref. Data, Vol. 34, No. 2, 2005, 573-656.
Ruzinov 75	Ruzinov L. P. and Guljanickij B. S.: Ravnovesnye prevrasoenija metallugiceskin reaktseij, Moskva, 416, 1975.
SGTE 94	Scientific Group Thermodata Europe, Grenoble Campus, 1001 Avenue Centrale, BP 66, F-38402 Saint Martin d'Héres, France, 1994.
SGTE 99	Scientific Group Thermodata Europe, Grenoble Campus, 1001 Avenue Centrale, BP 66, F-38402 Saint Martin d'Héres, France, 1999.
THDA 94	THERMODATA, Grenoble Campus, 1001 Avenue Centrale, BP 66, F-38402 Saint Martin d'Héres, France.
Waldner 04	Waldner, P., Pelton, A.D., Critical Thermodynamic Assessment and Modeling of the Fe-Ni-S System, Metallurgical and Materials Transactions B: Process Metallurgy and Materials Processing Science, Vol. 35B(5), pp. 897-907, 2004.
Yaws 06	Yaws C. L.,The YAWS handbook of Thermodynamic properties for Hydrocarbons and Chemicals, Houston, 2006.
Zhu 02	Zhu, L., Bozzelli, J. W., Thermodynamic properties of chloroacetylene, dichloroacetylene, ethynyl radical, and chloroethynyl radical, Chemical Physics Letters 362 (2002) 445-452.

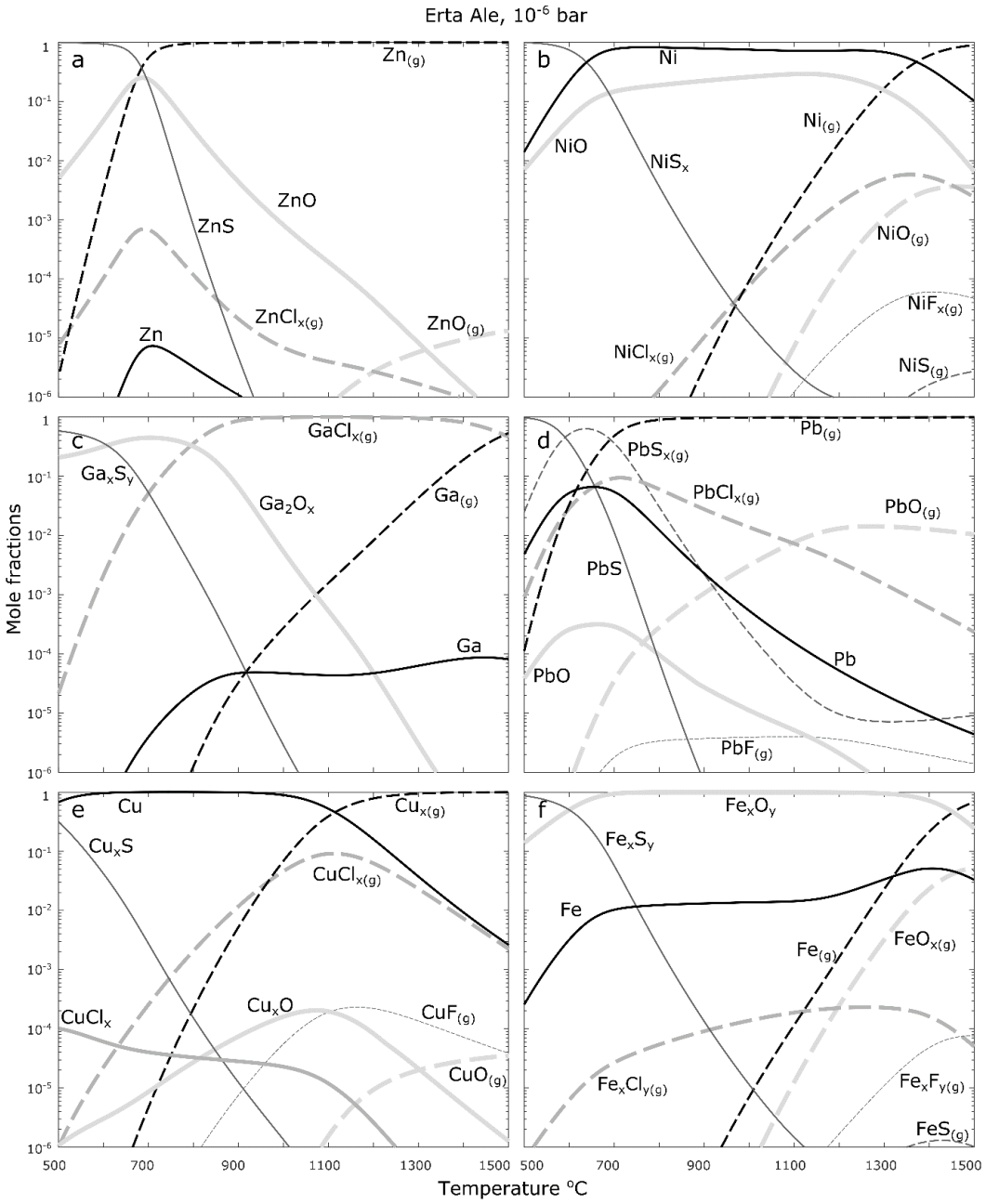

Figure 8-1: Metal speciation in the Erta Ale volcanic gas at 10^{-6} bar.

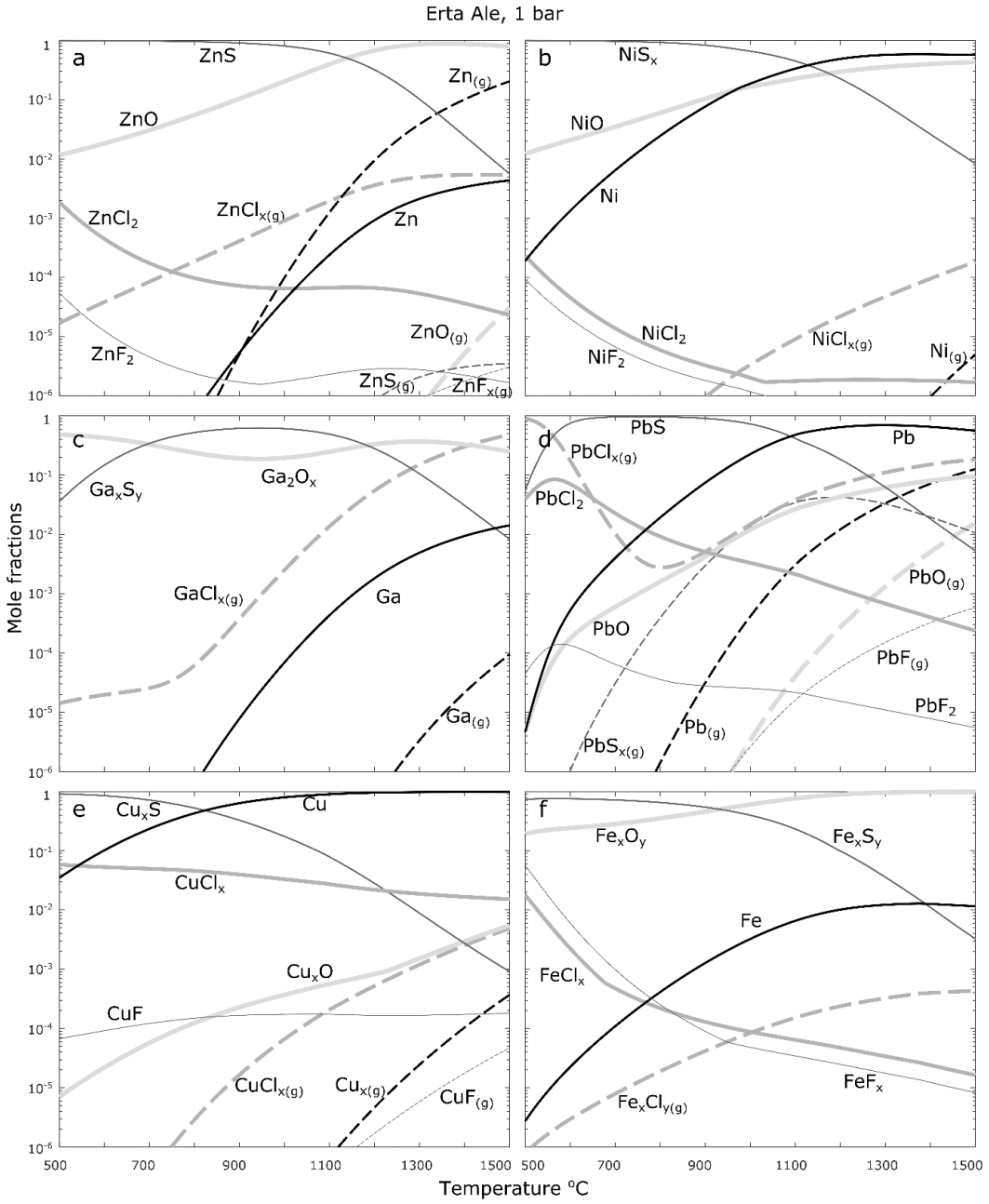

Figure 8-2: Metal speciation in the Erta Ale volcanic gas at 1 bar. The gas was sampled at 1084 °C. At this temperature the total mole fractions of metals in the gas phase are: $X_{Pb}=6.6*10^{-2}$, $X_{Ga}=10^{-2}$, $X_{Zn}=2.6*10^{-3}$, $X_{Fe}=1.4*10^{-4}$, $X_{Cu}=1.8*10^{-4}$ *and* $X_{Ni}=7.7*10^{-6}$.

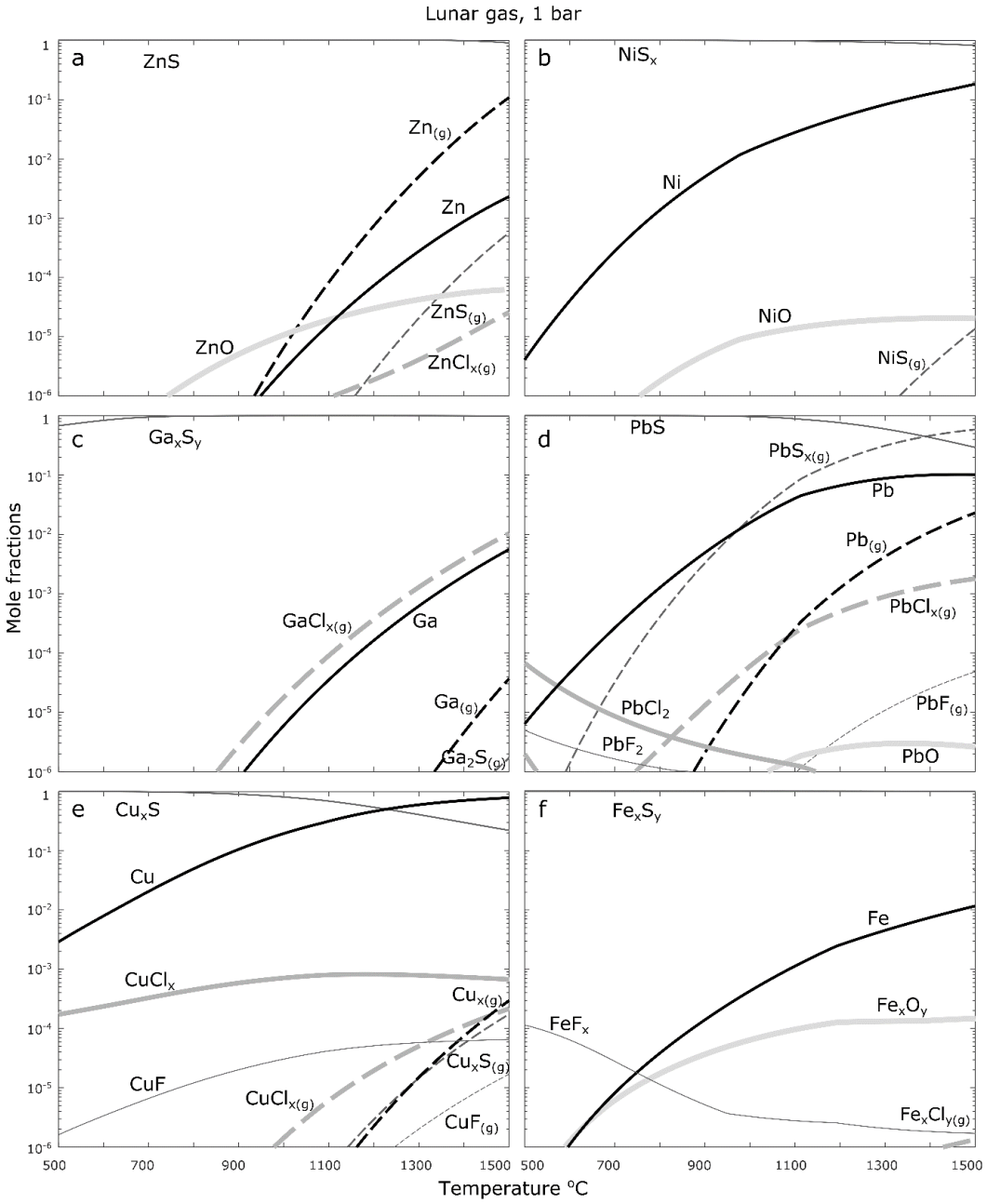

Figure 8-3: Metal speciation in the lunar volcanic gas at 1 bar at IW-2. Sulfides are the dominant solid species except for Cu above 1220 °C where elemental Cu is more abundant.

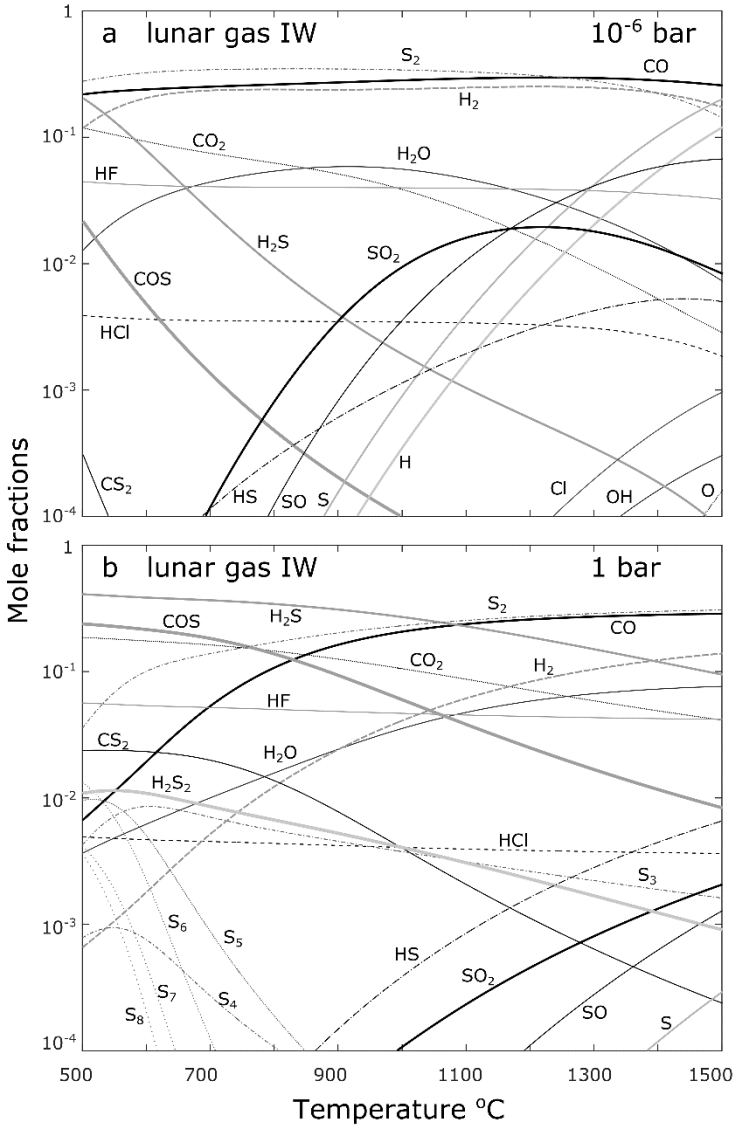

Figure 8-4: Lunar volcanic gas at the Iron-Wüstite buffer, at (a) 10^{-6} bar and at (b) 1 bar. In comparison to Figure 2-2 the concentrations of CO_2, SO_2 and H_2O are higher, but the three main species (CO, S_2 and H_2) remain dominant.

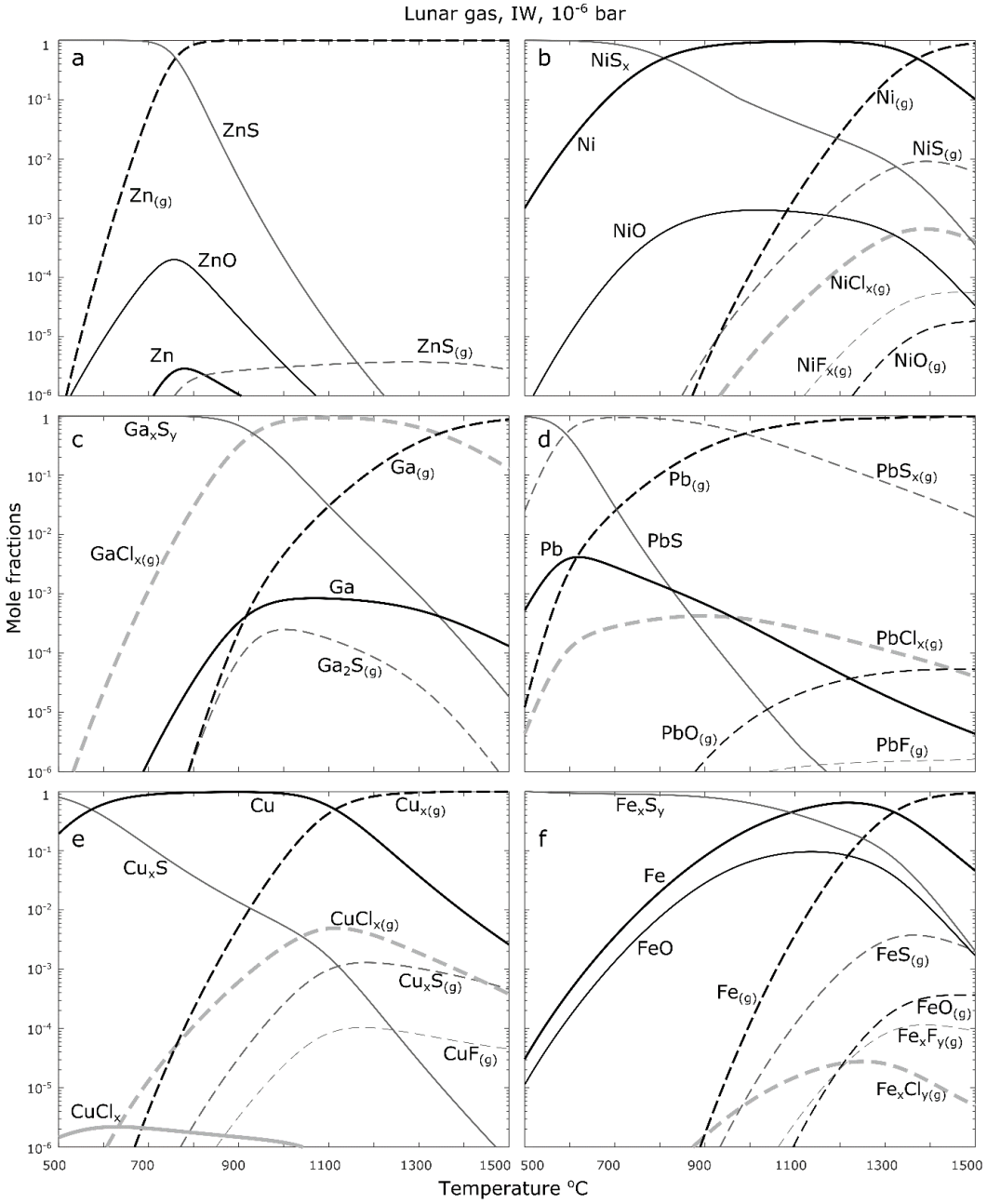

Figure 8-5: Metal speciation in the lunar gas at the Iron-Wüstite buffer at 10^{-6} bar. Iron and Ni are most affected by the higher oxygen fugacity, by the main species remain the same (see Figure 2-3). For Ga and Cu oxide species remain below 10^{-6} mole fractions.

Table 8-1: Volcanic gas compositions in mole% of the lunar volcanic at IW-2 and IW, and the composition of the volcanic gas from Erta Ale volcano in Ethiopia (Zelenski et al., 2013; de Moor et al., 2013). The gases are compared using ratios of molar abundances. The fO_2 is given relative to the iron-wüstite buffer (IW).

	Lunar gas IW-2	Lunar gas IW	Erta Ale 1084 °C
H	31.83	29.95	46.30
O	15.45	20.44	42.29
C	15.92	14.98	6.52
Cl	0.17	0.16	0.50
S	34.65	32.61	3.69
F	1.98	1.86	0.70
N	0.001	0.001	0.001
H/C	2.00	2.00	7.11
H/O	2.06	1.47	1.09
H/S	0.9	0.9	12.6
H/Cl	184.4	184.4	92.8
O/C	0.97	1.36	6.49
S/C	2.18	2.18	0.57
Cl/C	0.01	0.01	0.08
F/C	0.12	0.12	0.11
H/(F+Cl)	14.8	14.8	38.6
fO_2	IW-2	IW	IW+3.6

9 Appendix to Chapter 3

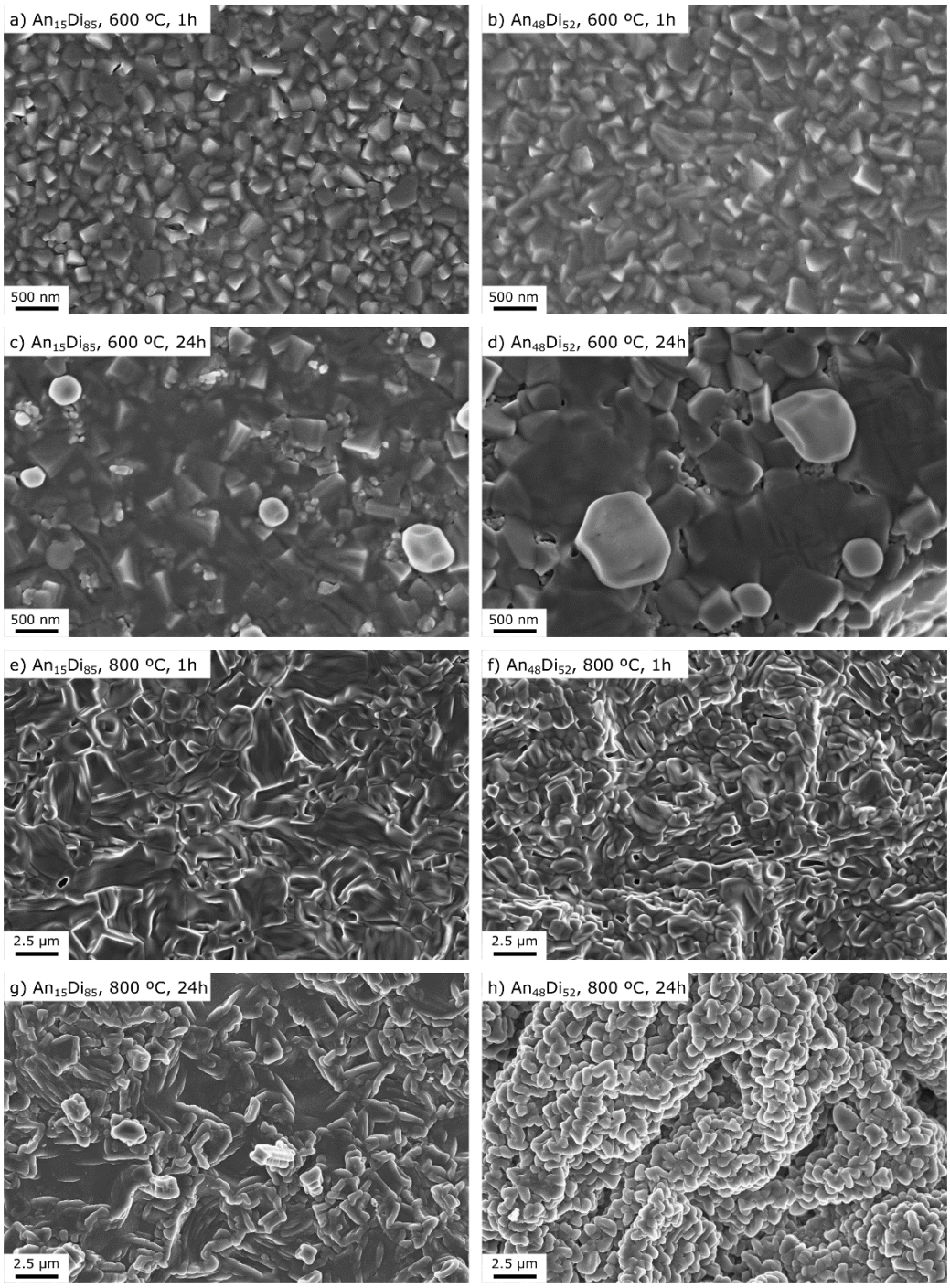

Figure 9-1: FE-SEM images of the surface textures on the $An_{15}Di_{85}$ and $An_{48}Di_{52}$ glasses.

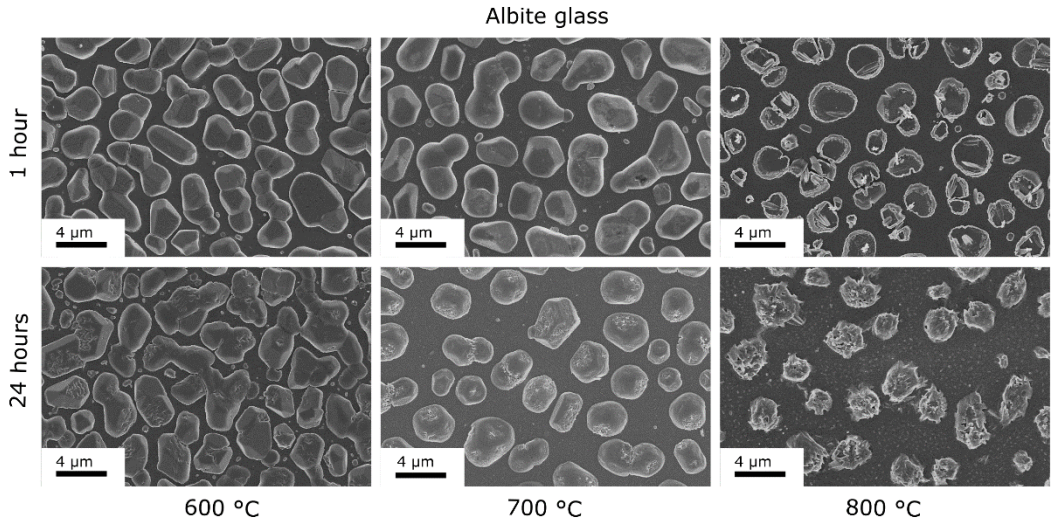

Figure 9-2: Na_2SO_4 coatings on albite glass reacted with $SO_{2(g)}$ for 1 h (upper row) and 24 h (lower row), at 600 °C (left), 700 °C (middle) and 800 °C (right).

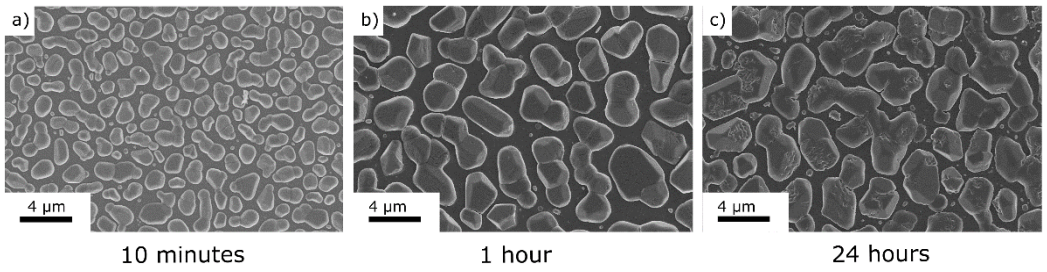

Figure 9-3: Na_2SO_4 coatings on albite glasses reacted with $SO_{2(g)}$ at 600 °C for (a) 10 minutes, (b) 1 h and (c) 14 h.

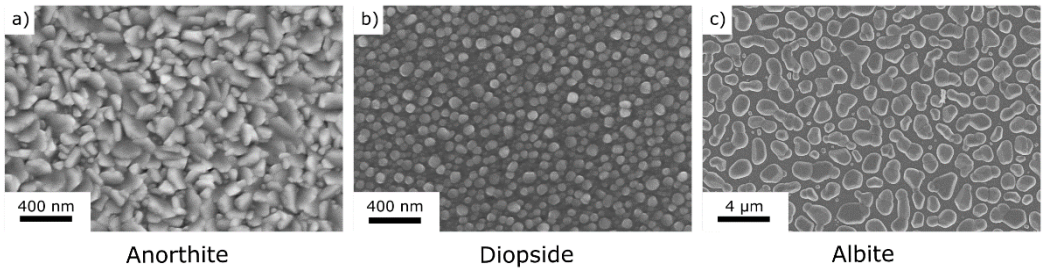

Figure 9-4: Sulfate coatings formed after 10 minutes at 600 °C on (a) anorthite glass, (b) diopside glass and (c) albite glass.

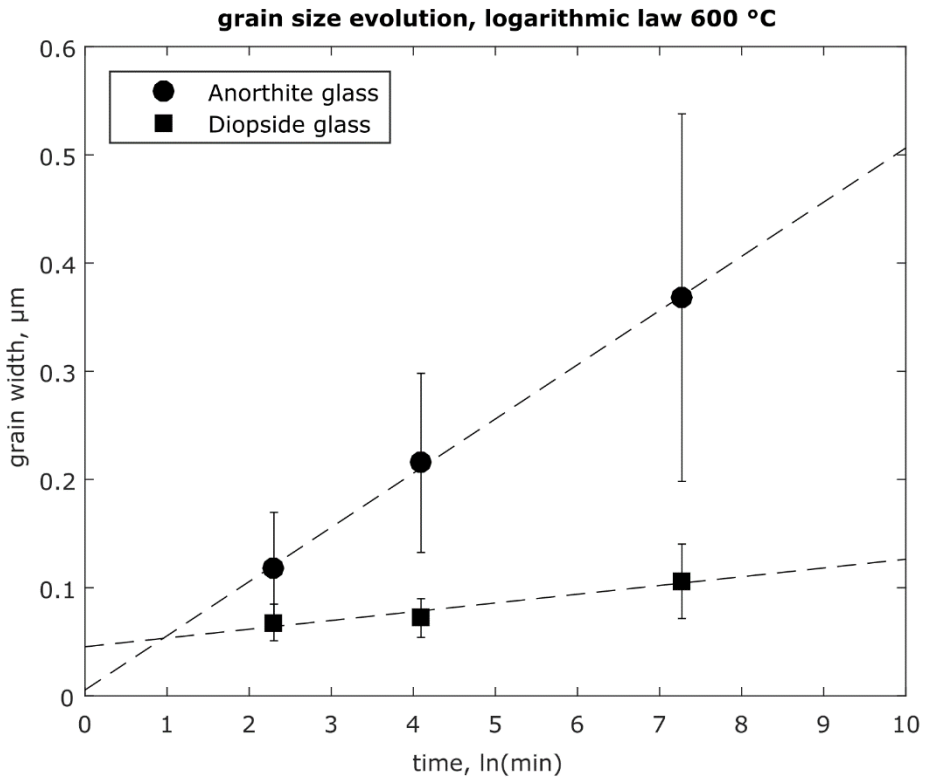

Figure 9-5: Grain size evolution of the sulfate grains on the continuously coated anorthite and diopside glasses reacted with $SO_{2(g)}$ at 600 °C. Each data point is the mean of 100 measured grain widths with one standard deviation.

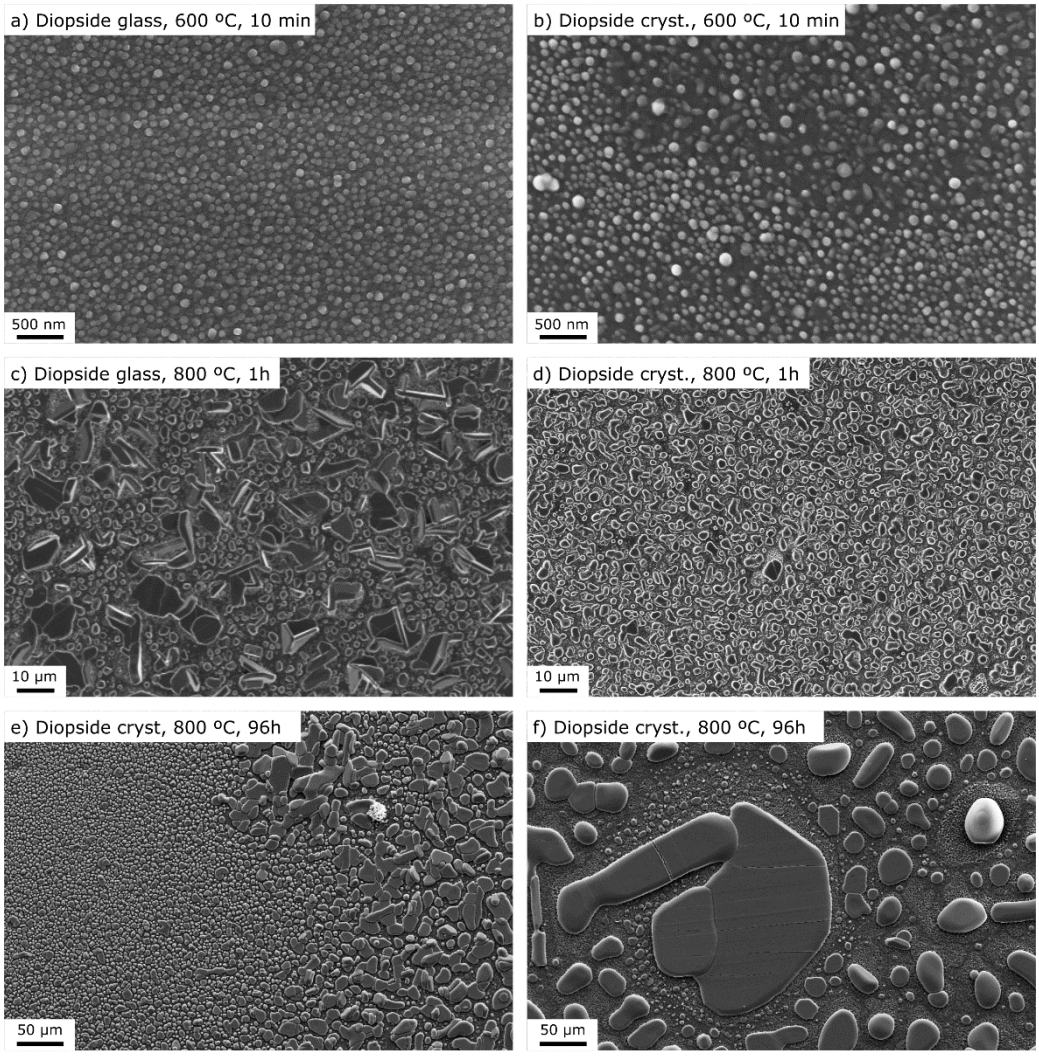

Figure 9-6: Diopside glass and diopside crystal (from Jaipur, Rajasthan, provided by Bruce Fegley) reacted with $SO_{2(g)}$; a) diopside glass, 600 °C, 10 min; b) diopside crystal, 600 °C, 10 min; c) diopside glass, 800 °C, 1h; d) diopside crystal, 800 °C, 1h; e) diopside crystal, 800 °C, 96h; f) diopside crystal, 800 °C, 96 h. All surface coating materials are anhydrite. Coatings textures on the glass and crystal are similar. Anhydrite grain sizes vary over two orders of magnitude on the diopside crystal reacted with $SO_{2(g)}$ at 800 °C for 96 h. These variations occur over the same crystal surface with constant crystal orientation. The variations may be due to defects and cracks in the crystal which allow a higher flux of Ca to the surface for the formation of $CaSO_4$.

10 Appendix to Chapter 4

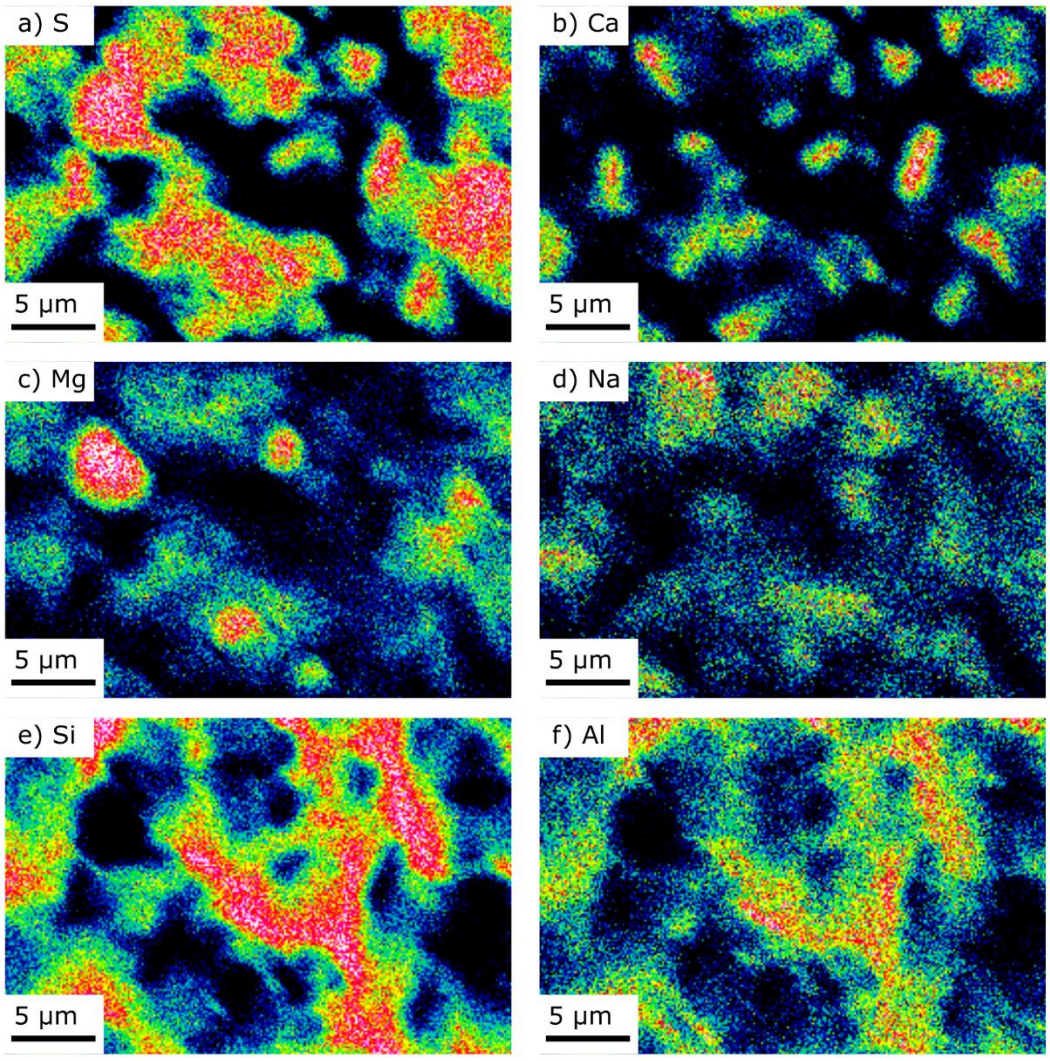

Figure 10-1: EDS maps of the coating on the Fe-free basalt glass reacted with $SO_{2(g)}$ at 700 °C for 1 h. a) S; b) Ca; c) Mg; d) Na; e) Si; f) Al.

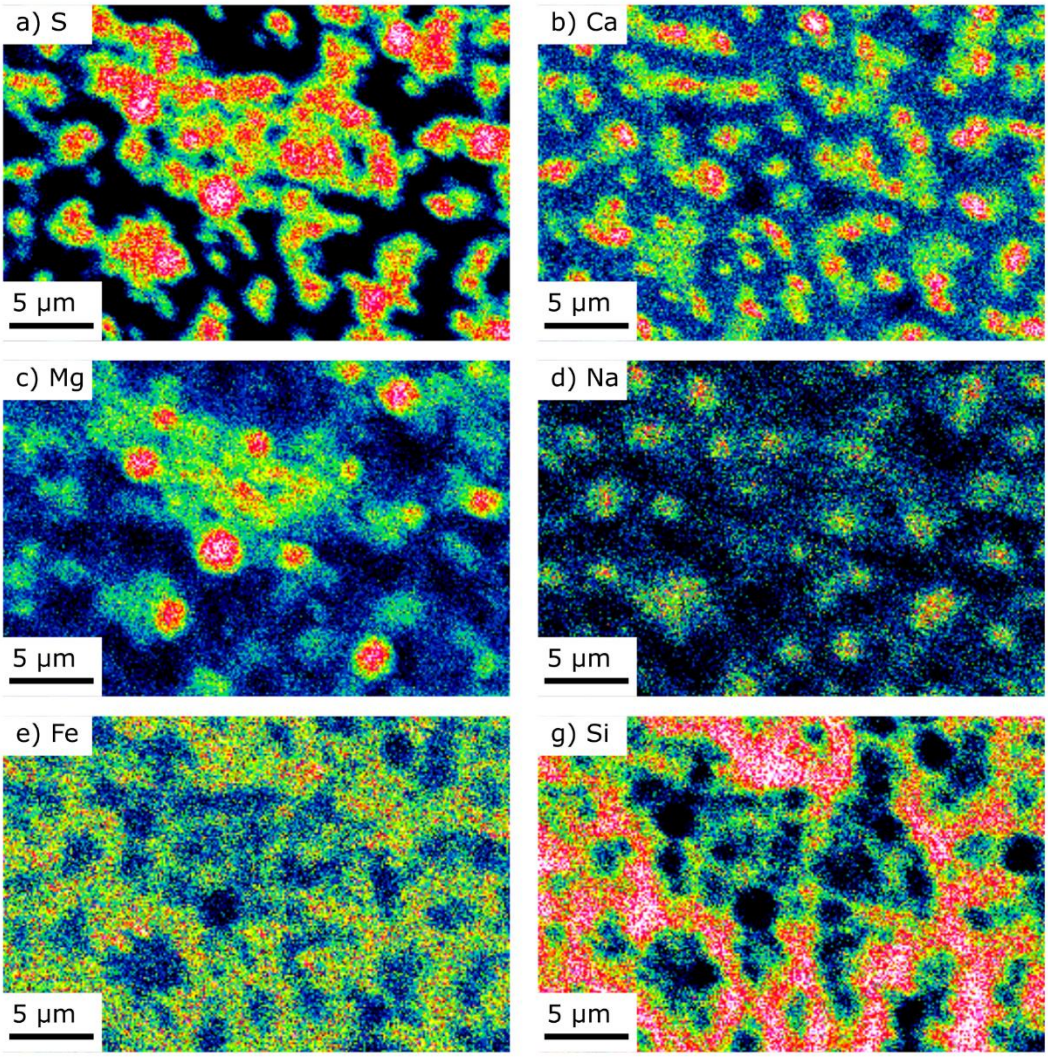

Figure 10-2: EDS maps of the coating on the tholeiitic basalt glass pre-equilibrated at NNO-1.5, reacted with $SO_{2(g)}$ at 700 °C for 1 h. a) S; b) Ca; c) Mg; d) Na; e) Fe; f) Si.

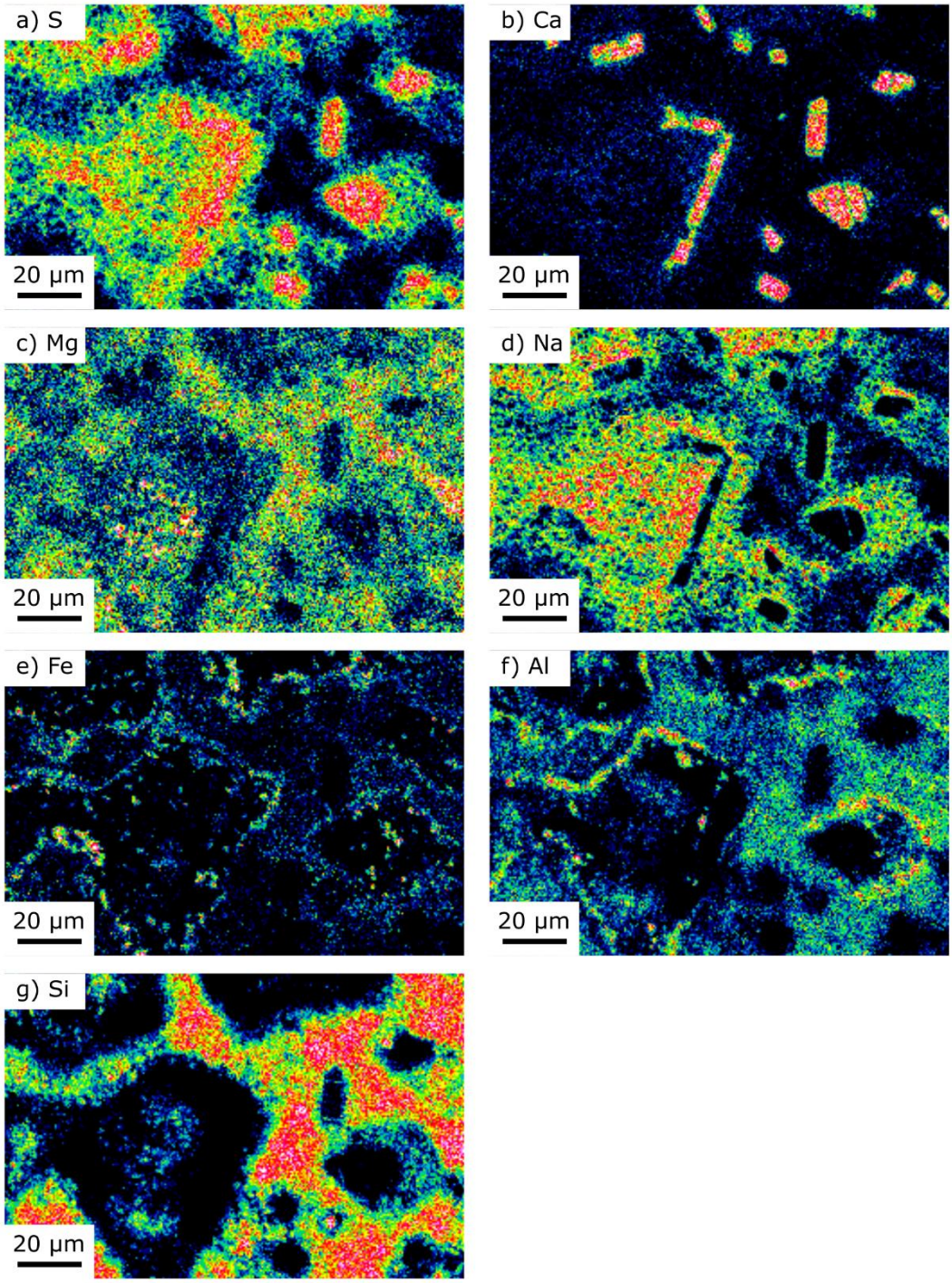

Figure 10-3: EDS maps of the coating on the tholeiitic basalt glass pre-equilibrated at NNO, reacted with $SO_{2(g)}$ at 700 °C for 1 h. a) S; b) Ca; c) Mg; d) Na; e) Fe; f) Al; g) Si.

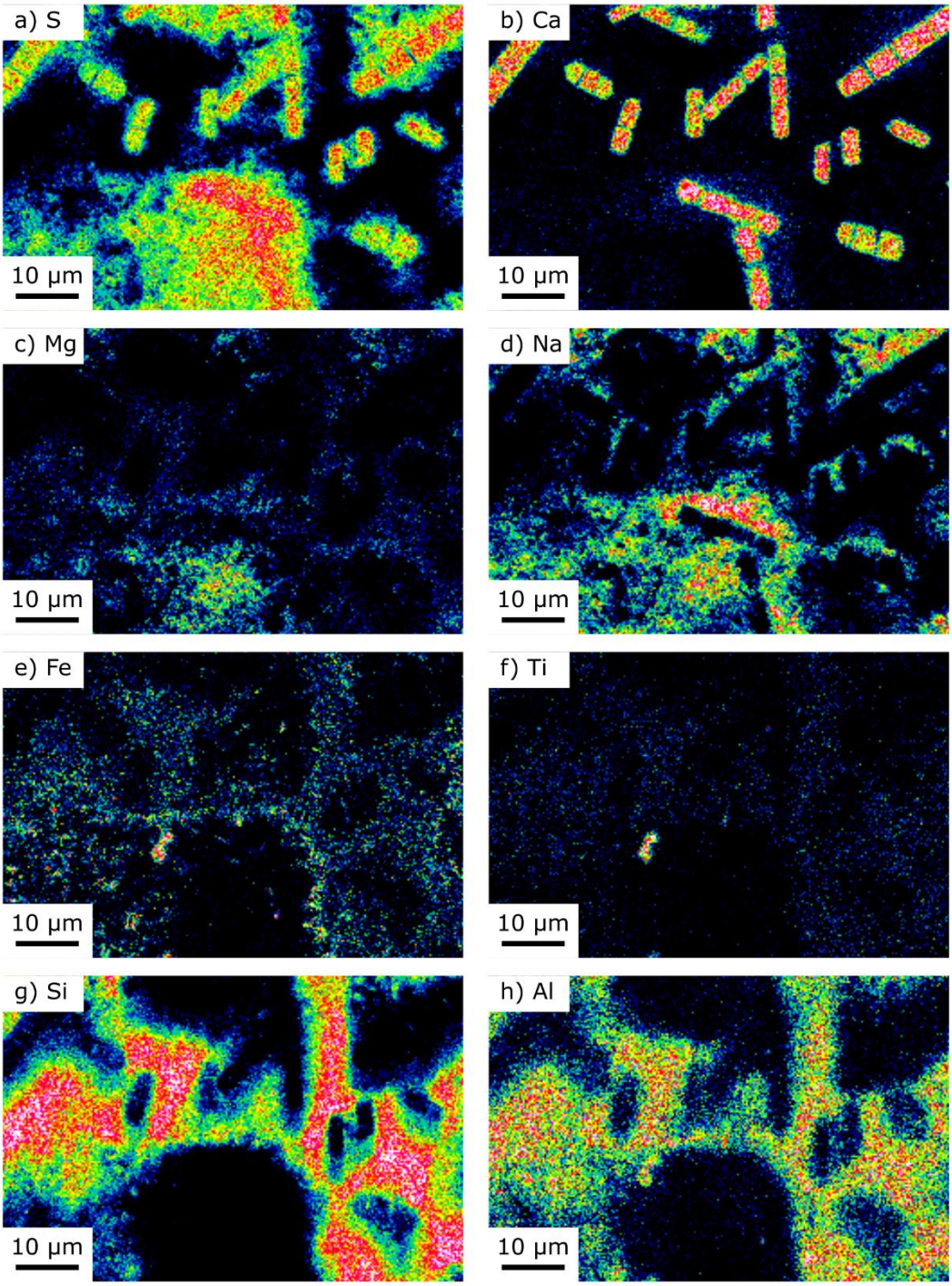

Figure 10-4: EDS maps of the coating on the tholeiitic basalt glass pre-equilibrated at NNO+1, reacted with $SO_{2(g)}$ at 700 °C for 1 h. a) S; b) Ca; c) Mg; d) Na; e) Fe; f) Ti; g) Si; h) Al.

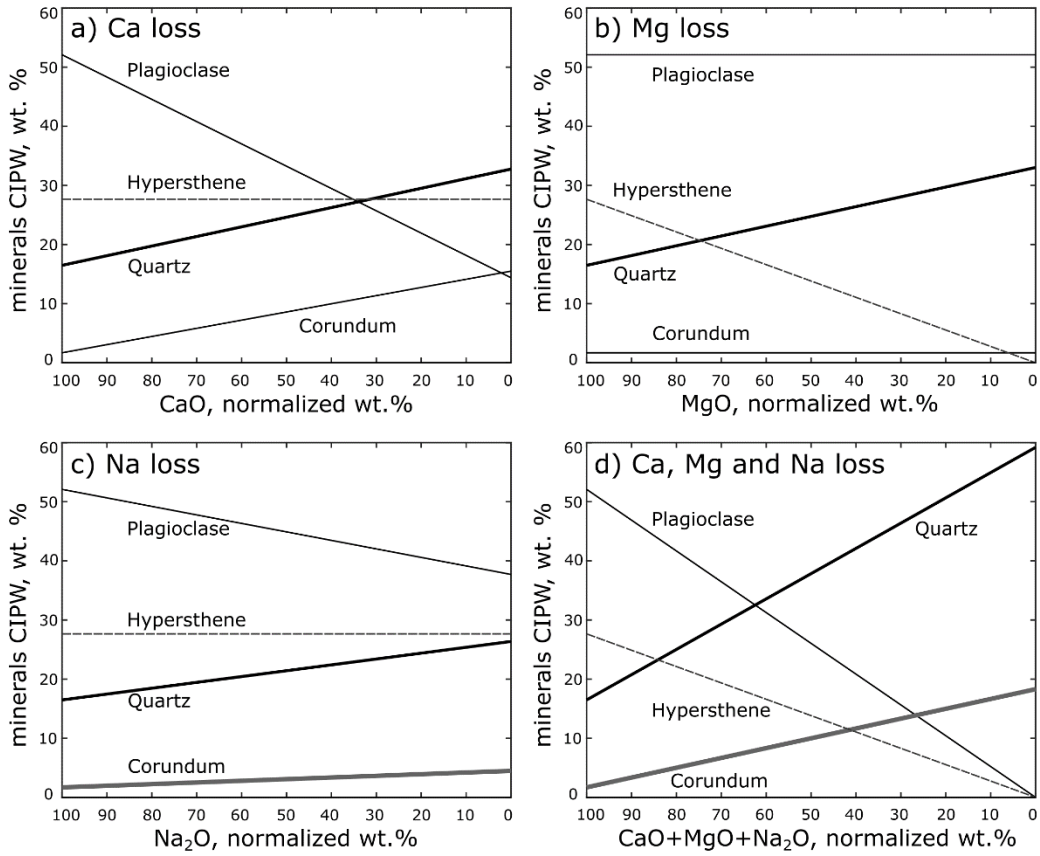

Figure 10-5: Normative mineralogy of the Fe-free basalt as a function of the loss of a) CaO, b) MgO, c) Na_2O and d) CaO+MgO+Na_2O from the glass substrate. Additionally, the normative mineralogy also includes rutile, which is not affected by the modelled compositional changes and not shown in this figure (see Table 4-1).

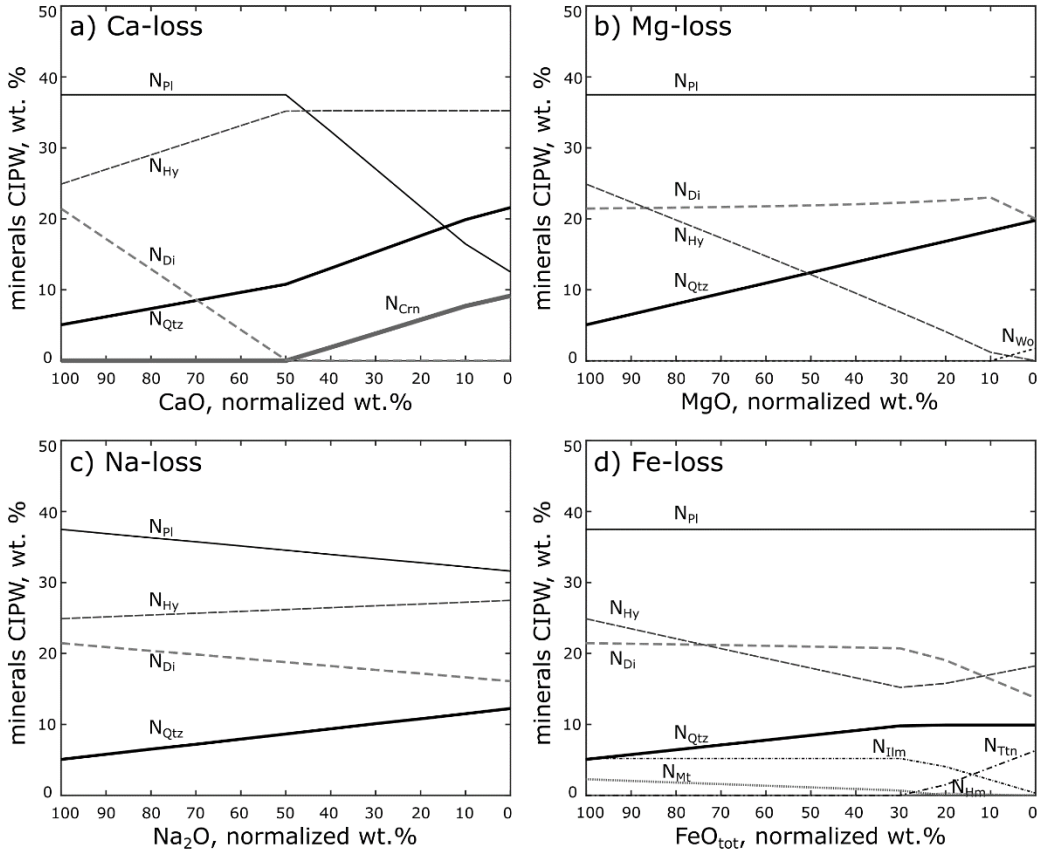

Figure 10-6: Normative mineralogy of the tholeiitic basalt pre-equilibrated at NNO-1.5, as a function of the loss of a) CaO, b) MgO, c) Na_2O and d) FeO_{tot} from the glass substrate. Additionally, the normative mineralogy includes the phases orthoclase, ilmenite, magnetite and apatite which are not affected by the modelled compositional changes and not shown in this figure (see Table 4-1).

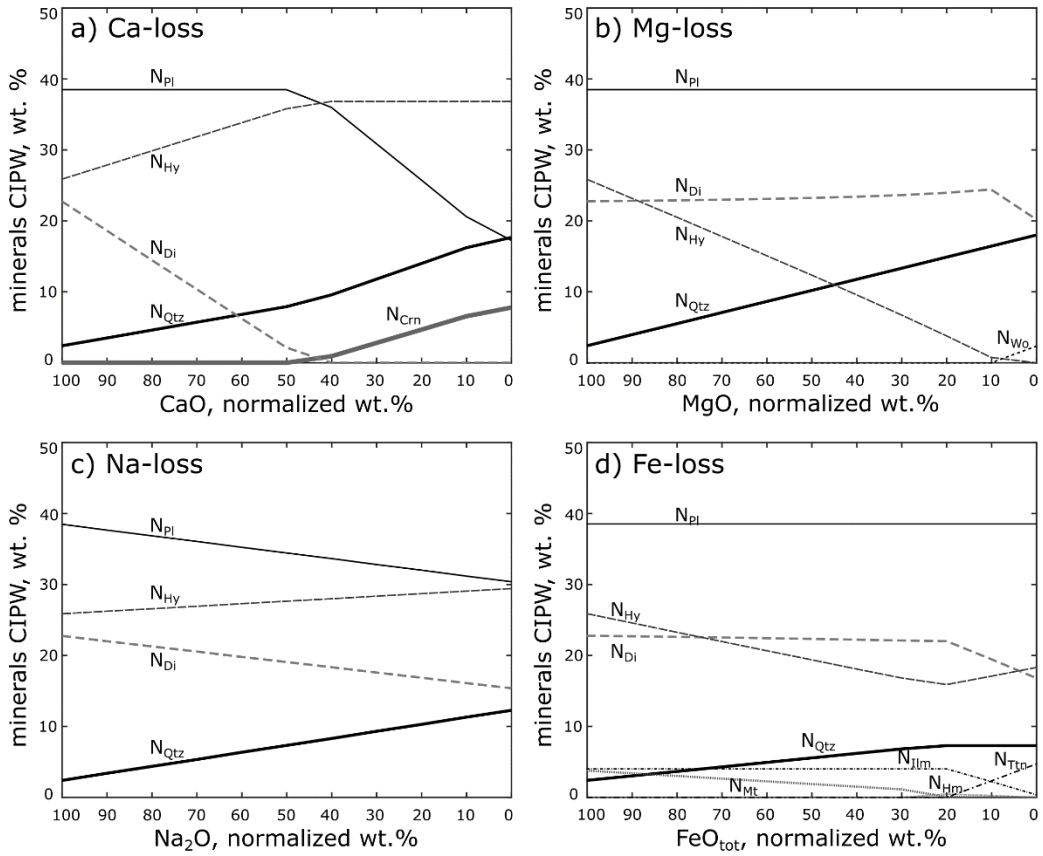

Figure 10-7: Normative mineralogy of the tholeiitic basalt pre-equilibrated at NNO, as a function of the loss of a) CaO, b) MgO, c) Na_2O and d) FeO_{tot} from the glass substrate. Additionally, the normative mineralogy includes the phases orthoclase, ilmenite, magnetite and apatite which are not affected by the modelled compositional changes and not shown in this figure (see Table 4-1).